Nonlinear approaches for phase retrieval in the Fresnel region for hard X-ray imaging

Valentina Davidoiu Ion

Numéro d'ordre :
2013-ISAL-0089

Année 2013

THÈSE

Délivrée par

L'Institut National des Sciences Appliquées de Lyon
Specialité : Images et Systèmes

DIPLÔME DE DOCTORAT

ÉCOLE DOCTORALE : Électronique, Électrotechnique, Automatique

Soutenue publiquement le 26 Septembre 2013 par

Valentina DAVIDOIU

Nonlinear approaches for phase retrieval in the Fresnel region for hard X-ray imaging

Jury

Tilo BAUMBACH	Professeur	Rapporteur
Laurent DESBAT	Professeur	Rapporteur
Peter CLOETENS	Chercheur ESRF	Examinateur
Ali MOHAMMAD DJAFARI	Directeur de recherche CNRS	Examinateur
Max LANGER	Chargé de recherche (CR2) CNRS	Invité
Bruno SIXOU	Maître de Conférence INSA	Directeur de thèse
Françoise PEYRIN	Directeur de recherche INSERM	Co-directeur de thèse

INSA Direction de la Recherche - Ecoles Doctorales – Quinquennal 2011-2015

SIGLE	ECOLE DOCTORALE	NOM ET COORDONNEES DU RESPONSABLE
CHIMIE	**CHIMIE DE LYON** **http://www.edchimie-lyon.fr** Insa : R. GOURDON	M. Jean Marc LANCELIN Université de Lyon – Collège Doctoral Bât ESCPE 43 bd du 11 novembre 1918 69622 VILLEURBANNE Cedex Tél : 04.72.43 13 95 directeur@edchimie-lyon.fr
E.E.A.	**ELECTRONIQUE, ELECTROTECHNIQUE, AUTOMATIQUE** **http://edeea.ec-lyon.fr** Secrétariat : M.C. HAVGOUDOUKIAN eea@ec-lyon.fr	M. Gérard SCORLETTI Ecole Centrale de Lyon 36 avenue Guy de Collongue 69134 ECULLY Tél : 04.72.18 60 97 Fax : 04 78 43 37 17 Gerard.scorletti@ec-lyon.fr
E2M2	**EVOLUTION, ECOSYSTEME, MICROBIOLOGIE, MODELISATION** **http://e2m2.universite-lyon.fr** Insa : H. CHARLES	Mme Gudrun BORNETTE CNRS UMR 5023 LEHNA Université Claude Bernard Lyon 1 Bât Forel 43 bd du 11 novembre 1918 69622 VILLEURBANNE Cédex Tél : 04.72.43.12.94 e2m2@biomserv.univ-lyon1.fr
EDISS	**INTERDISCIPLINAIRE SCIENCES-SANTE** **http://ww2.ibcp.fr/ediss** Sec : Safia AIT CHALAL Insa : M. LAGARDE	M. Didier REVEL Hôpital Louis Pradel Bâtiment Central 28 Avenue Doyen Lépine 69677 BRON Tél : 04.72.68 49 09 Fax :04 72 35 49 16 Didier.revel@creatis.uni-lyon1.fr
INFOMATHS	**INFORMATIQUE ET MATHEMATIQUES** http://infomaths.univ-lyon1.fr	M. Johannes KELLENDONK Université Claude Bernard Lyon 1 INFOMATHS Bâtiment Braconnier 43 bd du 11 novembre 1918 69622 VILLEURBANNE Cedex Tél : 04.72. 44.82.94 Fax 04 72 43 16 87 infomaths@univ-lyon1.fr
Matériaux	**MATERIAUX DE LYON** Secrétariat : M. LABOUNE PM : 71.70 –Fax : 87.12 Bat. Saint Exupéry Ed.materiaux@insa-lyon.fr	M. Jean-Yves BUFFIERE INSA de Lyon MATEIS Bâtiment Saint Exupéry 7 avenue Jean Capelle 69621 VILLEURBANNE Cédex Tél : 04.72.43 83 18 Fax 04 72 43 85 28 Jean-yves.buffiere@insa-lyon.fr
MEGA	**MECANIQUE, ENERGETIQUE, GENIE CIVIL, ACOUSTIQUE** Secrétariat : M. LABOUNE PM : 71.70 –Fax : 87.12 Bat. Saint Exupéry mega@insa-lyon.fr	M. Philippe BOISSE INSA de Lyon Laboratoire LAMCOS Bâtiment Jacquard 25 bis avenue Jean Capelle 69621 VILLEURBANNE Cedex Tél :04.72.43.71.70 Fax : 04 72 43 72 37 Philippe.boisse@insa-lyon.fr
ScSo	**ScSo*** M. OBADIA Lionel Sec : Viviane POLSINELLI Insa : J.Y. TOUSSAINT	M. OBADIA Lionel Université Lyon 2 86 rue Pasteur 69365 LYON Cedex 07 Tél : 04.78.69.72.76 Fax : 04.37.28.04.48 Lionel.Obadia@univ-lyon2.fr

*ScSo : Histoire, Geographie, Aménagement, Urbanisme, Archéologie, Science politique, Sociologie, Anthropologie

"In the memory of my mother!"

"Wovon man nicht sprechen kann, darüber muss man schweigen"
Ludwig Wittgenstein
"Logisch-philosophische Abhandlung"

Abstract

The development of highly coherent X-ray sources offers new possibilities to image biological structures at different scales exploiting the refraction of X-rays. The coherence properties of the third-generation synchrotron radiation sources enables efficient implementations of phase contrast techniques. One of the first measurements of the intensity variations due to phase contrast has been reported in 1995 at the European Synchrotron Radiation Facility (ESRF). Phase imaging coupled to tomography acquisition allows three-dimensional imaging with an increased sensitivity compared to absorption CT. This technique is particularly attractive to image samples with low absorption constituents. Phase contrast has many applications, ranging from material science, paleontology, bone research to medicine and biology. Several methods to achieve X-ray phase contrast have been proposed during the last years. In propagation based phase contrast, the measurements are made at different sample-to-detector distances.

While the intensity data can be acquired and recorded, the phase information of the signal has to be "retrieved" from the modulus data only. Phase retrieval is thus an ill-posed nonlinear problem and regularization techniques including a priori knowledge are necessary to obtain stable solutions. Several phase recovery methods have been developed in recent years. These approaches generally formulate the phase retrieval problem as a linear one. Nonlinear treatments have not been much investigated. The main purpose of this work was to propose and evaluate new algorithms, in particularly taking into account the nonlinearity of the direct problem.

In the first part of this work, we present a Landweber type nonlinear iterative scheme to solve the propagation based phase retrieval problem. This approach uses the analytic expression of the Fréchet derivative of the phase-intensity relationship and of its adjoint, which are presented in detail. We also study the effect of projection operators on the convergence properties of the method. In the second part of this thesis, we investigate the resolution of the linear inverse problem with an iterative thresholding algorithm in wavelet coordinates. In the following, the two former algorithms are combined and compared with another nonlinear approach based on sparsity regularization and a fixed point algorithm. The performance of theses algorithms are evaluated on simulated data for different noise levels. Finally the algorithms were adapted to process real data sets obtained in phase CT at the ESRF at Grenoble.

Keywords: Phase contrast, phase retrieval, Fresnel diffraction, coherent imaging, inverse problems, nonlinear problems, Fréchet derivative, X-ray imaging, X-ray microscopy, in-line phase tomography, nonlinear optimization.

Résumé français

Le développement de sources cohérentes de rayons X offre de nouvelles possibilités pour visualiser les structures biologiques à différentes échelles en exploitant la réfraction des rayons X. La cohérence des sources synchrotron de troisième génération permettent des implémentations efficaces des techniques de contraste de phase. Une des premières mesures des variations d'intensité dues au contraste de phase a été réalisée en 1995 à l'Installation Européenne de Rayonnement Synchrotron (ESRF). L'imagerie de phase couplée à l'acquisition tomographique permet une imagerie tridimensionnelle avec une sensibilité accrue par rapport à la tomographie standard basée sur absorption. Cette technique est particulièrement adaptée pour les échantillons faiblement absorbante ou bien présentent des faibles différences d'absorption. Le contraste de phase a ainsi une large gamme d'applications, allant de la science des matériaux, à la paléontologie, en passant par la médecine et par la biologie. Plusieurs techniques de contraste de phase aux rayons X ont été proposées au cours des dernières années. Dans la méthode de contraste de phase basée sur le phénomène de propagation l'intensité est mesurée pour différentes distances de propagation obtenues en déplaçant le détecteur.

Bien que l'intensité diffractée puisse être acquise et enregistrée, les informations de phase du signal doivent être "récupérées" à partir seulement du module des données mesurées. L'estimation de la phase est donc un problème inverse non linéaire mal posé et une connaissance a priori est nécessaire pour obtenir des solutions stables. Si la plupart de méthodes d'estimation de phase reposent sur une linéarisation du problème inverse, les traitements non linéaires ont été eux très peu étudiés. Le but de ce travail était de proposer et d'évaluer des nouveaux algorithmes, prenant en particulier en compte la non linéarité du problème direct.

Dans la première partie de ce travail, nous présentons un schéma de type Landweber non linéaire itératif pour résoudre le problème de la récupération de phase. Cette approche utilise l'expression analytique de la dérivée de Fréchet de la relation phase-intensité et de son adjoint. Nous étudions aussi l'effet des opérateurs de projection sur les propriétés de convergence de la méthode. Dans la deuxième partie de cette thèse, nous étudions la résolution du problème inverse linéaire avec un algorithme en coordonnées ondelettes basé sur un seuillage itératif. Par la suite, les deux algorithmes sont combinés et comparés avec une autre approche non linéaire basée sur une régularisation parcimonieuse et un algorithme de point fixe. Les performances des algorithmes sont évaluées sur des données simulées pour différents niveaux de bruit. Enfin, les algorithmes ont été adaptés pour traiter des données réelles acquises en tomographie de phase à l'ESRF à Grenoble.

Mots-clés: Contraste de phase, récupération de la phase du rayon X, diffraction de Fresnel, l'imagerie cohérente, problème inverse, problème non linéaire, dérivée de Fréchet, imagerie par rayons X, microscopie à rayons X, tomographie de phase en ligne, optimisation non linéaire.

Contents

List of Figures

List of Tables

I Principles

Introduction générale

La micro-tomographie par rayons X (μCT) est devenue aujourd'hui une technique incontournable en imagerie biomédicale. Elle permet de révéler les structures internes en trois dimensions de petits animaux entiers ou de matériaux, et en plus d'accéder à des informations quantitatives. La tomographie standard est basée sur l'atténuation des rayons X. La micro-tomographie par rayons X (μCT) est utilisée dans une grande variété d'applications biologiques [Davis and Wong (1996), Salomé *et al.* (1999), Nuzzo *et al.* (2002), Bayat *et al.* (2005), Chappard *et al.* (2006), Ito *et al.* (2006), Kazakia *et al.* (2008)] et en science des matériaux [Baruchel *et al.* (2000), Bonse (1999)].

Dans le domaine des rayons X durs (énergies supérieures à 6keV), un problème bien connu du contraste d'atténuation des rayons X est le manque de sensibilité et de spécificité. Par rapport aux techniques d'imagerie d'atténuation conventionnelles, le principal intérêt de l'imagerie de phase par rayons X est la possibilité d'étudier des objets avec soit une absorption négligeable ou des multi-matériaux qui ont une absorption similaire. Par ailleurs, le déphasage pour des éléments à faible Z, améliore la sensibilité avec trois ordres de grandeur [Momose *et al.* (1995)b], ce qui rend cette modalité d'imagerie attrayante pour l'imagerie biomédicale des tissus mous.

La mise au point des synchrotrons de troisième génération a ouvert la possibilité de développer de nouvelles techniques d'imagerie par rayons X basées sur l'imagerie de contraste de phase par propagation. Dans ce cas, la notion clé pour accéder à l'information de phase est une forte cohérence du faisceau de rayons X.

Une des premières mesures des variations d'intensité dues au contraste de phase par propagation a été réalisée en 1995 à l'Installation Européenne de Rayonnement Synchrotron (ESRF) [Cloetens *et al.* (1999)] (Figure 1). Une variété de méthodes de contraste de phase a été développée dans le passé et peut être classifiée ainsi: les techniques à base de cristal analyseur [Boettinger and Kuriyama (1979), Davis *et al.* (1995), Chapman *et al.* (1997), Stampanoni *et al.* (2006), Modregger *et al.* (2007)], les méthodes interférométriques [Bonse and Hart (1965), Momose *et al.* (1996)], l'interférométrie avec des grilles [David *et al.* (2002), Momose *et al.* (2003), Zanette (2011)] et les techniques basées sur la propagation [Snigireva *et al.* (1995), Cloetens *et al.* (1996)].

Si la cohérence spatiale du faisceau de rayons X est suffisante, la façon la plus simple expérimentalement d'obtenir une image de contraste de phase consiste à laisser le faisceau se propager dans l'espace libre après l'interaction avec l'objet [Snigireva *et al.* (1995), Cloetens *et al.* (1996)] (Figure 2). La relation entre le décalage de phase induit par un échantillon et l'intensité enregistrée à une distance échantillon-détecteur D repose sur la théorie de la diffraction de Fresnel. L'information de phase n'est pas explicitement accessible dans la mesure de l'intensité et elle doit être extraite. Le décalage de la phase est proportionnel à une projection de la distribution de la partie réelle de l'indice de réfraction complexe δ_r dans l'objet. En couplant la micro-tomographie et le contraste

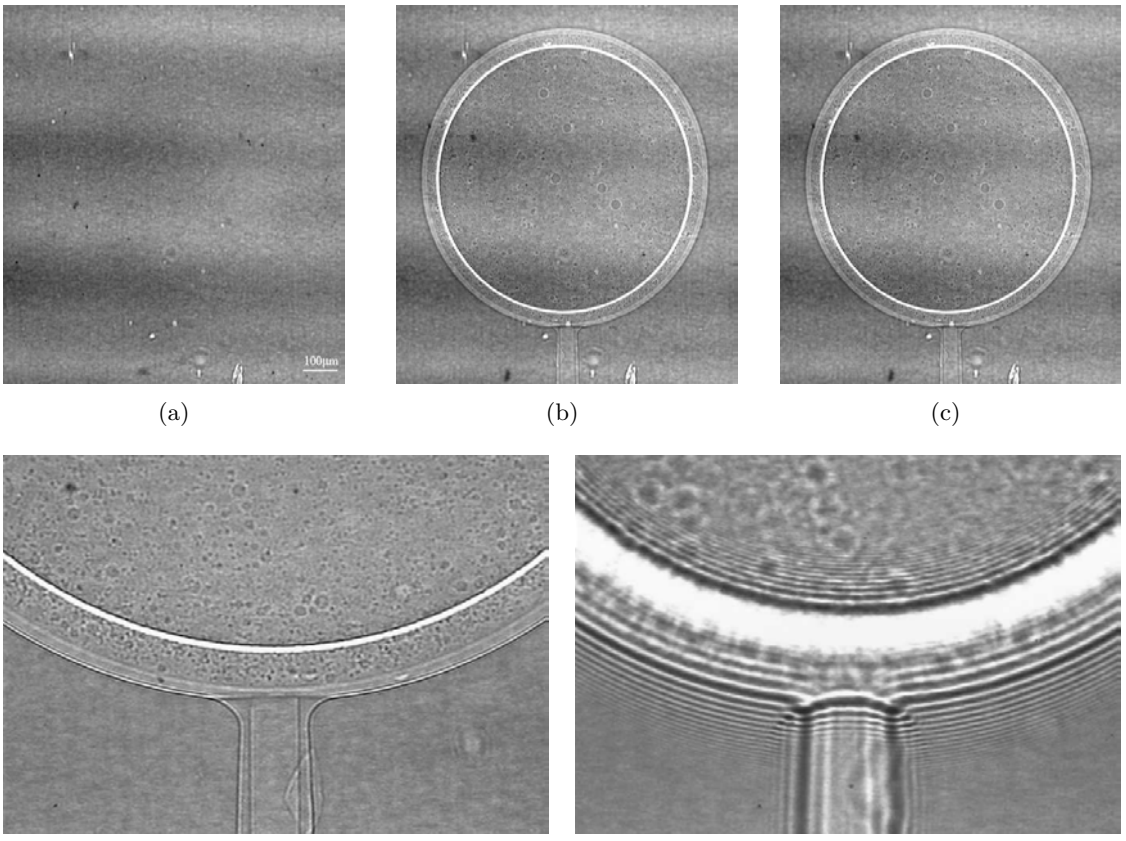

Figure 1: Des images de contraste de phase par rayons X pour un échantillon de matière à deux couches: une couche de polystyrène de 30 μm couverte d'une deuxième couche de 15 μm de parylène pour (a) $D = 0.3$ cm, (b) $D = 19$ cm et (c) $D = 83$ cm. L'acquisition des données ont été réalisées à l'ESRF pour E = 18keV. Détails de l'image pour le distances échantillon-détecteur (d) $D = 15$ cm et (e) $D = 310$ cm. Reproduit à partir de [Cloetens *et al.* (1999)].

de phase, on peut reconstruire une carte 3D de l'indice δ_r, étroitement relié à la densité électronique [Cloetens *et al.* (1997)b, Momose *et al.* (1998), Weitkamp *et al.* (2008)]. Ce processus peut être obtenu par deux étapes:

1. Dans un premier temps, le décalage de phase induit par objet est estimé pour chaque angle de projection, processus appelé estimation de phase (phase retrieval).

2. Dans un second temps, un algorithme standard de reconstruction tomographique est appliqué en utilisant les images de phase estimées, produisant de cette façon une reconstruction en 3D de δ_r.

Diverses méthodes ont été proposées dans la littérature pour résoudre le problème d'estimation de la phase [Nugent (2010)]. Les méthodes bien connues sont: l'équation de transport de l'intensité (TIE) [Nugent *et al.* (1996), Barty *et al.* (1998), Gureyev *et al.* (1999), Beleggia *et al.* (2004), Turner *et al.* (2004), Paganin (2006)] qui est basée

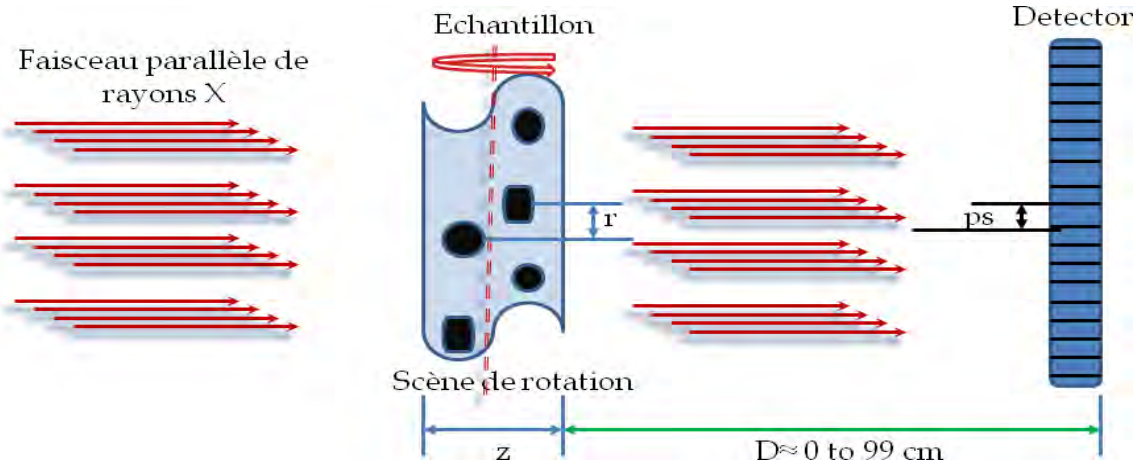

Figure 2: Montage expérimental pour la technique de contraste de phase par propagation pour un faisceau de rayons X parallèle. Le champ incident est supposé avoir un degré de cohérence élevé et passe à travers un échantillon de diamètre z. Les images de contraste de phase sont enregistrées sur le détecteur à la taille du pixel ps pour différentes distances D dans le domaine de Fresnel. r définit la taille de la plus petite microstructure interne de l'échantillon.

sur l'utilisation de mesures de l'intensité obtenues à des distances de propagation courtes (généralement deux distances D). Ces méthodes peuvent être affinées par d'autres techniques comme les algorithmes Gerchberg-Saxton-Fienup (GSF) [Fienup (1982), Gureyev (2003)]. Les autres méthodes s'appuient sur la fonction de transfert de contraste (CTF) [Guigay (1977), Cloetens *et al.* (1996), Zabler *et al.* (2005)], qui donnent de bons résultats pour une absorption faible et une phase variant lentement ou sur l'approche mixte entre les deux méthodes: TIE et CTF [Guigay *et al.* (2007)]. Toutes ces méthodes reposent sur la linéarisation de la relation entre la phase et l'intensité mesurée, valable sous certaines hypothèses restrictives, entraînant ainsi quelques approximations du problème direct de la formation de l'image de contraste de phase.

Plusieurs méthodes ont été proposées pour améliorer ces algorithmes linéaires. Langer et al. [Langer *et al.* (2010)] ont proposé d'introduire dans l'approche mixte l'a priori que la phase et l'absorption sont proportionnelles. Une approche de récupération de phase basée sur la méthode TIE utilisant une seule distance de propagation, pour un objet homogène avec un rapport entre la partie imaginaire et la partie réelle de l'indice de réfraction a été proposée par Paganin [Paganin *et al.* (2002)] et a été étendue à deux matériaux homogènes [Beltran *et al.* (2010)]. Ce type d'a priori est valable pour les objets multi-matériaux composés de plusieurs matériaux homogènes [Wu *et al.* (2005), Beltran *et al.* (2010)]. Une nouvel a priori sur la phase a été proposé dans [Langer *et al.* (2012)a]. Cet a priori est obtenu à partir de la reconstruction tomographique de l'image d'absorption à partir de l'intensité mesurée à la distance de propagation de $D = 0$ m. Cet a priori est introduit dans la gamme des basses fréquences seulement. Tout en évitant les hypothèses concernant l'objet, le bruit de basse fréquence peut être réduit et la résolution spatiale

peut être améliorée.

Malgré les limitations actuelles, ces méthodes ont trouvé de nombreuses applications en science des matériaux [Baruchel *et al.* (2006), Mayo *et al.* (2012)], en paléontologie [Tafforeau *et al.* (2006)] ou en imagerie biomédicale [Cancedda *et al.* (2007), Langer *et al.* (2012)b, Marinescu *et al.* (2013)]. Cette technique possède également un potentiel pour les applications cliniques tels que la mammographie [Castelli *et al.* (2011)] et des recherches sont en cours pour l'étendre à des de laboratoire [Mayo *et al.* (2003)].

Le problème d'estimation de phase est un problème inverse mal posé dans le sens de Hadamard, c'est à dire qu'une solution peut ne pas exister, être non unique et ne pas dépendre continuement des données. Des méthodes de régularisation sont donc nécessaires. Ce problème a reçu une attention considérable au cours des dernières années dans de nombreux domaines, par exemple, l'optique, la cristallographie par rayons X, l'astronomie ou le traitement de signal audio . Les méthodes reposant sur une linéarisation du problème direct peuvent être affinées par d'autres méthodes prenant en compte la non linéarité du problème. Récemment, de nouveaux algorithmes ont été proposés et appliqués en radiographie sur données simulées [Gureyev (2003), Moosmann *et al.* (2010), Moosmann *et al.* (2011)] et en tomographie sur des données expérimentales [Hofmann *et al.* (2011), Moosmann *et al.* (2013)]. Toutefois, la prise en compte de la non linéarité n'a pas été beaucoup étudiée dans la littérature.

Objectifs

L'objectif principal de ce travail est de proposer et d'évaluer de nouveaux algorithmes, en tenant compte de la non linéarité du problème direct. Une autre motivation importante de ce travail est également de réduire le nombre de mesures en utilisant seulement deux distances de propagation, y compris celle permettant de mesurer l'absorption.

Il s'agit donc de développer un nouveau modèle mathématique en utilisant comme point de départ les solutions obtenues par une approche linéarisée. Une attention importante a été consacrée à la solution mixte car il a été montré que c'est la solution linéaire la plus robuste. Nous avons proposé des méthodes basées sur la dérivée de Fréchet de la relation phase-intensité. Différents type d'a priori ont été considérés. Les performances des méthodes proposées en présence du bruit sont également discutées. Les méthodes non linéaires proposées sont itératives impliquant un important temps de calcul, donc une attention particulière a été consacrée à l'efficacité du calcul en raison du très grand nombre de données expérimentales utilisées. Nos algorithmes ont été évalués en utilisant à la fois des données simulées et des images réelles acquises à l'ESRF de Grenoble.

Résumé

Les grandes lignes de ce manuscrit sont les suivantes:

La partie I est un bref résumé des modalités d'imagerie par rayons X et des problèmes physiques relatifs à cette thèse. Après avoir introduit différentes notions de base, telles que la notion de *cohérence* d'un faisceau de rayons X, le chapitre 2 présente les différentes techniques de contraste de phase. Le rôle important du détecteur est également discuté. Le chapitre 3 décrit le problème direct de la formation de l'image et présente les principales méthodes linéaires d'estimation de phase dans le domaine de Fresnel, ainsi que les algorithmes non linéaires proposés récemment. Le chapitre 4 qui présente les notions du problème inverse mal posé, le principe de la régularisation de type Tikhonov, ainsi que la méthode de Landweber adaptée aux problèmes non linéaires conclut cette partie.

Dans la partie II de ce manuscrit, nous proposons de nouveaux algorithmes non linéaires itératifs d'estimation de phase à partir de la diffraction de Fresnel, reposant sur l'utilisation de la dérivée de Fréchet. Le chapitre 5 présente un algorithme non linéaire itératif de type Landweber évalué sur des images de phase 2D simulées. Cet algorithme est amélioré en exploitant une expression analytique de la dérivé de Fréchet et de son adjoint. Enfin, dans le chapitre 6, le schéma proposé précédemment est affiné en introduisant des opérateurs de projection et un nouveau type de régularisation. Il est évalué sur deux types d'images de phase.

Dans la partie III, des algorithmes exploitant des représentations multirésolution de la phase sont proposés sur l'hypothèse que la phase a une représentation parcimonieuse. Cette partie commence avec le chapitre 7, qui donne un aperçu de la théorie des ondelettes et des méthodes d'optimisation basées sur le seuillage doux. Dans le chapitre 8, une méthode d'inversion du problème linéarisé pour une seule distance de propagation, reposant sur une hypothèse de parcimonie de la phase dans l'espace ondelettes, est proposé. Cet algorithme est ensuite combiné avec la méthode non linéaire itérative présentée dans la partie II avec des opérateurs de projection. La dernière section de cette partie est consacrée à une comparaison approfondie des différents algorithmes itératifs non linéaires et des stratégies de régularisation qui peuvent être appliquées au problème d'estimation de phase à partir d'une seule distance de propagation.

La partie IV est consacrée à l'application de la méthode non linéaire développée à la reconstruction micro-tomographique de phase. Dans le chapitre 9, après avoir rappelé le principe de la tomographique, l'application de la méthode non linéaire proposée dans le chapitre 5 est évaluée tout d'abord sur des données simulées à différents niveaux de bruit, puis sur des données expérimentales acquises à l'ESRF.

Finalement, le chapitre 10 résume brièvement les travaux présentés et donne quelques perspectives.

Chapter 1

Introduction

In biomedical imaging, X-ray computed tomography (CT) has nowadays an invaluable role. The goal of X-ray CT is to reveal the three-dimensional internal structure of entire small animals or materials and to access quantitative information. Traditional CT is based on the attenuation of X-rays. X-ray microtomography (μCT) has a large variety of applications such as bone imaging [Davis and Wong (1996), Salomé *et al.* (1999), Nuzzo *et al.* (2002), Bayat *et al.* (2005), Chappard *et al.* (2006), Ito *et al.* (2006), Kazakia *et al.* (2008)] and material science [Baruchel *et al.* (2000), Bonse (1999)].

In the hard X-ray region (energies above 6keV), a well-known problem of X-ray attenuation contrast is the lack of sensitivity and specificity. Compared with the attenuation-based imaging techniques, the main interest in X-ray phase imaging is the possibility to study objects with either negligible absorption or multi-material objects which have similar absorption. Moreover, in the hard X-rays region, the phase-shift for low-Z elements improves the sensitivity with three order of magnitude [Momose *et al.* (1995)b], which makes this imaging modality attractive for biomedical imaging of soft tissues.

The availability of third-generation synchrotrons has opened the possibility to develop new X-ray imaging techniques based on phase contrast imaging. The key of phase contrast information is a highly coherent X-ray beam like that one obtained from synchrotron sources. Furthermore, for highly energetic X-rays, the phase-contrast remains strong even if the absorption is weak, which allows lowering the dose.

The X-ray phase contrast imaging technique relies on the measurement of the Fresnel diffraction intensity pattern associated to the phase shift induced by the object in the X-ray beam. The first observations which attested the unexpected large variation of intensity was

reported by Cloetens et al. at European Synchrotron Radiation Facility (ESRF) [Cloetens *et al.* (1999)] (Figure 1.1). A variety of phase contrast methods have been developed in the past and they can be roughly divide into crystal analyzer based techniques [Boettinger and Kuriyama (1979), Davis *et al.* (1995), Chapman *et al.* (1997), Stampanoni *et al.* (2006), Modregger *et al.* (2007)], interferometric methods [Bonse and Hart (1965), Momose *et al.* (1996)], grating interferometry [David *et al.* (2002), Momose *et al.* (2003), Zanette (2011)] and propagation based technique [Snigireva *et al.* (1995), Cloetens *et al.* (1996)].

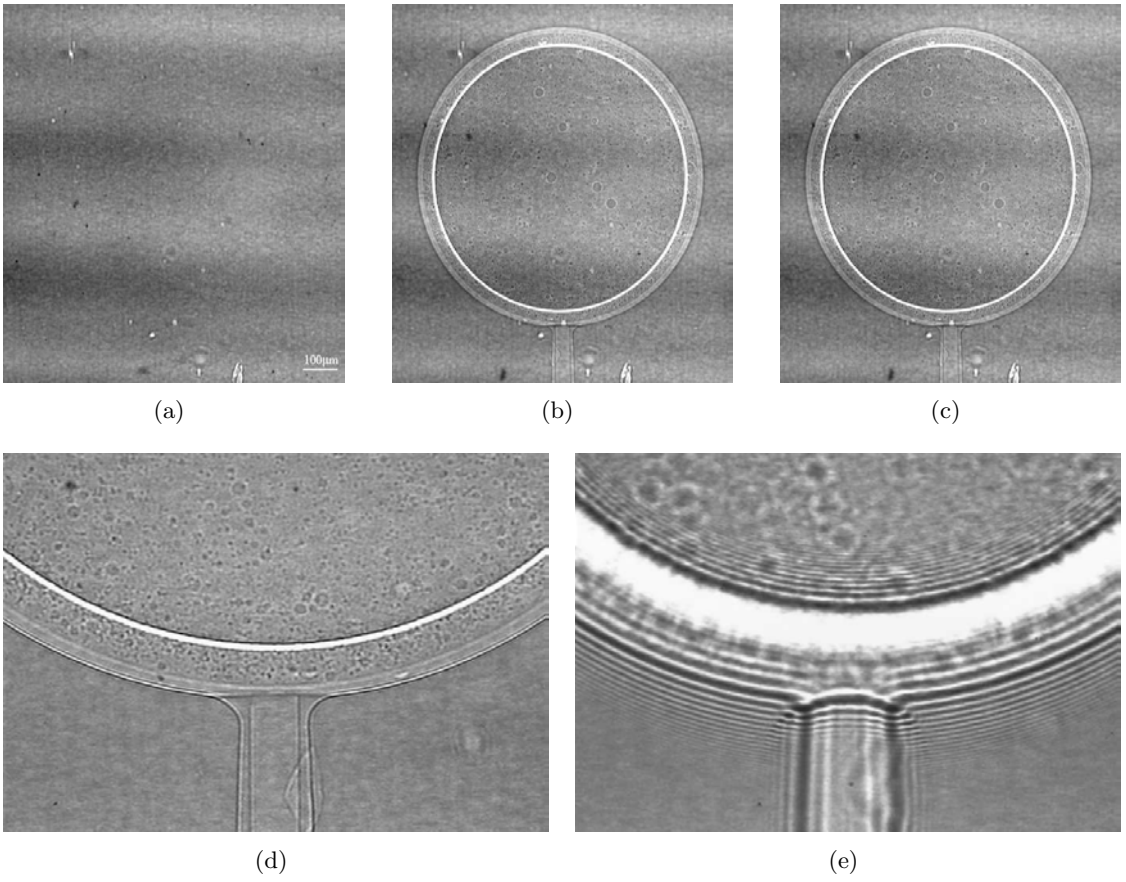

Figure 1.1: X-ray phase contrast images for a two-layered sphere sample. A 30 μm layer of polystyrene covered by a 15 μm layer parylene for (a) $D = 0.3$ cm, (b) $D = 19$ cm and (c) $D = 83$ cm. Data acquisition have been performed at ESRF for E=18keV. Image details for (d) $D = 15$ cm and (e) $D = 310$ cm. Reproduced from [Cloetens *et al.* (1999)].

If the spatial coherence of the X-ray beam is sufficient, the easiest way to get a phase contrast image is to let the beam propagate in free-space after interaction with the object [Snigireva *et al.* (1995), Cloetens *et al.* (1996)] (Figure 1.2). Phase contrast from Fresnel diffraction pattern is now a problem of paramount importance in various areas of applied physics. In several cases, such as biomaterials, bone and small animal imaging, both dense and soft tissues are present in the image object, hence strong absorption and phase contrast will be contained in the recorded images. Coupling X-ray microtomography and phase contrast allows improving the sensitivity of the method [Cloetens *et al.*

(1997)b, Momose *et al.* (1998), Weitkamp *et al.* (2008)].

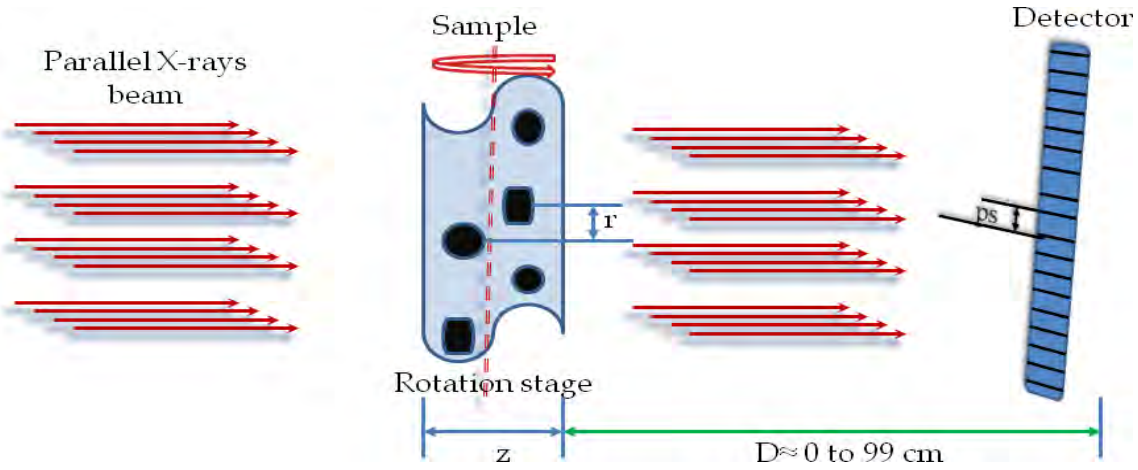

Figure 1.2: Experimental setup for propagation based technique or "in-line phase tomography" technique for a parallel X-ray beam. The incident field is assume to have a degree of partial coherence and passes through a probed sample of diameter z . Phase contrast images will be registered on the detector with the pixel size ps for different distances D in the Fresnel field. r defines the size of the smallest internal microstructures of the sample.

The relationship between the phase shift induced by a sample and the intensity recorded at a sample-to-detector distance D relies on Fresnel diffraction theory. The phase information from a diffracted wave field is not explicitly recorded in the measured intensity and must be extracted from the diffraction pattern. The phase shift is proportional to a projection of the complex refractive index distribution in the object, and therefore phase retrieval can be coupled to tomography.

The goal of hard X-ray phase tomography is to reconstruct the real part of the complex refractive index [Cloetens *et al.* (1999)]. This process can be obtained in two steps:

1. the phase shift induced by the object is first retrieved for each projection angle, process known as ***phase retrieval***

2. a standard tomographic reconstruction algorithm is applied using the phase projections, yielding in this way a 3D reconstruction of the refractive decrement index δ_r.

A variety of methods for the phase retrieval problem have been proposed in the literature and reviewed by Nugent [Nugent (2010)]. Well-known methods are the *Transport of Intensity Equation (TIE)* [Nugent *et al.* (1996), Barty *et al.* (1998), Gureyev *et al.* (1999), Beleggia *et al.* (2004), Turner *et al.* (2004), Paganin (2006)] which is based on the use of a series of image measurements obtained at different short propagation distances (usually two distances D). These methods can be refined by other techniques like Gerchberg-Saxton-Fienup algorithms (GSF) [Fienup (1982), Gureyev (2003)]. The others methods rely on the *Contrast Transfer Function (CTF)* [Guigay (1977), Cloetens *et al.*

(1996), Zabler *et al.* (2005)], which gives good results for weak absorption and slowly varying phase or on the *mixed* approach between the two former methods [Guigay *et al.* (2007)]. All these approaches rely on a linearized relation between the phase and the intensity valid under some restrictive assumptions, thus involving some approximations of the direct problem of phase contrast image formation. Several methods have been studied extensively. Langer et al. [Langer *et al.* (2010)] have proposed to introduce in the mixed approach the prior that the phase and the absorption are proportional on the retrieved phase. A single-distance phase retrieval approach using TIE method for a homogeneous object for a given ratio of the imaginary to the real part of the refractive index has been developed by Paganin [Paganin *et al.* (2002)] and extended to two homogeneous materials in [Beltran *et al.* (2010)]. This type of prior is valid for multi-material objects comprised of several homogeneous materials [Wu *et al.* (2005), Beltran *et al.* (2010)]. A new inversion method where a prior phase estimate at each projection angle is obtained from an approximate absorption index map evaluated with the intensity measured for a propagation distance D=0 m is described in [Langer *et al.* (2012)a]. This prior is introduced in the low-frequency range only.

Despite current limitations, these methods have found various applications in material science [Baruchel *et al.* (2006), Mayo *et al.* (2012)], paleontology [Tafforeau *et al.* (2006)] or biomedical imaging [Cancedda *et al.* (2007), Langer *et al.* (2012)b, Marinescu *et al.* (2013)]. This technique has been also extended to laboratory sources [Mayo *et al.* (2003)] and clinical experience for mamography [Castelli *et al.* (2011)].

Furthermore, this phase retrieval problem is an inverse ill-posed problem in the sense of Hardamard, i.e. a solution may not exist, be non-unique and not depend continuously on the data and hence regularization methods are required for a precise phase recovery. Such a problem has received considerable attention over the last years in many fields e.g., optics, X-ray crystallography, astronomy or speech processing.

The limitations of linear methods due to the linearization of the direct problem can be refined by other methods which take into account the nonlinearity of the phase problem. While avoiding object assumptions, the low frequency noise can be reduced and the spatial resolution can be improved. Recently, new algorithms that take into account this aspect for the radiographic case have been proposed [Gureyev (2003), Moosmann *et al.* (2010), Moosmann *et al.* (2011)] for simulated data and applied for the tomographic case [Hofmann *et al.* (2011), Moosmann *et al.* (2013)] for experimental data. Yet, the effects of the nonlinearity have not been much investigated in the literature.

Objectives

The main purpose of this work was to propose and evaluate new algorithms, in particularly taking into account the nonlinearity of the direct problem. These methods are based on the Fréchet derivative of the phase-intensity relationship. The introduction of

prior information to regularize the problem was particularly investigated.

The objective was to develop a new mathematical model using as input the former linear phase solutions in order to improve the resolution and decrease low frequency noise without any object assumptions. An important attention was dedicated to the mixed solution since it has been demonstrated to be the most robust linear solution. One the other hand an important motivation was also to reduce the number of measurements by using only two distances, including the absorption one. The performance of the proposed methods in presence of noise is also discussed.

Moreover, the nonlinear proposed methods are iterative involving important computational time, therefore special attention was devoted to computing efficiency due to the large experimental data set. Our algorithms were evaluated using both simulated data and real images obtained at the ESRF in Grenoble.

Outline

The outline of this manuscript is the following:

Part I is a short summary of the X-ray imaging modalities and of the physics problems relevant to this thesis. An overview of the key property (*coherence*) of the third generation synchrotron sources together with the most common phase-contrast imaging techniques is given in Chapter 2. The important role of the detector in X-ray imaging is also discussed. Chapter 3 outlines the direct problem of image formation and the main linear methods of phase retrieval in Fresnel field, but also the nonlinear algorithms proposed for the in-line phase contrast technique. Chapter 4 concluded this part, where details of well-posed and ill-posed inverse problems, Tikhonov regularization scheme together with the Landweber iteration method extended to nonlinear problems are given.

In the second Part of this manuscript, nonlinear iterative phase retrieval algorithms from Fresnel diffraction patterns using the Fréchet derivative for microradiography are detailed. We give the foundation of the nonlinear ill-posed problem and we propose a Landweber type iterative algorithm and the mathematical expression of the Fréchet derivative matrix and analytical in Chapter 5. Finally, in Chapter 6 the previously proposed scheme is refined by introducing projection operators and a new regularization scheme for two types of varying phases is described.

In Part III, under the assumption that the phase has a sparse representation, a new linear iterative algorithm is proposed for the radiographic case. This part starts with the Chapter 7, where an overview of wavelet theory and an iterative optimization method are given. In Chapter 8 an iterative thresholding algorithm in wavelet coordinates for a single propagation distance is presented first. This algorithm is then combined with the previously proposed iterative nonlinear method with a Tikhonov regularization and projection operators in Section 8.2. The last section of this part is devoted to an extensive comparison of the various nonlinear iterative algorithms and regularization strategies that

can be applied to the phase retrieval problem using one single propagation distance.

Phase microtomographic reconstruction is performed in Part IV using the nonlinear algorithm with Tikhonov regularization. First, the principles of tomography are reviewed in Chapter 9, followed by the phase tomography for simulated data at different levels of noise. Finally, the nonlinear algorithm is applied for experimental data. The last Chapter 10 of this manuscript is devoted to briefly summarize the presented work and to give some perspectives.

Chapter 2

Imaging with hard X-rays

Contents

In this chapter we briefly present the physical properties of the 3^{rd} generation synchrotron radiation (SR) sources followed by an overview of the spatial and temporal *coherence* property. The important role of the detector in phase imaging techniques is discussed in Section 2.1.3. Section 2.2 reports the X-rays interaction with matter and the phase contrast formation phenomenon. The description of the most common phase-contrast imaging techniques using SR is given in Section 2.3.

2.1 The 3^{rd} generation synchrotron sources

2.1.1 What is a synchrotron?

Worldwide there are more than 70 synchrotrons radiation sources (http://www.lightsources.org) exploring several scientific areas. The advent of the third generation synchrotron X-ray sources has revolutionized all aspects of X-ray sciences [Millson (2002), Bilderback *et al.* (2005), Namkung (2010)]. Synchrotron applications can be performed in varoius fields, such as:

- Applied materials science (imaging materials at nanoscales, defining intelligent polymers, light metals and alloys)
- Engineering (imaging different samples at different scale in real time at high resolution)
- Chemistry (catalysts operation in large chemical processes)
- Structural biology (crystallography and cell biology)
- Life sciences (animal and plant imaging)
- Environment(toxicology and atmospheric research)
- Medicine (high resolution imaging for micro and nano biology samples, the understanding of the disease mechanisms).

Figure 2.1: Hand with Rings: print of Wilhelm Röntgen's first medical X-ray, of his wife's hand (https://www.nlm.nih.gov/dreamanatomy/da_g_Z-1.html).

The X-rays were discovered in 1895 by W.C. Rontgen. It has soon be observed that they were able to pass through the human body (Figure 2.1). Since their discovery, X-rays have helped to solve many problems over the last century. In 1912, M. von Laue and P. Knipping obtained the first diffraction pattern of a crystal using X-rays. The emission of

synchrotron light was first observed in 1947 at General Electric in the USA and has been reported as undesirable, but after 1960s synchrotron radiation began to be recognized as an exceptional tool for condensed matter research.

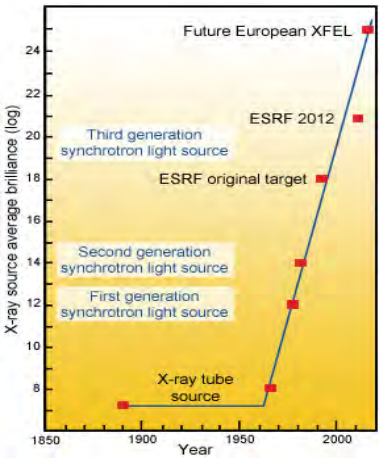

Figure 2.2: Evolution of the brilliance of the X-ray sources (http://www.esrf.eu/).

Throughout history synchrotron sources have undergone several stages of development (Figure 2.2). The establishment of SURF (Synchrotron Ultraviolet Radiation Facility) at NBS (National Bureau of Standards) began the first generation of synchrotron-radiation facilities, followed by the second-generation facilities in 1971 in U.K. at the Synchrotron Radiation Source (SRS) at the Daresbury Laboratory. This invaluable tool led to the construction in the late 1980s and early 1990s of the European Synchrotron Radiation Facilities (ESRF) in Grenoble, France and shortly thereafter of other two *third-generation* synchrotrons the Advanced Photon Source in the United States and SPring-8 in Japan.

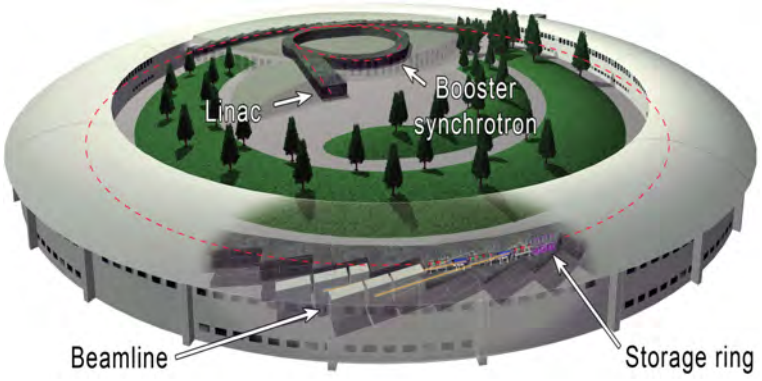

Figure 2.3: Principal structures of the European Synchrotron Radiation Facilities (ESRF) (http://http://www.esrf.eu/)

A typical synchrotron facility can be defined as a source of brilliant light produced by using powerful electro-magnets and radio frequency waves to accelerate electrons to extremely high energy. The interaction between the synchrotron beam and the matter is observed at the end stations at the corresponding beamline. Figure 2.3 presents the

internal structures of the *third-generation* synchrotron. The principal structures of a synchrotron are: 1. Electron gun, 2. Linac, 3. Booster ring, 4. Storage ring, 5. Beamline and 6. End station.

The storage ring is a closed-loop vacuum pipe where electrons are circulated nearly to the speed of light. Along this pipe, wiggler or undulators are inserted in the straight sections (Figure 2.4). Consequently, the synchrotron light is produced when the electrons in the storage ring are accelerated transversally by either bending magnets or insertion devices. They are kept circulating in closed orbited by a sophisticated system of magnetic electron optics. The insertion devices have been added to the synchrotron with the aim to improve the brilliance of the radiation.

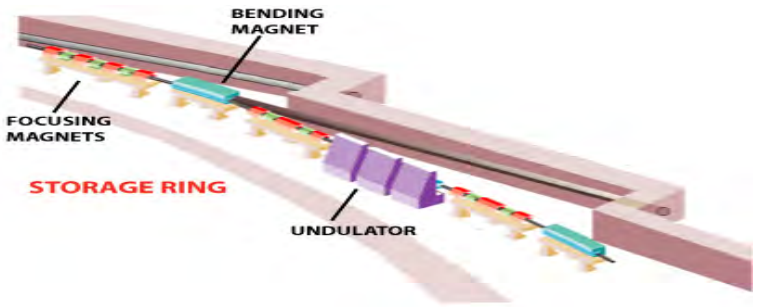

Figure 2.4: The ESRF storage ring includes in alternating order 32 curved and 32 straight sections. The path of the electrons is forced into a racetrack-shaped orbit by two large bending magnets, inserted in each curved section. The electrons are kept close to their ideal orbital path by several focusing magnets placed in each straight section. The undulators are placed in straight sections, there where the intense X-ray beams are produced (`http://www.esrf.eu/`).

A *wiggler* is a multipole magnet made up of a periodic series of magnets which has the role of laterally accelerating the charged particle beam. The electrons will *wiggle* and create a curved trajectory with a smaller local radius of curvature with respect to the bending magnet. The emitted radiation is the incoherent sum of the radiation emitted by each individual pole, therefore the total intensity is higher due to the contribution of many magnet dipoles. Furthermore, the wavelength (λ) is inversely proportional to frequency which is directly proportional to energy, hence, the wiggler creates a wavelength of light with a larger energy.

Undulators consists of a periodic structure of dipole magnets which makes them very similar to wigglers. In this case the wiggling angle of the electrons traversing the periodic magnet structure is close to the photon natural emission angle. Between the photons emitted at different points along the orbit, the radiation displays interference patterns which lead to narrow energy bands. Moreover, for an undulator with N poles the emitted radiation is mainly composed by a fundamental wavelength, hence the intensity is directly proportional to the square of the number of poles N^2. Some other useful information concerning synchrotron radiation and the insertion devices can be found in [Onuki and

Elleaume (2002), Clarke (2004), Hofmann (2004)].

The quality of the synchrotron sources can be quantitatively measured by a parameter, the *brilliance*, which is directly proportional to the *brightness* of the source and indirectly proportional to the source size (S_x,S_y), where S_x and S_y are the dimensions of the transverse area of the source. This quantity can be write as $brilliance = \frac{brightness}{S_x S_y}$ and the *brightness* can be expressed as following [Raoux (1993)]:

$$B(photons/sec/mrad^2/\frac{\Delta\lambda}{\lambda} = 10^{-3}) = 1.327 * 10^{13} {E_p}^2[GeV] I[A] H_2(\frac{\lambda_c}{\lambda}) \tag{2.1}$$

where E_p defines the particle energy, I the current in the storage ring and H_2 a dimensionless function of the reduced variable $\frac{\lambda_c}{\lambda}$, where λ_c represent the critical wavelength and the maximum of the H_2 function. Brightness can be understood also as being the quantity that takes into account the number of photons and their concentration. Increasing the brightness of the X-ray sources is equivalent to increase the flux, meaning that more signal is available for the experiments. New projects for new powerful high brilliant X-ray sources are developed and a short history of the brilliance evolution is reported in (Figure 2.2).

2.1.2 What is *coherence*?

An important aspect of the 3^{rd} X-ray generation sources is the high degree of partial coherence property of the X-ray beam. Optical coherence exists if the phase differences between all pairs of points of the signal have definite values and are constant in time.

Why is coherence so important? A wave can be characterized by its capacity to produce interference and diffraction phenomena. "Coherence" is the wave property that makes possible the observation of the interference and diffraction phenomena.

For simplicity, let us considering the fact that the diffraction phenomenon is produced by a circular slits of diameter d. If the wave source is a point source that emits a single wavelength λ with a single frequency $f = c/\lambda$. This phenomenon is a series of circular fringes at the detector (Figure 2.5). Therefore, we conclude that a single-wavelength (monochromatic) point source is a coherent source.

Two types of coherence are distinguished: 1) longitudinal (temporal) coherence which is related to the monochromaticity of the source and 2) transverse (spatial) coherence related to the physical size of the source. The concepts of spatial and temporal coherence are illustrated in Figure 2.5 and are important in discussing the phase characteristics of imaging system. In general, the stability and the predictability of X-ray phase are related to coherence property of the beam.

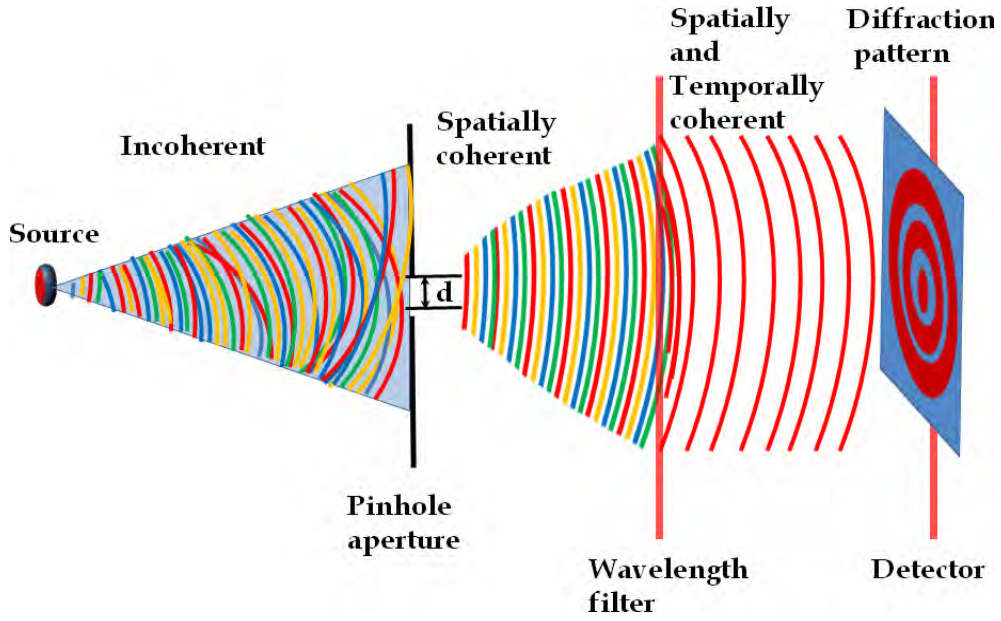

Figure 2.5: Light wave coherence. An incoherent light source emits spherical wavefronts. A small pinhole aperture focused and passes through the spherical wavefronts improving the spatial coherence of the source. Light emitted by the source pass then through a filter to yield monochromatic light, achieving in this way temporal and spatial coherence. This phenomenon is a series of circular fringes at the detector.

Transverse (spatial) coherence - the "diffraction limit"

The spatial coherence is related to the source size and gives information on how uniform the phase of the wavefront is. Spatial coherence is the cross-correlation between two points in a light wave for all times (Figure 2.6(b) $\Delta\Phi(A_1 : A_2)$). A wave is perfectly spatially coherent if has only 1 value of amplitude over an infinite length.

Let us assume that we have two point sources P_1 and P_2 placed at a distance s one from each other (Figure 2.7(a)). The fringes patterns produced by each point source are received superimposed on the detector. If the distance source-pinhole is denoted D, then the centers of the two fringes patterns are at a distance of s/D from each other [Margaritondo *et al.* (2003)]. It is known from the elementary theory of diffraction that the angular distance between two adjacent fringes is $\approx \lambda/d$ radians. If $\lambda > s\left(\frac{d}{D}\right)$, the superimposed sets of fringes are visible but blurred. This condition ensures *spatial coherence* or *lateral coherence* [Margaritondo *et al.* (2003)]. Since, the "illumination angle" γ_s of the two slits is $d/D \approx \gamma_s$, the spatial coherence equation becomes:

$$\lambda > s\gamma_s. \tag{2.2}$$

This equation means that the spatial coherence can be enhanced if the source size s is reduced.

Another important parameter for spatial coherence is the source *angular collimation*

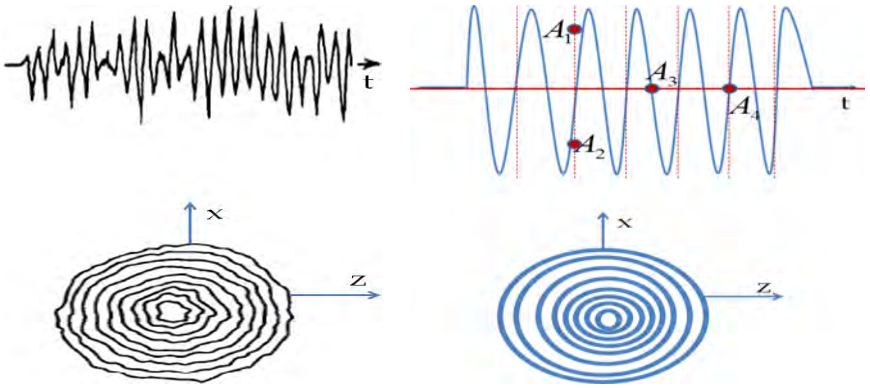

(a) (b)

Figure 2.6: Time dependence and wavefronts of (a) random light and (b) coherent light like monochromatic spherical wave. *Temporal* coherence measures the correlation between the phases of the light wave at different points along the direction of propagation ($\Delta\Phi(A_3 : A_4)$). *Spatial* coherence is the cross-correlation between two points in the light wave for all times ($\Delta\Phi(A_1 : A_2)$)

.

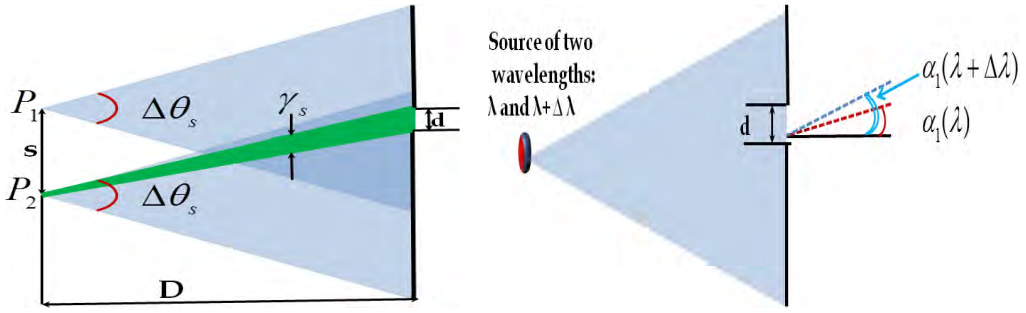

(a) (b)

Figure 2.7: Simplified analysis of (a) spatial coherence and (b) temporal coherence.

$\Delta\theta_s$. The spatial coherence can be increased by increasing the brightness, meaning that the source geometry parameters s and $\Delta\theta_s$ have to be decreased. If $\lambda = s\Delta\theta_s$ then the *diffraction limit* is reached and the source is *fully coherent*. In practice, no source exceeds the diffraction limit and they correspond to full spatial coherence and maximum brightness.

Longitudinal (temporal) coherence

Temporal coherence is a measure of the correlation between the phases of a light wave at different points along the direction of propagation (Figure 2.6(b) $\Delta\Phi(A_3 : A_4)$). This coherence condition tells us how *monochromatic* a source is, i.e., it gives information about its bandwidth $\Delta\lambda$. Suppose a point source emitting only two wavelengths, λ and $\lambda + \Delta\lambda$, which at some point in space constructively interfere (Figure 2.7(b)). If $\Delta\lambda/\lambda \ll 1$ the fringes are difficult to observe, but they are still visible. This equation gives the condition

of *longitudinal coherence* or *temporal coherence*. The same reasoning can be applied to two waves with wavelength λ and $\lambda + \Delta\lambda$, which will destructively interfere after some optical path length $l_c \approx \lambda^2/(2\Delta\lambda)$, where l_c is called the coherence length. This parameter l_c can be understood by looking at the two wave patterns at a specific point: if the two waves are in phase at this point in space they will be out of phase beyond this point. Moreover, the minimum on the wave with wavelength λ will coincide with the maximum of the wave with wavelength $\lambda + \Delta\lambda$ after a distance l_c. We can conclude that a synchrotron source is monochromatic when the source is bright, therefore the temporal coherence is more directly connected to the brightness than the spatial coherence.

2.1.3 Detector and phase contrast

A limiting factor in exploring the full potential of the X-ray synchrotron facilities is the detector resolution rs. The detector is the key feature to observe X-ray phase contrast. The detection of the studied sample is correlated to the pixel size, the noise level and the efficiency of the digital system used to image this object. The gain of the detector is quantified by the detective quantum efficiency (DQE) parameter defined as [Rose (1946)]:

$$DQE = \frac{{SNR_{out}}^2}{{SNR_{in}}^2} \tag{2.3}$$

where $SNR_{out} = \sqrt{N_0(1 - a\mu)}$ is the output signal-to-noise ratio and $SNR_{in} = \sqrt{N_0}$ is the input signal-to-noise ratio of the system. a denotes the detector thickness, N_0 the gamma ray photons and μ the linear attenuation coefficient. In practice $DQE \neq 1$ due to the imperfection of the optical apparatus. Two types of detectors are commonly used: photographic film and charge coupled devices (CCDs). CCDs are characterized by large dynamic range, high spatial resolution and fast data acquisition. CCDs are most commonly used instead of the photographic films because they are able to capture a large number of two-dimensional frames with a fixed field of view, even if the photographic films offer nearly infinite field of view and better resolution ($\approx 1\mu$m), but due to the nonlinearity of the detector with the incident wave their applicability is limited.

Principles of the detector system

Currently most experiments are performed with high quality X-ray CCD systems [Bravin (2003), Phillips *et al.* (2002)] in order to obtain phase contrast images. The conversion from the incident X-ray to the visible spectrum of radiation is realized with a phosphor screen. When the conversion is achieved, visible light photons with a defined wavelength are emitted thanks to the scintillator element. The spatial resolution in the detected image is fixed by an additional converting optics system. The detection system components are: scintillator, magnifying lens system, mirror and CCD camera (Figure 2.8).

The general operation principle of the detection system is described below. The photons from the scintillator output are designed with the first set of lens (Lens I in Figure 2.8) into an image at infinity, which will then be deflected by the plane mirror, positioned between the two sets of lens, with an angle of 90 degrees into the vertical direction. The mirror image will be then the input of the second set of lens (Lens II in Figure 2.8) as an image to infinity. The chip of a CCD sensor will register the image obtained using the output of Lens II, and this image will represent the intensity image used in retrieving the phase map of the X-ray wave. The formalism of the image formation of Fresnel diffraction is described in Section 2.2, but first a brief description of scintillator is given since this component is critical in synchrotron imaging.

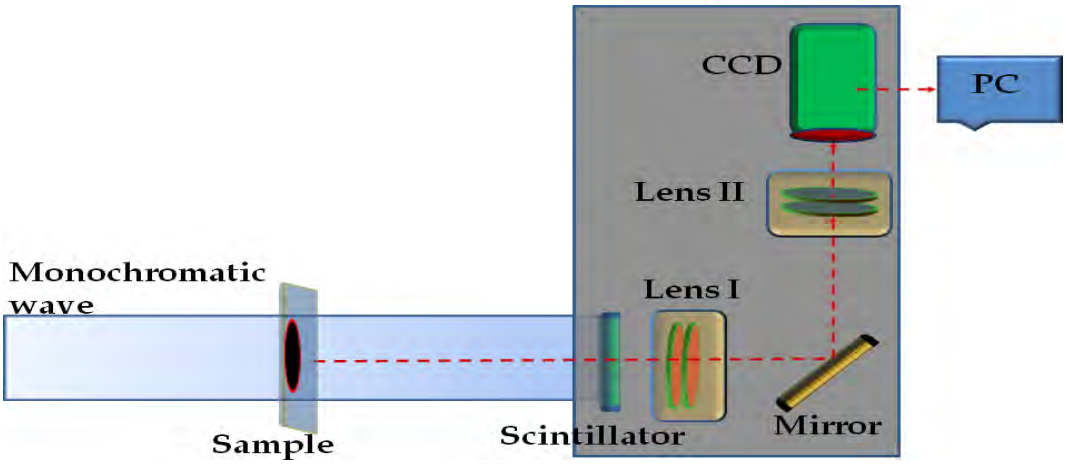

Figure 2.8: Principle of an indirect high-resolution detector system, widely used in hard X-ray imaging.

Spatial resolution

A *scintillator* is a material that has the property to emit luminous light [Dyer (2001)]. Spatial resolution is strongly influenced by the scintillating material used. In soft X-ray energies range (<6 keV) commercially scintillators such as $Y_3Al_{15}O_{12}$: Ce (YAG:Ce) and $Lu_3Al_5O_{12}$: Eu (LAG:Eu) are used as sensor materials. Other phenomena like photoelectric absorption, Rayleigh scattering and Compton scattering which strongly influence the spatial resolution of the scintillator were studied in detail for several types of the scintillators in [Martin and Koch (2006)].

Thin-film scintillators are widely used in synchrotron beamlines, because they offer many advantages compared to powder phosphors and conventional free standing single crystals. For X-ray energies below 63 keV GGG:Eu is preferred to be used, but recently new LSO:Tb single crystal films [Douissard *et al.* (2010), Cecilia *et al.* (2011)] have been reported. Moreover LSO:Tb single crystal films obtained better absorption and higher conversion efficiency than the usual YAG:Ce, LAG:Eu, LAG:Tb and GGG:Eu thin films.

According to Abbe's theorem, the maximum resolution rs that can be achieved with

a detector located not in the direct X-ray path (Figure 2.8) and is directly proportional to the numerical aperture (NA) of the front objective and indirectly proportional with the wavelength of the scintillator (λ_{sci}). This relationship represents the diffraction limit and is given by the Rayleigh criterion [Born and Wolf (1997)]:

$$rs = 0.66\lambda_{sci}/NA. \tag{2.4}$$

The spatial resolution of the detector depends on NA [Born and Wolf (1997)]. The effective pixel size of the camera should be adjusted according to the actual field of view and the desired resolution (Shannon's sampling theorem [Shannon and Weaver (1964)]).

A CCD camera specially designed for synchrotron radiation was developed at ESRF (*FReLoN* [Labiche *et al.* (2007)]) in order to provide a higher dynamic-range with moderate read-out speed of several frames per second. Different versions of the camera were developed. In this work we mostly uses the 2048 $\times$ 2048 FReLoN camera with physical pixel size 14μm with appropriate optics. The effective pixel size of the detector covers the range between 0.8 and 30μm [Weitkamp *et al.* (2010)].

2.2 X-rays - matter interaction

Before describing phase contrast techniques, the formalism of the image formation in the case of Fresnel diffraction must be understood. An overview of fundamental aspects of the theory of X-ray interaction with matter can be found in [Paganin (2006), Als-Nielsen and McMorrow (2010)].

2.2.1 3D complex refractive index

A radiographic X-ray image represents the image recorded by the detector of the X-ray beam intensity after the propagation through the investigated object. During propagation through matter, X-rays undergoes some changes such as absorption and/or scattering phenomena. The most common technique used to achieve contrast in radiography is based on absorption.

Let us consider an object illuminated with an almost parallel and monochromatic X-ray beam of wavelength λ. Its interaction with the X-rays can be described by the 3D complex refractive index of the medium, usually written as [Born and Wolf (1997)]:

$$n(x, y, z) = 1 - \delta_r(x, y, z) + i\beta(x, y, z) \tag{2.5}$$

with

$$\mu(x, y, z) = \frac{4\pi}{\lambda}\beta(x, y, z), \tag{2.6}$$

where δ_r is the refractive index decrement, β the absorption index and μ the attenuation

coefficient for the spatial coordinates (x, y, z). The z denotes the propagation direction of the X-rays (Figure 2.9). These two quantities depend on the radiation frequency and on the material of the investigated object. Assuming a thin object the diffraction within the object is neglected.

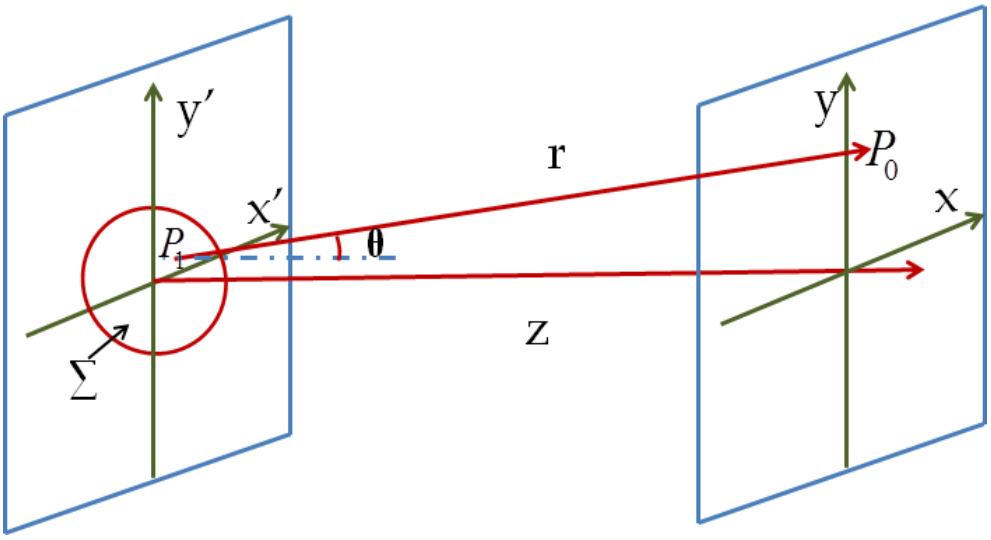

Figure 2.9: Fresnel diffraction geometry, showing aperture (or diffracting object) plane. The (x, y) are the coordinates in image plane, z is the beam propagation direction. Each point from the aperture Σ contribute to each point in the diffracted plane.

The real decrement δ_r is due to Thomson scattering and the imaginary part β is the result of the photoelectric effect and of the inelastic Compton scattering. Moreover, the wave plane is defined by:

$$\exp\left[in(x, y, z)kz\right] = \exp\left[-kz\beta(x, y, z)\right] \exp\left[ikz\left(1 - \delta_r(x, y, z)\right)\right], \tag{2.7}$$

where $k = 2\pi/\lambda$ is the wave number in vacuum. If k' denotes the wave number in the material, a direct relationship exists between k and k' and is given by $n = k'/k$. According to Eq. 2.7 the absorption index β is coupled to the absorption coefficients and the phase shift is associated to the refractive index decrement δ_r.

2.2.2 Absorption versus Phase

The refractive index decrement δ_r and the absorption index β can be formulated in terms of atomic cross sections in the energy range (8-100 keV) typically used in radiographic or tomographic imaging.

If we assume that σ_a^{ab} and σ_a^{φ} are respectively the attenuation and phase shift cross sections for an element a, then δ_r and β can be written as [Momose *et al.* (2009)b]:

$$\delta_r(x, y, z) = \frac{\lambda}{2\pi} \sum_a N_a \sigma_a^{\varphi} \tag{2.8}$$

and

$$\beta(x,y,z) = \frac{\lambda}{4\pi}\sum_a N_a \sigma_a^{ab}. \tag{2.9}$$

where λ is the wavelength and N_a the atomic density of an element a. If λ from Eq. 2.8 is replaced by hc/E then the refractive index decrement can be express as:

$$\delta_r(x,y,z) = \frac{hc}{2\pi E}\sum_a N_a \sigma_a^{\varphi}, \tag{2.10}$$

where h is the Planck constant and c is the speed of light. The phase contrast images permit the direct access to the electron density distribution:

$$\rho_e(x,y,z) = \frac{2\pi E^2}{r_0 h^2 c^2}\delta_r(x,y,z). \tag{2.11}$$

The *total* or *linear attenuation coefficient* μ is the quatity measured when an attenuation contrast image is acquired and is based on the attenuation cross section σ_a^{ab} (see last term in Eq.2.9), composed of three types of photon interactions:

$$\sigma_a^{ab} = \sigma_a^{photoelectric} + \sigma_a^{Rayleigh} + \sigma_a^{Compton}. \tag{2.12}$$

The three processes that contribute to the formation of attenuation cross section σ_a^{ab} are precisely formulated and described in [Als-Nielsen and McMorrow (2010)]. Depending on the photon energy and material structure, each term of Eq.2.12 has more or less a dominant contribution, e.g. for light materials and energies between 30 and 50 keV the dominant process is the photoelectric one. Moreover, the absorption part of the attenuation cross section σ_a^{ab} is due to the photoelectric effect. The photoelectric effect cross section $\sigma_a^{photoelectric}$ is strongly dependent on the photon energy E and the atomic number Z_a of the material a [Wang (2007)]:

$$\sigma_a^{photoelectric} \propto \frac{Z_a^5}{E^{3.5}}. \tag{2.13}$$

This equation holds far from "absorption edges" or discontinuities related with the binding energy of the electron e.

The coherent sum of scatterings obtained from all the electrons in an atom is given by Rayleigh scattering effect or elastic scattering. This effect dependent on the photon energy E and the atomic number Z_a of the material a [Wang (2007)]:

$$\sigma_a^{Rayleigh} \propto \left(\frac{Z_a}{E}\right)^2. \tag{2.14}$$

In other words, Rayleigh effect has a small contribution to the attenuation coefficients. On the other hand the incoherent sum of scatterings from all electrons in an atom is given

by Compton scattering effect or inelastic scattering. This cross section is:

$$\sigma_a^{Compton} \propto \frac{cm_e Z_a}{E + m_e c^2} \tag{2.15}$$

where $m_e c^2 = 511$ keV is the electron rest energy. The inelastic scattering effect is approximately proportional to the atomic number Z_a of the material a.

The phase shift cross section is directly proportional with the atomic number Z_a and is expressed as:

$$\sigma_a^{\varphi} \propto \frac{Z_a}{E}. \tag{2.16}$$

As previously mentioned the photoelectric effect is dominant for the cross section of the attenuation process, so we can make a rough approximation $\sigma_a^{ab} \approx \sigma_a^{photoelectric} \propto Z_a^5/E^{3.5}$. By comparing this approximation with Eq. 2.16 for low photon energies, it can be observed that the attenuation cross section diminishes with energy much faster in comparison with the phase shift cross section. Imaging low-Z dose-sensitive object using phase contrast technique is more advantageous than traditional methods based on absorption, because by increasing the energy the phase contrast is much less reduced than absorption.

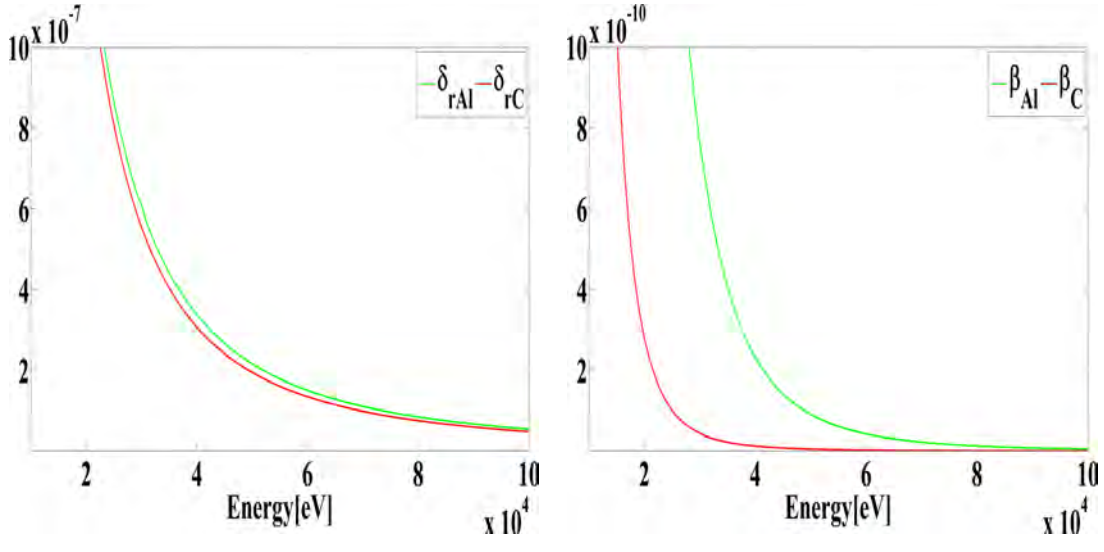

(a) (b)

Figure 2.10: (a) Refractive index δ_r and (b) absorption index β evolution as a function of energy [eV] for carbon (red line) and aluminum (green line using tabulated values XOP software [Sanchez del Rio and Dejus (2004)]).

In practice attenuation and phase shift cross section values, together with δ_r and β values are obtained using tabulated values like XOP software [Sanchez del Rio and Dejus (2004)]. For a better understanding, in Figure 2.10(a) and Figure 2.10(b) respectively, the theoretical values of δ_r and β for two materials with low atomic number are displayed as a function of energy E[eV] (10 to 100 keV). These values for carbon C (Z=6) and aluminum Al (Z=13) were obtained with the software XOP 2.3 BETA (ESRF) using the XCOM

library.

In agreement with Figure 2.11 it can be observed that the values of δ_r surpass those of β with two or three orders of magnitude. Figure 2.11 shows the ratio for the two materials. It can be observed that at $E = 100$ keV the ratio for carbon is higher with one order magnitude than for aluminum.

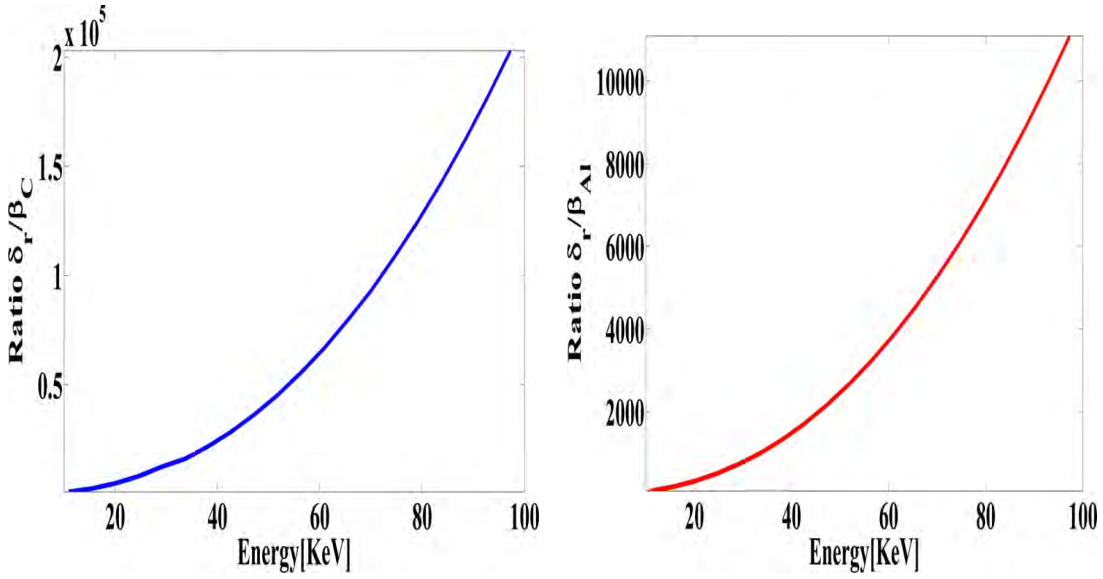

(a) (b)

Figure 2.11: Ratio between the refractive index and absorptive part for two low-Z materials (a) C (Z=6) and (b) Al (Z=13).

2.2.3 Attenuation and phase shift

The physical process in which a X-ray wave passes through a specific material and suffers a loss of its initial amplitude is called attenuation. The wavefield $E(x, y, z)$ downstream from the object, with a complex refractive index $n(x, y, z)$, can be computed with the following equation:

$$E(x,y,z) = E_0(x,y,0)\left[\exp\left(-\frac{2\pi}{\lambda}\int_0^z \beta(x,y,z)dz\right)\right]\left[\exp\left(\frac{2i\pi}{\lambda}\int_0^z [1-\delta_r(x,y,z)dz]\right)\right], \tag{2.17}$$

where $E_0(x, y, 0)$ is the incident wavefield at $z = 0$ m. This equation holds if the propagation distance z is inferior to the object thickness l_o known as *projection approximation*. This approximation assumes that the changes of the X-ray wave are negligible within the object.

The wave intensity $I(x, y, z)$ recorded on the detector can be written according to the transmission radiation function $Tr(x, y, z)$ yielding:

$$Tr(x,y,z) = \frac{|E(x,y,z)|^2}{|E_0(x,y,0)|^2} = \frac{I(x,y,z)}{I(x,y,0)} = \exp\left[\frac{-4\pi}{\lambda}\int \beta(x,y,z)dz\right]. \tag{2.18}$$

The term on the right side of above equation can be written as the Beer-Lambert law:

$$Tr(x,y,z) = \exp\left[\frac{-4\pi}{\lambda}\int \beta(x,y,z)dz\right] = \exp\left[-\int \mu(x,y,z)dz\right], \tag{2.19}$$

where $\mu(x,y,z)$ is the *linear attenuation coefficient*, hence the attenuation is:

$$a(x,y,z) = 1 - Tr(x,y,z). \tag{2.20}$$

The wavefield $E(x,y,z)$ (Eq. 2.17) can be rewritten as a multiplicative function between the incident wavefield and the *object transmission function* $\mathcal{T}(x,y,z)$, yielding:

$$\mathcal{T}(x,y,z) = \frac{E(x,y,z)}{E_0(x,y,0)} = Tr(x,y,z)\exp[-i\Delta\varphi(x,y,z)]. \tag{2.21}$$

For a homogeneous object the transmission function is defined as:

$$Tr(x,y,l_o) = \exp(-\mu l_o). \tag{2.22}$$

and the phase shift of the X-ray beam as:

$$\Delta\varphi(x,y,l_o) = k\int_0^{l_0} \delta_r(x,y,z)dz = k\delta_r l_o, \tag{2.23}$$

meaning that the phase shift $\Delta\varphi$ increases with the object thickness l_o.

2.3 X-ray phase contrast imaging

When the X-ray wave passes through a thin sample, the amplitude decreases and the phase is shifted. As seen in the previous section, these changes can be modeled by:

$$B(\mathbf{x}) = \frac{2\pi}{\lambda}\int \beta(x,y,z)dz \tag{2.24}$$

and

$$\varphi(\mathbf{x}) = -\frac{2\pi}{\lambda}\int \delta_r(x,y,z)dz \tag{2.25}$$

where $B(\mathbf{x})$ is the absorption, $\varphi(\mathbf{x})$ the phase shift introdued by the sample for (x,y) the spatial coordinates in the perpendicular plane to the propagation direction z (Figure 2.9). Based on these equations, phase contrast can be coupled to tomography using the same setup and algorithms like in conventional CT. As has been showed in the previous section the phase contrast technique allows to increase significantly the sensitivity of X-ray radiography and X-ray tomography.

At present, several experimental techniques to obtain phase contrast are used. These techniques are divided into: 1) interferometry with an X-ray crystal interferometer [Momose and Fukuda (1995)a, Momose (1995), Takeda *et al.* (1995)], 2) diffractometry with a

perfect analyzer crystal [Davis *et al.* (1995), Ingal and Beliaevskaya (1995), Chapman *et al.* (1997)], 3) gratting inferometry [Momose *et al.* (2003), Weitkamp *et al.* (2005)] and 4) propagation based technique with a Fresnel pattern [Snigireva *et al.* (1995), Cloetens *et al.* (1996)]. All these methods have advantages and drawbacks depending on the beamline setup and also by the studied sample. In the following we give a brief overview of these different phase contrast techniques.

2.3.1 Crystal interferometry imaging

In 1965 Bonse and Hart [Bonse and Hart (1965)] implemented for the first time a X-ray interferometer system. This system is based on a conventional crystal interferometer, which is composed of three parallel crystal lamellas spaced one from each other at the same distance. These three parallel lamellas are cut from a single perfect silicon monocrystal [Momose (1995), Lewis (2004), Zhou and Brahme (2008)].

The basic principle of this technique is to split and recombine the X-ray wave. A possible system configuration is known in the literature as the triple Laue-case (LLL) X-ray interferometer [Bonse and Hart (1965)], and is illustrated in Figure 2.12, where S denotes the beam splitter, M the mirrors and A the analyser.

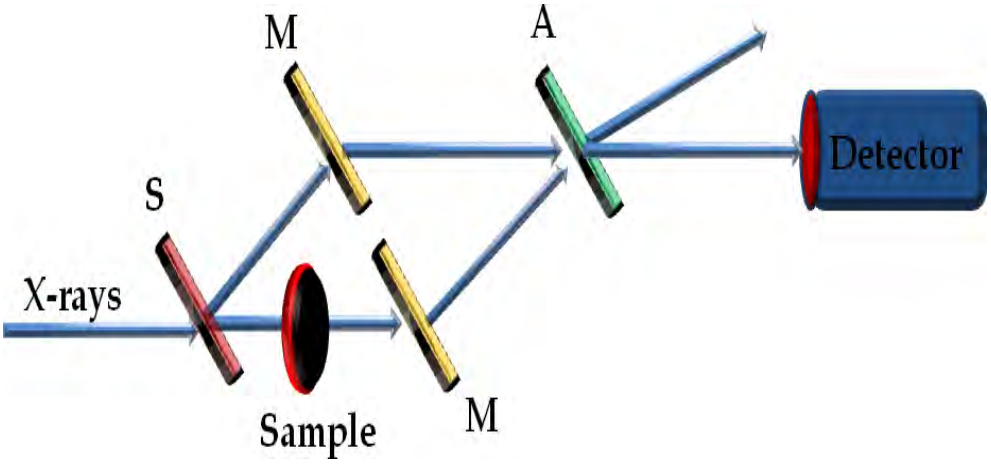

Figure 2.12: Principle of monolithic LLL interferometer system.

Phase contrast is obtained due to interference between the reference beam (not passing through) and the beam transmitted through the object. Via Laue diffraction, the incoming white synchrotron X-ray beam is split in two by amplitude division using the first crystal lamella (the beam splitter S), which will be then diffracted by the mirrors M (the second crystal lamella) and recombined by the analyser A (the last lamella). The sample is placed in one of the arms and the phase shift information is retrieved using the phase stepping technique. The detector is located downstream after the analyser and will record the interference pattern caused by the investigated object. The interference intensity of the

beam I_{INT} is given by:

$$I_{INT} = I_{ref} + I_{obj} + 2\sqrt{I_{ref} I_{obj}}\vartheta \cos(d\theta), \tag{2.26}$$

where I_{ref} is the intensity of the reference beam, I_{obj} is the intensity of the sample, ϑ is the absolute value of the degree of coherence and $d\theta$ is the phase shift.

The phase information in this case suffers of phase-wrapping effect (the obtained phase map $\cos\theta(x, y)$ is modulo 2π). With the aim to record phase maps, a X-ray interferometry system must fulfill the following requirements [Momose *et al.* (2003)]: (a) the coherence of the X-ray, (b) the coherence division of a X-ray incoming beam and (c) the mechanical optical stability.

The spatial coherence length necessary for this method is $l_s = \lambda(\frac{\Delta\alpha}{\alpha})^{-1} > 10^{-6}$, where λ is the wavelength of the X-ray beam and $\frac{\Delta\alpha}{\alpha} < 10^{-4}$ is the angular acceptance of the device. On the other hand, the temporal coherence length has to be $l_c = \lambda(\frac{\Delta E}{E})^{-1} > 10^{-6}$ with $\frac{\Delta E}{E} < 10^{-4}$ the X-ray energy bandpass of the device, resulting a total coherence volume of $\vartheta = 10^{-18}\text{m}^3$ [Krol (2011)]. Moreover, the density resolution obtained with this technique is 4 mg/cm^3 [Momose *et al.* (1996)]. These conditions can be met by high brilliance X-ray sources, but also by the free electron lasers [Grubel *et al.* (2007)] equipped with an interferometer made of a large single crystal and a crystal monochromator.

The most difficult part in crystal interferometry is related to the mechanical stability of the optical system, meaning subangstrom stability. The simplest case from the stability point of view is to use a single ingot of silicon, however, the field of view will be limited by the size of the crystal ingot diameter (7cm $\times$ 7cm). To improve this disadvantage interfereometer system with two independent crystal blocks was developed, achieving in this way a field of view greater than 10cm $\times$ 10cm and with the possibility of placing the sample at some distance from the crystal lamellae [Becker and Bonse (1974)]. However, the requirements are very restrictive because the mechanical stability and rigidity has to be achieved (subnanoradian stability). Another way to obtain phase contrast is based on three Bragg diffraction processes (BBB X-ray interferometer [Koyama *et al.* (2003)]). Spatial resolution is affected by the blurring effect due to the analyser beam A, and for overcoming these drawback in the BBB configuration the beam passing through the sample does not go through the analyzer A but is reflected and then is reached by the detector [Momose *et al.* (2003)]. The BBB technique shows some advantages for the spatial resolution, but has not attracted much attention in experimental applications.

2.3.2 Analyser based imaging

Analyser based imaging (ABI) or diffraction-enhanced imaging (DEI) [Ingal and Beliaevskaya (1995), Davis *et al.* (1995), Chapman *et al.* (1997), Bravin (2003)] showed an interesting potential for applications such as mammography [Bravin *et al.* (2007)] and

orthopedics [Mollenhauer *et al.* (2002)].

A schematic view of this system is shown in Figure 2.13.

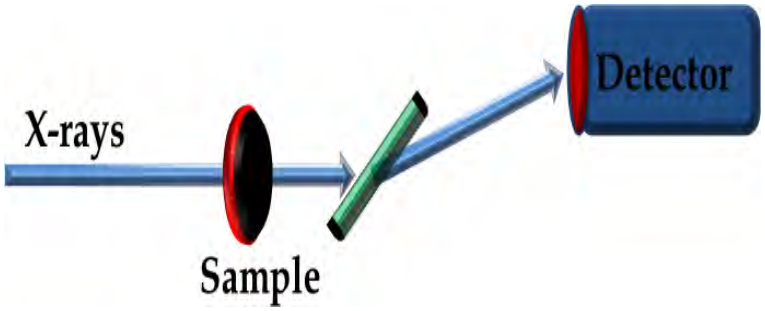

Figure 2.13: Principle of analyser based imaging.

This technique relies on the use of a perfect analyzer crystal placed between the sample and the image detector. This crystal analyzer plays the role of an angular filter and detects the X-rays that have passed through the sample and satisfy the Bragg law. The image that will be registered by the detector will be formed only by this narrow range of X-rays, in this fashion a sensitive X-ray phase contrast imaging technique is obtained. The angular filter function is given by the rocking curve (RC) of the analyzer crystal and is related to the the full width at half maximum (FWHM) of the rocking curve (RC). The typical acceptance window is from few to tens of microradians. This method in comparison with crystal interferometry Section 2.3.1 presents the advantage of stability and simplification of the imaging setup. Details on ABI setup can be found in [Fiedler *et al.* (2004)]. Briefly, the diffraction from a silicon crystal system create a monochromatic X-ray beam highly collimated, and this beam passes through the sample. The refracted and scattered X-rays are then analyzed by a second crystal identical with the first one, which represents the angular filter described above. The phase contrast is due here to the refraction of the incident beam produced by the sample placed in the monochromatic X-ray beam. The incident intensity for the diffraction plane is given by [Pavlov *et al.* (2004)]:

$$I_{ABI} = I_0 T_s A \left[\theta_{an} - \frac{\lambda}{2\pi} \left(\frac{\partial \phi}{\partial y} \right) \right], \tag{2.27}$$

where I_0 is the incident beam, T_s the sample transmission, A is the analyzer crystal for the RC corresponding value and θ_{an} the angular position of the analyser crystal.

The phase information acquired with ABI is not sensitive to the angular deviations because it is given only in one direction (e.g. the diffraction direction). A qualitative differential phase map is recorded for one position on the rocking curve (RC) of the analyzer crystal. The refraction angle information and the scattering signal can be retrieved using several approaches [Pagot *et al.* (2003)]. Finally, ABI was coupled to tomography using different phase images for different positions of analyzer based [Dilmanian *et al.* (2000)].

The disadvantage of ABI/DEI is the limit of the field of view and the spatial resolution,

which is dependent on the properties of the crystal.

2.3.3 Grating inferometry imaging

Grating inferometry (GI) known also as Talbot interferometry is a X-ray phase contrast imaging technique developed since 2002 [David *et al.* (2002)]. This technique exploits the Fresnel diffraction from periodic structures and is based on the Talbot effect [Talbot (1836)] caused by a grating illuminated with spatial coherent X-rays. The Talbot effect with hard X-rays was reported for the first time in 1997 [Cloetens *et al.* (1997)a], used in the context to measure the coherence of a synchrotron X-ray beam. It is possible to perform X-ray Talbot interferometry with a conventional X-ray source and thus, to expand it to clinical use [Donath *et al.* (2010)].

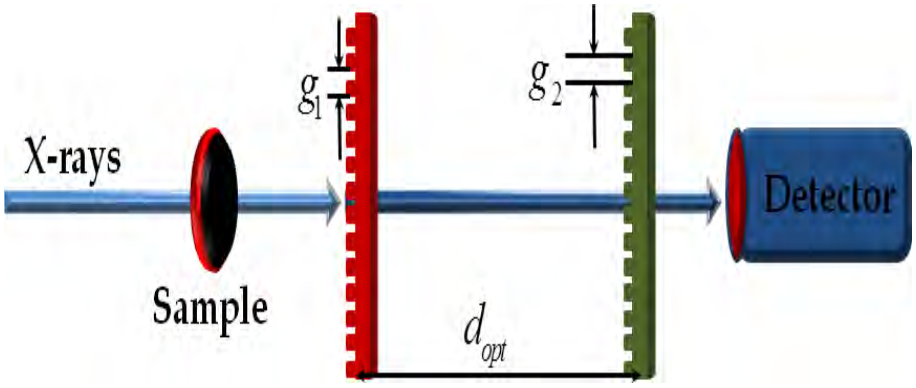

Figure 2.14: Principle of grating inferometry system.

Several different setups exist for this technique. Figure 2.14 illustrates principle of the widely-used X-ray grating interferometer [Momose *et al.* (2003)]. Usually grating interferometry uses one phase and one absorption grating with the same period downstream of the sample. The phase grating is the first grating situated at a Talbot distance d_{Talbot} from the second one, the absorption grating. The key of this technique is the phase grating which acts as a beam splitter. The absorption grating or the analyzer grating is placed at an optimal distance from the phase grating, where the fringes pattern show maximum contrast. The need of the analyzer grating is due to small period of the interference pattern, usually few micrometers (see Section 4.1 in [Zanette (2011)]). The period of the absorption grating matches the period of the interference pattern (i.e. $g_1 = 2g_2$).

Briefly, the incident X-ray beam will be shifted by the phase grating giving rise to periodic fringes at an optimal distance along the optical axis from the absorption grating. The optimal distance between the two gratings called Lohmann distance is given by [Suleski (1997)]:

$$d_{opt} = (m - \frac{1}{2})\frac{g_1^2}{4\pi} \tag{2.28}$$

where m is the diffraction order and is equal to $m = 1, 2, 3....$ The differential phase

maps and the scattering signals can be recovered using two methods: phase stepping scan technique (laterally scanning) or Moiré imaging. A final image registered using phase stepping technique is obtained by acquiring multiple scans for the phase grating or for the absorption grating. On the other hand, using Moiré method [Momose *et al.* (2009)a] a single-shot radiography and high-speed tomography (0.5 s for tomography scan) can be performed.

The beam distribution for each pixel recorded by the detector can be expressed as [Diemoz *et al.* (2011)]:

$$I_{GI} = I_0 T_s T_G \left[1 + F_{viz} \sin\left(\psi + \frac{2\pi}{g_2} y_G - \frac{\lambda}{g_2}\frac{\partial\phi}{\partial y}\right) d_{Talbot}\right], \tag{2.29}$$

where T_G is the average transmission factor of the grating, F_{viz} the visibility of the fringe pattern and ψ the sinusoidal fringe profile shift measured when the object is not present in the X-ray beam and y_G is the relative position of the two gratings in the perpendicular direction y. The fringe visibility F_{viz} is given by [Bech (2009)]:

$$F_{viz} \approx \frac{8}{\pi^2} \exp[-2\pi^2 (SD_{proj})/g_2], \tag{2.30}$$

where SD_{proj} is the standard deviation of the projected source size, meaning that GI has a low requirement for temporal beam coherence but the requirements for spatial coherence are more demanding.

An important advantage of this method is the high value of the density sensitivity, e.g. 0.5 mg/mm^3 for an aqueous specimen [Zanette (2011)], but thermal and mechanical stability are still remaining important issues for GI. Grating interferometry has been extended also to commercial X-ray tubes [Pfeiffer *et al.* (2006), Engelhardt *et al.* (2007)]. There where long acquisitions are required like in computer tomography or multiple images processing for phase retrieval information GI requires high stability. The two gratings introduced in the X-ray beam path limit the spatial resolution, which cannot be better than two periods of the analyzer grating g_2 [Weitkamp *et al.* (2005)]. Finally, GI suffers from the phase wrapping effect.

2.3.4 Propagation based imaging

The so-called "in-line phase" contrast or propagation based technique (PBI) is a phase sensitive imaging method which does not require any additional optical element in the beam path. The setup of PBI is essentially the same as for absorption radiography. The spatial resolution achieved using PBI can be very high of the order of the micron or less [Cloetens *et al.* (2006)], since no additional optical element is used in the beam path.

It has been shown that if the spatial coherence of the X-ray beam is sufficient, phase contrast can be achieved, by letting the beam propagate in free space after the interaction with an object [Snigireva *et al.* (1995), Cloetens *et al.* (1996)]. This technique is based on

the detection of the Fresnel diffraction pattern when the object is irradiated. PBI has also been applied to laboratory X-ray sources, since the radiation can be polychromatic [Wilkins *et al.* (1996)].

If the detector is located directly behind the object at distance D_1, a conventional attenuation image is recorded, while moving the detector further away from the object at different distances D_2, D_3 various phase contrast images are formed. This principle is shown in Figure 2.15.

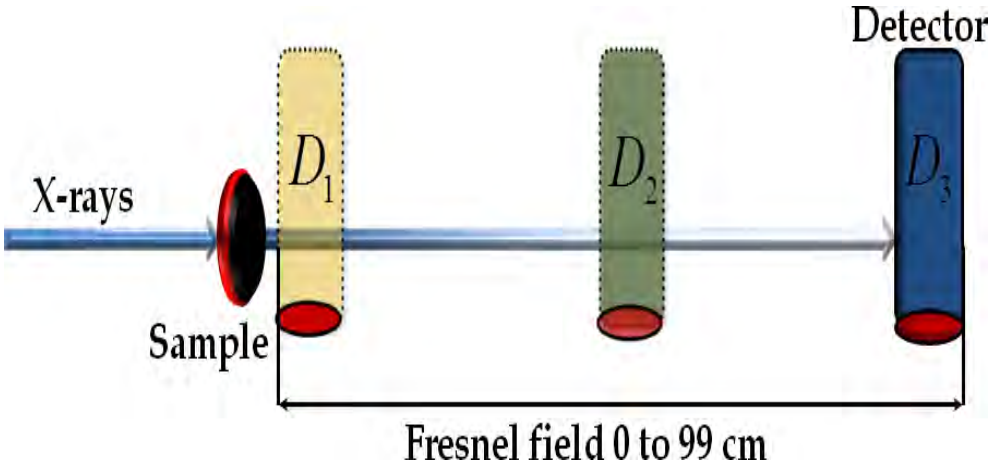

Figure 2.15: Principle of propagation based imaging system.

The interference fringes localized at the edges of the different sample structures are due to the phase changes, a regime known as "edge-detection". Phase contrast achieved in the Fresnel field is proportional to the second derivative of the phase of the wavefront [Cloetens (1999)]. The phase contrast images obtained using PBI technique can be used directly as input to a tomographic reconstruction algorithm. A first application of this kind was made on the artery specimen [Spanne *et al.* (1999)] and clinical experience for mammography [Castelli *et al.* (2011)].

Furthermore, by using more sophisticated phase retrieval approaches the contrast can be significantly improved. A variety of phase retrieval methods valid under different assumptions have been proposed in the literature. The majority of these algorithms use multiple projections recorded at different distances from the investigated object to recover the phase. This regime is known as "holographic regime" [Cloetens (1999)]. The direct problem of image formation and the details of these linear approaches are reported in the next Chapter 3.

The phase retrieval methods using PBI have been coupled also to tomography. In-line phase tomography has found applications in material science [Baruchel *et al.* (2006), Mayo *et al.* (2012)], paleontology [Tafforeau *et al.* (2006)], biomedical imaging [Cancedda *et al.* (2007), Langer *et al.* (2012)b, Marinescu *et al.* (2013)] and 4D in-vivo investigation [Moosmann *et al.* (2013)]. This technique also has been implemented using laboratory sources [Mayo *et al.* (2003)].

Chapter 3

Quantitative phase retrieval in PBI

Contents

This chapter presents the direct problem of phase-contrast image formation in in-line phase contrast imaging and the conventional linear methods of phase retrieval in the Fresnel field, and also the nonlinear algorithms previously proposed for in-line phase contrast.

3.1 Direct problem of image formation

While phase contrast pattern can be directly observed in PBI, the quantitative exploitation of the image requires solving the phase retrieval problem.

As described in Section 2.2.1, let us assume an object illuminated with an almost parallel and monochromatic X-ray beam of wavelength λ. The interaction object-X-rays can be described by the 3D complex refractive index of the medium (Eq. 2.5). If, the diffraction within the object is neglected, the interaction of X-rays with the object can be described by a transmittance function T of the coordinates $\mathbf{x} = (x, y)$ in a plane perpendicular to the propagation direction z (Figure 2.9):

$$T(\mathbf{x}) = \exp[-B(\mathbf{x}) + i\varphi(\mathbf{x})] = a(\mathbf{x}) \exp[i\varphi(\mathbf{x})]. \tag{3.1}$$

As seen in Section 2.3 the absorption, $a(\mathbf{x})$ and phase shift $\varphi(\mathbf{x})$ induced by the object can be considered as projections of the absorption:

$$B(\mathbf{x}) = \frac{2\pi}{\lambda} \int \beta(x, y, z) dz, \tag{3.2}$$

and refraction index respectively:

$$\varphi(\mathbf{x}) = -\frac{2\pi}{\lambda} \int \delta_r(x, y, z) dz. \tag{3.3}$$

Considering a plane wave, the Fresnel or the Fraunhofer diffraction region is determined by the radius of the first Fresnel zone $r_F = \sqrt{D\lambda}$, where D is the sample-to-detector distance (Figure 1.2). If the sample size s is much smaller than r_F, then the diffraction pattern is described by the Fraunhofer approximation. In this case the recorded intensity is related to the square modulus of the Fourier transform of the transmitted wave:

$$I_D(\mathbf{x}) = \left| F\{T\} \left(\frac{\mathbf{x}}{D\lambda} \right) \right|^2 \tag{3.4}$$

where F denotes the Fourier operator.

In the opposite case, when $r_F \approx s$, the recorded intensity at distance D is given by the squared modulus of the exit wave in the Fresnel field:

$$I_D(\mathbf{x}) = |T(\mathbf{x}) * P_D(\mathbf{x})|^2 \tag{3.5}$$

where $*$ denotes the 2D convolution of the transmittance with the Fresnel propagator,

$$P_D(\mathbf{x}) = \frac{1}{i\lambda D} \exp\left(i \frac{\pi}{\lambda D} |\mathbf{x}|^2 \right), \tag{3.6}$$

D being the propagation distance along z (Figure 2.9). The corresponding Fourier transform of the Fresnel propagator is:

$$\tilde{P}_D(\mathbf{f}) = \exp\left(-i\pi D\lambda |\mathbf{f}|^2 \right). \tag{3.7}$$

The direct problem can also be written in terms of Fourier transform. The Fourier

transform F of the intensity measurement can be written as [Guigay (1977)]:

$$F\{I\}(\mathbf{f}) = \tilde{I}(\mathbf{f}) = \int T\left(\mathbf{x} - \frac{\lambda D\mathbf{f}}{2}\right) T^*\left(\mathbf{x} + \frac{\lambda D\mathbf{f}}{2}\right) \exp(-2i\pi\mathbf{x}\cdot\mathbf{f})d\mathbf{x}, \tag{3.8}$$

where $\mathbf{f}$ is the variable in the Fourier domain. If $D \to 0$ then the partial coherence effect disappears and the attenuation image is obtained. Moreover, if the propagation distance increases then the phase contribution to the intensity image will grow. The resolution of the phase contrast projection without magnification is anyway limited by the pixel size of the detector. The maximum spatial frequency that can be measured is inversely proportional to the double of the detector pixel size [Nugent (2010)].

3.2 *Inverse* phase retrieval problem - *Linear* models

A variety of X-ray methods for phase retrieval were proposed in the literature and reviewed by Nugent [Nugent (2010)]. The Transport of intensity equation (TIE) [Teague (1982), Teague (1983), Nugent *et al.* (1996), Barty *et al.* (1998), Gureyev *et al.* (1999), Beleggia *et al.* (2004), Turner *et al.* (2004), Paganin (2006)] valid in the limit of small distances, the Contrast Transfer Function (CTF) [Guigay (1977), Cloetens *et al.* (1996), Cloetens *et al.* (1999), Zabler *et al.* (2005)] valid for several distances and the mixed approach [Guigay *et al.* (2007)] based on CTF, which becomes CTF under the assumption of weak absorption and TIE for short distances respectively (Figure 3.1).

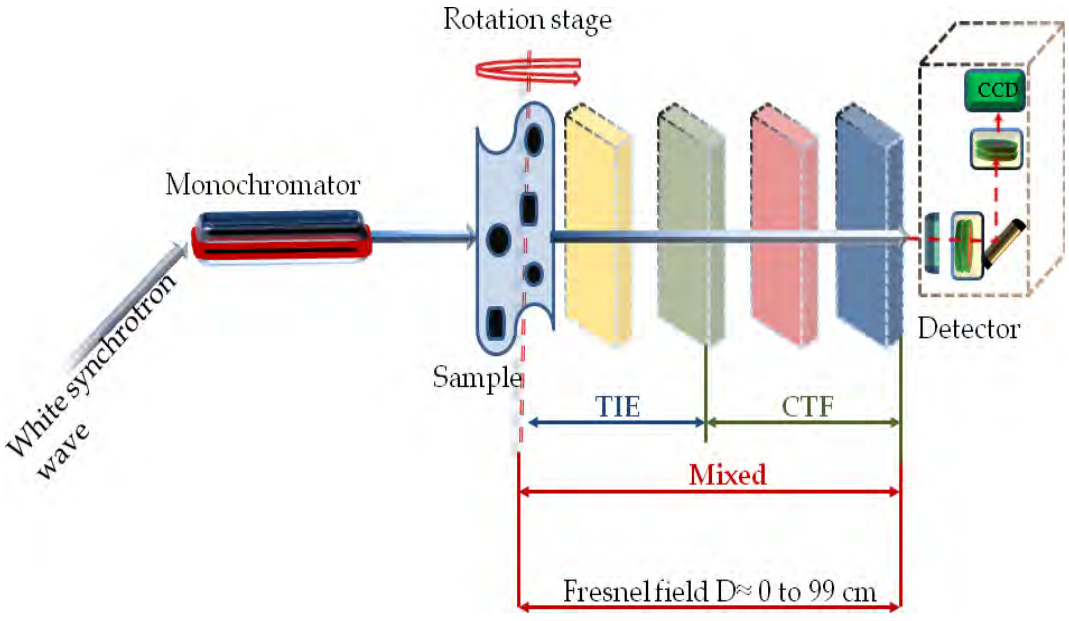

Figure 3.1: Principle of in-line phase tomography or propagation based imaging system.

All these phase retrieval approaches are based on a linearization of intensity Eq. 3.5.

3.2.1 Transport of intensity equation - TIE

In 1995 Gureyev et al. [Gureyev *et al.* (1995)] studied the possibility to retrieve the phase information using the spatial intensity derivative along the optical axis $\partial I(\mathbf{x})/\partial z$.

The transmittance function in Eq. 3.8 can be linearized with respect to the propagation distance D by Taylor expansion. If the first order term is expressed as $T(\mathbf{x} \pm \frac{\lambda D \mathbf{f}}{2}) \approx T(\mathbf{x}) \pm \frac{\lambda D \mathbf{f}}{2} \cdot \nabla T(\mathbf{x})$, Eq. 3.8 can be rewritten as:

$$I_D(\mathbf{x}) = I_0(\mathbf{x}) - \frac{D\lambda}{2\pi} \nabla \cdot [I_0(\mathbf{x}) \nabla \varphi(\mathbf{x})]. \tag{3.9}$$

Eq. 3.9 is valid only for short propagation distances D. Including this assumption, the difference $[I_D(\mathbf{x}) - I_0(\mathbf{x})]/D$ can be approximated in the propagation direction z by :

$$\nabla \cdot [I_0(\mathbf{x}) \nabla \varphi(\mathbf{x})] = -\frac{2\pi}{\lambda} \frac{\partial I_0(\mathbf{x})}{\partial z}. \tag{3.10}$$

This expression is known as transport of intensity (TIE) and was developed for the first time by Teague in 1982 [Teague (1982)]. A number of algorithms have been developed in the near field based on TIE with the aim to improve the retrieved phase map. These approaches are based on Fourier transform including some a priori information [Paganin *et al.* (2002)] or on the linear partial differential equation [Gureyev and Nugent (1996), Allen and Oxley (2001)].

3.2.2 TIE Fourier solution

The phase map can be recovered using the following equation [Paganin and Nugent (1998)] :

$$\varphi(\mathbf{x}) = -\frac{2\pi}{\lambda} \nabla^{-2} \left\{ \nabla \cdot \left[\frac{1}{I_0(\mathbf{x})} \nabla \left(\nabla^{-2} \frac{\partial I_0(\mathbf{x})}{\partial z} \right) \right] \right\}, \tag{3.11}$$

where ∇^{-2} is the inverse Laplacian operator. The Laplacian and the inverse Laplacian operators can be implemented in the Fourier domain [Paganin (2006)].

This method needs to recover the phase image from two intensity measurements, one for the $I_0(\mathbf{x})$ and a second one for $I_D(\mathbf{x})$. These two planes have to be separated by a small distance to form an estimate of the longitudinal intensity derivative [Paganin and Nugent (1998)].

3.2.3 TIE weak absorption

This method is known as Bronnikov's algorithm [Bronnikov (2002)] based on TIE equation under the assumption that the absorption has insignificant variations and can be approximated with a constant. The intensity equation in this case is:

$$I_D(\mathbf{x}) = I_0(\mathbf{x}) \left[1 - \frac{D\lambda}{2\pi} \nabla^2 \varphi(\mathbf{x}) \right]. \tag{3.12}$$

When phase CT is concerned, the filtering process involved in this retrieval method can be included in the inverse Radon Transform. The absorption a priori can be relaxed if a regularization parameter α is introduced in the filter function [Groso *et al.* (2006)]. This method is known in the literature as "modified Bronnikov" yielding the phase equation:

$$\varphi(\mathbf{x}) = \frac{2\pi}{D\lambda}\nabla_{\alpha}^{-2}\left[1 - \frac{I_D(\mathbf{x})}{I_0(\mathbf{x})}\right] \tag{3.13}$$

where the invers Laplacian ∇_{α}^{-2} is defined as [Paganin (2006)]:

$$\nabla_{\alpha}^{-2} = -\frac{1}{4\pi^2}F^{-1}\frac{1}{(f_x^2 + f_y^2 + \alpha)}F. \tag{3.14}$$

The small values of the Laplacian at low frequencies and the singularity at $f_x = f_y = 0$ are handled if $(f_x^2 + f_y^2)^{-1}$ is replaced with zero at the Fourier domain origin $\mathbf{f} = (0, 0)$ and introducing α. This method requires images in two planes: a plane for a small distance from the object, to get $I_D(\mathbf{x})$ and the contact plane for the $I_0(\mathbf{x})$ image.

3.2.4 TIE homogeneous object

A single-distance phase retrieval method for a homogeneous object having a constant ratio δ_r/β was developed by Paganin [Paganin *et al.* (2002)]. This a prior is called "homogeneous object approximation". This phase recovery method has been originally derived based on the assumption that the object consists of a single homogeneous material with a constant fraction β/δ_r. The phase reconstruction formula for the phase can be written as:

$$\varphi(\mathbf{x}) = \frac{1}{2}\ln\left(F^{-1}\left\{\frac{F\left[I_D(\mathbf{x})/I_0(\mathbf{x})\right]}{\beta/\delta_r + |\mathbf{f}|^2(\lambda D/4\pi)}\right\}\right) \tag{3.15}$$

where $\mathbf{f}$ is the Fourier variable. Due to its simplicity Eq. 3.15, is used also with inhomogeneous objects [Weitkamp *et al.* (2011)] in order to obtain a non-quantitative phase map, which facilitates the segmentation and visualization of internal structures of the studied object.

The homogeneous object approximation has been extended to two or more homogeneous materials [Beltran *et al.* (2010)]. This method under the assumption that the thickness of the embedding material varies slowly requires knowledge of the total projected thickness of the object at each projection angle.

3.2.5 Contrast transfer function - CTF

This method linearizes the forward model by Taylor expansion. The transmittance function (Eq. 3.1) can be rewritten then as [Cloetens *et al.* (1999), Zabler *et al.* (2005)]:

$$T(\mathbf{x}) \approx 1 - B(\mathbf{x}) + i\varphi(\mathbf{x}). \tag{3.16}$$

Under the assumption that the phase is slowly varying and the absorption is weak [Guigay (1977)]:

$$|\varphi(\mathbf{x}) - \varphi(\mathbf{x} + D\lambda\mathbf{f})| \ll 1, \qquad B(\mathbf{x}) \ll 1 \tag{3.17}$$

the intensity equation (Eq. 3.5) can be expressed as [Cloetens *et al.* (2002)]:

$$\tilde{I}(\mathbf{f}) = \delta(\mathbf{f}) - 2\cos(D\pi\lambda\,|\mathbf{f}|^2)\tilde{B}(\mathbf{f}) + 2\sin(D\pi\lambda\,|\mathbf{f}|^2)\tilde{\varphi}(\mathbf{f}). \tag{3.18}$$

where $\delta(\mathbf{f})$ is the unit impulse function, $\tilde{B}(\mathbf{f})$ is the Fourier transform of the absorption and $\tilde{\varphi}(\mathbf{f})$ is the Fourier transform of the phase. The sinus term of the above equation is the so-called *contrast factor* or *phase contrast transfer function*.

This term introduces zero crossings, therefore multiple propagation distances have to be used to cover the Fourier domain. If $\mathbf{f} \to 0$ then the sum of the contrast factor goes to zero. By choosing multiple distances, typically three or four distances, zeros are avoided.

Absorption $\tilde{B}(\mathbf{f})$ and phase $\tilde{\varphi}(\mathbf{f})$ can be simultaneous retrieved using CTF. Assuming different distances D and that for each distance a intensity map I_D is acquired, then the phase solution if the Fourier domain origin $\mathbf{f} \neq (0,0)$ can be recovered by solving a least square problem as:

$$\tilde{\varphi}(\mathbf{f}) = \frac{1}{\alpha + 2A}\left[B\sum_D \tilde{I}_D(\mathbf{f})\sin(D\pi\lambda\,|\mathbf{f}|^2) - C\sum_D \tilde{I}_D(\mathbf{f})\cos(D\pi\lambda\,|\mathbf{f}|^2)\right], \tag{3.19}$$

where $A = \chi B - C^2$ and α is a Tikhonov regularization parameter chosen in order to minimize the standard deviation outside the sample. The three quantities A, B, χ are defined as:

$$B = \sum_D \cos^2(D\pi\lambda\,|\mathbf{f}|^2), \tag{3.20}$$

$$C = \sum_D \sin(D\pi\lambda\,|\mathbf{f}|^2)\cos(D\pi\lambda\,|\mathbf{f}|^2), \tag{3.21}$$

and

$$\chi = \sum_D \sin^2(D\pi\lambda\,|\mathbf{f}|^2). \tag{3.22}$$

Recently, a single-distance phase-retrieval model based on CTF and tomographic reconstruction have been coupled into a single step reconstruction algorithm based on Total Variation minimization [Kostenko *et al.* (2013)].

3.2.6 Mixed approach

As seen above, the TIE or CTF methods rely on different assumptions. TIE is valid for short propagation distances where the contrast is weak and use images in two planes. On the other hand, CTF is not restricted to short distances but is valid for weak absorption and use multiple distances to retrieve the phase. In order to extend the validity of the

approximations made in CTF or TIE, a mixed approach was proposed [Guigay *et al.* (2007)].

If $D \to 0$ TIE and CTF does not yield the same expression. In order to overcome this aspect the phase term from the transmittance function (Eq. 3.8) is Taylor expand. If only the first term of this expansion is retained the Fourier transform of the intensity can be expressed as:

$$\tilde{I}_D(\mathbf{f}) = \int \exp(-i2\pi\mathbf{x}\cdot\mathbf{f}) a\left(\mathbf{x} - \frac{D\lambda\mathbf{f}}{2}\right) a\left(\mathbf{x} + \frac{D\lambda\mathbf{f}}{2}\right) \times \left[1 + i\varphi\left(\mathbf{x} - \frac{D\lambda\mathbf{f}}{2}\right) - i\varphi\left(\mathbf{x} + \frac{D\lambda\mathbf{f}}{2}\right)\right] d\mathbf{x}. \tag{3.23}$$

In particular, assuming that the absorption is slowly varying:

$$|B(\mathbf{x} + D\lambda\mathbf{f}) - B(\mathbf{x} - D\lambda\mathbf{f})| \ll 1 \tag{3.24}$$

the above equation can be written as:

$$\tilde{I}_D(\mathbf{f}) = \tilde{I}_D^{\varphi=0}(\mathbf{f}) + 2\sin(\pi\lambda D|\mathbf{f}|^2) \times \int \exp(-i2\pi\mathbf{x}\cdot\mathbf{f})\varphi(\mathbf{x})a^2(\mathbf{x})d\mathbf{x} + 2i\cos(\pi\lambda D|\mathbf{f}|^2)\lambda D\mathbf{f} \cdot \int \exp(-i2\pi\mathbf{x}\cdot\mathbf{f})\varphi(\mathbf{x})a(\mathbf{x})\nabla a(\mathbf{x})d\mathbf{x}. \tag{3.25}$$

The integrals of the above equation are Fourier transform, yielding:

$$\tilde{I}_D(\mathbf{f}) = \tilde{I}_D^{\varphi=0}(\mathbf{f}) + 2\sin(\pi\lambda D|\mathbf{f}|^2) F\left\{I_0\varphi\right\}(\mathbf{f}) + \frac{\lambda D}{2\pi}\cos(\pi\lambda D|\mathbf{f}|^2) F\left\{\nabla\cdot(\varphi\nabla I_0)\right\}(\mathbf{f}). \tag{3.26}$$

This equation recovers the TIE solution if $D \to 0$ (Eq. 3.10), but also the CTF solution if $I_0 \to 0$ (Eq. 3.18). This equation is usually used as the mixed approach [Guigay *et al.* (2007)]. To include several distances, a least squares minimization procedure is used and the phase map is recovered iteratively. By introducing the phase-absorption product $\psi(\mathbf{x}) = I_0(\mathbf{x})\varphi(\mathbf{x})$, the phase retrieval problem can be solved as:

$$\tilde{\psi}^{(n+1)}(\mathbf{f}) = \frac{\sum_D A_D(\mathbf{f})[\tilde{I}_D(\mathbf{f}) - \tilde{I}_D^{\varphi=0}(\mathbf{f}) - \Delta_D^{(n)}(\mathbf{f})]}{\sum_D |A_D^2(\mathbf{f})|^2 + \alpha} \tag{3.27}$$

with

$$A_D(\mathbf{f}) = 2\sin(\pi\lambda D|\mathbf{f}|^2) \tag{3.28}$$

and

$$\Delta_D^{(n)}(\mathbf{f}) = \frac{\lambda D}{2\pi}\cos(\pi\lambda D|\mathbf{f}|^2) F\left\{\nabla\cdot[\psi^{(n)}\nabla\ln(I_0)]\right\}(\mathbf{f}) \tag{3.29}$$

where α is a regularizing parameter and $\tilde{\psi}^{(n)}(\mathbf{f})$ is the phase-absorption product at iteration n with $\tilde{\psi}^{(0)}(\mathbf{f}) = 0$. Several methods of regularization have been proposed [Langer *et al.*

(2008),Langer *et al.* (2009),Langer *et al.* (2010)] to solve this linear inverse problem, such as classical quadratic Tikhonov regularization and wavelet shrinkage.

A comparison for mixed absorption and phase objects between CTF, TIE and mixed approach has been done in [Langer *et al.* (2008)]. The mixed method seems to be more accurate and robust to noise than the two other methods. On the other hand, TIE is most accurate without noise.

Recently, the mixed algorithm has been extended to multi-material objects including some a priori knowledge. This regularization schemes are accomplished first by a tomographic reconstruction of the attenuation. Then the proportionality of the attenuation index β and of the refractive index δ_r is introduced in the regularization functional [Langer *et al.* (2012)a,Langer *et al.* (2013)].

3.2.7 Conclusions

The phase retrieval problem is an ill-posed inverse problem. To summarize the linear phase retrieval methods a classification of the a priori assumptions about the object is presented in Table 3.1.

Table 3.1: Classification of linear methods as a function of assumptions

	Validity	Terms in the object function	Propagation distances
TIE	Homogeneous object	$\frac{\delta_r}{\beta}$=constant ratio	1
TIE	Short propagation distances	$B(\mathbf{x})\ll 1$	2 close
CTF	Weak absorption and slowly varying phase	$\lvert\varphi(\mathbf{x})-\varphi(\mathbf{x}+\lambda D\mathbf{f})\rvert \ll 1$ and $B(\mathbf{x})\ll 1$	2
Mixed	Slowly varying object	$\lvert B(\mathbf{x}+\lambda D\mathbf{f})-B(\mathbf{x}-\lambda D\mathbf{f})\rvert \ll 1$	2

A more detailed comparison between different non-iterative phase retrieval methods can be found in [Burvall *et al.* (2011)].

3.3 *Inverse* phase retrieval problem-*Nonlinear* algorithms

Despite current limitations, the linear methods have found various applications in practice. The limitations of these approaches due to the linearization of the direct problem can be refined by other methods which take into account the nonlinearity of the phase problem. Phase retrieval from Fresnel diffraction pattern is sensitive to noise in the low frequency range, due to the weak transfer of the low frequency information by the Fresnel transform. Low frequency noise makes the image analysis very difficult (Figure 3.2). While avoiding object assumptions, the low frequency noise can be reduced. On the other hand, another important aspect is the spatial resolution, which can be refined if the nonlinear contribution is take into account.

Furthermore, this phase retrieval problem is an inverse ill-posed problem in the sense

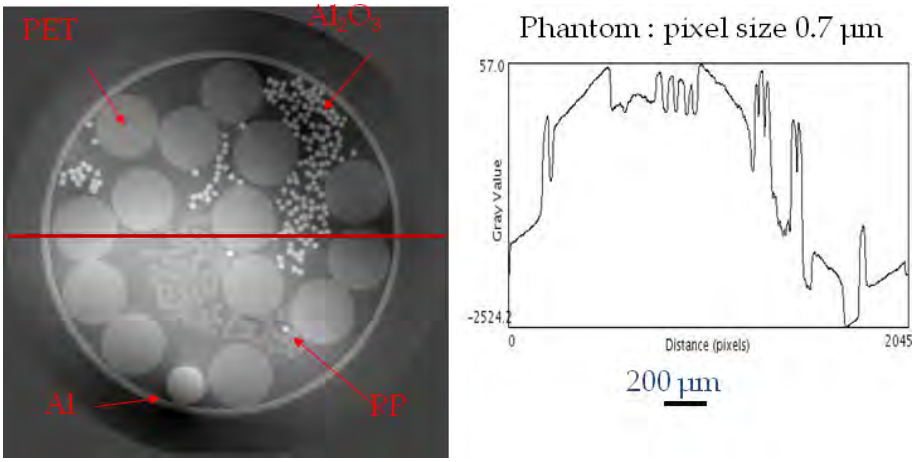

Figure 3.2: Low frequency artifacts present in the tomographic slice reconstructed with mixed approach for a constructed object. Projection data were acquired at the ID19 beamline at the ESRF using E=20.5 keV for 1500 angles of view over a 180° rotation of the sample, at four sample-to-detector distances (D=[2; 10; 20; 45] mm).

of Hardamard, i.e a solution may not exist, be non-unique and not depend continuously on the data, therefore regularization methods are required for a precise phase recovery. The nonlinear contributions in the image contrast formation are non-negligible since large propagation distances and high spatial resolution are used. Consequently, the nonlinearity of the phase-intensity relationship is a crucial aspect.

By introducing the nonlinearity of the optical system the sensitivity and the accuracy of the phase retrieval solution can be considerably increased. Recently, new algorithms that take into account this aspect have been proposed. Yet, the effects of the nonlinearity have not been much investigated in the literature.

One of the first nonlinear phase retrieval method was proposed by Gureyev [Gureyev (2003)], in order to improve the phase solution. This method use the phase map obtained with TIE as an initial approximation and then is refined by Gerchberg-Saxton-Fienup (GSF) method [Fienup (1982)]. By using the linear TIE solution as a starting point the amount of computations is reduced and stagnation traps are avoided. The TIE equation (Eq. 3.10) is modified and becomes:

$$\frac{2\pi}{\lambda}\frac{\partial I_0(\mathbf{x})}{\partial z} = -\nabla\cdot[I_0(\mathbf{x})\nabla\varphi(\mathbf{x})] + O(N_F^{-1}) \tag{3.30}$$

where N_F is the Fresnel number, $I_0(\mathbf{x}) \geq C > 0$ and C is a positive constant. The symbolic form $O(N_F^{-1})$ preserved the nonlinear terms discarded in TIE equation (Eq. 3.10). In the Fresnel field ($N_F > 1$) all the nonlinear terms behave like $O(N_F^{-1})$ and are smaller than the first (linear) term. The proposed method has been applied for simulated data only.

Recently, a new nonlinear algorithm for in-line propagation technique based on TIE has been proposed [Moosmann *et al.* (2010)]. The phase map is obtained from a single propagation distance and has been applied for the radiographic case on simulated

data (pure phase, non-periodic objects). The nonlinearity is introduced with the entire paraxial wave equation. The TIE equation (Eq. 3.10) in the limit of constant absorption ($I_{D=0}(\mathbf{x})$=const) yields:

$$\frac{2\pi}{\lambda}\frac{\partial g_D(\mathbf{x})}{\partial z} = -\nabla\cdot[(g_D(\mathbf{x})+1)\nabla\varphi_D(\mathbf{x})]. \tag{3.31}$$

where $g_D(\mathbf{x}) = \frac{I_D(\mathbf{x})}{I_0(\mathbf{x})} - 1$ is the intensity contrast. If D is sufficiently small $g_D(\mathbf{x})$ varies in an approximately linear way in z, then $g_D(\mathbf{x})$ takes the following form:

$$g_D(\mathbf{x}) = -\frac{D\lambda}{2\pi}\nabla^2\varphi_{D=0}(\mathbf{x}) \tag{3.32}$$

which correspond to Bronnikov's algorithm [Bronnikov (2002)] (Section 3.2.3). Since this equation break down at large propagation distances D, a more general form is needed:

$$g_D(\mathbf{x}) = \sum_{l=1}^{l_{max}} g_l(\mathbf{x})D^l. \tag{3.33}$$

The $\varphi_D(\mathbf{x})$ can be also expanded in power of z yielding:

$$\varphi_D(\mathbf{x}) = \sum_{m=0}^{m_{max}} \varphi_m(\mathbf{x})D^m. \tag{3.34}$$

A nonlinear partial differential equation (PDE) for $\varphi_{D=0}(\mathbf{x})$ subject to the single-distance source term $g_D(\mathbf{x})$ is obtained for $l_{max} \geq 2$. If $l_{max} = 2$ and $m_{max} = 1$ the explicit expansion of $g_D(\mathbf{x})$ is given by [Moosmann *et al.* (2011)]:

$$\begin{aligned} g_D(\mathbf{x}) \approx & -\tfrac{D\lambda}{2\pi}\nabla^2\varphi_{D=0}(\mathbf{x}) + \tfrac{D^2\lambda^2}{8\pi^2} \\ & \left\{[\nabla\nabla^2\varphi_{D=0}(\mathbf{x})]\cdot\nabla\varphi_{D=0}(\mathbf{x}) + [\nabla^2\varphi_{D=0}(\mathbf{x})]^2 + \tfrac{1}{2}\nabla^2[\nabla\varphi_{D=0}(\mathbf{x})]^2\right\}. \end{aligned} \tag{3.35}$$

This equation is called next-to-leading order (NLO). In order to find $\varphi_{D=0}(\mathbf{x})$ the above equation is solved in a perturbative way, for the leading order $l_{max} = 1$ obtaining a solution called PNLO. Then the PNLO solution is used in estimating the next-to-leading order and finally the Laplacian is invert on $-\frac{2\pi}{D\lambda}[g_D(\mathbf{x})$-PNLO]. The inversion of the Laplacian is performed using the discrete Fast Fourier Transform:

$$\frac{1}{\kappa^2} \rightarrow \frac{1}{\kappa^2+\alpha^2}. \tag{3.36}$$

where α is a real constant. This nonlinear scheme gives good results at very large relative phase shifts over the entire projection.

Another nonlinear, noniterative approach modifying CTF equation called projected CTF, has been proposed in [Moosmann *et al.* (2011)]. By introducing an intensity contrast filtered in Fourier space the artificial peaks introduced by CTF in the spectrum of $\varphi_{D=0}(\mathbf{x})$

are removed. This filter is defined as:

$$\widetilde{g_D}(\mathbf{f}) \equiv \Theta\left(\left|\sin(D\lambda\pi\mathbf{f}^2)\right| - \tau\right)\tilde{g}_D(\mathbf{f}) \tag{3.37}$$

where Θ is the Heaviside step function, τ is the threshold for this binary filter ($0 \leq \tau < 1$) and $D\lambda\pi\mathbf{f}^2 > \frac{\pi}{2}$. The proposed algorithms have been tested on Lena image in [Moosmann *et al.* (2011)]. It has be reported that TIE+PNOL improves TIE with 40% in terms of mean retrieval error per pixel there where the phase varies sufficiently slowly. For the case where TIE+PNOL is compared with projected CTF with mean retrieval error per pixel is reduced with 42%. However, these methods sufferers of artificially hollows there where the are strong phase variations. The projected CTF has been also discussed in [Hofmann *et al.* (2011)] and has been tested on a Xenopus embryo giving better results than linearized TIE (Eq 3.32) or CTF in term of spatial resolution. This method has been also applied for 4D in vivo microtomography [Moosmann *et al.* (2013)].

Recently, the mixed approach using an iterative procedure based on a nonlinear conjugate gradient method was proposed for tomographic reconstruction [Langer *et al.* (2012)b]. This method has been applied on a human bone.

In the next Part II of this manuscript, new iterative algorithms based on the Fréchet derivative of the intensity operator for propagation based technique are proposed. The objective of these new regularization schemes is to improve the linear solutions presented in this chapter, especially the mixed solution (Section 3.2.6).

Chapter 4

Inverse problem

Contents

This chapter of the manuscript is organized in four sections as follows. A brief presentation of well-posed and ill-posed inverse problems is given in Section 4.1. An overview of the regularization schemes for linear inverse problems is given in Section 4.2. The Tikhonov regularization scheme together with the Landweber iteration method extended to nonlinear problems are detailed in Section 4.4.1. This chapter is concluded in Section 4.4.3 where we introduce the Fréchet derivative that will be used in the following.

Inverse problems have an important role in many fields of research. "Solution of an inverse problem entails determining unknown causes based on observation of their effects. This is in contrast to the corresponding direct problem, whose solution involves finding

effects based on a complete description of their causes." This statement is attributed to O.M. Alifanov [Alifanov *et al.* (1995)], and is probably the best definition of an inverse problem.

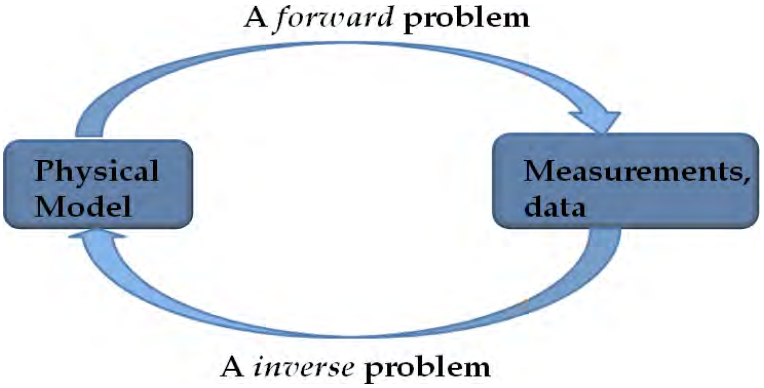

Figure 4.1: An inverse problem scheme.

The general equation defining a discrete linear inverse problem can be written as:

$$\mathbf{y} = \mathbf{K}\mathbf{x}, \tag{4.1}$$

where $\mathbf{y} \in \mathbb{R}^n$ are the known measurements, $\mathbf{x} \in \mathbb{R}^m$ the unknown desired parameters transformed by a linear operator $\mathbf{K} \in \mathbb{R}^{n \times m}$ called also observation matrix. The searched solution $\mathbf{x}$ of the linear equation (Eq. 4.1) is not easy to find because the inverse operator $\mathbf{K}^{-1}$ of the forward operator $\mathbf{K}$ is not necessarily bounded and does not always exit.

4.1 Well-posedness versus ill-posedness

The notion of well-posed or ill-posed problem is a notion due to Hadamard. Considering Eq. 4.1 with $\mathbf{K} : A \to B$, then this problem will be *well-posed* if the three following conditions hold:

1. there exists a solution for all $\mathbf{y} \in B$
2. the solution is unique
3. the solution depends continuously on the data measurements $\mathbf{y}$.

The problem becomes *ill-posed* if one or more of these conditions fail.

If the problem is well-posed, then the solution of the Eq. 4.1 can be computed directly:

$$\mathbf{x} = \mathbf{K}^{-1}\mathbf{y} \tag{4.2}$$

meaning that $\mathbf{K}^{-1}$ exists and is continuous and $\mathbf{K}$ is non-singular. If the contrary is true, this linear problem is ill-posed and a classical approach to solve the problem is the least

squares (LS) approach [Björck (1996)]:

$$\widehat{\mathbf{x}}_{LS} = \underset{\mathbf{x}}{\operatorname{argmin}} \|\mathbf{K}\mathbf{x} - \mathbf{y}\|^2 . \tag{4.3}$$

In other words, this means to find an optimal solution that is closest to the true solution in the least squares sense. In this way, the generalized solution $\widehat{\mathbf{x}}$ always exists and it is unique because it is given by the minimum norm element from all the minimizers. The searched solution $\widehat{\mathbf{x}}$ of the Eq. 4.3 may take the following form:

$$\widehat{\mathbf{x}} = \widehat{\mathbf{K}}\mathbf{y}, \tag{4.4}$$

where the operator $\widehat{\mathbf{K}}$ is known as the pseudo-inverse or Penrose-Moore generalized inverse of the operator $\mathbf{K}$. The pseudo-inverse defined in this way is a linear operator. The pseudo-inverse $\widehat{\mathbf{K}}$ can be written as:

$$\widehat{\mathbf{K}} = \begin{cases} \mathbf{K}^T(\mathbf{K}\mathbf{K}^T)^{-1} & \text{if} \quad n \leq m \\ (\mathbf{K}^T\mathbf{K})^{-1}\mathbf{K}^T & \text{if} \quad n \geq m. \end{cases} \tag{4.5}$$

We assume that $\mathbf{K} \in \mathbb{R}^{n \times m}$ has full rank, and if $\mathbf{K}$ is an invertible square matrix $n = m$ then:

$$\widehat{\mathbf{K}} = \mathbf{K}^T(\mathbf{K}\mathbf{K}^T)^{-1} = (\mathbf{K}^T\mathbf{K})^{-1}\mathbf{K}^T = \mathbf{K}^{-1}, \tag{4.6}$$

meaning that in this case the pseudo-inverse of the operator $\mathbf{K}$ is reduced to the inverse of this operator. It was shown that, in practice the pseudo-inverse performs poorly [Vogel (2002)], since it must be computed by inverting arbitrary small singular values leading in this way to instability problems.

4.1.1 Conditioning

In practical applications, the exact data are never available just noisy data due to the measurement process, hence the Eq. 4.4 becomes:

$$\widehat{\mathbf{x}}^{\delta} = \widehat{\mathbf{K}}\mathbf{y}^{\delta}, \tag{4.7}$$

where δ is the perturbation of the data (i.e. noise), which occurs both in measurements and in the searched solution. The perturbation δ on $\widehat{\mathbf{x}}$ is linearly related to the perturbation data $\mathbf{y}^{\delta}$:

$$\left\|\widehat{\mathbf{x}}^{\delta}\right\| \leq \left\|\widehat{\mathbf{K}}\right\| \left\|\mathbf{y}^{\delta}\right\| . \tag{4.8}$$

where $\|.\|$ denotes the Euclidean length or the L_2 norm.

A measure of the ill-posedness of Eq. 4.1 is given by the condition number of matrix $\mathbf{K}$ defined as:

$$\kappa(\mathbf{K}) = \|\mathbf{K}\| \left\|\widehat{\mathbf{K}}\right\| . \tag{4.9}$$

The condition number $\kappa(\mathbf{K})$ can be written as a function of singular values of $\mathbf{K}$ as:

$$\kappa(\mathbf{K}) = \frac{\sigma_{\max}(\mathbf{K})}{\sigma_{\min}(\mathbf{K})} \tag{4.10}$$

where $\sigma_{\max}(\mathbf{K})$ and $\sigma_{\min}(\mathbf{K})$ are the maximal and minimal singular values of $\mathbf{K}$ respectively. This definition is used for any consistent norm that satisfies the condition:

$$\kappa(\mathbf{K}) \geq 1. \tag{4.11}$$

If the condition number $\kappa(\mathbf{K}) = 1$ then the algorithm has find with an arbitrary precision an approximation of the searched solution. Depending on the value that $\kappa(\mathbf{K})$ takes, we can classify whether the problem is well-posed or ill-posed. If $\kappa(\mathbf{K})$ is larger but close to 1 then the problem is well-posed, in the opposite case ($\kappa(\mathbf{K})$ bigger that 1) the problem is ill-posed and $\mathbf{K}$ is singular. In this case, a small deviation in data yields large variations of the inverse solution. This phenomenon is known as overfitting.

4.2 Principles of regularization

In order to overcome the instabilities related to the ill-posed nature of the inverse problem, regularization methods can be used. The principle of the regularization is to split the ill-posed problem into a set of well-posed problems by finding a family of operators $\mathcal{R}_\alpha$, satisfying the following conditions:

$$\lim_{\alpha \to 0} \mathcal{R}_\alpha = \widehat{\mathbf{K}} \tag{4.12}$$

and

$$\|\mathcal{R}_\alpha\| \leq \left\|\widehat{\mathbf{K}}\right\| \tag{4.13}$$

where $\alpha > 0$ is a regularization parameter. This parameter gives a tradeoff between fidelity to the measurements and noise sensitivity. When $\alpha \to 0$ (Eq. 4.12) a sequence of operators which converge to the pseudo-inverse matrix $\widehat{\mathbf{K}}$ is searched, in this way an optimal solution $\widehat{\mathbf{x}}$ in the absence of noise can be found. On the other hand, the noise sensitivity can be reduced if the sequence operators found at the antecedent step have a smaller norm that the norm of the pseudo-inverse (Eq. 4.13).

A very common regularization method used in this thesis is to construct a regularization functional with a well-defined minimizer. It is also possible to stop iterative methods to avoid the noise amplification. The stopping index then plays the role of regularization parameter. In the following, we detail the Tikhonov regularization.

Tikhonov-Philips regularization

The most popular regularizer function is the Tikhonov-Philips type regularizer. The Tikhonov-Philips regularization is the most basic method. This consists in approximating the solution of the inverse problem through a minimization problem by adding a quadratic regularization term to the Eq. 4.3:

$$\underset{\lambda}{\operatorname{argmin}} \{\chi(\mathbf{x})\} = \underset{\mathbf{x}}{\operatorname{argmin}} \left\{ \|\mathbf{y} - \mathbf{K}\mathbf{x}\|_Y^2 + \alpha \|\mathcal{L}(\mathbf{x} - \mathbf{x}_0)\|_X^2 \right\} \tag{4.14}$$

where X and Y are Hilbert spaces. The regularization parameter is $\alpha > 0$ and $\mathbf{x}_0 \in X$ is an initial guess. $\mathcal{L}$ is the Tikhonov-Philips matrix and common choices are the identity or a matrix approximating the first or the second order of the derivative operator [Tikhonov and Arsenin (1977)]. By adding the second term more regular solutions are favored. If $\mathcal{L}$ is the identity and $\mathbf{x}_0 = 0$, an equivalent form of the above equation can be written as:

$$\chi(\mathbf{x}) = (\mathbf{y} - \mathbf{K}\mathbf{x})^T(\mathbf{y} - \mathbf{K}\mathbf{x}) + \alpha \mathbf{x}^T\mathbf{x}. \tag{4.15}$$

The location of the minimum of the Eq. 4.15 is given by:

$$\frac{\partial \chi(\mathbf{x})}{\partial \mathbf{x}} = -2\mathbf{K}^T\mathbf{y} + 2\mathbf{K}^T\mathbf{K}\mathbf{x} + 2\alpha\mathbf{x}. \tag{4.16}$$

If $\frac{\partial \chi(\mathbf{x})}{\partial \mathbf{x}} = 0$ then an explicit solution, denoted by $\mathbf{x}_\alpha$, is obtained:

$$\mathbf{x}_\alpha = (\mathbf{K}^T\mathbf{K} + \alpha\mathbf{I})^{-1}\mathbf{K}^T\mathbf{y} \tag{4.17}$$

where $\mathbf{I}$ is the identity. If $\alpha = 0$ then the first part of the above equation becomes $(\mathbf{K}^T\mathbf{K})^{-1}\mathbf{K}^T$ which is equivalent to Eq. 4.6. The searched solution is in this case $\mathbf{x}_\alpha = \widehat{\mathbf{x}}$ and the problem can be very sensitive to noise. If $\alpha \to \infty$ the obtained solution $\mathbf{x}_\alpha \to 0$ and the problem will be insensitive to noise but very unsatisfactory.

Choosing the optimal value for the regularization parameter is crucial. In the literature, several schemes have been studied for the selection of the regularization parameter, as the minimization of the generalized cross-validation function or L-curve [Hansen (1987), Desbat and Girard (1995)]. If the noise level is known, the Morozov's discrepancy principle [Morozov (1984)] gives good results. The regularization parameter must be chosen such that:

$$\|\mathbf{K}\mathbf{x}_\alpha^\delta - \mathbf{y}^\delta\| \leq \tau\delta \tag{4.18}$$

where τ is of the order of 1.

4.3 Minimization algorithms

In order to obtain the solution of the inverse problem, the regularization functional must be minimized. We detail in the following some algorithms used for this minimization task. We first review the basic gradient descent method.

4.3.1 Gradient descent method

The simplest method is the one of the gradient or gradient descent. Gradient descent is also known as steepest descent. As its name indicates, a local minimum of a function can be found using the gradient descent at the current point by taking steps proportional to the negative of the gradient. The solution of Eq. 4.1 can be obtained in an iterative way using the steepest descent algorithm. Let us first define the general quadratic objective function to minimize as:

$$\Phi(\mathbf{x}) = \frac{1}{2}\mathbf{x}^T\mathbf{K}\mathbf{x} - \mathbf{y}^T\mathbf{x}. \tag{4.19}$$

where $\mathbf{K}$ is a square matrix. The gradient of $\Phi(\mathbf{x})$ is :

$$\nabla\Phi(\mathbf{x}) = \mathbf{K}\mathbf{x} - \mathbf{y}, \tag{4.20}$$

in other words the minimum is obtained as the solution of Eq. 4.1. Using the above equation we define the residual $\mathbf{r}$ as:

$$\mathbf{r} = -\nabla\Phi(\mathbf{x}) = \mathbf{y} - \mathbf{K}\mathbf{x}. \tag{4.21}$$

The residual $\mathbf{r}$ is also known as the search direction $\mathbf{d}$. The solution of Eq. 4.19 is obtained iteratively with the following equation:

$$\mathbf{x}_{k+1} = \mathbf{x}_k + \alpha_k\mathbf{r}_k \tag{4.22}$$

where α_k determines the speed of convergence of the method. If the step α_k is lower than the optimal α the method converges slowly. In the opposite case, if α_k is too high than the optimal α the method can easily diverge from the true solution. Since $\Phi(\mathbf{x})$ is a quadratic function of $\mathbf{x}$ the optimal α_k can be obtained explicitly:

$$\Phi(\mathbf{x}_{k+1}) = \frac{1}{2}(\mathbf{x}_k + \alpha_k\mathbf{r}_k)^T\mathbf{K}(\mathbf{x}_k + \alpha_k\mathbf{r}_k) - \mathbf{y}^T(\mathbf{x}_k + \alpha_k\mathbf{r}_k). \tag{4.23}$$

This equation can be rewritten in a simpler form as:

$$\Phi(\mathbf{x}_{k+1}) = \Phi(\mathbf{x}_k) + \frac{1}{2}\alpha_k^2\mathbf{r}_k^T\mathbf{K}\mathbf{r}_k - \alpha_k\left\|\mathbf{r}_k\right\|^2. \tag{4.24}$$

The optimal α is chosen so that

$$\Delta\Phi = \Phi(\mathbf{x}_{k+1}) - \Phi(\mathbf{x}_k) = \frac{1}{2}\alpha_k^2 \mathbf{r}_k^T \mathbf{K}\mathbf{r}_k - \alpha_k \|\mathbf{r}_k\|^2 \tag{4.25}$$

is as small as possible. This equation depends quadratically on a single variable α_k therefore the minimum is obtained at:

$$\alpha_k = \frac{\|\mathbf{r}_k\|^2}{\langle \mathbf{r}_k, \mathbf{K}\mathbf{r}_k \rangle}. \tag{4.26}$$

The actual change in $\Phi(\mathbf{x})$ can be found easily as:

$$\Delta\Phi = -\frac{1}{2}\frac{\|\mathbf{r}_k\|^4}{\langle \mathbf{r}_k, \mathbf{K}\mathbf{r}_k \rangle} \tag{4.27}$$

According to Eq. 4.25 it follows that the objective function Eq. 4.19 decreases for the choice:

$$\alpha_k = \rho\frac{\|\mathbf{r}_k\|^2}{\langle \mathbf{r}_k, \mathbf{K}\mathbf{r}_k \rangle} \tag{4.28}$$

where ρ is a constant that takes values between $0 < \rho < 2$. The maximum decrease is obtained when $\rho = 1$.

4.3.2 Conjugate gradient method

The basic idea of the conjugate gradient algorithm is to modify the search direction $\mathbf{d} = \mathbf{r}$ to be orthogonal to the previous search direction. The current search direction $\mathbf{d}_k$ is built out of the previous search direction $\mathbf{d}_{k-1}$.

The residual equation (Eq 4.29) for the kth step is:

$$\mathbf{r}_k = -\nabla\Phi(\mathbf{x}_k) = \mathbf{y} - \mathbf{K}\mathbf{x}_k. \tag{4.29}$$

The solution is obtained iteratively in this case as:

$$\mathbf{x}_{k+1} = \mathbf{x}_k + \alpha_k \mathbf{d}_k \tag{4.30}$$

with

$$\alpha_k = \frac{\mathbf{d}_k^T \mathbf{y}}{\mathbf{d}_k^T \mathbf{K}\mathbf{d}_k} = \frac{\mathbf{d}_k^T(\mathbf{r}_{k-1} + \mathbf{K}\mathbf{x}_{k-1})}{\mathbf{d}_k^T \mathbf{K}\mathbf{d}_k} = \frac{\mathbf{d}_k^T \mathbf{r}_{k-1}}{\mathbf{d}_k^T \mathbf{K}\mathbf{d}_k} \tag{4.31}$$

and

$$\mathbf{d}_k = \mathbf{r}_k - P_k \mathbf{d}_{k-1}. \tag{4.32}$$

Different versions of the algorithm exist, depending on the manner in which P_k from Eq. 4.32 is calculated. In this way the conjugate gradient method was extended to nonlinear optimization. For example, the method of Fletcher-Reeves (FR), known as nonlinear

conjugate gradient method, where P_k is:

$$P_k = \frac{\mathbf{r}_k^T \mathbf{r}_k}{\mathbf{r}_{k-1}^T \mathbf{r}_{k-1}}. \tag{4.33}$$

In other words, P_k is the ratio of the of the current gradient and the square norm of the previous gradient.

Other methods to calculate P_k are:

- Polak-Ribiére (PR) method:

$$P_k = \frac{\mathbf{r}_k^T (\mathbf{r}_k - \mathbf{r}_{k-1})}{\mathbf{r}_{k-1}^T \mathbf{r}_{k-1}}. \tag{4.34}$$

- Hestenes-Stiefel (HS) method:

$$P_k = -\frac{\mathbf{r}_k^T (\mathbf{r}_k - \mathbf{r}_{k-1})}{\mathbf{d}_{k-1}^T (\mathbf{r}_k - \mathbf{r}_{k-1})}. \tag{4.35}$$

4.3.3 Landweber iteration

The regularization functional must be minimized to obtain the solution of the inverse problem. It is possible to perform this minimization task with a gradient descent. For example, for least squares, the minimization is performed on the data term and an iterative way to get the solution of Eq. 4.1 is the Landweber algorithm [Hanke (1991)]:

$$\mathbf{x}_{k+1} = \mathbf{x}_k + \gamma \mathbf{K}^* (\mathbf{y} - \mathbf{K}\mathbf{x}_k) \qquad k = 0, 1, 2, 3, ... \tag{4.36}$$

where $\mathbf{K}^*$ is the adjoint operator of $\mathbf{K}$, $\mathbf{x}_0$ an initial guess and γ a positive number. In order to ensure the convergence of the algorithm γ must satisfy the following relation [Hanke (1991)]:

$$0 < \gamma < \frac{2}{\|\mathbf{K}\mathbf{K}^*\|}. \tag{4.37}$$

The speed of the convergence rate of the Landweber iteration is discussed in [Hanke (1991)]. The Landweber iteration method presents an easy form of implementation and is very robust. For linear problems, alternate direction minimization algorithms (ADMM) have been extensively studied recently [Esser (2009)]. These algorithms are very efficient for the minimization of various regularization functionals. They will not be used in this thesis, since we focus on nonlinear inverse problems.

4.4 Regularization method for nonlinear inverse problems

4.4.1 Nonlinear Tikhonov regularization

In Hilbert space framework, a nonlinear ill-posed inverse problem can be defined as:

$$\mathbf{y} = \mathcal{M}(\mathbf{x}), \tag{4.38}$$

where $\mathcal{M} : D(\mathcal{M}) \subset X \to Y$ is a nonlinear operator between Hilbert spaces X and Y with a domain D. An extensive treatment of this type of problem can be found in [Engl *et al.* (1989), Neubauer (1989), Scherzer *et al.* (1993)].

Since in practice there are only noisy data we are interested to solve a nonlinear problem defined as:

$$\mathbf{y}^\delta = \mathcal{M}\mathbf{x}^\delta, \tag{4.39}$$

where δ is the noise level of the model. The noise level δ is given by:

$$\left\|\mathbf{y}^\delta - \mathbf{y}\right\| \leq \delta. \tag{4.40}$$

The problem that we are searching to solve here is an ill-posed one therefore regularization is required. A well known and effective technique is the Tikhonov regularization presented in Section 4.2. Tikhonov regularization for linear problems has been expanded also for nonlinear problems.

The solution $\widehat{\mathbf{x}}$ is obtained with:

$$\widehat{\mathbf{x}} = \underset{\mathbf{x}}{\operatorname{argmin}} \left\{ \left\|\mathbf{y}^\delta - \mathcal{M}(\mathbf{x})\right\|_Y^2 + \alpha \left\|(\mathbf{x} - \mathbf{x}_0)\right\|_X^2 \right\} \tag{4.41}$$

where $\alpha > 0$ is the regularization parameter and $\mathbf{x}_0 \in X$ is an initial guess. The stability and convergence of the method have been studied in the references above. The following two theorems summarize the main results. They can be applied for continuous and weakly sequentially closed operators.

Theorem 1. *Let $\alpha > 0$ and let $(\mathbf{y}_k)$ and $(\mathbf{x}_k)$ be sequences where $\mathbf{y}_k \to \mathbf{y}^\delta$ and $\mathbf{x}_k$ is a minimizer of Eq. 4.41 with $\mathbf{y}^\delta$ replaced by $\mathbf{y}_k$. Then, there exists a convergent subsequence of $(\mathbf{x}_k)$ and the limit of every convergent subsequence is a minimizer of Eq. 4.41.*

Theorem 2. *Let $\widehat{\mathbf{y}} \in Y$ with $\left\|\mathbf{y}^\delta - \widehat{\mathbf{y}}\right\|$ and let $\alpha(\delta)$ be such that $\alpha(\delta) \to 0$ and $\frac{\delta^2}{\alpha(\delta)} \to 0$ as $\delta \to 0$. Then every sequence $\mathbf{x}_{\alpha_k}^{\delta_k}$, where $\delta_k \to 0$, $\alpha_k = \alpha(\delta_k)$ and $\mathbf{x}_{\alpha_k}^{\delta_k}$ is a solution to Eq. 4.41, has a convergent subsequence. The limit of every convergent subsequence is a $\mathbf{x}_0$-minimum norm solution.*

The convergence rate of the method can be estimated when conditions describing the smoothness of the solution ('source condition') and the regularity of the Fréchet derivative are assumed [Engl *et al.* (1989), Neubauer (1989), Scherzer *et al.* (1993)].

4.4.2 Nonlinear Landweber iteration

As in the linear case, the regularization functional may be minimized by a Landweber iteration. We assume that $\mathcal{M}$ is Fréchet differentiable. The solution of Eq. 4.1 is obtained using the following nonlinear Landweber iteration [Hanke *et al.* (1995)]:

$$\mathbf{x}_{k+1}^{\delta} = \mathbf{x}_{k}^{\delta} + \mathcal{M}'(\mathbf{x}_{k}^{\delta})^{*}[\mathbf{y}^{\delta} - \mathcal{M}(\mathbf{x}_{k})] + \alpha(\mathbf{x}_{k} - \mathbf{x}_{0}), \qquad k = 0, 1, 2, 3, ... \tag{4.42}$$

where $\mathbf{x}_{0}^{\delta}$ is an initial guess and $\mathcal{M}'^{*}$ the adjoint of the Fréchet derivative. If $\mathcal{M}$ is a linear operator, then the nonlinear Landweber iteration (Eq. 4.42) coincides with the linear Landweber algorithm. The reconstruction algorithms developed in this thesis are based on these formulations. More details concerning the Landweber type iterative method used in this thesis are given in Section 5.1.

4.4.3 Fréchet derivative

In this section of this manuscript a brief overview of the Fréchet derivative is given. The Fréchet derivative is named after Maurice Fréchet and it is commonly used to generalize the derivative of a real-valued function and to define the functional derivative widely used in the calculus of variations. We consider a functional f from an Hilbert space A into an Hilbert space B. The operator f is Gâteaux differentiable at x, if there is a bounded linear operator $\mathcal{T}_x$ such that:

$$\lim_{t \to 0} \frac{f(x + th) - f(x)}{t} = \mathcal{T}_x(h) \tag{4.43}$$

for every $h \in A$. If the convergence is uniform for h small enough the operator is Fréchet differentiable. Another equivalent definition is:

$$\lim_{y \to 0} \frac{f(x + y) - f(x) - \mathcal{T}_x(y)}{\|y\|} = 0. \tag{4.44}$$

for $\forall\ y \in A$. Our nonlinear algorithms for phase retrieval in in-line phase tomography are developed using the Fréchet derivative of the intensity measurements, which will be detailed in the next Section 5.2.

II Nonlinear iterative phase retrieval from Fresnel diffraction patterns using the Fréchet derivative for microradiography

Résumé général

Les méthodes étudiées précédemment dans la littérature sont basées sur la linéarisation de la relation entre le déphasage induit par l'objet et l'intensité diffractée de Fresnel. Les méthodes linéaires les plus communes sont: l'équation de transport de l'intensité (TIE) (Section 3.2.1), la fonction de transfert de contraste (CTF) (Section 3.2.5), ou l'approche mixte (Section 3.2.6). Dans cette partie du manuscrit, nous introduisons de nouveaux algorithmes non linéaires itératifs d'estimation de la phase à partir du module de la transformée de Fresnel en utilisant la dérivée de Fréchet.

Premièrement, dans le chapitre 5 nous donnons les bases du problème inverse non linéaire mal posé que constitue l'estimation de phase et nous proposons un algorithme non linéaire itératif de type Landweber. Les algorithmes étudiés dans ce manuscrit sont basés sur ce type de schéma itératif. La dérivée de Fréchet est calculée avec une méthode de différences finies avec un incrément de phase adapté au niveau de bruit. Les différentes distances de propagation sont utilisées de manière cyclique.

Les résultats numériques obtenus avec cette nouvelle méthode non linéaire itérative sont ensuite présentés dans la section 5.1.1. L'évaluation a été effectuée en utilisant un fantôme numérique, employé pour simuler des données de tomographie de phase avec et sans bruit. Cette méthode s'appuie sur l'intensité des projections obtenues pour différentes distances de propagation. Pour les données simulées, l'erreur quadratique moyenne normalisée a été mesurée mais nous avons observé une mauvaise convergence de l'algorithme non linéaire ou le phénomène de stagnation des itérations loin de la vraie solution de phase lorsqu'aucun schéma préalable de régularisation n'a été pas inclus. Notre approche améliore l'approche linéaire mixte [Guigay *et al.* (2007)] et donne de bons résultats sur des données bruitées simulées. Ainsi, si la précision de la reconstruction est l'objectif principal, surtout dans une analyse quantitative, cette méthode pourrait être très intéressante.

Afin de surmonter les limitations liées au temps de calcul et la mémoire pour l'application à des images de taille réaliste, nous avons proposé d'exploiter une expression analytique de la dérivée de Fréchet et de son adjoint.

Plusieurs algorithmes non linéaire itératifs ont été proposés et analysés dans la littérature, basés sur des fonctionnelles de régularisation définies dans le cadre d'espaces de Hilbert [Scherzer *et al.* (2008)]. Si l'analyse de la convergence de ces méthodes a été effectuée, elles n'ont jamais auparavant été testées dans le contexte de l'estimation de phase. Dans la section 5.2.1, nous analysons les propriétés de régularité de l'opérateur d'intensité I_D et de sa dérivée de Fréchet, quand il est défini entre des espaces Hilbert appropriés. Ces propriétés sont des conditions nécessaires pour la convergence des approches de régularisation utilisées dans ce travail dans le cadre des espaces de Hilbert. Ces conditions nécessaires n'avaient pas été étudiées avant. Enfin dans la section 5.2.2, en exprimant l'opérateur à inverser comme une composition d'opérateurs élémentaires, nous obtenons une expression analytique de la dérivée de Fréchet de l'intensité et de son adjoint.

Dans la section 5.2.4, nous évaluons plusieurs approches non linéaires itératives d'estimation de phase en partant d'une solution initiale donnée par l'algorithme mixte (Chapitre 3). Nos approches itératives non linéaires utilisent la dérivée de Fréchet de l'intensité enregistrée à des différentes distances de propagation. Nous avons comparé la convergence des trois algorithmes, deux basées sur le gradient de différences finies et un sur l'expression analytique du gradient. Plus précisément, le calcul de la direction de descente et des itérations dans notre étude peut être réalisé en utilisant trois méthodes : 1) à l'aide des différences finies avec une longueur de pas ajustable, 2) en rajoutant un procédé de filtrage implicite aux différences finies ou 3) avec un calcul analytique de l'adjoint de l'intensité diffractée. Les meilleurs résultats sont obtenus lorsque le problème inverse est régularisé avec une norme de type L_2 du gradient de la phase et lorsque les différentes distances de propagation objet-détecteur sont traitées par une méthode de type Kaczmarz où une itération de descente est effectuée pour chaque distance de propagation.

L'évaluation de la méthode a été réalisée en utilisant une carte de phase simple, à la fois avec et sans bruit. Pour les données simulées, l'erreur quadratique moyenne normalisée a été mesurée. Afin d'obtenir la meilleure convergence de $J(\varphi)$ (Eq. 5.4) le paramètre de régularisation α est choisi par une méthode de type essai et erreur. Ce type de méthode a été utilisée dans plusieurs ouvrages dans le cadre des problèmes non linéaires mal posés [Daubechies *et al.* (2008)]. Notre approche améliore les méthodes linéaires sur des données bruitées simulées pour différentes niveaux de bruit au-dessus de 20dB et les non linéarités de la diffraction de Fresnel sont bien prises en compte. La vitesse de convergence de notre algorithme et les limitations de mémoire présentées dans la Section 5.2.2, sont surmontées grâce au calcul analytique de la dérivée de Fréchet et de son adjoint.

Il a été montré dans cette première partie, que l'approche non linéaire itérative améliore les résultats obtenus en utilisant la solution linéaire mixte comme initialisation, mais des stagnations éloignées de la vraie solution de phase sont observées (Section 5.1.1 et Section 5.2.3). Pour surmonter ce problème dans la deuxième partie du manuscrit, la méthode itérative de type Landweber basée sur la dérivée de Fréchet de l'opérateur non linéaire I_D, proposée précédemment (Section 5.2.3) est affinée en introduisant des opérateurs de projection. Dans la section 6, nous utilisons des opérateurs de projection afin de respecter certaines contraintes sur la phase récupérée et pour améliorer l'ancien algorithme linéaire d'estimation de phase.

Les algorithmes classiques basés sur des projections d'intensité conçus pour résoudre le problème d'estimation de phase ont été examinés dans le contexte mathématique des opérateurs de projection à valeurs multiples et de l'optimisation convexe [Bauschke *et al.* (2002)]. La connexion a été établie entre les méthodes d'estimation de la phase tels que les approches de la réduction d'erreur de type Fienup [Fienup (1982)] et les algorithmes d'optimisation convexe standard. Les approches communes pour résoudre le problème de la récupération de phase classique consistent à appliquer alternativement les contraintes

dans le domaine objet et dans le domaine de Fourier. Dans ce travail, nous avons considéré une contrainte de module de l'image dans le domaine de l'objet, permettant ainsi de mieux comprendre les opérateurs de projection convexe ou non convexe présentés dans la section 5.2.3

La nouvelle méthode itérative non linéaire combine la dérivée de Fréchet de l'intensité enregistrée à différentes distances de propagation et la méthode de projection sur des ensembles convexes ou non convexes comme dans les algorithmes de type Fienup. Cette méthode a été testée en utilisant deux types d'initialisations. Une donnée par la même carte de phase simulée avec un bruit blanc gaussien additif (PPNSR = 24 dB), comme dans la section 5.2.3, et une autre loin de la vrai solution de phase.

L'erreur quadratique moyenne normalisée sur la phase diminue dans le cas de l'initialisation mixte de **0.1471** à **0. 0268** et dans le cas de l'initialisation éloignée de la vraie phase de **0.8121** à **0.0234** respectivement. Un schéma de régularisation lisse a été choisi (α = 0,01). L'utilisation des projecteurs permet d'améliorer la propriété de convergence de la méthode itérative non linéaire présentée dans la section 5.2.3).

Pour conclure, notre nouvelle approche améliore la méthode linéaire mixte (Section 3.26) fondée sur une linéarisation de la relation entre le déphasage induit par l'objet et l'intensité diffractée mais aussi notre première approche non linéaire (Section 5.2.3) pour des données simulées bruitées.

Cette partie du manuscrit se termine avec la section 6.3, où la résolution du problème inverse non linéaire est étudiée avec une régularisation de type Tikhonov (Section 5.1) et avec des opérateurs de projection (Section 6.2) proposés précédemment. Comme il est précisé dans la section 5.1 le problème inverse mal posé de la phase est stabilisé par un terme de régularisation de type Tikhonov avec le carré de la norme de type L_2 du gradient de la phase. Dans cette section, l'algorithme itératif de type Landweber est modifié en remplaçant ce terme $\nabla\varphi$ avec la norme de type L_2 de la phase φ. L'algorithme est évalué en utilisant des projections d'intensité pour un fantôme plus complexe en présence du bruit. Le fantôme utilisé dans ce travail est le 3D Shepp-Logan pour deux types de phase: variant fortement ou faiblement. La qualité de la reconstruction pour la projection d'un fantôme 3D Shepp-Logan a été évaluée quantitativement avec et sans bruit. Dans ces tests, trois distances de propagation sont utilisées d'une manière aléatoire pour obtenir une bonne reconstruction de phase.

Nous montrons que cette nouvelle approche non linéaire conduit à une réduction importante des erreurs quadratique moyenne sur les reconstructions de phase. La méthode non linéaire proposée est comparée avec les approches linéaires (Chapitre 3). L'approche basée sur l'équation de l'intensité du transport (TIE) donne la meilleure solution pour des cartes de phase variant lentement sans bruit. Pourtant, pour la phase fortement variable et les données bruitées la méthode non linéaire proposée améliore les méthodes linéaires.

Chapter 5

Nonlinear phase retrieval using Fréchet derivative

Contents

This chapter of the manuscript is organized in four sections as follows. The details of the Landweber type iterative method on which our proposed nonlinear algorithms are based is first given in Section 5.1 and then followed by the presentation of the Fréchet derivative of the intensity in Section 5.2. The numerical results obtained with the proposed

nonlinear iterative method are shown in Section 5.1.1. Section 5.2.2 details the analytic calculation of the Fréchet derivative and of its adjoint.

5.1 A Landweber type iterative method

In view of Eq. 3.5, the intensity can be regarded as a function of φ, $I_D(\varphi)$. The operator $I_D(\varphi)$ can be considered as a nonlinear operator which is Fréchet differentiable in its domain. In the following, we will consider that the phase has a Lipschitz bounded support Ω and that the domain $\mathcal{D}[I_D(\varphi)]$ of the operator $I_D(\varphi)$ belongs to the functional Sobolev space $H^{2,2}_{\diamond}(\Omega)$ [Scherzer *et al.* (2008)]:

$$H^{2,2}_{\diamond}(\Omega) = \{\varphi \in H^{2,2}(\Omega), \quad \frac{\partial \varphi}{\partial \vec{n}} = 0\} \tag{5.1}$$

where $\frac{\partial \varphi}{\partial \vec{n}}$ is the normal derivative of the phase. This functional space $H^{2,2}$ corresponds to functions whose second order derivatives belong to L_2. Other functional spaces can be chosen. The detailed study of the convergence conditions will not be detailed here. We thus consider the problem of minimizing the functional:

$$J(\varphi) = \|I_D(\varphi) - I_\delta\|^2_{L_2(\Omega)} \tag{5.2}$$

where $\|.\|_{L_2(\Omega)}$ denotes the $L_2(\Omega)$ norm, I_δ approximates the exact data I_D with the accuracy ι:

$$\|I_D - I_\delta\|_{L_2(\Omega)} \leq \iota. \tag{5.3}$$

In order to regularize the problem, we introduce a Tikhonov's functional of the following form:

$$J_\alpha(\varphi) = \frac{1}{2}\|I_D(\varphi) - I_\delta\|^2_{L_2(\Omega)} + \frac{\alpha}{2}\|\nabla\varphi\|^2_{L_2(\Omega)} \tag{5.4}$$

where α is a regularizing parameter. The stabilizing norm is thus a Sobolev type regularizing term based on the gradient of the phase to be retrieved. The optimality condition is:

$$J'_\alpha(\varphi) \cdot h = 0, \qquad \forall h \in H^{2,2}_{\diamond}(\Omega) \tag{5.5}$$

It can be written with the Fréchet derivative of the intensity $I'_D(\varphi)$, where $\langle , \rangle$ denotes the scalar product

$$2\Big\langle I_D(\varphi) - I_\delta, I'_D(\varphi).h\Big\rangle_{L_2(\Omega)} + 2\alpha\langle\nabla\varphi, \nabla h\rangle_{L_2} = 0 \tag{5.6}$$

or with the adjoint $I'(\varphi)^*$ of the Fréchet derivative

$$2\Big\langle I'_D(\varphi)^*[I_D(\varphi) - I_\delta], h\Big\rangle_{L_2(\Omega)} + 2\alpha\langle\nabla\varphi, \nabla h\rangle_{L_2} = 0. \tag{5.7}$$

The optimality condition is then:

$$I_D^{'}(\varphi)^*[I_D(\varphi) - I_\delta] - \alpha\nabla\cdot(\nabla\varphi) = 0. \tag{5.8}$$

The step length parameter τ_k is chosen in order to minimize the Tikhonov's functional along the descent direction:

$$\tau_k = \underset{\tau}{\operatorname{argmin}} J_k(\varphi_k - \tau\delta_k), \tag{5.9}$$

where $\delta_k = I_D^{'}(\varphi_k)^*[I_D(\varphi_k) - I_\delta] - \alpha_k\triangle\varphi_k$ is the descent direction. An approximate value is obtained with a dichotomy strategy. This optimality condition defines the descent direction of our steepest descent iterative method, the next phase iterate φ_{k+1} is obtained from the iterate φ_k with:

$$\varphi_{k+1} = \varphi_k - \tau_k\nabla J_k(\varphi_k). \tag{5.10}$$

Starting from the current phase estimate φ_k at the iteration k, a linear search procedure is introduced with a variable step τ_k yielding the following modification of the standard Landweber method:

$$\varphi_{k+1} = \varphi_k - \tau_k\{I_D^{'}(\varphi_k)^*[I_D(\varphi_k) - I_\delta] - \alpha\triangle\varphi_k\}. \tag{5.11}$$

The regularizing parameter is chosen by trial-and-error in order to obtain the best decrease of $J(\varphi)$. These equations correspond to a Landweber method with a regularizing smoothing term and an adaptive step length. This type of method has been used in several works on nonlinear ill-posed problems [Hanke *et al.* (1995), Daubechies *et al.* (2008)].

The described algorithm involves a single distance. In order to include the intensity maps obtained for the different distances, we consider a cyclic iteration over several distances, one iteration being performed for each distance. This method may be seen as a Kaczmarz type method. The use of several distances should improve the reconstruction since it allows a better coverage of the frequency domain and it improves the statistics.

5.1.1 Numerical results

The results of this section have been published in the following article:

B. Sixou, V. Davidoiu, M. Langer, and F. Peyrin,

"Non-linear phase retrieval from Fresnel diffraction patterns using the Fréchet derivative"

IEEE International Symposium on Biomedical Imaging - ISBI2011, Chicago, USA, pp. 1370–1373, 2011.

In this section, we apply the proposed nonlinear iterative approach using intensity measurements recorded at a few number of propagation distances. The evaluation of the method was performed using a simple phase map, both with and without noise.

In order to save computing time, the algorithm is initialized with the mixed approach presented in Section 3.2.6. The mixed approximation of the forward problem (Eq. 3.26) is an initial guess, close enough to the ideal result to ensure convergence of our algorithm. Several regularization schemes have been tested to solve this linear inverse problem, like classical quadratic Tikhonov regularization and wavelet shrinkage.

5.1.2 Simulation of the diffracted intensity

Following [Langer *et al.* (2008)], the imaging system was simulated in a deterministic fashion. Two phantoms were defined, one for the absorption coefficient and one for the refractive index decrement. Theoretical values for the absorption coefficient and the refractive index, δ_r and β, for different materials at 24 keV ($\lambda = 0.5166$ angstrom) were used for the phantom. Propagation in free-space was simulated using Eq. 3.5. The phase contrast images were all corrupted with additive Gaussian white noise with various peak-to-peak signal to noise ratios (PPSNR), between 24 dB and 0 dB. The peak-to-peak signal to noise ratio is defined by:

$$\text{PPSNR} = 20\log\left(\frac{f_{max}}{n_{max}}\right), \tag{5.12}$$

where f_{max} is the maximum signal amplitude and n_{max} is the maximum noise amplitude.

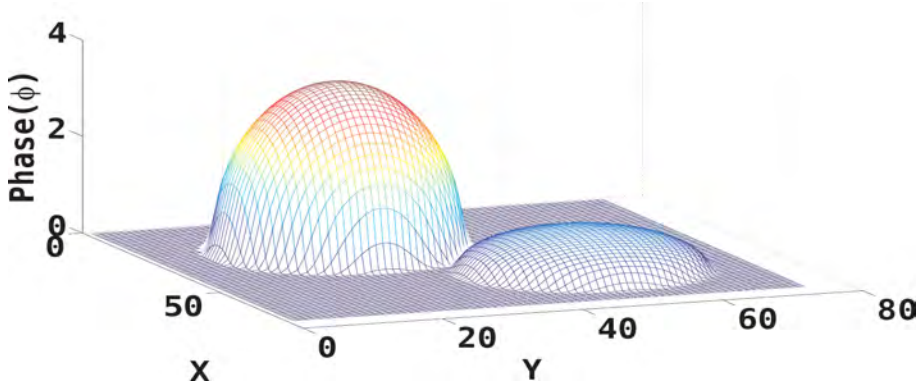

Figure 5.1: Original phase map to be retrieved.

The convolution product was calculated by Fourier transforms and the intensity has been obtained as the squared modulus in the spatial domain of this convolution. Using the free-space propagation equation, images were calculated for the eight propagation distances 0.2 m, 0.4 m, 0.6 m, 0.8 m, 1.0 m, 1.2 m, 1.4 m and 1.6 m. The corresponding pixel size was 1.5 μm.

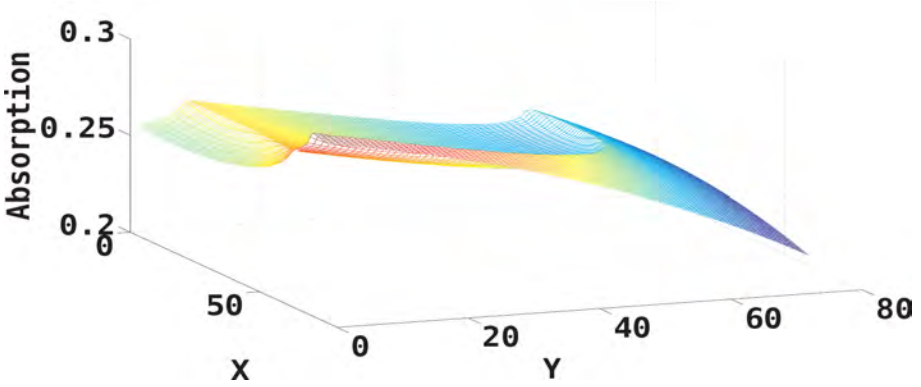

Figure 5.2: Original absorption.

The original phase map to be retrieved is displayed in Figure 5.1, together with the absorption map in Figure 5.2. The corresponding Fresnel diffraction patterns for the propagation distance D=1.4 m without noise and with noise (PPSNR=24dB) are displayed in Figure 5.3(a) and Figure 5.3(b) respectively. These distances are suitable for testing and comparing the phase retrieval methods.

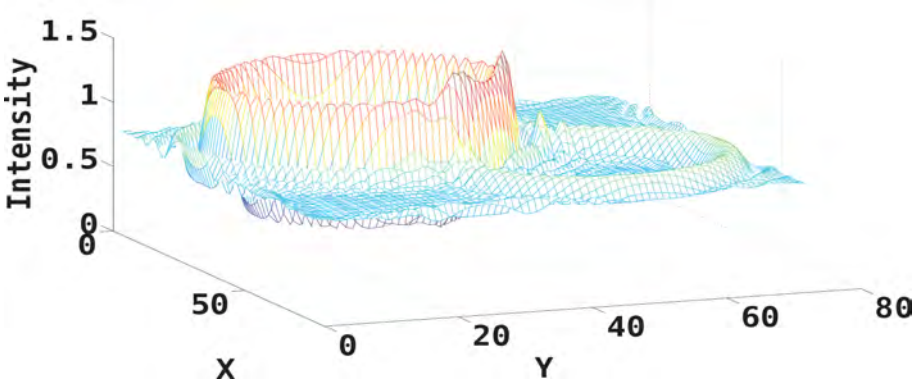

(a)

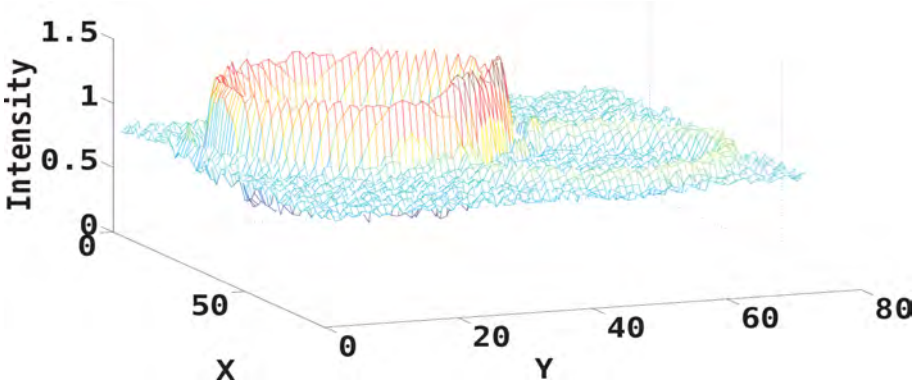

(b)

Figure 5.3: Fresnel diffraction pattern at propagation distance D=1.4 m (a) without noise and (b) with PPSNR=24dB.

5.1.3 Results and discussions

The diffracted intensity was simulated as described in Section 5.1.2. The images obtained were downsampled to $N = 75 \times 75$ pixels. The phase contrast images were corrupted with additive Gaussian white noise with peak-to-peak signal to noise ratios (PPSNR Eq 5.12) of 20dB, 0dB and without noise.

As a first approach, in order to calculate the gradient of the potentially noisy intensity function, we have applied the implicit filtering method described by Kelley et al. [Kelley (1999)]. In its simplest form, implicit filtering is the steepest descent algorithm with finite difference gradients, where the difference increment varies as the iteration progresses. Because the gradient is only an approximation, the computed descent direction may fail to be a descent direction, and the line search may fail. In this case the difference increment is reduced. The derivatives in the gradient I'_D are approximated by centered difference formulas. This finite difference method requires many evaluations of the Tikhonov's functional. The Fréchet derivative G_k calculated with the finite difference method at the point φ_k is a thus matrix of $\mathbb{R}^{N\times N}$.

In the iteration, we have chosen to not introduce any a priori information on the phase values. The iteration was stopped when the data term $\|I_D(\varphi_k) - I_\delta\|$ was equal to the noise level.

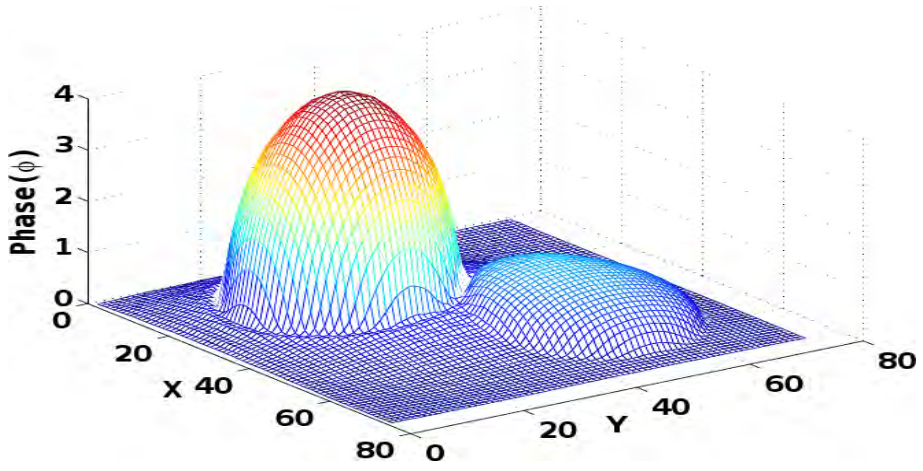

Figure 5.4: Reconstructed phase for our Landweber type method and noise free simulations.

The phase maps obtained with our method are displayed in Figure 5.4 and Figure 5.5, without noise and with noise at 20dB. The Kaczmarz type finite difference Landweber type method has been tested on noise-free and noisy data. If φ^* is the phase to be recovered, the normalized least square error of $L_2(\Omega)$ norm $\|\varphi_k - \varphi^*\|/\|\varphi^*\|$ is used to measure the quality of the phase recovery. The results obtained with noise-free and noisy data are displayed in Figure 5.6 as a function of the number of iterations. Our iterative phase retrieval algorithm retrieves the phase better than the linear mixed approach. The errors on the phase have been significantly reduced for the noise free simulations.

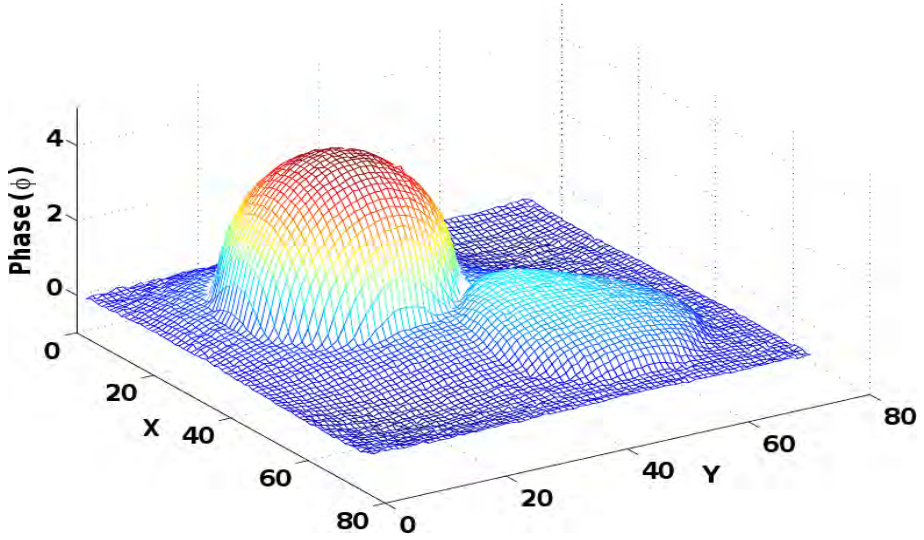

Figure 5.5: Reconstructed phase for our Landweber type method and 20dB PPSNR.

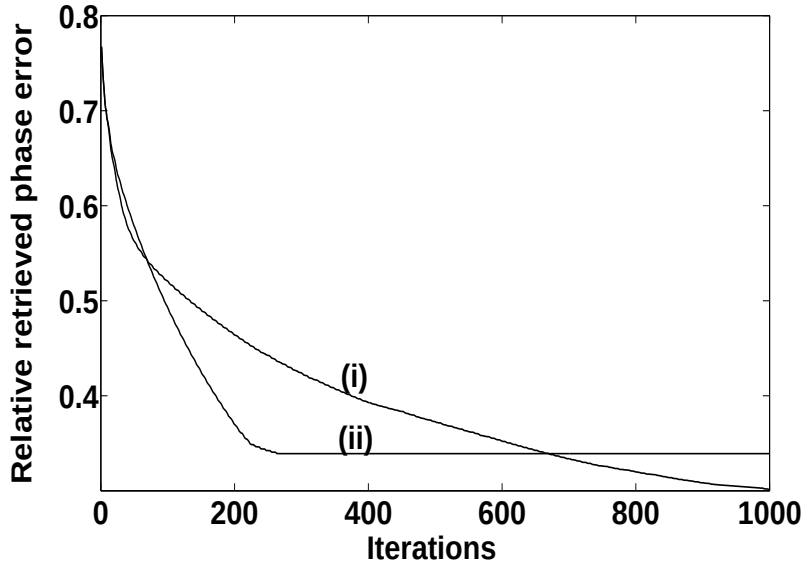

Figure 5.6: Evolution of the mean square error for the phase for (i) the noise free and (ii) the noisy data with PPSNR=20dB.

5.1.4 Conclusions

In this section we have presented a new nonlinear iterative method of phase retrieval for in-line phase tomography based on the Fréchet derivative of intensity. This method uses the intensity projections obtained for different propagation distances in a Kazcmark type cyclic iteration. The Fréchet derivative is evaluated with a finite difference method with a phase increment adapted to the noise level.

The evaluation was performed using a numerical phantom, used to simulate phase contrast tomography data with and without noise. For the simulated data, the normalized mean square error was measured. Our approach outperforms the mixed approach and it

performs well on simulated noisy data. Thus, if the accuracy of the reconstruction is the primary goal, especially in a quantitative analysis, this method could be very interesting.

In order to overcome the long computation time and memory limitation of the proposed method, the Fréchet derivative and its adjoint must to be calculate in an analytical way. The details concerning the explicit computation of the Fréchet derivative are given in the next section of this chapter.

5.2 Fréchet derivative of the intensity

In this section we present the Fréchet derivative of the intensity properties.

5.2.1 Regularity properties of the Fresnel intensity operator and its Fréchet derivative

In this section, we investigate some new regularity properties of the forward intensity operator I_D and of its Fréchet derivative when it is defined between suitable Hilbert spaces. These functional properties are necessary conditions for the convergence of the regularization approaches used in the following in a Hilbert space framework. These necessary conditions have not been investigated before. We use here some general results detailed in [Dicken (1999)].

We assume that the function $\varphi(\mathbf{x})$ is defined on Ω, which is a compact subset of $\mathbb{R}^2$, and that the forward operator is a nonlinear mapping $I_D : L_2(\Omega) \to L_2(\mathbb{R}^2)$. We first show that the Fresnel intensity operator $I_D(\varphi)$ can be decomposed in simple operators between suitable function spaces. We consider first the bilinear multiplication operator $M : L_\infty(\mathbb{R}^2) \times L_\infty(\mathbb{R}^2) \to L_\infty(\mathbb{R}^2)$ defined by $M(u, v)(\mathbf{x}) = u(\mathbf{x})v(\mathbf{x})$, i.e., as the product between the functions $u(\mathbf{x})$ and $v(\mathbf{x})$. It is clear that this operator is continuous, and thus Fréchet differentiable. The next operator entering in the decomposition of the intensity operator is the complex exponential operator, $E : L_2(\Omega) \to L_\infty(\Omega)$ defined by:

$$E(u(\mathbf{x})) = \exp(-iu(\mathbf{x})). \tag{5.13}$$

It is Fréchet differentiable and its Fréchet derivative E' is Lipschitz continuous. The proof of this result can be found in [Dicken (1999)]. Let us denote F_D the linear operator corresponding to the convolution by the Fresnel kernel P_D defined in Eq. 3.6. The operator F_D can be considered as a linear mapping between $L_\infty(\Omega)$ and $L_\infty(\mathbb{R}^2)$. With the above-defined operators, the nonlinear intensity operator $I_D : L_2(\Omega) \to L_2(\mathbb{R}^2)$ admits the decomposition:

$$I_D(\varphi) = M \circ (F_D \circ \psi, \overline{F_D \circ \psi})(\varphi) \tag{5.14}$$

with $\psi(.) = a(\mathbf{x})E(.)$. The Fresnel intensity operator $I_D(\varphi)$ is thus continuous. Its Fréchet differentiability can be calculated from the chain rule. The Fréchet derivative at the point

φ is given for $\epsilon \in L_2(\Omega)$ by:

$$\epsilon \mapsto I'_D(\varphi)(\epsilon) = M(A, \overline{F_D \circ \psi(\varphi)}) + \ c.c \tag{5.15}$$

with $A = F_D(aE'(\varphi)(\epsilon))$ and where $c.c$ is the complex conjugate term.

It can been shown that the derivative E' of the exponential is locally Lipschitz continuous [Dicken (1999)]. The same result thus holds for the forward intensity operator and its Fréchet derivative. To summarize, the forward Fresnel intensity operator is a continuous operator with a Lipschitz continuous Fréchet derivative, which is the main regularity assumptions of the regularization methods used in the following in a Hilbert space setting.

5.2.2 Explicit Fréchet derivative computation

In the case of the intensity-phase relationship, the Fréchet derivative of the operator $I_D(\varphi)$ at the point φ_k is the linear operator defined by the relationship:

$$I_D(\varphi_k + \varepsilon) = I_D(\varphi_k) + G_k(\varepsilon) + O(\varepsilon^2). \tag{5.16}$$

Using the results of the former section and the formula 5.15 we obtain that the linear operator $I'_D(\varphi_k)(\varepsilon) = G_k(\varepsilon)$ can be given explicitly as:

$$\begin{aligned} G_k(\varepsilon) = &\{-[ia\varepsilon \exp(-i\varphi)] * P_D\}\{[(a \exp(i\varphi)] * \overline{P_D}\} \\ &+\{[a \exp(-i\varphi)] * P_D\}\{[ia\varepsilon \exp(i\varphi)] * \overline{P_D}\} \end{aligned} \tag{5.17}$$

where $*$ denotes the convolution operator. An equivalent form of this equation is:

$$G_k(\varepsilon) = 2\text{Real}\left(\{-[ia\varepsilon \exp(-i\varphi_k)] * P_D\}\{[a \exp(i\varphi_k)] * \overline{P_D}\}\right). \tag{5.18}$$

This formula was obtained from 5.15 with $A = -[ia\varepsilon \exp(-i\varphi)] * P_D$ and $\overline{F_D \circ \psi(\varphi)} = [a \exp(i\varphi_k)] * \overline{P_D}$. The adjoint operator G_k^* can be obtained using standard definition of the scalar product in L_2 spaces. It is defined by:

$$\begin{aligned} G_k^*(\varepsilon) = &\{\varepsilon \left[a \exp(-i\varphi)\right]^* P_D\}^* \left\{[ia \exp(i\varphi)] * \overline{P_D}\right\} \\ &+ \{[ia \exp(-i\varphi)]^* P_D\}^* \left\{[-a\varepsilon \exp(i\varphi)] * \overline{P_D}\right\} \end{aligned} \tag{5.19}$$

or

$$G_k^*(\varepsilon) = 2\text{Real}\left[\left(\{\varepsilon[a \exp(-i\varphi_k)^* P_D]\}^* \overline{P_D}\right)\{ia \exp(i\varphi_k)\}\right]. \tag{5.20}$$

In order to retrieve the phase from the intensity measurements and to obtain a rather smooth solution, we consider the problem of minimizing a Tikhonov's functional presented in Section 5.1 using the Fréchet derivative of the intensity (Eq. 5.17) and its adjoint (Eq. 5.19). This is detailed in the following section.

5.2.3 *Analytic* expression of the Fréchet derivative

In this section several nonlinear iterative approach for phase retrieval including a prior knowledge about the phase map are studied. In order to solve the inverse problem, we have searched for a smooth solution because failure of convergence or stagnation of the iterates away from the solution were observed when no prior information was included. Numerous iterative algorithms have been proposed and analyzed in the literature, based on regularization functional defined in a Hilbert space context [Scherzer *et al.* (2008)]. In this section, a convergence analysis of the proposed methods is not performed. We show that it gives good results for typical phase maps found in in-line phase tomography applications, with various levels of noise.

The calculation of the descent direction and of the iterates can be performed using finite differences with an adaptive step length, the implicit filtering method or with an analytic calculation of the adjoint of the diffracted intensity.

5.2.4 Numerical calculation by implicit filtering

The results of this section have been published in the following article:
V. Davidoiu, B. Sixou, M. Langer, and F. Peyrin,
"Non-linear iterative phase retrieval based on Fréchet derivative"
Optics Express, vol. 19, No. 23, pp.22809-22819, 2011.

In the following, we have compared the numerical results for the simple test case introduced above with the following algorithms:

1. A_1: Kaczmarz type finite difference Landweber method with a regularization term or without any regularization ($\alpha = 0$).

2. A_2: Sequential type finite difference Landweber method with a regularization term or without regularization term performed with N=100 iterations for each distance.

3. A_3: Kaczmarz type analytic Landweber method with the former stopping conditions with a regularization term or without any regularization ($\alpha = 0$).

The phase retrieval is performed using noise-free and noisy intensity data. The gradient has been computed using implicit filtering method described by Kelley et al in [Gilmore and Kelley (1985), Stoneking *et al.* (1992), Kelley (1999)]. The derivatives in the gradient $I'_D(\varphi)$ are thus approximated by centered differences formulas. It is noteworthy that this finite difference method requires 2N evaluations of the Tikhonov functional, where N is the phase vector dimension and it leads to a squared matrix of size N^2. In this work, the

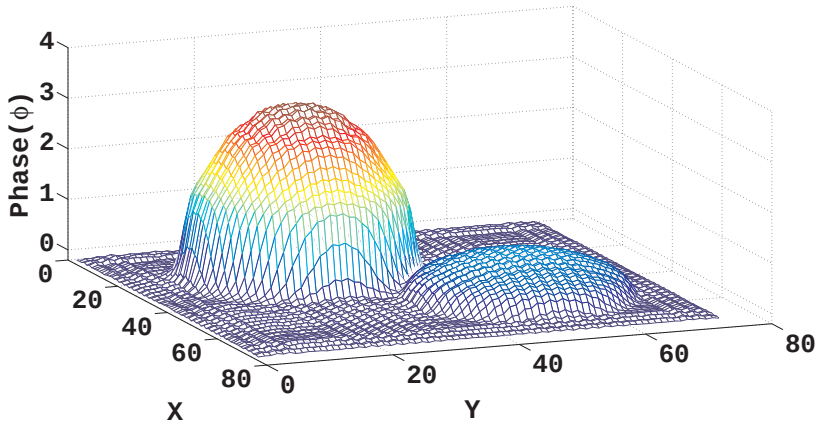

Figure 5.7: Phase obtained with the mixed approximation.

phase increment is set to 0.05 rad which is the estimated noise level on the phase. This phase increment must be small enough so that the linearization is valid and higher than the noise level.

5.2.5 Initialization and stopping conditions

Our phase retrieval algorithms are not globally convergent algorithms. The method will be quantitatively evaluated by measuring the normalized mean square error (NMSE) using the $L_2(\Omega)$ norm. If φ^* is the phase to be recovered and φ_k the current estimate, the NMSE is calculated as:

$$\|\varphi_k - \varphi^*\|/\|\varphi^*\| \tag{5.21}$$

The mixed approximation of the linear problem has been used as the starting point of our simulations. It is displayed in Figure 5.7. The initial NMSE is 0.147. This a priori guess of the solution ensures the convergence of the algorithms.

To avoid problems at the image boundary, the phase support is assumed to be included in the 70×70 inner pixels and the border pixels have been fixed to zero. Since several intensity maps obtained at different distances are available, the inverse problem may be split into a finite number of sub-problems. In order to take into account more than one intensity map, we propose two variants of a cyclic iteration over the distances. When one steepest descent iteration is performed for each image recording distance, this method will be called a *Kaczmarz* type method in the following discussion. When a hundred or more iterations are performed for each distance, this methodology will be called a *sequential* one.

In the following, the iterate φ_{k+1} is accepted if the following two conditions are satisfied:

$$J_\alpha(\varphi_{k+1}) \leq J_\alpha(\varphi_k) \tag{5.22}$$

and

$$\|I(\varphi_{k+1}) - I_\delta\|_{L_2(\Omega)} \leq \|I(\varphi_k) - I_\delta\|_{L_2(\Omega)}. \tag{5.23}$$

The iterations are terminated when

$$\|I(\varphi_k) - I_\delta\| \leq \delta \tag{5.24}$$

with the residual value δ equal to the noise level. A divergence of the iterates away from the solution is obtained if these stopping conditions are not imposed.

5.2.6 Results and discussions

Algorithms differ by the number of descent iterations performed for each propagation distances, by the calculation of the adjoint of the Fréchet derivative which is based on finite difference or on an analytic expression and by the regularization term. The difference between the algorithms A_1 and A_2 is the way of the cyclic iteration in the intensity maps is performed. The last algorithm A_3 represents the Kaczmarz type analytic Landweber method with the stopping conditions (5.22), (5.23) and (5.24) both without regularization term or with the regularization method.

Figure 5.8 displays the difference maps between the solution and the true phase to be retrieved. Figure 5.8(a) is the initial error map obtained from the mixed approach showing that errors are mostly concentrated at the edges. Figures 5.8(b), 5.8(c) and 5.8(d) illustrate the differences maps respectively obtained with the algorithm A_1 (PPSNR=24 dB), A_2 (noisy-free) and A_3 (PPSNR=24 dB). The regularization parameter was set to $\alpha = 0.01$. In order to have more quantitative information about the convergence rates and to compare the algorithms, we have studied NMSE for the phase shift as a function of the number of iterations. Figure 5.9 shows the evolution of the NMSE as a function of the number of iterations for the different algorithms on the noise-free and noisy data (PPSNR=24 dB) for $\alpha = 0.01$.

The errors on the phase have been significantly reduced with all algorithms. The use of several distances improves the reconstruction because it allows a better coverage of the frequency domain and it improves the statistics. Yet, a very slow convergence is obtained with the algorithm A_2. Kaczmarz type methods are thus to be preferred.

It is well known that the Landweber iteration has a regularizing effect, the number of iterations being the regularization parameter. The regularization term is not crucial in that case and improves only slightly the convergence rate. Yet, a divergence of the iterates away from the solution has been observed for other phase maps, if this term is not included in the functional. The regularization parameter has been selected from trial-and-error. As displayed in Figure 5.9(a) and 5.9(b) for noise-free and noisy data, the use of a weak ($\alpha = 0.01$) smoothing regularization yields good phase retrieval convergence results.

In Figure 5.9 it can observed that the algorithm A_3 has good convergence properties.

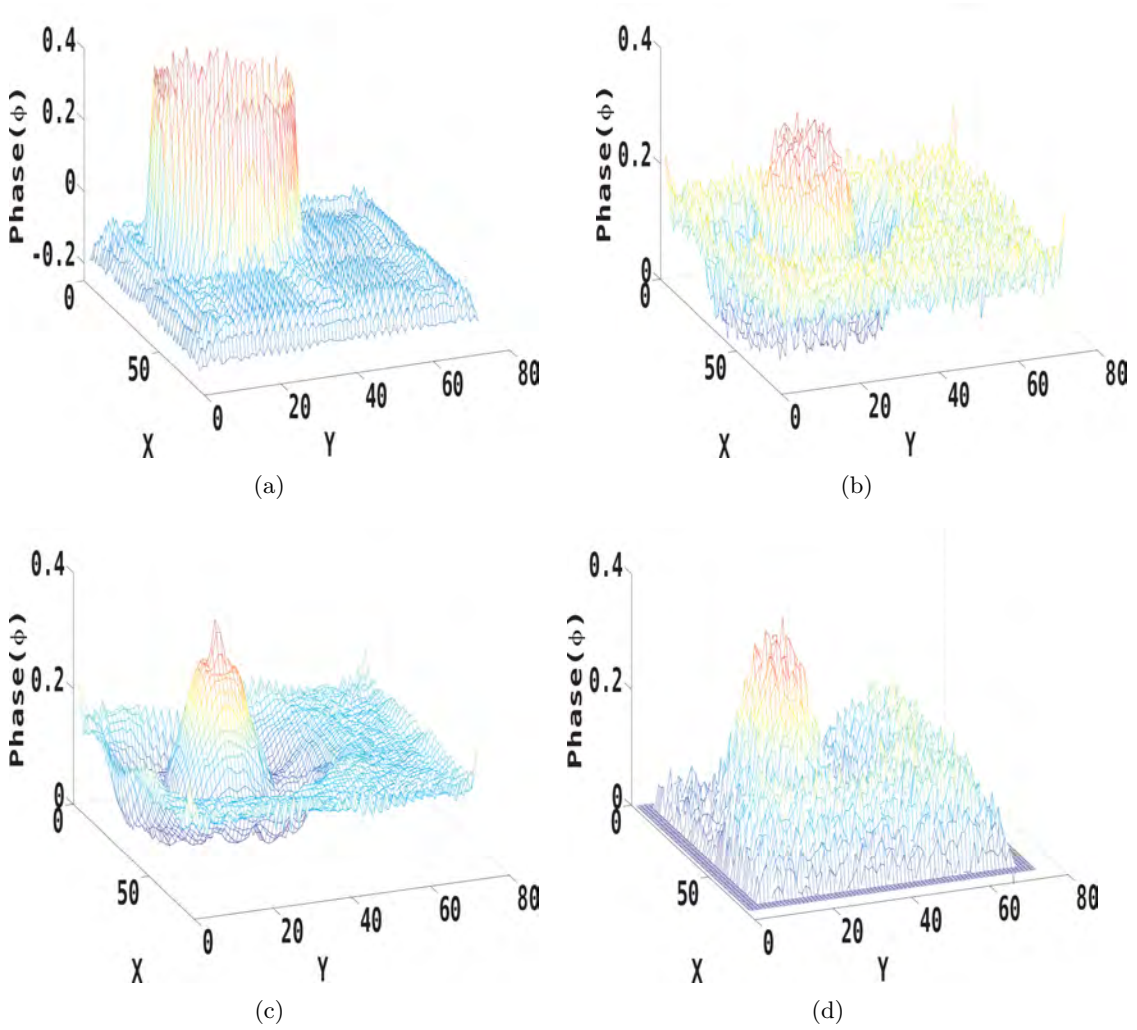

Figure 5.8: (a) Error map for the phase retrieved with the mixed approach [Guigay *et al.* (2007)], (b) error map for the phase retrieved with the algorithm A_1 (PPSNR=24 dB, $\alpha = 0.01$, $\delta = 0.01$), (c) error map for the phase obtained with the algorithm A_2 ($\alpha = 0.01$, $\delta = 0.01$) and (d) error map for the phase obtained with the algorithm A_3 (PPSNR=24 dB, $\alpha = 0.01$, $\delta = 0.01$).

The algorithm A_3 is also much faster since the large scale matrix used in the finite difference methods is replaced by the analytic expression of the adjoint of the Fréchet derivative. It should be noted that at the end of the iterations, the condition of Eq. 5.24 is fulfilled and that we have to stop the iterations considering the noise level.

The phase maps obtained with the algorithm A_3 for the noise-free data and noisy data (PPSNR=24 dB) with a smooth regularization $\alpha = 0.01$ are displayed in Figure 5.10(a) and Figure 5.10(b) respectively. The final NMSE are **0.095** for noisy-data (PPSNR=24 dB) and **0.09** for noise-free data.

The phase retrieval error may still be decreased. The drawbacks of the regularization functional $\|\nabla\varphi\|_{L_2}$ are well-known. An isotropic smoothing effect is obtained and

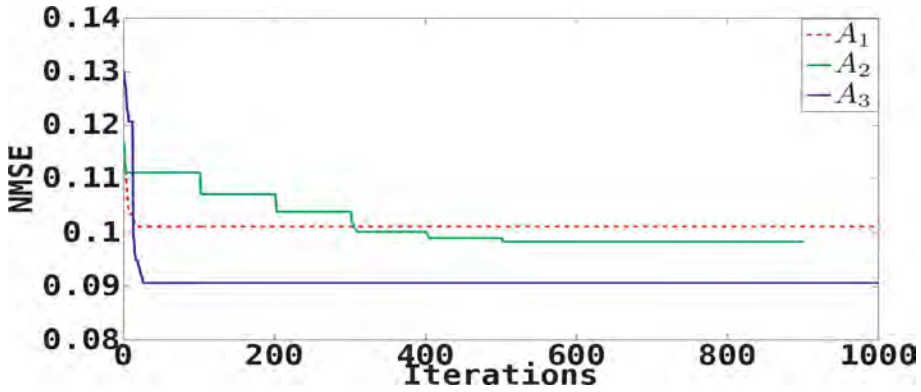

(a)

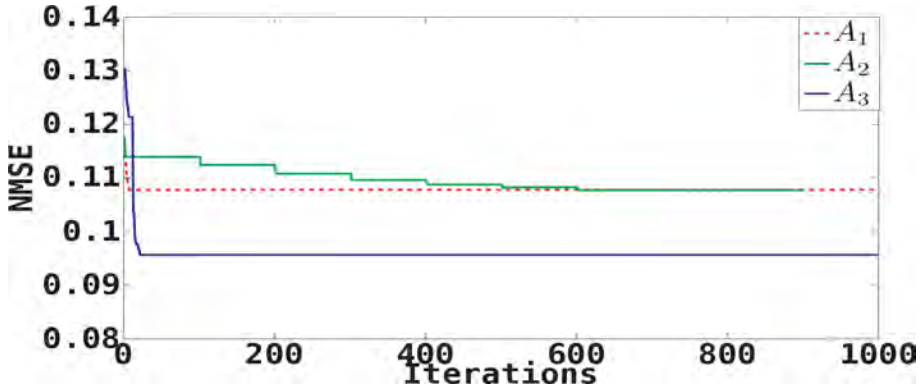

(b)

Figure 5.9: Normalized mean square error for the phase versus iteration number with the edge fixed to zero: (a) for the noise-free data ($\alpha = 0.01$, $\delta = 0.01$) and (b) for the noisy data ($\alpha = 0.01$, $\delta = 0.01$, PPSNR= 24dB).

the boundaries are not well preserved. This is obvious in Figure 5.8(c). The noise is suppressed but the high values of the gradient are too greatly penalized on the edge. In future works, the gradient $\nabla\varphi$ may be replaced by a nonlinear functional of φ as in semi-quadratic regularization or by the bounded variation semi-norm [Scherzer *et al.* (2008)] or by anisotropic terms.

5.2.7 Conclusions

In this section, several nonlinear iterative approaches for phase retrieval have been proposed. The methods investigated previously were based on the linearization of the relation between the phase shift induced by the object and the diffracted intensity. They have used the Transport Intensity Equation (TIE) (Section 3.2.1), the Contrast Transfer Function (CTF) (Section 3.2.5), or mixed approaches (Section 3.2.6). Our nonlinear iterative approaches use the Fréchet derivative of the intensity recorded at different propagation distances. We have compared the convergence rates for three algorithms, two based on the finite difference gradient and one, on the analytic expression of the gradient. The best

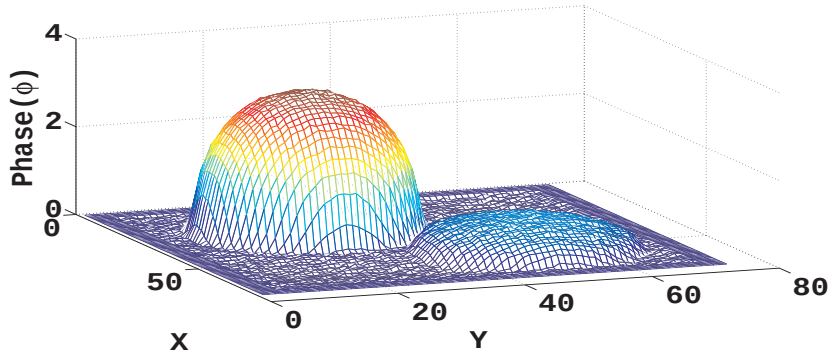

(a)

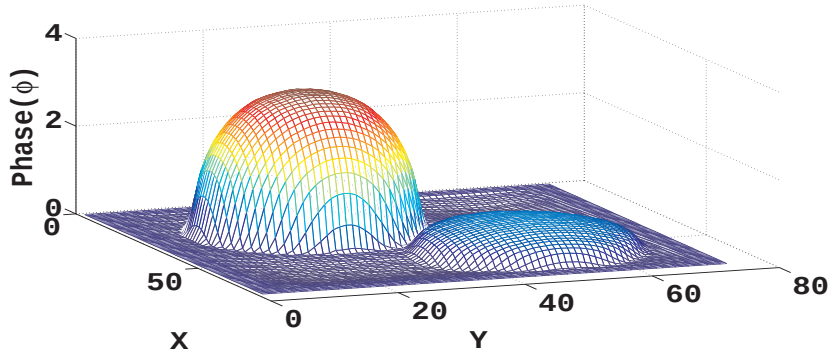

(b)

Figure 5.10: Reconstructed phase with A_3 algorithm for (a) noisy-data (PPSNR=24 dB, $\alpha = 0.01$) and (b) for noise-free simulations ($\alpha = 0.01$).

results are obtained when the inverse problem is regularized with the smoothing L_2 norm of the phase gradient. The best convergence rates are found when the various distances are treated with a Kaczmarz type method where one descent iteration is performed for each distance. The evaluation of the method was performed using a simple phase map, both with and without noise. For the simulated data, the normalized mean square error was measured. Tikhonov regularization based on linear filtering used in this section has some well-known drawbacks since it does not only smooth noise but also blurs important features such as edges. To avoid these shortcomings, nonlinear partial differential diffusion equations may be useful. Therefore, other regularization methods will be tested in the next sections. Our approach outperforms the linear methods on simulated noisy data for PPSNR above 20dB and the nonlinearities of the Fresnel diffraction are well taken into account. The analytic calculation of the adjoint of the Fréchet derivative speeds up the calculations and overcomes memory limitations due to the Fréchet derivative matrix (Section 5.2.2).

Chapter 6

Projection Operators

Contents

6.1 Introduction

In this chapter, we refine the scheme proposed in Section 5.2.3 by introducing projection operators in the algorithm. The new method was tested on noisy simulated data. It was shown that the new iterative schemes proposed improve the results obtained in a linear framework, yet stagnation away from the true phase is observed (Sections 5.1.1, 5.2.3). The proposed method here outperforms the approaches based on the linearization of the relation between the phase shift induced by the object and the diffracted intensity and the former nonlinear algorithm with no projectors (Section 5.2.3).

The aim of this chapter is to introduce Fienup like projection operators in the former nonlinear phase retrieval approach (Section 5.2.3). Classical algorithms based on projections and designed for solving phase retrieval problems have been discussed in the mathematical context of multi-valued projection operators and convex optimization [Bauschke *et al.* (2002)]. The connection has been established between the widely used phase retrieval methods like Error Reduction Fienup approaches [Fienup (1982)] and the standard convex optimization algorithms. The error reduction algorithm is identified with a non-convex alternating projection algorithm [Bauschke *et al.* (2002)] and it is shown that the Fienup's basic input-output, and hybrid input-output algorithms corresponds to Dykstra and Douglas-Rachford algorithm. This work provides a theoretical framework to better understand and improve the new phase recovery scheme presented in Section 5.2.3 by means of projection operators designed to satisfy convex or non-convex constraints.

The iterative Landweber type method based on the Fréchet derivative of the nonlinear operator I_D has been described in Section 5.1. Furthermore, it was possible to decrease the computation time and to obtain a better convergence by using the analytical expression of the Fréchet derivative and of its adjoint operator.

In order to obtain the best decrease of $J(\varphi)$ (Eq. 5.4) the regularizing parameter α is chosen by trial-and-error. This type of method has been used in several works on nonlinear ill-posed problems [Daubechies *et al.* (2008)]. In this chapter, we use projectors in order to enforce some constraints on the retrieved phase and to improve the former phase recovery algorithm. Common approaches for solving the classical phase retrieval problem is to enforce alternatively object domain and the Fourier constraints. In this work, we have considered an image modulus constraint in the object domain.

6.2 Projector Operator

The results of this section have been published in the following article:

V. Davidoiu, B. Sixou, M. Langer, and F. Peyrin,

"Non-linear iterative phase retrieval based on the Fréchet derivative and projection operators."

IEEE International Symposium on Biomedical Imaging - ISBI2012, Barcelona, Spain, pp. 106-109, 2012.

For each distance D and diffracted intensity I_D, we consider the set $\mathcal{M}_D = \{u \in L_2, |u| = \sqrt{I_D}\}$. This set is closed but not-convex and this lack of convexity is related to the difficulty of the phase retrieval problem. Let $\varphi_{k+\frac{1}{2}}$ be the phase obtained at the end

of the Landweber step. For a given transmission T_k at the iteration k, obtained with the former iterative method, defined by:

$$T_k(\mathbf{x}) = a(\mathbf{x}) \exp[i\varphi_{k+\frac{1}{2}}(\mathbf{x})] \tag{6.1}$$

we consider the projection of $T_k * P_D$ on the set $\mathcal{M}_D$. The set $\mathcal{M}_D$ defines a non-convex constraint, the associated projector is multi-valued and a particular selection must be picked. We have thus defined the projection $P_{\mathcal{M}_D}$ by:

$$P_{\mathcal{M}_D}(T_k * P_D) = \begin{cases} \sqrt{I_D} \cdot \frac{T_k * P_D}{|T_k * P_D|} & \text{if } T_k * P_D \neq 0 \\ T_k * P_D & \text{if } T_k * P_D = 0. \end{cases} \tag{6.2}$$

The new transmission T'_k is calculated with successive Fourier and inverse Fourier transforms:

$$T'_k = F^{-1}\left\{F\left[P_{\mathcal{M}_D}\left(T_k * P_D\right)\right] / F\left(P_D\right)\right\} \tag{6.3}$$

and projected phase is defined by :

$$P_D(\varphi_{k+\frac{1}{2}}(\mathbf{x})) = \underset{\varphi}{\operatorname{argmin}} \left\{ |T'_k(\mathbf{x}) - a(\mathbf{x}) \exp\left[i\varphi(\mathbf{x})\right]| \right\} \tag{6.4}$$

where P_D is an additional projector. We have also considered a support constraint and a projection $P_{\mathcal{S}}$ on the support $\mathcal{S}$ of the phase $P_{\mathcal{S}} = \varphi.1_{\mathcal{S}}$.

At each iteration the projectors $P_{\mathcal{M}_D}$ and $P_{\mathcal{S}}$ are applied successively as in the Error Reduction algorithm (ER) [Fienup (1982)]. The iterate φ_{k+1} is obtained from $\varphi_{k+1/2}$ using the modified standard Landweber method (Eq. 5.11) :

$$\varphi_{k+1} = P_{\mathcal{S}} P_D(\varphi_{k+1/2}). \tag{6.5}$$

This additional projection step leads to an alternative phase retrieval scheme. The distances are stepped through randomly.

6.2.1 Results and discussions

This algorithm was tested on simulated noisy data obtained as described in Section 5.1.2. The original phase map to be retrieved is displayed in Figure 5.1, together with the corresponding Fresnel diffraction pattern for D=1.4 m with 24dB in Figure 5.3(b).

A Gaussian white noise well adapted to our synchrotron imaging system with a peak-to-peak signal to noise ratio (PPSNR) of 24dB was added to the image (Eq. 5.12). In our simulations the distances were considered in a *random* way. The phase support $\mathcal{S}$ is assumed to be restricted to the 70×70 inner pixels.

Two different starting points have been used to test our algorithm. Figure 6.1(a) displays the difference maps between the phase obtained with the algorithm and the true

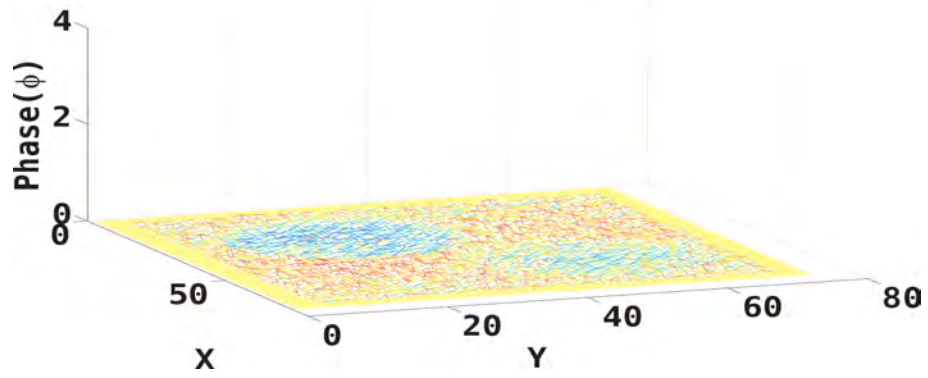

(a)

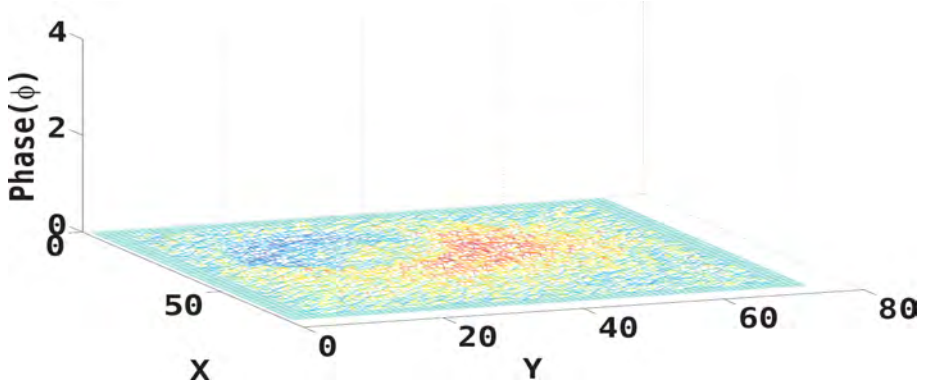

(b)

Figure 6.1: Error map for the phase retrieved with the new algorithm initialized with (a) the mixed approach and (b) an arbitrary solution.

phase to be retrieved with the initial phase obtained from the mixed method proposed in [Langer *et al.* (2008)]. Figure 6.1(b) displays the difference map between the true phase and the phase obtained with the new algorithm for an initialization far from the solution.

The method works well with a weak smoothing regularization ($\alpha = 0.5$) when the initialization is performed far from the solution. For a starting point obtained with the mixed approach, the regularization does not improve the phase recovery and one may choose $\alpha = 0$.

The evolution of the mean square error obtained for noisy-data with 24dB (PPSNR) is displayed in Figure 6.2(a) and Figure 6.2(b) as a function of the number of iterations. The normalized mean square error on the phase decreases from 0.1471 to **0.0268** and 0.8121 to **0.0234** respectively. It should be noted that for a smooth regularization ($\alpha = 0.01$) with additive white Gaussian noise (PPNSR=24 dB) without projectors the final errors are **0.359** and **0.095** (Section 5.2.3). The use of the projectors improves the convergence properties of the nonlinear iterative method presented in Section 5.2.3.

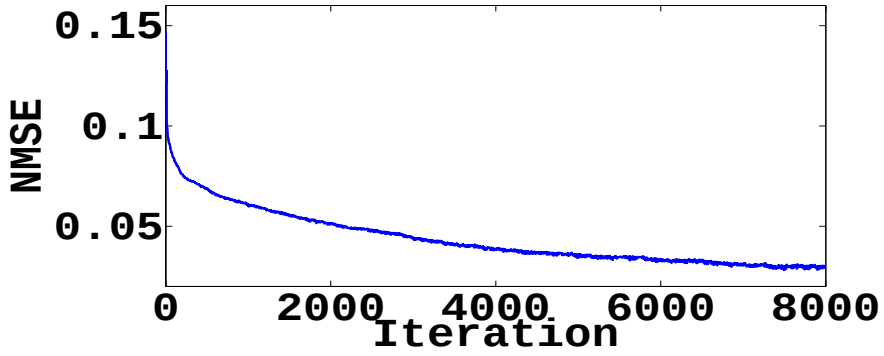

(a)

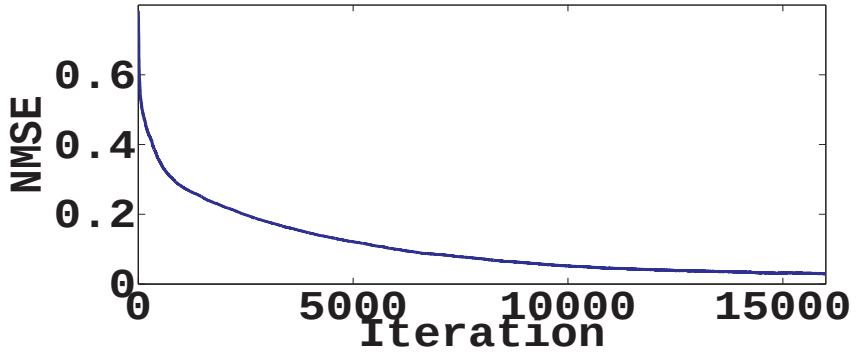

(b)

Figure 6.2: Normalized mean square error for the phase versus iteration number for noisy-data (PPSNR 24dB): (a) initialized with the mixed solution ($\alpha = 0$), (b) initialized with the arbitrary solution ($\alpha = 0.5$).

6.2.2 Conclusions

To conclude, the proposed nonlinear iterative method uses the Fréchet derivative of the intensity recorded at different propagation distances (D=0.2; 0.4; 0.6; 0.8; 1.0; 1.2; 1.4; 1.6) and projection method on convex or non-convex sets as in the Fienup algorithms. It outperforms the linear mixed method (Section 3.26) and our former nonlinear approach (Section 5.2.3) for simulated noisy data.

6.3 Nonlinear Tikhonov regularization with projection operators

In this section, we investigate the resolution of the inverse problem with nonlinear Tikhonov regularization (Section 5.1) and projection operators (Section 6.2). The algorithm is evaluated using projections for a 3D Shepp-Logan phantom in the presence of noise, for a weakly or a strongly varying phase. We show that this new nonlinear approach leads to a significant reduction of the phase errors. In this section, the inverse

problem is regularized with the L_2 norm of the phase because the choice of this term leads to best numerical results for the Shepp-Logan phantom.

6.3.1 The iterative reconstruction method

As detailed in Section 5.1 the inverse ill-posed problem of the phase is stabilized by a Tikhonov type regularization term with the square of the gradient phase term. In the following the Landweber iterative algorithm is modified by replacing this term $\|\nabla\varphi\|^2_{L_2}$ with the phase term $\|\varphi\|^2_{L_2}$. In this way, the optimality condition becomes:

$$I_D^{'}(\varphi)^*[I_D(\varphi) - I_\delta] + \alpha \cdot \varphi = 0. \tag{6.6}$$

The phase estimate φ_{k+1} at the iteration $k+1$ is obtained starting from the previous iteration k, so from the previous retrieved phase φ_k with:

$$\varphi_{k+1} = \varphi_k - \tau_k\{I_D^{'}(\varphi_k)^*[I_D(\varphi_k) - I_\delta] + \alpha\varphi_k\} \tag{6.7}$$

The standard Landweber method is thus modified by introducing a linear search procedure with a variable step size τ_k. An approximate value for τ_k is obtained with a dichotomy strategy. The algorithm is a simplified version of the iterative Gauss-Newton method considered in [Bakushinsky (1992), Bakushinsky and Smirnova (2005)].

The regularizing parameter α is chosen by trial-and-error in order to obtain the best decrease of the regularization functional. This regularization methodology is more general than the one investigated in Section 5.2.3 and it gives goods results for noisy and non smooth phase maps. Other regularization terms have been tested in Section 5.2.3, but the best results are obtained with the approach detailed above.

The computation of the iterates is based on the calculation of the adjoint of the Fréchet derivative of the intensity (Section 5.2). At each step of the optimization process Fienup like projections of the current iterate are also calculated (Section 6.2).

6.3.2 Simulations on a Shepp-Logan phantom

Two phantoms were defined, one for the absorption index and one for the refractive index decrement. Figure 6.3(a) displays the 3D Shepp-Logan [Kak and Slaney (1989)], consisting of a series of ellipsoids on which the projections are based. Theoretical values for the absorption coefficient β and for the refractive index δ_r of different materials at 24 keV were used in different regions (Table 6.1) and the corresponding pixel size was 1μm. Numerical projections were calculated in a parallel beam geometry with 2048×2048 pixels and the two resulting data sets were combined to form a complex representation of the wave exiting the object using Eq. 3.1. In order to test our algorithm, two types of objects were considered for short propagation distances and weak absorption, one with a slowly varying phase and another with a strongly varying phase.

Table 6.1: Values of the absorption coefficient and refractive index at 24keV for the materials used in the 3D phantom for strong phase (where (weak phase)=(strong phase)/10)

	$\frac{4\pi\beta}{\lambda}(cm^{-1})$	$\frac{2\pi\delta_r}{\lambda}(\times 100 cm^{-1})$
Aluminum	5.130	11.4
Ethanol	0.305	4.00
Oil	0.262	4.36
PMMA	0.425	5.63
Water	0.482	4.87
Polymer	0.306	5.00

The intensity images are obtained as the squared modulus of the convolution product calculated by Fourier transforms using Eq. 3.5. They were calculated for three propagation distances 0.035 m, 0.072 m and 0.222 m. The propagation distances are taken into account randomly during the phase retrieval algorithm. Simulations were also performed for additive uniformly distributed white noise with zero mean and with a peak-to-peak signal to noise ratios (PPSNR) of 24dB, where the peak-to-peak signal to noise ratio is defined by Eq. 5.12.

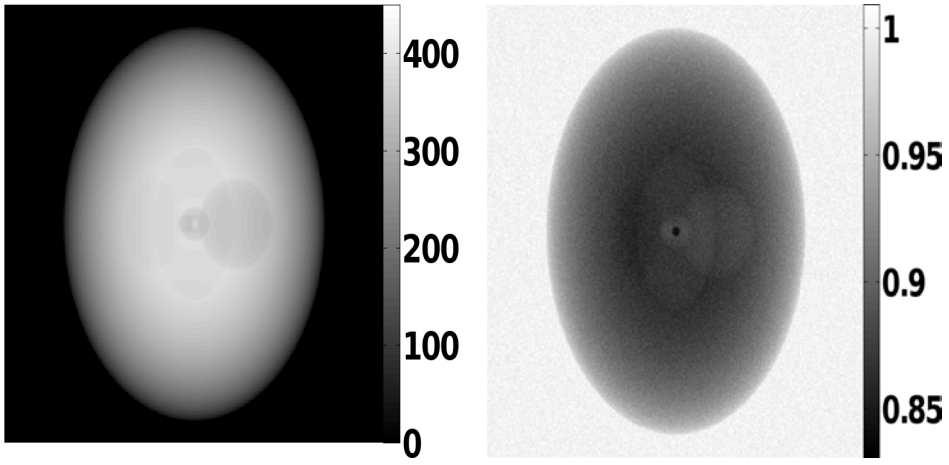

(a) (b)

Figure 6.3: (a) Ideal phase to be retrieved and (b) absorption image with PPSNR=24dB for strongly varying phase.

The original phase map for strong absorption to be retrieved digitized to 512×512 pixels together with the absorption map are displayed in Figure 6.3(a) and Figure 6.3(b). Figure 6.4(a) and Figure 6.4(b) shows the intensity maps for different distances corrupted with PPSNR=24dB, respectively. The corresponding Fresnel diffraction pattern for the weakly varying phase at $D = 0.222$ m are displayed, without noise in Figure 6.5 and with a PPSNR of 24dB. The diagonal profiles of these intensity maps for weakly varying phase are displayed in Figure 6.6.

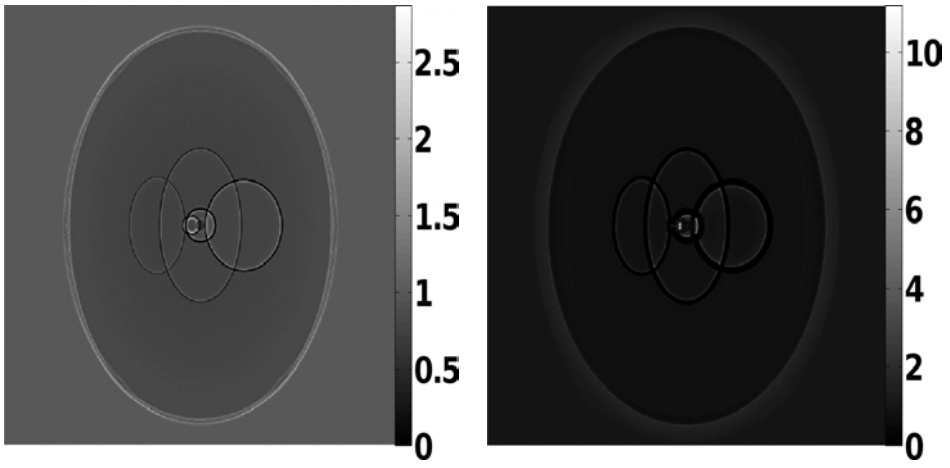

(a) (b)

Figure 6.4: Intensity images at (a) $D = 0.035$ m and (b) $D = 0.222$ m for strongly varying phase.

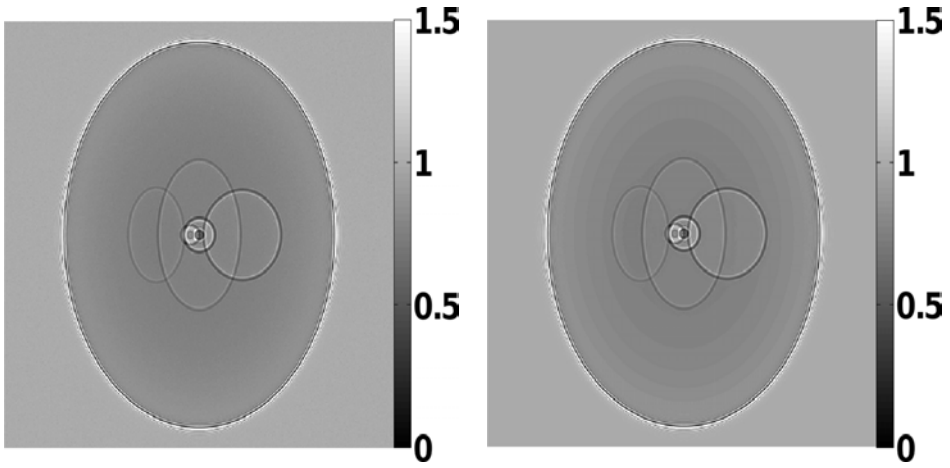

(a) (b)

Figure 6.5: Intensity images for weakly varying phase at $D = 0.222$ m (a) without noise and (b) with PPSNR=24dB.

6.3.3 Initialization and Stopping Rules

The phase retrieval algorithm proposed is not globally convergent. In our simulations, the mixed approximation of the linear problem has been used as starting point. The errors maps obtained with the mixed approach for the two phases are displayed in Figure 6.7(a) and Figure 6.7(b).

An important role in the algorithms is played by the regularization parameter. In order to avoid obtaining solutions diverging far away from the real solution, this parameter is chosen by trial-and-error. The parameter in the mixed approach may be set at a very small value (i.e 10^{-100}), and in the nonlinear algorithm its values vary from 10^{-3} to 10^{-9}, depending on the noise level and on the type of object.

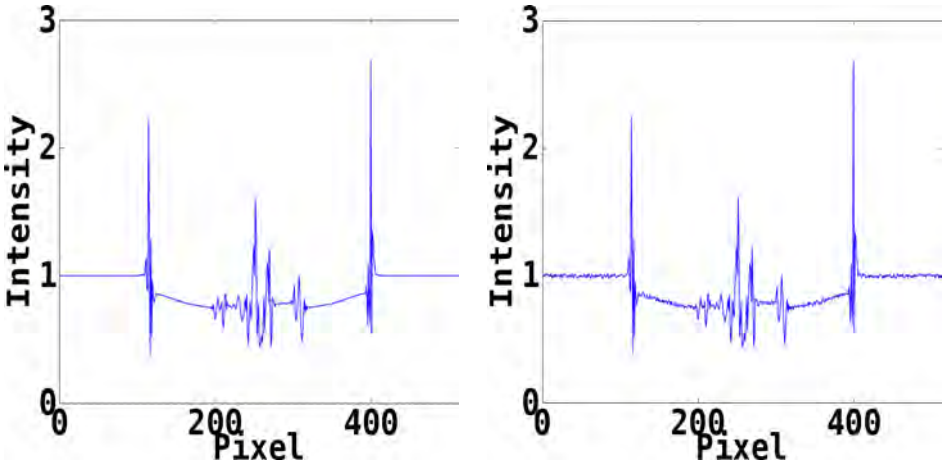

(a) (b)

Figure 6.6: Diagonal profile of the (a) intensity image for weakly varying phase at $D = 0.222$ m without noise (Figure 6.5(a)) and (b) with 24dB (Figure 6.5(b)).

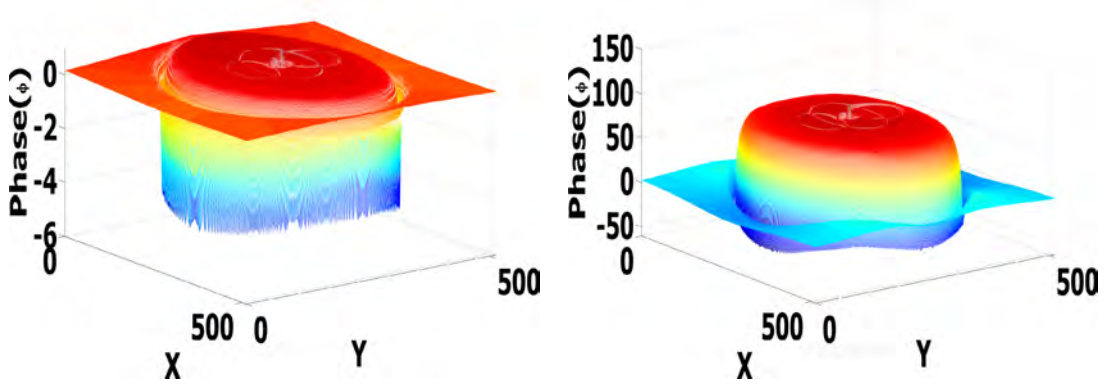

(a) (b)

Figure 6.7: Error maps obtained with the mixed approach without noise used as a starting point (a) for weakly varying phase and (b) for strongly varying phase.

In this work, the iterations are terminated when

$$\|I_D(\varphi_{k+1}) - I_D(\varphi_k)\|_{L_2(\Omega)} \leq \omega \|I_D(\varphi_k)\|_{L_2(\Omega)} \tag{6.8}$$

where ω is a parameter that was set at 0.01 by trial-and-error, and

$$\|I_\delta - I\|_{L_2(\Omega)} \leq \delta. \tag{6.9}$$

Since ideal reconstruction is available direct comparisons can be made. The method will be quantitatively evaluated by measuring the normalized mean square error (NMSE) using the $L_2(\Omega)$ norm:

$$\text{NMSE} = 100 \times \frac{\|\varphi - \varphi_k\|_{L_2(\Omega)}}{\|\varphi\|_{L_2(\Omega)}}, \tag{6.10}$$

where φ_k is the phase recovered at iteration k and φ the ideal phase to be recovered.

6.3.4 Results and discussions

In order to analyze the performance of the proposed method, we compared the numerical results obtained with the nonlinear method with the phases retrieved with the CTF, TIE and mixed approach (Section 3.2). The four methods were tested in two different contexts (for weakly and strongly varying phase) for noise-free and noisy data.

Table 6.2: NMSE(%) values for different algorithms and objects

	TIE	CTF	Mixed	Nonlinear
Strong phase without noise	25.54	42.52	26.81	***7.57***
Weak phase without noise	***1.5***	24.37	3.16	2.35
Strong phase PPSNR=24dB	262.13	56.54	27.78	***11.58***
Weak phase PPSNR=24dB	459	54.67	12.36	***8.69***

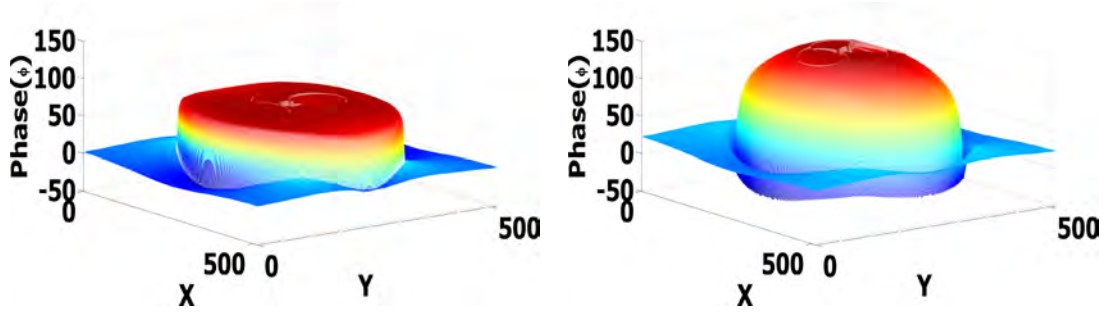

(a) TIE (b) CTF

(c) Mixed (d) Nonlinear

Figure 6.8: Error maps and corresponding NMSE values for strongly varying phase without noise obtained for different algorithms (a) 25.54%, (b) 42.52%, (c) 26.81% and (d) 7.57%.

The NMSE (Eq. 6.10) for all the methods are presented in Table 6.2. For the strongly varying phase without noise, the nonlinear approach gives the most accurate results. For the weakly varying phase for noise-free data, the TIE method gives the best solution. On the other hand, for noisy simulated data with PPSNR=24dB, TIE yields the worst reconstructions. As shown in Table 6.2, the errors on the phase have been significantly reduced with our algorithm using as starting point the mixed phase map solution.

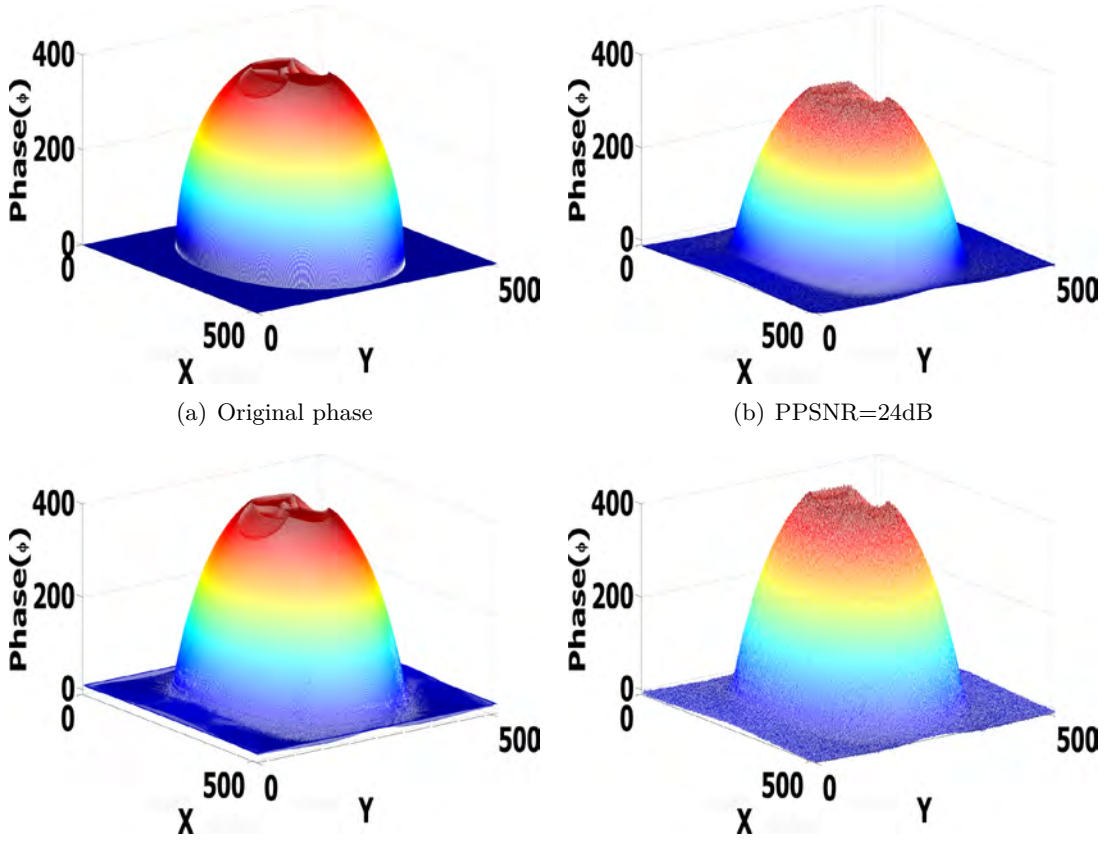

(a) Original phase (b) PPSNR=24dB

(c) Without noise (d) PPSNR=24dB

Figure 6.9: (a) Original phase map to be retrieved for strongly varying phase and reconstructed phase for the same object with (b) the mixed approximation, (c)and (d) with the nonlinear algorithm.

Figure 6.8 shows the errors maps obtained with strongly varying phase without noise for the four methods. The evolution of the NMSE as a function of the iterations number is displayed in Figure 6.11 for the various cases investigated. In these plots, one iteration corresponds to a random cycle through the intensity images obtained for the three distances. These curves show that the proposed algorithm has good convergence properties. The phase retrieval errors obtained with the algorithm for the noise-free data and noisy data (PPSNR=24dB) with the nonlinear Tikhonov regularization are displayed in Figure 6.10.

The original phase map to be retrieved for strongly varying phase is displayed in Figure 6.9(a). Figure 6.9(b) and Figure 6.9(d) shows the phase maps for noisy data (PPSNR=24 dB) obtained with the mixed approximation and with the nonlinear algorithm using this mixed solution map as starting point respectively. The phase map retrieved for noise-free data with the nonlinear algorithm is displayed in Figure 6.9(c).

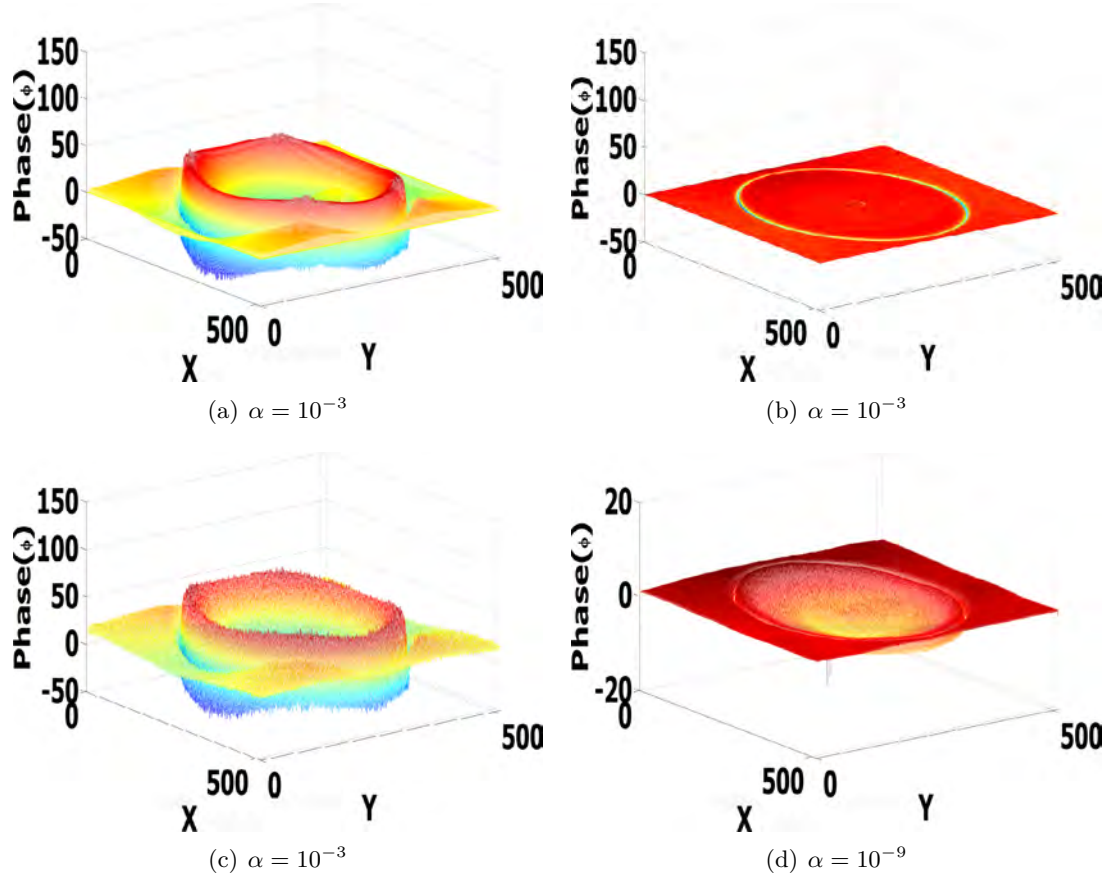

Figure 6.10: Error map for the phase retrieved with the nonlinear algorithm for: (a) strongly varying phase without noise, (b) weakly varying phase without noise, (c) strongly varying phase with PPSNR=24dB and (d) weakly varying phase with PPSNR=24dB.

6.3.5 Conclusions

In this section, we have presented a new nonlinear phase retrieval approach based on the Fréchet derivative of the intensity, a nonlinear Tikhonov regularization and Fienup like projection operators. The algorithm uses a Landweber type iteration to minimize the regularization functional. Three propagation distances are used in a random way to achieve a good reconstruction. The reconstruction quality for a projection of a 3D Shepp-Logan phantom has been quantitatively evaluated for strongly and weakly varying phases, both with and without noise. The nonlinear method proposed is compared with linear approaches. The TIE method gives the best solution for slowly varying phase and noise-free data. Yet, for the strongly varying phase and the noisy data the nonlinear method outperforms the linear methods.

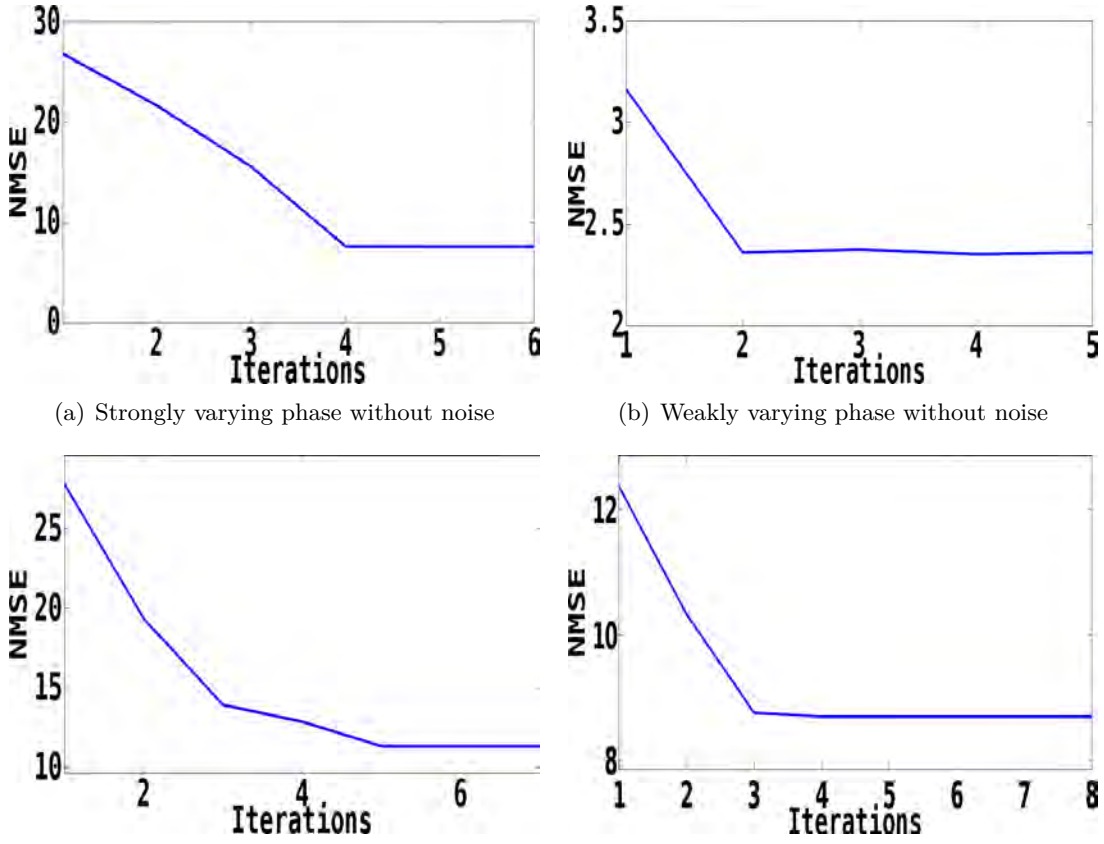

(a) Strongly varying phase without noise

(b) Weakly varying phase without noise

(c) Strongly varying phase with PPSNR=24dB

(d) Weakly varying phase with PPSNR=24dB

Figure 6.11: Normalized mean square error for the phase versus iteration number

III Phase retrieval and wavelet regularization

Résumé général

L'introduction de cette partie comporte un bref rappel sur les ondelettes continues. Durant les dernières décennies, la théorie des ondelettes a attiré une attention considérable parce qu'elle proposait une extension intéressante de la théorie de Fourier. Le principal inconvénient de l'analyse de Fourier est le fait que l'information temporelle est perdue quand la transformation dans le domaine des fréquences est effectuée. Une propriété importante des ondelettes est qu'elle permet d'obtenir une représentation du signal à la fois en temps et en fréquences. La transformation en ondelettes repose sur l'utilisation d'une ondelette " mère " qui va être translatée et dilatée afin de couvrir le domaine temps-fréquence.

La transformée en ondelettes continues a été développée dans le but de pallier aux inconvénients de la transformée de Fourier à court terme. Ses propriétés les plus importantes sont présentées dans la section 7.2. Ensuite, la transformée en ondelettes discrètes 1D et son extension en 2D par produit tensoriel d'ondelettes 1D, ainsi que les ondelettes utilisées dans cette thèse sont décrites dans la section 7.3. Une méthode itérative d'optimisation en coordonnées ondelettes basée sur le seuillage doux itératif est introduite.

Comme cela a été détaillé dans la partie II, le problème de l'estimation de phase est mal posé. Dans cette partie, sous l'hypothèse que la phase a une représentation parcimonieuse dans une base d'ondelettes orthogonales, nous proposons un nouvel algorithme pour résoudre le problème d'estimation de la phase reposant sur un algorithme de seuillage itératif. Cette méthode n'a pas été étudiée auparavant dans le cadre de l'estimation de phase dans les méthodes de propagation.

La régularisation de type Tikhonov pour le problème de l'estimation de phase a été étudiée en détail dans [Langer *et al.* (2008), Langer *et al.* (2009), Langer *et al.* (2010)]. Cette approche donne des bonnes reconstructions pour de niveaux de bruit faibles, mais elle est insuffisante dans le cas des signaux très bruités. Il est bien connu que la représentation parcimonieuse de signaux sur des bases adaptées, associée à la norme l_1, permet la reconstruction du signal à partir de données très bruitées ou incomplètes [Daubechies *et al.* (2004), Combettes and Wajs (2005), Candes *et al.* (2006), Donoho (2006), Daubechies *et al.* (2008), Chaux *et al.* (2007), Wright *et al.* (2009), Dupe *et al.* (2009)]. Nous nous sommes donc intéressés à la résolution du problème inverse en coordonnées ondelettes.

Pour cela, nous nous sommes tout d'abord placés sous l'hypothèse que le problème direct peut être linéarisé et qu'une seule distance de propagation est disponible. Nous avons proposé une approche itérative de type Landweber associée à un seuillage doux des coefficients ondelettes dans une base d'ondelettes orthogonales. Cette méthode est détaillée dans la section 8.1. L'algorithme a été testé sur des données simulées avec un bruit blanc gaussien. Nous montrons que cette approche améliore les résultats par rapport aux approches linéaires classiques.

En conclusion, cette méthode exploitant une régularisation par la norme l1 des co-

efficients ondelettes améliore les approches linéaires utilisées jusqu'à maintenant dans l'estimation de phase principalement basées sur la régularisation de Tikhonov. Le problème direct linéarisé a été inversé par un algorithme itératif de type Landweber en utilisant une base d'ondelettes orthogonales. Cependant les résultats restent très bruités.

Dans la première partie du manuscrit, nous avons vu que la solution non linéaire reposant sur la dérivée de Fréchet décrite dans la section 6.3, améliore les solutions obtenues avec les approches linéaires mais n'est pas optimale pour des données bruitées. Afin d'obtenir une meilleure reconstruction et d'améliorer la résolution spatiale de la carte de phase reconstruite avec la méthode non linéaire, dans la section 8.2 nous avons étudié une approche combinant l'algorithme non linéaire et la méthode linéaire multirésolution détaillée dans la section 8.1.

Les méthodes linéaires sont utilisées pour obtenir une solution initiale de la phase, supposée n'être pas trop éloignée de la vraie solution. Les hautes et basses fréquences de la phase estimée sont améliorées et la méthode est moins sensible au bruit. Trois distances de propagation ont été utilisées de manière aléatoire pour obtenir une bonne reconstruction. Cet algorithme non linéaire d'estimation de la phase a été testé sur les images de projection du fantôme 3D Shepp-Logan en présence de bruit. Les résultats montrent que l'approche combinée donne de meilleurs résultats que l'approche mixte (Section 3.2.6), et que l'approche basée sur la fonction de transfert de contraste (CTF) (Section 3.2.5). Elle améliore aussi les méthodes non linéaires présentées précédemment.

L'utilisation de contraintes de parcimonie est devenue récemment une tendance très importante dans les études des problèmes inverses. Plusieurs algorithmes exploitant des contraintes de parcimonie pour le problème de l'estimation de phase ont été étudiés dans [Candes *et al.* (2011), Ohlsson *et al.* (2012), Candes and Li (2012), Waldspurger *et al.* (2012), Mukherjee and Seelamantula (2012), Newton (2012), Gaass *et al.* (2012)]. Ces approches sont limitées à des données de petite taille impliquant un temps de calcul important et donc ne peuvent pas être utilisées pour l'estimation de la phase couplée à la tomographie, car la quantité de données à traiter est trop importante. D'autre part, une stratégie visant à résoudre les problèmes non linéaires mal posés avec des contraintes de parcimonie a été étudiée par Ramlau et Teschke [Ramlau and Teschke (2006)] mais n'a jamais été appliquée au problème d'estimation de la phase. Cette approche qui sera noté RTS (Ramlau et Teschke Schéma) dans ce manuscrit, est résumée dans la section 8.3.2. Nous montrons que les conditions de convergence sont satisfaites. Nous détaillons aussi un algorithme de point fixe basé sur une fonction de substitution utilisée pour minimiser la fonctionnelle de régularisation [Ramlau and Teschke (2006)]. Cette approche constitue un traitement alternatif à l'approche combinée "ondelette non linéaire" (WNL) présentée dans la section précédente.

Le but de la section 8.3 est de faire une comparaison approfondie entre les différents algorithmes itératifs non linéaires et les stratégies de régularisation associées qui peuvent

être appliquées au problème d'estimation de la phase en n'utilisant qu'une seule distance. Le problème inverse à partir d'une seule distance de propagation est plus sévèrement mal posé que lorsque plusieurs distances sont utilisées [Beleggia *et al.* (2004), Zabler *et al.* (2005), Guigay *et al.* (2007)]. La convergence des différentes méthodes est étudiée sur des données simulées. Pour cela, nous avons utilisé une image de projection du fantôme 3D Shepp-Logan avec et sans bruit blanc gaussien pour une seule distance de propagation. Les cartes de phase extraites avec les algorithmes non linéaires et linéaires ont été comparées en termes d'erreur quadratiques moyennes normalisées. Les principales hypothèses de régularité pour la convergence des algorithmes ont été mis en évidence pour l'opérateur de Fresnel dans la deuxième partie du manuscrit (Section 5.2.1). Ce travail démontre la robustesse et l'efficacité de la méthode non linéaire combiné (WNL) pour l'estimation de la phase pour une seule distance de propagation. Cet algorithme couple un traitement non linéaire du problème de l'estimation de la phase basé sur la dérivée de Fréchet de l'intensité avec un schéma de type Landweber, et une solution itérative du problème linéaire en coordonnées ondelettes avec une régularisation de type l_1. Nos résultats indiquent que l'approche WNL est plus robuste au bruit que l'approche RTS. Des améliorations significatives par rapport aux méthodes linéaires pour les cartes de phases reconstruites sont obtenues en utilisant l'algorithme non linéaire WNL.

Chapter 7

Wavelet Transforms

Contents

In the introduction of this chapter a brief introduction about continuous wavelet is given. 1-D and 2-D discrete wavelet transform are described in Section 7.3.2 and Section 7.3.3 respectively. An iterative optimization method in wavelet coordinates is presented in Section 7.4.

7.1 Introduction to wavelets

During the last decades, the wavelet theory has attracted an important attention because an interesting extension of the Fourier theory has been possible. The main drawback of the Fourier analysis is that the time information is lost when the transformation to the frequency domain occurs. In addition, an important property of wavelets is their capability to describe details both in time and in frequency. In other words, if you want

more accurately low-frequency or high-frequency information, wavelet analysis provides this possibility by using long intervals or short time intervals respectively. In the following a brief presentation of the continuous and discrete wavelet transform is given in Section 7.2 and Section 7.3 respectively.

7.2 Continuous wavelet transform

In this section, the continuous wavelet transform together with its most important features are presented. The continuous wavelet transform (CWT) was developed with the aim to overcome the resolution problem given by the short time Fourier transform (STFT). The main differences between the two methods are:

- The Fourier transforms of the windowed signals are not considered (i.e. the negative frequencies are not calculated).
- The window width for each spectral component is modified during the transform calculation.

7.2.1 Analysis and Synthesis

A signal $s(x)$ may be decomposed into a set of basis functions called *wavelets*. The most general form of the wavelet transform is:

$$\Psi_{(i,j)}(x) = \frac{1}{\sqrt{i}}\Psi\left(\frac{x-j}{i}\right) \qquad i \in \mathbb{R}^{+*}, j \in \mathbb{R} \tag{7.1}$$

where $\Psi(x)$ is a *mother wavelet*. The translation parameter is defined by j and the scale parameter by i. $\frac{1}{\sqrt{i}}$ is the scale factor introduced to normalize the energy across different scales. The translation term corresponding to the time domain is related to the windows location through the signal $s(x)$. The size of the windows automatically varies thanks to the term called scale term, related to the frequency domain. In other words, the scaling operation acts either as dilatation or compression of the wavelet. The coverage of the wavelet spectrum is determined by the scaling function. We will not give here all the details of the wavelet theory. A full introduction to wavelets can be found in [Daubechies (1992), Mallat (1999), Strang and Nguyen (1996), Vetterli and Kovacevic (1995)].

The mother wavelet has a crucial role in wavelet analysis. Two important properties are that it has to be (almost) compactly supported (finite length) and be oscillating. More precisely, it has to satisfy the admissibility condition.

Definition : A function Ψ is a wavelet if the *admissibility* condition is met:

$$C_\psi = \int \frac{\left|\widehat{\Psi}(\omega)\right|^2}{|\omega|} d\omega < \infty \tag{7.2}$$

where the Fourier transform of the wavelet Ψ is denoted with $\widehat{\Psi}$. In practice, the admissibility condition is reduced to $\widehat{\Psi}(0) = 0$ since $\widehat{\Psi}(\omega)$ will always have sufficient decay:

$$\int \Psi(x)dx = \widehat{\Psi}(0) = 0. \tag{7.3}$$

In this way an oscillating character is imposed to the wavelets, hence their name (i.e. little wave). Since the wavelet $\Psi \in L_2(\mathbb{R})$ and its Fourier transform $\widehat{\Psi} \in L_2(\mathbb{R})$, then:

$$\int \left|\widehat{\Psi}(\omega)\right|^2 d\omega < \infty. \tag{7.4}$$

Another important property of the continuous wavelet is the regularity. This property can be defined using vanishing moments:

$$\int_{\mathbb{R}} x^k \Psi(x)dx = m_k = 0 \tag{7.5}$$

where $k = 0, 1, ..., p-1$. The order of a wavelet transform is given by the number of vanishing moments, in this case p. The regularity of the CWT denotes the rate of decay.

As we saw above a wavelet can be defined as a waveform of short duration that has an average value equal to zero. The continuous wavelet transform of the signal $s(x)$ is defined as follows:

$$CWT_s(i,j) = \int \Psi^*_{(i,j)}(x)s(x)dx = \left\langle \Psi_{(i,j)}(x), s(x) \right\rangle, \tag{7.6}$$

where Ψ^* is the complex conjugate of the Ψ. The results of the CWT are the wavelet coefficients as function of scale i and position j.

The final step is the reconstruction of the signal $s(x) \in L_2(\mathbb{R})$ which can be written as a superposition of dilated and shifted wavelets. The reconstruction formula is given by:

$$s(x) = \frac{1}{C_\Psi} \int_j \int_i \Psi_{(i,j)}(x) CWT_s(i,j) \frac{didj}{i^2}. \tag{7.7}$$

This equation is called also the *resolution of the identity* [Vetterli and Kovacevic (1995)].

7.3 Multiresolution analysis

7.3.1 Discrete wavelet transform

The discrete wavelet transform (DWT) is a wavelet transform where the scale and the translational takes a discrete set of values. DWT provides sufficient information for the analysis and the synthesis of a discrete signal, therefore the computation time and the resources required to compute the coefficients can be significantly reduced.

Frames in Hilbert Spaces

The discrete wavelet is obtained by rewriting the Eq 7.1 as [Daubechies (1992)]:

$$\Psi_{(i,j)}(x) = \frac{1}{\sqrt{h^i}}\Psi\left(\frac{x - j\tau h^i}{h^i}\right) \tag{7.8}$$

where i and j are integers, $h > 0$ is a fixed dilatation step and τ the translation factor. If $i = c^{-k}$ and $j = nc^{-k}$ and $c = 2$ then the wavelets are called dyadic DWT. A vector f in a Hilbert space H can be decomposed using discrete wavelets by wavelet series decomposition, but the reconstruction step is possible only if these wavelets constitute a frame [Daubechies (1992)]. A frame and a basis are not the same but they have common properties. A sequence $\{\phi_n\}_{n\in\Gamma}$ is a frame in a Hilbert space H if there exist two constants $A > 0$ and $B > 0$, such that for any $f \in H$ [Mallat (1999)]:

$$A\|f\|^2 \leq \sum_{n\in\Gamma} |\langle f, \phi_n\rangle|^2 \leq B\|f\|^2, \tag{7.9}$$

where Γ is an index set (finite or infinite). The redundancy of the discrete wavelet basis functions is measured by the frame bounds A and B. If $A = B$ the frame is called tight frame and if $A = B = 1$ then the frame is an orthonormal basis. When $A \neq B$, the reconstruction is achieved using dual frame. By imposing that the wavelet basis functions have to be orthogonal, it is possible to remove the redundancy of the discrete wavelet transform. This is ensured if the mother wavelet is chosen as:

$$\left\langle \Psi_{(i,j)}, \Psi_{(i',j')} \right\rangle = \delta_{i-i'}\delta_{j-j'} \qquad i, i' \in L_2(\mathbb{Z}^n); \quad j, j' \in L_2(\mathbb{Z}^n) \tag{7.10}$$

where δ is the Dirac function.

Let us consider a finite family of functions $\Psi = \left\{\Psi^1, \Psi^2, \Psi^3, .., \Psi^L\right\} \subset L_2(\mathbb{R}^n)$. We say that Ψ is a wavelet family if $\left\{\Psi^l_{i,j} : i \in \mathbb{Z}, j \in \mathbb{Z}^n, l = 1, 2, ..., L\right\}$ is an orthonormal basis for $L_2(\mathbb{R}^n)$. Here, we consider the following convention for a function $s \in L_2(\mathbb{R}^n)$:

$$s_{i,\mathbf{j}}(\mathbf{x}) = |\det\mathbf{D}|^{-i/2}\, s(\mathbf{D}^{-i}\mathbf{x} - \mathbf{j}) \quad i \in \mathbb{Z}, \mathbf{j} \in \mathbb{Z}^n, \tag{7.11}$$

where $\mathbf{D}$ is the dilatation matrix (where all the proper values are higher than 1: $\sigma_1 \geq \sigma_2 \geq ... \geq \sigma_n \geq 1$ and $|\det\mathbf{D}| = d = \sigma_1\sigma_2...\sigma_n$).

Multiresolution analysis (MRA) consists of a sequence of nested subspaces $0.... \subset V_0 \subset V_1 \subset V_2.... \subset V_i \subset V_{i+1}... \subset L_2(\mathbb{R}^n)$, which verify the following properties :

1. $V_{i+1} \subset V_i$, $\bigcup_{i\in\mathbb{Z}} V_i$ is dense for $L_2(\mathbb{R}^n)$ and $\bigcap_{i\in\mathbb{Z}} V_i = \{0\}$;
2. $\forall s \in L_2(\mathbb{R}^n)$ and $\forall i \in \mathbb{Z}$, $s(\mathbf{x}) \in V_{i+1} \Leftrightarrow s(\mathbf{Dx}) \in V_i$;
3. $\exists\Phi \in V_0 \subset L_2(\mathbb{R}^n)$ so that for $\forall\mathbf{j} \in \mathbb{Z}^n$, $\Phi(\mathbf{x} - \mathbf{j})$ is an orthogonal basis for V_0.

The real function Φ is continuous and is called scale function, and is defined as:

$$\int_{\mathbb{R}^n} \Phi(\mathbf{x}) d\mathbf{x} = 1. \tag{7.12}$$

In accord with (2) and (3), for a fixed i the basis functions $\{\Phi_{i,\mathbf{j}}, \mathbf{j} \in \mathbb{Z}^n\}$ is an orthonormal basis for V_i.

Let us consider a subspace $\{W_i\}_{i\in\mathbb{Z}}$ for $L_2(\mathbb{R}^n)$ defined as:

$$V_{i-1} = V_i \bigoplus W_i, \tag{7.13}$$

where $\bigoplus$ is the direct sum. In accord with (1) and (2), a sampling density $d = |\det\mathbf{D}|$ is required to pass from the scale i to the scale $i-1$. In other words, $(d-1)$ elementary functions $\left\{\Psi^l_{i,\mathbf{j}}; i \in \mathbb{Z}, \mathbf{j} \in \mathbb{Z}^n, l = 1, 2, ..., d-1\right\}$ are necessary to form an orthonormal basis for W_i. Moreover, the original signal can be written in terms of dilated version of the function Φ. The projection operator into the space V_i is defined as:

$$\mathrm{Proj}_{\mathrm{V_i}}(s) = \overbrace{\sum_{\mathbf{j}\in\mathbb{Z}^n} \underbrace{\langle s, \Phi_{i,\mathbf{j}}\rangle}_{Analyse} \Phi_{i,\mathbf{j}}}^{Synthesis}. \tag{7.14}$$

Then, a function $s \in L_2(\mathbb{R}^n)$ can be obtained as:

$$\mathrm{Proj}_{\mathrm{V_{i-1}}}(s) = \mathrm{Proj}_{\mathrm{V_i}}(s) + \underbrace{\sum_{\mathbf{j}\in\mathbb{Z}^n} \sum_{l=1}^{d-1} \left\langle s, \Psi^l_{i,\mathbf{j}}\right\rangle \Psi^l_{i,\mathbf{j}}}_{\mathrm{Proj}_{W_i}(s)}. \tag{7.15}$$

The role of the projection operator $\mathrm{Proj}_{W_i}(s)$ of the subspace W_i is to give the details which are lost when the approximation occurs between the two consecutive scales.

The discrete coefficients of a signal s at the scale i are given by the approximation coefficient:

$$A_i s[\mathbf{j}] = \langle s, \Phi_{i,\mathbf{j}}\rangle \tag{7.16}$$

and by the detail coefficients:

$$D^l_i s[\mathbf{j}] = \left\langle s, \Psi^l_{i,\mathbf{j}}\right\rangle \qquad l = 1, 2, ..., d-1. \tag{7.17}$$

The next section describes the implementation of the discrete wavelet transform (DWT).

7.3.2 1-D Discrete wavelet transform

In 1-D discrete wavelet transform the signal will go through a series of FIR (finite impulse response) high-pass and low-pass filters. The associated filters $h(n)$, $g(n)$ are known as scaling and wavelet filter and correspond to the analysis step. For an orthogonal

analysis, we can consider that $h(n) = \widetilde{h}(n)$ and $g(n) = \widetilde{g}(n)$, where $\widetilde{h}(n)$ and $\widetilde{g}(n)$ are the high-pass and low-pass filters in the synthesis parte.

The general form of an one-dimensional (1-D) discrete wavelet transform is shown in Figure 7.1.

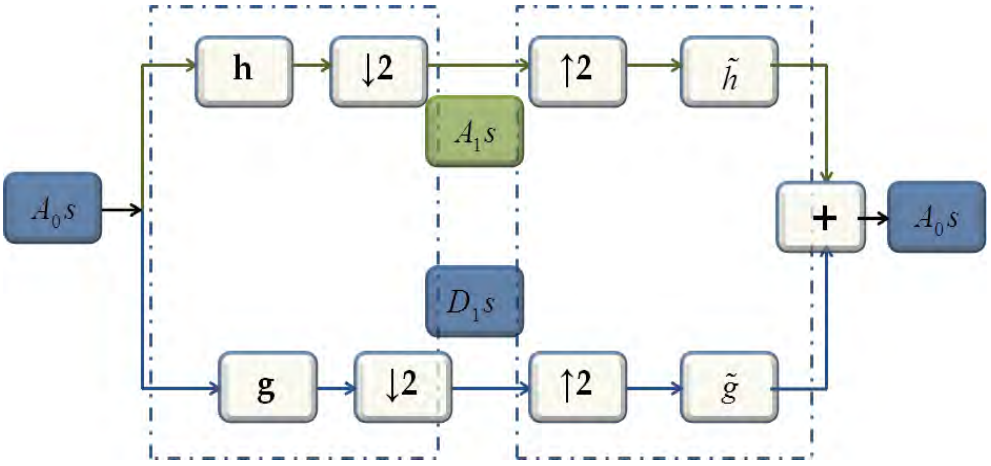

Figure 7.1: 1D Discrete wavelet transform scheme.

The DWT of a signal $s[n]$ at the scale i is described by approximation coefficients (from the low-pass):

$$A_i s[n] = \langle s, \Phi_{i,n} \rangle = \sum_{k \in \mathbb{Z}} h[k - 2n] A_{i-1} s[k] \tag{7.18}$$

and details coefficients (from the high-pass filter)

$$D_i s[n] = \langle s, \Psi_{i,n} \rangle = \sum_{k \in \mathbb{Z}} g[k - 2n] A_{i-1} s[k]. \tag{7.19}$$

The approximation coefficients of a signal $s[n]$ at scale $i - 1$ can be reconstructed by summing the approximation and details coefficients obtained at the scale i:

$$A_{i-1} s[k] = \sum_{n \in \mathbb{Z}} A_i s[n] \tilde{h}[k - 2n] + \sum_{n \in \mathbb{Z}} D_i s[n] \tilde{g}[k - 2n]. \tag{7.20}$$

In Figure 7.2 the coverage of the frequency domain is shown. In this case the frequency allocation is valid for four decomposition levels, meaning that the approximation coefficients have been splitted in two three times.

The general scheme of the decomposition process called *wavelet decomposition tree* is shown in Figure 7.3. Moreover, the right part of the scheme from Figure 7.3 is called decomposition or analysis and the left part is known as reconstruction or synthesis process, respectively. The decomposition part is performed by using discrete wavelet transform DWT and the reconstruction process is achieved with the inverse discrete wavelet transform (IDWT). The choice of the right filter is a crucial in wavelet analysis, because the

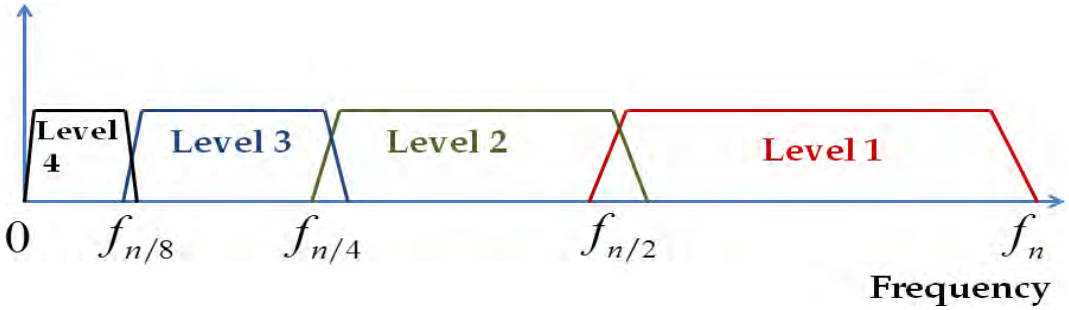

Figure 7.2: Illustration of the frequency domain for four levels of decomposition of the 1-D. At each iteration the resolution is split in 2 as details. Same process of separation is repeated sequentially only for the approximation coefficients.

filter will determine shape of the wavelet we use to perform the analysis. Details concerning the design of the low- and high-pass decomposition and reconstruction filters can be found in [Strang and Nguyen (1996), Vetterli and Kovacevic (1995)].

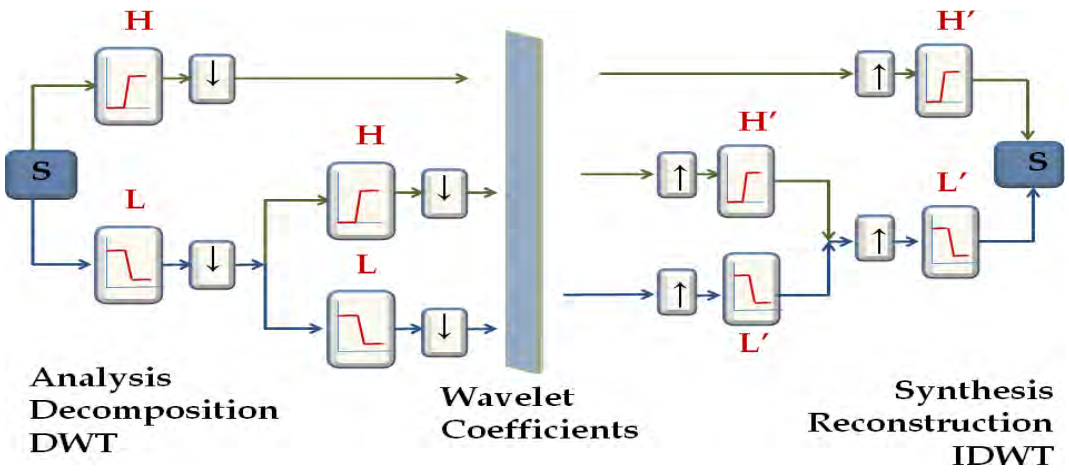

Figure 7.3: Analysis-synthesis process involves two steps: splitting up a signal to obtain the wavelet coefficients, and reassembling the signal from these coefficients.

7.3.3 2D Discrete wavelet transform

Multiple levels can be obtained by applying recursively the 1-D scheme (Figure 7.1). By using separable wavelet filters the 1-D scheme can be easily extended to a two dimensional (2-D) wavelets scheme. This extension preserves the 1-D properties: symmetry, regularity and finite support. The 2-D wavelet transform will be then computed by applying a 1-D wavelet transform to all the rows and then repeating the operation on the columns. Figure 7.4 shows the mathematical idea on which the wavelet decomposition relies together with the visualization of the wavelet coefficients at the first iterate in the analysis process. The high frequency sub-bands contain the vertical, horizontal and diagonal details. These details cannot be represented in the low frequency band, because in this sub-band only an unrefined version of the original signal is obtained. Regardless the

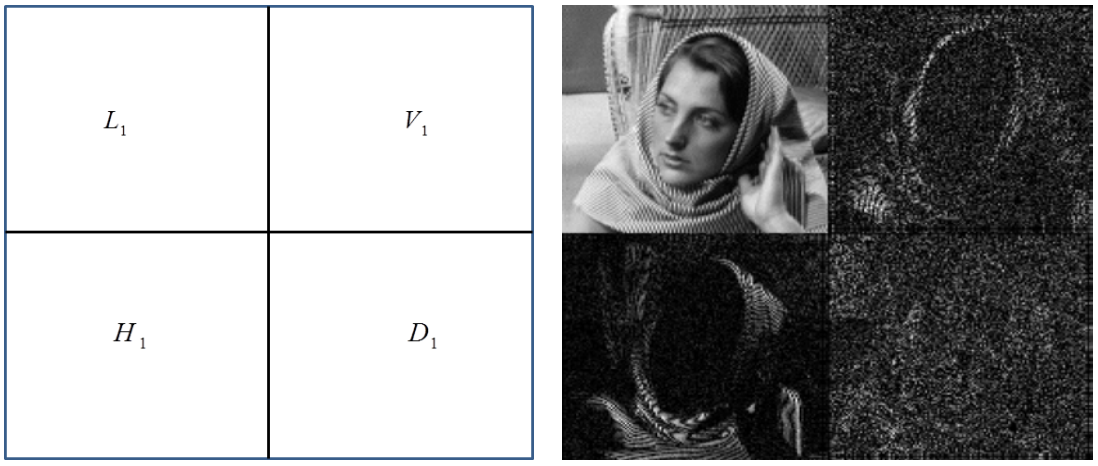

Figure 7.4: (a) First level of 2D separable wavelet decomposition with the low resolution L_1 and the three details V_1, H_1, D_1 and (b) visualization of the wavelet coefficients.

number of decomposition levels this interpretation of wavelet coefficients remains valid.

Considering a multiresolution analysis for four levels of decomposition ($d = |\det\mathbf{D}| = 4$), the wavelet basis is associated to a pair of function (Φ, Ψ) with (h, g) associated filters. In this case of decomposition we obtain a sub-image for the approximation coefficients and three sub-images along the vertical, horizontal and diagonal directions.

In the following, we note with $a = (a_1, a_2)^t$ a binary vector as an indicator of the monodimensional base, obtained using:

$$\varphi_{i,k_m} = \begin{cases} \Psi_{(i,j_m)} & \text{if } a_m = 1 \\ \phi_{(i,j_m)} & \text{otherwise.} \end{cases} \tag{7.21}$$

The translated scaling function in this case will be:

$$\Psi^l_{i,\mathbf{j}}(\mathbf{x}) = \prod_{m=1}^{2} \varphi_{i,j_m}(x_m); \quad l = 0, 1, 2, 3 \tag{7.22}$$

with

$$l = \sum_{m=1}^{2} a_m 2^{m-1} \tag{7.23}$$

The 2-D scaling function will be then: $\phi(\mathbf{x}) = \Psi^0(\mathbf{x}) = \phi(x)\phi(y)$ and $\left\{\Psi^l(\mathbf{x}); l = 1, 2, 3\right\}$, and corresponds to the 2-D wavelets oriented according to the vertical, horizontal and diagonal directions.

Wavelet families used in this thesis

Haar wavelet

A classical wavelet example is the Haar wavelet. This concept is due Alfred Harr in 1909 and is also the first concept of wavelets. Considering a signal $s(\mathbf{x}) \in L^2[0,1]$, Haar used the following piecewise constant function:

$$\Psi(x) = \begin{cases} 1 & \text{if} \quad 0 \leq x < \frac{1}{2} \\ -1 & \text{if} \quad \frac{1}{2} \leq x < 1 \\ 0 & \quad \text{otherwise.} \end{cases} \tag{7.24}$$

The Fourier transform of the Haar wavelet is:

$$\tilde{\Psi}(\omega) = \frac{1}{2i\pi\omega}\left(1 - e^{-i\pi\omega}\right)^2 = i \sin\left(\frac{\pi\omega}{2}\right) \text{sinc}\left(\frac{\pi\omega}{2}\right) e^{-i\pi\omega}, \tag{7.25}$$

where $sinc(x) = \frac{sin(x)}{x}$. The Haar wavelet has a limited support in space and can be found implemented in Matlab as $'db1'$.

Daubechies Wavelet

The Daubechies wavelets are also called compactly supported orthonormal wavelets [Daubechies (1992)]. These wavelets are obtained iteratively and are determined by number of vanishing moments m_k (Eq. 7.5). These wavelets have no explicit expression except the Haar wavelet. However, $\Phi \in V_0 \subset V_{-1}$ and $\{\Phi_{-1,\mathbf{j}}, \mathbf{j} \in \mathbb{Z}^n\}$ is an unconditional basis for V_{-1}, then a series of coefficients $\beta[\mathbf{j}], \mathbf{j} \in \mathbb{Z}^n$ exist such that:

$$\Phi(\mathbf{x}) = \sum_{\mathbf{j}\in\mathbb{Z}^n} \beta[\mathbf{j}]\Phi(\mathbf{D}\mathbf{x} - \mathbf{j}) = \sqrt{d} \sum_{\mathbf{j}\in\mathbb{Z}^n} h[\mathbf{j}]\Phi(\mathbf{D}\mathbf{x} - \mathbf{j}) \tag{7.26}$$

where $h[\mathbf{j}] = \langle \Phi, \Phi_{-1,\mathbf{j}} \rangle$. The Fourier transform of this equation is:

$$\Phi(\omega) = m_0\left[(\mathbf{D}^{-1})^t\omega\right] \Phi\left[(\mathbf{D}^{-1})^t\omega\right] \tag{7.27}$$

where:

$$m_0(\omega) = \frac{1}{\sqrt{d}} \sum_{\mathbf{j}\in\mathbb{Z}^n} h[\mathbf{j}] \exp[-i(\mathbf{j}, \omega)]. \tag{7.28}$$

Imposing a number of restrictions for m_0, then these wavelets can be computed in a iterative way using the following formula:

$$\Phi(\omega) = \prod_{i=1}^{\infty} m_0[(\mathbf{D}^{-k})^t\omega] \tag{7.29}$$

where $m_0(\mathbf{0}) = \mathbf{1}$.

In Matlab all these families are implemented as $'dbN'$, where N is the number of vanishing moments of Ψ. The support length of Ψ and Φ is given by $2N-1$.

Others wavelets families have been developped for different problems like: symlets, coiflets, biorthogonal wavelets, reverse biorthogonal wavelets, discrete approximation of Meyer wavelet, gaussian wavelets, complex Gaussian wavelets, Shannon wavelets, frequency B-Spline wavelets or complex Morlet wavelets. All these families of wavelets have been implemented in Matlab.

7.4 Iterative optimization method

In this thesis, under the assumption that the phase solution has a sparse representation with respect to an orthonormal wavelets basis, we have proposed a new algorithm to solve the phase problem using wavelets with an iterative thresholding step. This approach is detailed in the next chapter and is based on an iterative optimization method presented in the following.

As we have seen in Section 4.2 several regularization methods, like Tikhonov regularization, are used to solve linear and nonlinear problems. In the literature, a method that has attracted a considerable amount of attention is l_1 regularization.

Eq. 4.1 leads to the following l_1 regularized least-squares equation:

$$\underset{\mathbf{x}}{\operatorname{argmin}} \left\{ \|\mathbf{y}-\mathbf{K}\mathbf{x}\|_2^2 + \alpha \|\mathbf{x}\|_1 \right\} \tag{7.30}$$

where $\|\mathbf{x}\|_1$ is the sum of the absolute values of the components of $\mathbf{x}$:

$$\|\mathbf{x}\|_1 = |x_1| + |x_2| + ... + |x_n| \,. \tag{7.31}$$

The difference between l_2 and l_1 can be easily understood by comparing the two unit-ball represented in Figure 7.5. The l_1 norm of a vector composed of many small coefficients is higher that the norm of a vector composed of few large coefficients. An important advantage of the l_1 norm compared with the l_2 norm is that l_1 is less sensitive to outliers.

One of the most popular methods to solve the convex optimization problem (Eq. 7.30) is the iterative shrinkage-thresholding algorithm (ISTA) [Daubechies *et al.* (2004), Figueiredo and Nowak (2003), Hale *et al.* (2007)]. ISTA involves for each iteration a matrix-vector multiplication involving in this way $\mathbf{K}$ and $\mathbf{K}^T$ followed by a soft-threshold step.

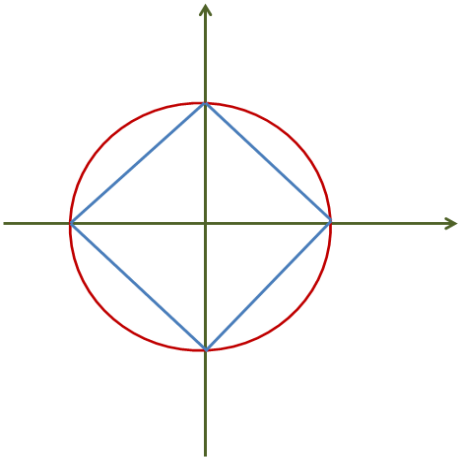

Figure 7.5: l_1 unit-ball in blue line and l_2 unit-ball in red line for the 2D case.

The general iterative optimization model

In the following we describe ISTA method for solving iteratively the convex problem:

$$\underset{\mathbf{x}}{\operatorname{argmin}} \left\{ \|\mathbf{y} - \mathbf{K}\mathbf{x}\|_2^2 + \alpha\psi(\mathbf{x}) \right\} \quad \text{where} \quad 1 \leq p \leq 2 \tag{7.32}$$

where

$$\psi(\mathbf{x}) = \frac{1}{p} \sum_{i=1}^{j} \|(\mathcal{B}\mathbf{x})_i\|_2^p \,. \tag{7.33}$$

Eq. 7.33 defines the potential functions $\psi(\mathbf{x})$, where $\mathcal{B}$ is a vector linear operator and j is the number of vector values returned by $\mathcal{B}$.

If $p = 2$, the solution of Eq. 7.32 is linear and is obtained as the solution to the following system:

$$(\mathbf{K}^T\mathbf{K} + \alpha\mathcal{B}^T\mathcal{B})\mathbf{x} = \mathbf{K}^T\mathbf{y}. \tag{7.34}$$

If $p < 2$, the solution of Eq. 7.32 is nonlinear. The solution in this case can be obtained as the general step of ISTA :

$$\mathbf{x}_{k+1} = \mathcal{T}_{\alpha t}(\mathbf{x}_k - 2t\mathbf{K}^T(\mathbf{K}\mathbf{x}_k - \mathbf{y})) \tag{7.35}$$

where t is an appropriate step-size and $\mathcal{T}_\gamma : \mathbb{R}^{\mathbb{N}} \to \mathbb{R}^{\mathbb{N}}$ is the soft-threshold operator:

$$(\mathcal{T}_\gamma[\mathbf{x}])_i = \begin{cases} \mathbf{x}_i - \gamma \text{sgn}(\mathbf{x}_i) & \text{if} \quad |\mathbf{x}_i| > \gamma \\ 0 & \text{otherwise.} \end{cases} \tag{7.36}$$

This algorithm can be related to a more general class of algorithms, the proximal forward-backward iterative approaches [Passty (1979), Facchinei and Pang (2003), Combettes and Wajs (2005)]. The advantage of this method is its simplicity, therefore it has seen many variants focusing on the convergence conditions of the sequence x_k to a solution

of the Eq. 7.32.

By rewriting the Eq. 7.35 the general step of ISTA will be:

$$\mathbf{x}_{k+1} = \mathcal{T}_{\alpha t}(\mathcal{G}(\mathbf{x}_k)) \tag{7.37}$$

where $\mathcal{G}$ is the gradient descent step on the misfit term and the threshold is the proximal operator associated to the l_1 norm. ISTA is known also as a slow reconstruction method in practice. Acceleration scheme of the algorithm have been proposed where the current iteration is built on the entire history. This type of approaches are called Fast ISTA (FISTA) [Beck and Teboulle (2009)] and NESTA [Nesterov (2005)].

Chapter 8

Phase retrieval in wavelet coordinates

Contents

As detailed in the previous Part II, the phase retrieval problem is ill-posed and the phase information can be recovered through the solution of a nonlinear relationship between the intensity measurements and the researched phase map (Eq. 3.5). The phase solution is assumed to have a sparse representation with respect to an orthonormal wavelets basis. In Section 8.1 we propose to solve the phase problem using wavelets with an iterative thresholding step for a single propagation distance. The proposed nonlinear approach which relies on the Fréchet derivative described in Section 6.3 and the solution of the linear problem in wavelet coordinates with an iterative thresholding are combined in order to improve the spatial resolution of the retrieved phase map in Section 8.2. A convergence comparison of several nonlinear approaches for the phase retrieval problem involving regularizations with sparsity constraints is presented in Section 8.3. The algorithms were tested on simulated data corrupted by white Gaussian noise.

8.1 Single-distance phase retrieval combined with iterative thresholding in wavelet coordinates

---

The results of this section have been published in the following article:
V. Davidoiu, B. Sixou, M. Langer, and F. Peyrin,
"Restitution de phase par seuillage itératif en ondelettes"
23th GRETSI, Bordeaux, France, 2011.

In this section, we investigate the resolution of the linear inverse problem in wavelet coordinates. In the following, this scheme will be combined with the nonlinear approach detailed above. The algorithm is evaluated using simulated noisy data. We show that this approach outperforms the classical linear approaches.

Tikhonov regularization for the phase retrieval problem has been studied in detail in [Langer *et al.* (2008), Langer *et al.* (2009), Langer *et al.* (2010)]. The linear approach gives good reconstructions for small levels of noise but it is insufficient in the case of signals very noisy. In order to obtain a better reconstruction we study in this section an alternative method of regularization. It is well known that the sparse representation of signals on adapted bases and associated with l_1 regularization allows signal reconstruction starting from very noisy or incomplete data [Daubechies *et al.* (2004), Combettes and Wajs (2005), Candes *et al.* (2006), Donoho (2006), Daubechies *et al.* (2008), Chaux *et al.* (2007), Wright *et al.* (2009), Dupe *et al.* (2009)]. Our work represents the first use of this type of approach to the problem of phase retrieval. We then focus on the inverse problem

resolution in wavelet coordinates and then we apply an iterative Landweber approach associated with a soft thresholding of the wavelet coefficients.

8.1.1 Resolution of the linear inverse problem using an iterative Landweber approach

The phase retrieval problem can be expressed as an inverse linear problem:

$$\mathcal{I} = \mathcal{B}\varphi + \varepsilon, \tag{8.1}$$

where $\mathcal{I} = I_D - I_D^{\varphi=0}$ is the noisy data, ε an additive Gaussian noise, φ the phase to be retrieved and $\mathcal{B}$ a linear operator. The solution associated with Tikhonov regularization is the initialization for the method used here.

In this section, we consider a resolution approach for the inverse problem based on the orthogonal wavelet representation. We suppose that the phase φ admits a sparse representation in an orthogonal wavelet base $\Psi = \{\psi_\lambda, \lambda \in \mathcal{I}\}$, which is written:

$$\varphi = \mathcal{W}^*\mathbf{v}, \tag{8.2}$$

where $\mathbf{v} \in l_2$ is a wavelet coefficients vector, and $\mathcal{W}^*$ is the synthesis operator. The corresponding family is indexed by the elements λ of an infinite set $\mathcal{I}$, which includes the level of the resolution, the position and the type of wavelet.

The phase retrieval problem can be formulated as an unconstrained optimization problem with an l_1 regularization term for the wavelet coefficients and with a regularization parameter κ. The wavelet coefficients are optimized as follows:

$$\min\left\{\frac{\|\mathcal{I} - \mathcal{B}\mathcal{W}^*\mathbf{v}\|_2^2}{2} + \kappa\|\mathbf{v}\|_1, \mathbf{v} \in l_2\right\} \tag{8.3}$$

where l_p is the norm of the vector $\mathbf{v}$ defined as :

$$\|\mathbf{v}\|_p = \left(\sum_i v_i^p\right)^{1/p}. \tag{8.4}$$

In terms of convex analysis, the first term is convex, semi-continuous and differentiable with β-Lipschitz continuous gradient for a coefficient $\beta > 0$. The regularizing term is semi-continuous and not differentiable. This optimization problem has been studied and efficient algorithms have been proposed [Daubechies *et al.* (2004), Combettes and Wajs (2005), Candes *et al.* (2006), Donoho (2006), Chaux *et al.* (2007), Daubechies *et al.* (2008), Wright *et al.* (2009), Dupe *et al.* (2009)].

We selected the following iterative method: $\mathbf{v}_0 \in l_2$, and $0 < \tau < 2/\beta$ and for each

$n \in N$, we construct the following sequence:

$$\mathbf{v}_{n+1} = \mathcal{S}_{\kappa\tau}\left\{\mathbf{v}_n - \tau\mathcal{W}\mathcal{B}^*\left[\mathcal{B}\mathcal{W}^*(\mathbf{v}_n)\right] - \mathcal{I}\right\} \tag{8.5}$$

where

$$\mathcal{S}_a(u) = \text{sign}(u)\max\left(|u| - a, 0\right) \tag{8.6}$$

is the soft thresholding operator. The solution is obtained from the final iterate $\mathbf{v}_\infty$ with $\varphi_\infty = \mathcal{W}^*\mathbf{v}_\infty$. Iterations described by Eq. 8.5 are implemented using a multiresolution approach. The operator $\mathcal{B}$ is approximated in the wavelet basis by calculating the elements $\langle\psi_\lambda, \mathcal{B}\psi_\mu\rangle$ for different orthogonal wavelets. The adjoint operator is obtained with the adjoint matrix of the above matrix. The Landweber thresholded iterations are nested by taking as initialization the lowest resolution level. The solution obtained when the algorithm stagnates is extended to the next higher resolution level completing the initialization with zeros, obtaining an appropriate initialization. This procedure is repeated until the highest resolution level is reached. This gives a progressive refinement of the solution in wavelet coordinates.

8.1.2 Results and discussions

Following Section 5.1.2, the imaging system was simulated in a deterministic fashion. The original phase map to be retrieved is displayed in Figure 8.1. This proposed algorithm was tested on noisy-data PPSNR=15dB (Eq. 5.12). Propagation in free-space was simulated using Eq. 3.5 using only *one* distance at D=0.6 m. The corresponding Fresnel diffraction pattern for 0.6 m with 15dB is shown in Figure 8.2.

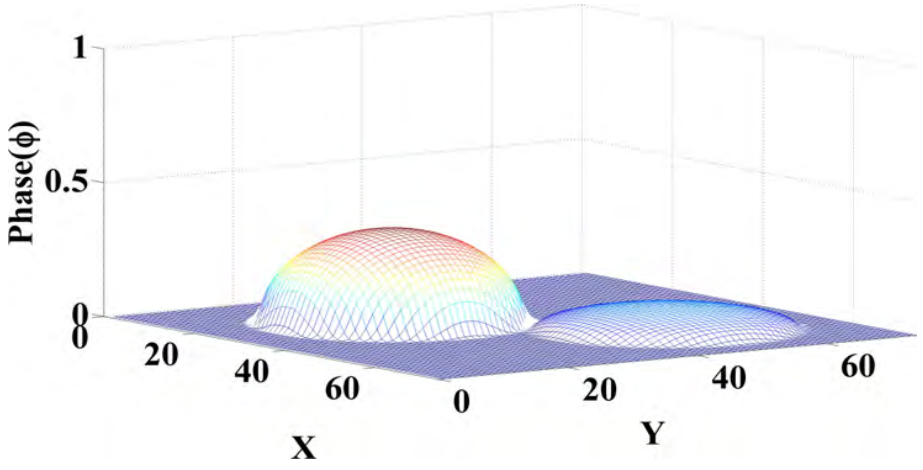

Figure 8.1: Ideal phase to recover.

In this section, the Dauchechies wavelet orthonormal wavelet system db_1 implemented in Matlab was used. The convex part of the functional to be minimized is differentiable. Its gradient has a Lipschitz constant $\|\mathcal{B}\mathcal{W}^*\|^2$. To evaluate this norm, we follow the approach

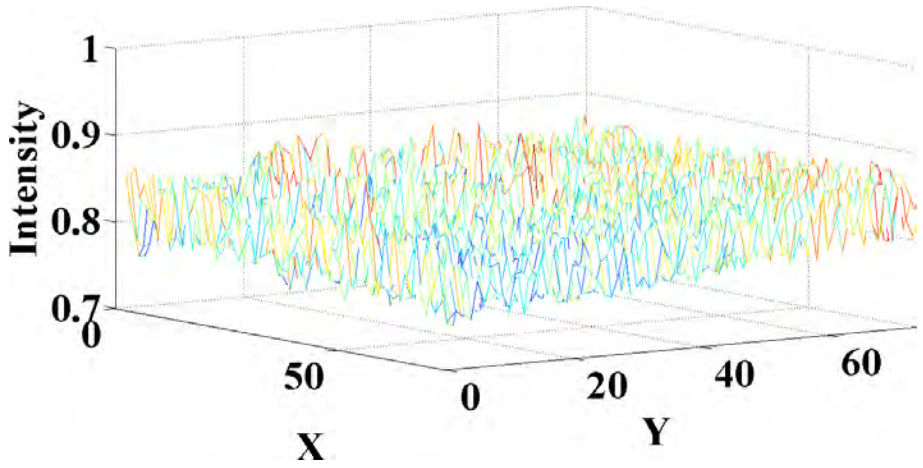

Figure 8.2: Fresnel diffraction pattern at propagation distance D=0.6m with PP-SNR=15dB.

proposed in [Chaari *et al.* (2009)]: given $\mathbf{v}_0$ and $A = \mathcal{B}\mathcal{W}^*$, we construct a sequence $(\mathbf{v}_n)$ such that $\mathbf{v}_n = A^* A \mathbf{v}_{n-1}$, and at each iteration $\rho_n = \frac{\|\mathbf{v}_n\|}{\|\mathbf{v}_{n-1}\|}$ is calculated. After convergence $\lim_{n\to\infty} \rho_n = \rho_\infty = \|\mathcal{B}\mathcal{W}^*\|^2$.

In the first approach, the descent step and regularization parameter, κ, are kept constant for a given resolution level. Good results are obtained with $\kappa = 0.1\|\mathcal{B}^T\mathcal{I}\|_\infty$ [Wright *et al.* (2009)]. The phase maps obtained with Tikhonov regularization and with the above algorithm are displayed in Figure 8.3 and Figure 8.4 respectively.

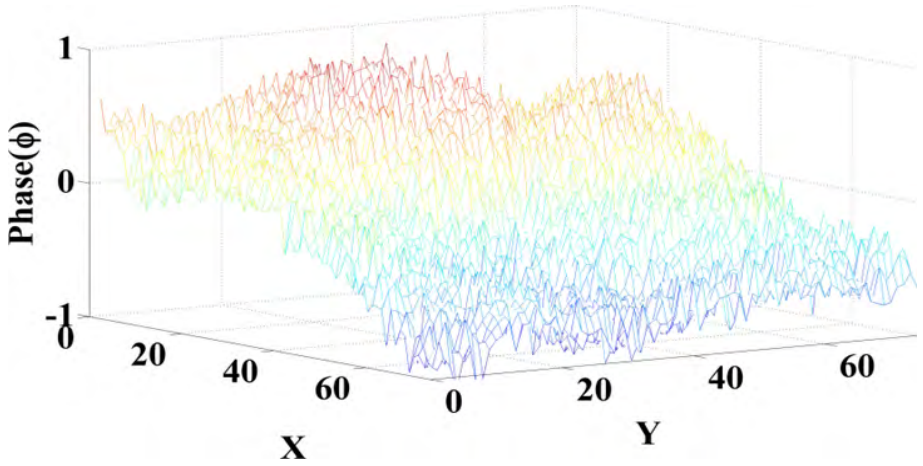

Figure 8.3: Reconstructed phase with Tikhonov regularization.

Tikhonov regularization gives good results for signal/noise ratios higher than 24dB. For higher noise levels, the phase reconstruction is very far from true phase as can be seen in Figure 8.3. To assess the quality of the reconstruction, the relative errors $\|\varphi_\infty - \varphi^*\|_{L_2}/\|\varphi^*\|_{L_2}$ were calculated. The relative error increases from **1.1** for the initial solution corresponding to Tikhonov regularization for a signal/noise ratio of 15dB to a value of **0.48** at the end of the iterative Landweber algorithm.

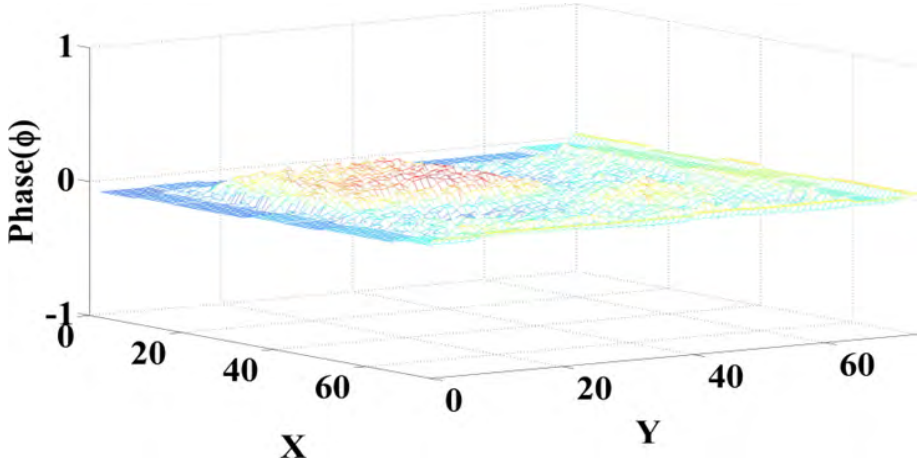

Figure 8.4: Reconstructed phase with the iterative Landweber algorithm l_1 regularization .

The approach adopted here is promising since it allows a significant improvement of the reconstruction phase map with respect to existing algorithms as shown the Figure 8.4.

8.1.3 Conclusions

In conclusion, this work significantly improves the approaches used until now in the X-ray phase imaging reconstruction, based on Tikhonov regularization. The direct problem can be linearized and reversed by a classical iterative Landweber algorithm using an orthogonal wavelet basis. The results remain very noisy. Taking into account different propagation distances and the nonlinearity of the inverse problem decrease the reconstruction errors. The use of other representations should also help to achieve better results, and taking into account the constraints of positivity.

8.2 Combined iterative algorithm

The results of this section have been published in the following article:
V. Davidoiu, B. Sixou, M. Langer, and F. Peyrin,
"Nonlinear phase retrieval and projection operator combined with iterative wavelet thresholding"
IEEE Signal Processing Letters, vol.19, No. 9, pp. 579 - 582 ,2012.

A nonlinear phase retrieval method based on the Fréchet derivative of the intensity has been investigated in Section 5.2.3. This solution outperforms the linear approaches but is not optimal and poor reconstructions are obtained for noisy data and low frequencies.

In this section, we investigate the resolution of this inverse problem with an iterative thresholding algorithm in wavelet coordinates combined with an iterative nonlinear method with a Tikhonov regularization and projection operators. The phase retrieval algorithm was tested for a 3D Shepp-Logan phantom in the presence of noise. The results show that the combined approach outperforms the mixed, the CTF and the nonlinear methods presented above.

8.2.1 Nonlinear phase retrieval with Tikhonov regularization

The previously proposed nonlinear approach presented in Section 5.2.3 is based on the L_2 norm of the phase gradient as regularization term. Better convergence results are obtained with the L_2 norm of the phase to stabilize the solution as has been detailed in Section 6.3. This regularization term will be used in this section.

The intensity I_D can be considered as a continuous and a nonlinear function of the phase φ which is Fréchet differentiable in its domain [Scherzer *et al.* (2008)]. We have assumed that the domain $\mathcal{D}[I_D(\varphi)]$ of the operator $I_D(\varphi)$ belongs to the functional Sobolev space $H^{2,2}_{\diamond}(\Omega) = \{\varphi \in H^{2,2}(\Omega),\ \frac{\partial\varphi}{\partial\vec{n}} = 0\}$, where $\frac{\partial\varphi}{\partial\vec{n}}$ is the normal derivative of the phase [Scherzer *et al.* (2008)]. The regularization functional J_α to minimize is given by:

$$J_\alpha(\varphi) = \frac{1}{2}\|I_D(\varphi) - I_\delta\|^2_{L_2(\Omega)} + \frac{\alpha}{2}\|\varphi\|^2_{L_2(\Omega)} \tag{8.7}$$

where α is a regularization parameter, I_δ the noisy intensity for a noise level δ and where $\|.\|_{L_2(\Omega)}$ denotes the $L_2(\Omega)$ norm.

Let φ_k be the phase at the iteration k. The phase estimate φ_{k+1} at the iteration $k+1$ is obtained from the phase φ_k at the previous iteration k in two steps. First, a gradient descent is performed leading to the phase $\varphi_{k+\frac{1}{2}}$:

$$\varphi_{k+\frac{1}{2}} = \varphi_k - \tau_k\{I_D^{'}(\varphi_k)^*[I_D(\varphi_k) - I_\delta] + \alpha\varphi_k\} \tag{8.8}$$

which will be used as input for the projection operator in the second step (Section 8.2.2). In this way, the standard Landweber method [Scherzer *et al.* (2008)] is modified by introducing a linear search procedure with a variable step τ_k, obtained with a dichotomy strategy. The regularizing parameter α is chosen by trial-and-error in order to obtain the best decrease of the regularization functional. The computation of the iterates is based on the calculation of the adjoint of the Fréchet derivative of the intensity detailed in Section 5.2.3.

8.2.2 Projection operators

We give here a brief presentation of this part since it has already been presented in Section 6.2. The former phase recovery can be improved by using non-convex projection

operators. In this section, we have considered an image modulus constraint in the object domain, so for each diffracted intensity I_D, we consider a set $\mathcal{M}_D = \{u \in L_2(\Omega), |u| = \sqrt{I_D}\}$. This set defines a non-convex constraint. The transmission T_k at the iteration k, obtained with the former iterative method, is given by Eq. 6.1, and we have projected the convolution product $T_k * P_D$ on the set $\mathcal{M}_D$. The simplest choice for the projection $P_{\mathcal{M}_D}$ is defined using Eq. 6.2. For each projection $P_{\mathcal{M}_D}(T_k * P_D)$, we calculated with successive Fourier and inverse Fourier transforms the new transmission T'_k as :

$$T'_k = F^{-1}\left\{F\left[P_{\mathcal{M}_D}\left(T_k * P_D\right)\right] / F\left(P_D\right)\right\}. \tag{8.9}$$

For each pixel, a new phase estimate is obtained from the current phase $\varphi_{k+\frac{1}{2}}$ by minimizing the modulus $|T'_k(\mathbf{x}) - a(\mathbf{x})\exp\left[i\varphi(\mathbf{x})\right]|$. A projection operator P_D is thus defined by the equation:

$$P_D\left[\varphi_{k+\frac{1}{2}}(\mathbf{x})\right] = \underset{\varphi}{\operatorname{argmin}}\left\{|T'_k(\mathbf{x}) - a(\mathbf{x})\exp\left[i\varphi(\mathbf{x})\right]|\right\}. \tag{8.10}$$

A support constraint and a projection $P_{\mathcal{S}}$ on the support $\mathcal{S}$ of the phase was also considered $P_{\mathcal{S}}(\varphi) = \varphi.1_{\mathcal{S}}$.

$$\varphi_{k+1} = P_{\mathcal{S}}P_D(\varphi_{k+\frac{1}{2}}). \tag{8.11}$$

8.2.3 Resolution of the linear inverse problem in wavelet coordinates

The nonlinear approach does not converge for high noise levels and for an initialization point far from the solution, even with the additional projection step. It is very sensitive to low frequency noise. We have thus also considered a resolution approach for the linear inverse problem based on the orthogonal wavelet representation and a classical thresholded Landweber algorithm presented in Section 8.1. The difference between the approach used in Section 8.1 and the method proposed here is that we are going to consider only the lowest wavelet coefficients for three propagation distances and not a multiresolution approach for a single distance. As we saw in Section 8.1.1 the phase φ admits a sparse representation in an orthogonal wavelet base $\Psi = \{\psi_\lambda, \lambda \in \mathcal{I}\}$ and can be written as in Eq. 8.1. Using the Eq. 8.5 a sparse solution is obtained iteratively with the soft threshold operator $S_{\kappa\tau}$ (Eq. 8.6).

Since we intend to use the wavelets to improve the low frequency phase retrieval, the iterations described by Eq. 8.8 are implemented only at the lowest level of resolution and the operator $\mathcal{W}\mathcal{B}\mathcal{W}^*$ is approximated with the lowest level of resolution of the wavelet basis.

Simulation methodology

The nonlinear approach based on the Fréchet derivative of the intensity with the Tikhonov regularization and the projection operators (Section 8.2.1, 8.2.2) and the linear wavelet algorithm (Section 8.2.3) are used alternatively. The solution obtained when the error stagnates with one method is used as initialization for the second one. By alternating the two phase retrieval approaches, we obtain a progressive refinement of the solution.

The phase retrieval algorithm proposed is not globally convergent. In our simulations, the mixed approximation and the CTF of the linear problem were used as starting point. In order to avoid obtaining solutions diverging far away from the real solution, the regularization parameters are chosen by trial-and-error. The best values obtained for α and κ (from Eq.8.3) are 10^{-3}. The iterations are terminated when the following conditions are fulfilled:

$$\begin{aligned} \|I_D(\varphi_k) - I_D(\varphi_{k-1})\|_{L_2(\Omega)} &\leq \omega \|I_D(\varphi_{k-1})\|_{L_2(\Omega)} \\ \|I_\delta - I_D\|_{L_2(\Omega)} &\leq \delta \end{aligned} \tag{8.12}$$

where ω is a parameter that was set at 0.01 by trial-and-error, I_δ is the measured intensity for distance D and δ is the noise level. For the wavelet representation, the orthonormal wavelet $db1$ Dauchechies implemented in Matlab was used with only 64 low resolution coefficients. The convex part of the functional to be minimized is differentiable with Lipschitz gradient with $\beta = \|\mathcal{W}\mathcal{B}\mathcal{W}^*\|^2$. Following [Chaari *et al.* (2009)], given $\mathbf{x}_0$ et $\mathcal{C} = \mathcal{W}\mathcal{B}\mathcal{W}^*$, we construct a sequence $(\mathbf{x}_n)$ such that $\mathbf{x}_n = \mathcal{C}^*\mathcal{C}\mathbf{x}_{n-1}$. After convergence, $\lim_{n\to\infty} \frac{\|\mathbf{x}_n\|}{\|\mathbf{x}_{n-1}\|} = \|\mathcal{W}\mathcal{B}\mathcal{W}^*\|^2$.

Since ideal reconstruction is available, direct comparisons can be made. The method will be quantitatively evaluated by measuring the normalized mean square error (NMSE) given by Eq. 6.10.

8.2.4 Results and discussions

The performance of the proposed combined approach was analyzed by comparison with the solutions obtained for noisy data with the CTF [Cloetens *et al.* (1996)] and the mixed approach [Langer *et al.* (2008)] used as starting points.

The evolution of the NMSE as a function of the iteration number is displayed in Figure 8.5 for the two starting points. In these plots, a single iteration corresponds to a random cycle through the intensity images obtained for the three distances. The successive decreases of the reconstruction error obtained with the two methods are clearly visible. These curves show that the proposed algorithm has good convergence properties. The error maps for noisy data are displayed in Figure 8.6.

A comparison of the diagonal profiles obtained with the three approaches is displayed

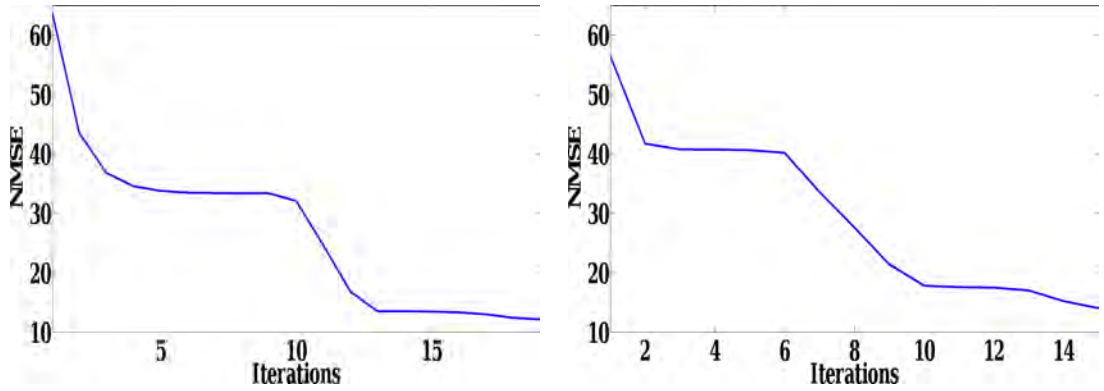

(a) (b)

Figure 8.5: Normalized mean square error for the phase versus iteration number with the proposed algorithm initialized with (a) the mixed solution and (b) with the CTF solution.

Table 8.1: NMSE(%) values for different algorithms

CTF	WNL (initialized with CTF)	mixed	WNL (initialized with mixed)
56.54	14.05	63.84	12.16

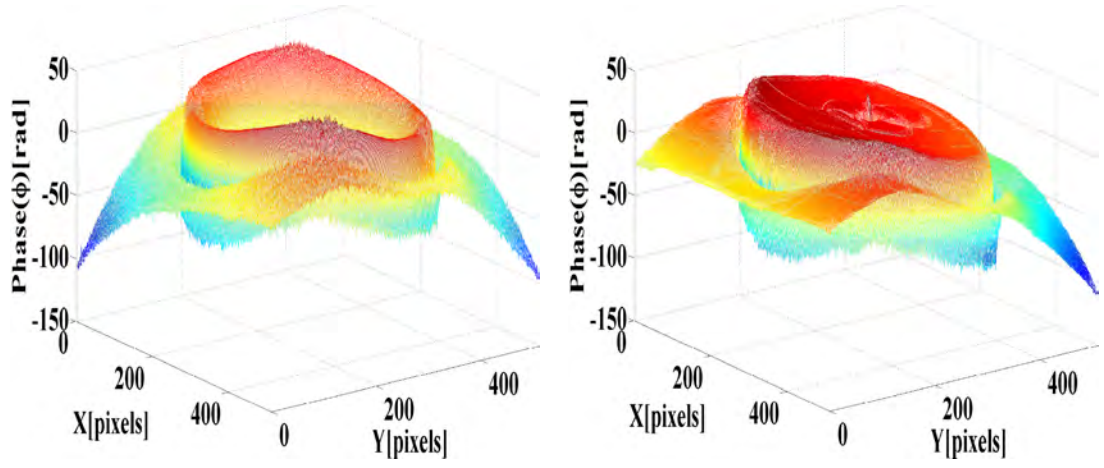

(a) (b)

Figure 8.6: Error map for the phase retrieved with the proposed algorithm initialized with (a) the mixed solution and (b) with the CTF solution.

in Figure 8.7. According to the results presented in Table 8.1, error decreases of 80.95% and 75.15% were obtained with the combined nonlinear and wavelet (WNL) method for the mixed and the CTF starting points. The phases used as starting points for our reconstruction are displayed in Figure 8.8(a), 8.8(b), together with the phase retrieved with the proposed algorithm Figure 8.8(c), 8.8(d).

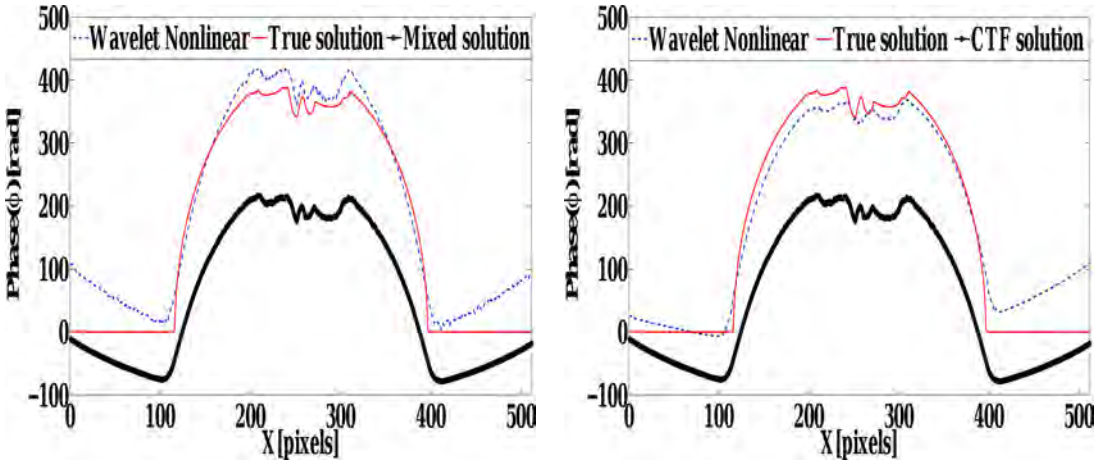

(a) (b)

Figure 8.7: Diagonal profiles for a Shepp-Logan phantom obtained with (a)the mixed method and the WNL approach initialized with the mixed solution, (b) the CTF method and the WNL approach with the CTF initialization.

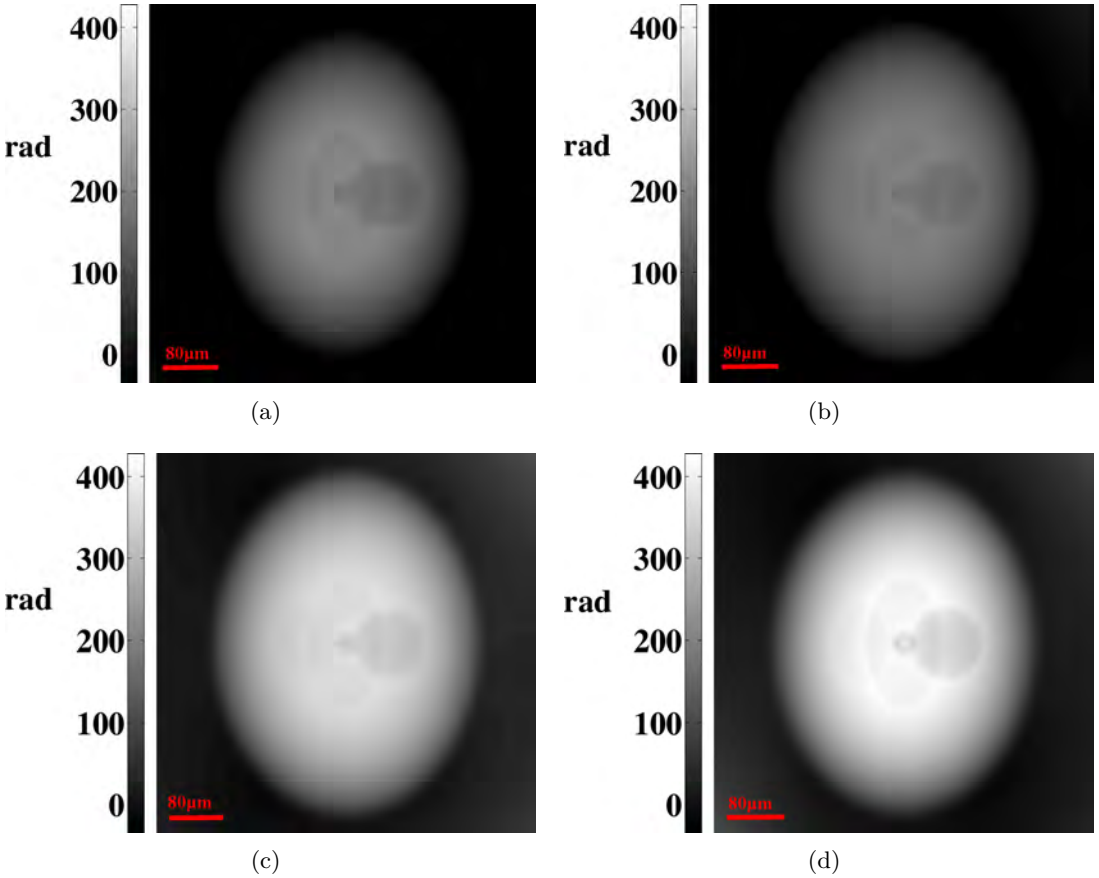

(a) (b)

(c) (d)

Figure 8.8: Phase maps obtained with the (a) mixed and (b) CTF algorithms and with the proposed algorithm for the starting point given by (c) mixed and (d) CTF algorithms respectively.

8.2.5 Conclusions

In this section, we have presented a new phase retrieval approach based on a nonlinear phase retrieval method with the Fréchet derivative of the intensity and projection operators combined with a thresholded Landweber algorithm in wavelet coordinates. The method is valid without any restrictive assumption. The linear schemes must be used to obtain a starting phase map near the true solution. Both the high and low frequency ranges of the phase retrieved are improved and the method is less sensitive to noise. Three propagation distances were used in a random way to achieve a good reconstruction. The reconstruction quality for a projection of a 3D Shepp-Logan phantom has been quantitatively evaluated with noise. The combined method outperforms the linear methods and the nonlinear one without projections and without the wavelet treatment.

8.3 Single-distance phase retrieval approaches involving sparsity constraints

---

The results of this section have been published in the following article:
V. Davidoiu, B. Sixou, M. Langer, and F. Peyrin,
"Nonlinear approaches for the single-distance phase retrieval problem involving regularizations with sparsity constraints"
Applied Optics,vol. 52, No. 17, pp. 3977 - 3986, 2013

Recently, various compressed sensing algorithms for the phase retrieval problem have been studied in [Candes *et al.* (2011), Ohlsson *et al.* (2012), Candes and Li (2012), Waldspurger *et al.* (2012), Mukherjee and Seelamantula (2012), Newton (2012), Gaass *et al.* (2012)], but they are restricted to small scale problems. They cannot be used for phase retrieval coupled to tomography with huge amounts of data. On the other hand, general iterative schemes for nonlinear ill-posed problems with sparsity constraints have been studied by Ramlau and Teschke [Ramlau and Teschke (2006)] but never applied to the phase retrieval problem in in-line phase radiography.

The aim of this section is to make an extensive comparison of the various nonlinear iterative algorithms and regularization strategies that can be applied to the phase retrieval problem using one single focal distance. This single-distance inverse problem is more severely ill-posed than the classical linear problems set with several radiographs [Beleggia *et al.* (2004), Zabler *et al.* (2005), Guigay *et al.* (2007)]. The functional properties of the forward intensity operator are investigated to show that the main assumptions necessary for the convergence of the algorithms are valid. The convergence of the various methods

is investigated on simulated data. Their efficiency, the decrease of low frequency errors and the improvement of the spatial resolution are compared using the 3D Shepp-Logan phantom in the presence of noise for a single propagation distance. In this section, we also summarize the method developed by Teschke et al. [Ramlau and Teschke (2006)] for nonlinear problems with sparsity constraints, followed by the numerical results obtained with our simulations. Some concluding remarks end this section.

8.3.1 Review of the WNL algorithm

The nonlinear iterative approach presented in Section 8.2 is based on the explicit calculation of the Fréchet derivative of the intensity $I_D{}'(\varphi_k)$, and of its adjoint $I_D^{'}(\varphi_k)^*$ given in Section 5.2.3. The classical Landweber method is modified with a variable step τ_k chosen using a dichotomy strategy. It was demonstrated in Section 5.2.1 that the existence of a Lipschitz continuous Fréchet derivative of the forward operator is a necessary condition for the convergence of this method [Scherzer *et al.* (2008)]. This nonlinear solution is not optimal despite the fact that it outperforms the linear solutions. Since only noisy data are available, poor reconstructions are obtained as detailed in Section 5.2.3. In order to reduce the low frequency noise, the former nonlinear algorithm has been combined with a wavelet treatment of the linear problem in Section 8.2. The wavelet method is used when the nonlinear solution stagnates and improves the recovery of the smooth part of the object. The combination of the two methods improves the efficiency of the phase recovery when the initialization is performed far from the true solution. This type of approach is preferred to the compressive sensing methods developed recently that cannot been applied to large scale problems [Candes *et al.* (2011), Ohlsson *et al.* (2012)].

8.3.2 Nonlinear sparsity regularization method with a fixed point algorithm

The use of sparsity constraints has become recently a very important trend in inverse problems studies. A strategy to solve nonlinear problems with a sparsity regularization has been proposed and investigated by Ramlau and Teschke [Ramlau and Teschke (2006)] but never applied to phase retrieval problems. It will be denoted RTS (Ramlau and Teschke Scheme) in the following. This approach is summarized in the next subsection and we show that the convergence conditions are satisfied. We detail also a fixed point iterative method based on a surrogate functional used to minimize the regularization functional [Ramlau and Teschke (2006)]. This scheme provides an alternative treatment to the combined wavelet-nonlinear (WNL) approach presented in the former section.

Nonlinear sparsity regularization

In this section, we assume again that we have one orthogonal wavelet frame $\{\phi_\lambda, \lambda \in \Lambda\}$ for $L_2(\Omega)$ such that the phase can be expressed with the wavelet coefficients $\mathbf{c} \in l_2$ by $\varphi = \mathcal{W}^*(\mathbf{c})$. The intensity is a nonlinear function of the wavelet coefficient $\mathbf{c} \in l_2$

$$I = I_D(\varphi) = I_D(\mathcal{W}^*(\mathbf{c})) = \tilde{I}_D(\mathbf{c}). \tag{8.13}$$

Following the arguments in [Ramlau and Teschke (2006)], a sparsity term $\|\mathbf{c}\|_{l_1}$ has been chosen to regularize the nonlinear inverse problem. The functional to minimize is the sum of misfit and regularization term defined by:

$$J_\alpha(\mathbf{c}) = \|\tilde{I}_D(\mathbf{c}) - I_\delta\| + \alpha\|\mathbf{c}\|_{l_1}, \tag{8.14}$$

where α is a regularization parameter, I_δ is the measured intensity for distance D and δ is the noise level. This regularization method is convergent for strongly continuous operators with a strongly continuous Fréchet derivative [Teschke and Ramlau (2007)]. It has been shown in Section 5.2.1 that the Fresnel intensity operator and its Fréchet derivative are continuous. As demonstrated in [Ramlau (2002)], to obtain a strongly continuous operators, it is necessary to assume some smoothness of the solution of the equation $I_D(\varphi) = I$. The forward intensity operator may be restricted to a Sobolev space of order $\rho > 0$, $H_0^\rho(\Omega)$ and thus considered as a strongly continuous operators. It has also been demonstrated in Section 5.2.1 that the Fresnel intensity operator is Fréchet differentiable with Lipschitz continuous first derivative. This result is also true for the operator $\mathbf{c} \rightarrow I_D(\mathcal{W}^*(\mathbf{c}))$ and this operator can also be considered as strongly continuous. Thus, the proposed regularization method should converge to a critical point of the regularization functional for a smooth phase map with a sparse representation.

A fixed point iterative algorithm

In order to minimize the regularization functional J_α, we have used a fixed point iteration algorithm based on a surrogate functional [Ramlau and Teschke (2006)]. The idea is to replace the variational functional by a sequence of functionals easier to treat and such that the sequence of minimizers converges to a critical point of the variational functional. For $\mathbf{c} \in l_2$, and $\mathbf{a} \in l_2$, Ramlau and Teschke have defined a surrogate functional:

$$J_\alpha^s(\mathbf{c}, \mathbf{a}) = J_\alpha(\mathbf{c}) + R\|\mathbf{c} - \mathbf{a}\|_{l_2}^2 - \|I_D[\mathcal{W}^*(\mathbf{c})] - I_D[\mathcal{W}^*(\mathbf{a})]\|_{l_2}^2 \tag{8.15}$$

where $\mathbf{c}$ is the wavelet coefficients vector, $\mathbf{a} \in l_2$ an auxiliary sequence and $R \in \mathbb{R}^+$. The iteration minimization process is defined as follows [Ramlau and Teschke (2006)]: for $\mathbf{c}_0 \in l_2$ and for some constant $R > 0$, a sequence of iterates $(\mathbf{c}_k)_{k\geq 0} \in l_2$ is derived with

the iteration:

$$\mathbf{c}_{k+1} = \underset{\mathbf{c}}{\operatorname{argmin}} J_{\alpha}^{s}(\mathbf{c}, \mathbf{c}_k) \qquad k = 0, 1, 2, ... \tag{8.16}$$

The norm convergence of this iterative scheme towards a critical point of the regularization functional has been shown in [Ramlau and Teschke (2006)]. It is easy to show from the decomposition of the forward operator of section 5.2.1 that the Fresnel diffraction operator is a twice continuously differentiable operator. The surrogate functional is thus strictly convex (See proposition 12, [Teschke and Ramlau (2007)]). The unique minimizer of the surrogate functional is characterized by a necessary condition which can be written as a fixed point equation. The necessary condition for a minimum of the surrogate functional $J_{\alpha,q}^{s}(\mathbf{c}, \mathbf{a})$ is given in terms of sub-differential of $\|.\|_{l_1}$ by:

$$0 \in I_D'^{*}[I_\delta - I_D(\mathbf{a})] + R(\mathbf{c} - \mathbf{a}) + \alpha \partial \|\mathbf{c}\|_{l_1}. \tag{8.17}$$

The λ-component wise fixed point necessary conditions for a minimizer of the surrogate functional can be recast as:

$$\mathbf{c}_\lambda = S_{\frac{\alpha}{R}} \left\{ \left[\mathcal{W} I_D'[\mathcal{W}^*(\mathbf{c})]^* \left(\frac{I_\delta - I_D[\mathcal{W}^*(\mathbf{a})]}{R} \right) + \mathbf{a} \right]_\lambda \right\} \tag{8.18}$$

where $S_{\frac{\alpha}{R}}$ is the soft thresholding operator. This fixed point equation can be written in compact form as $\mathbf{c} = \Psi_{\alpha,R}(\mathbf{c}, \mathbf{a})$. Let L be the Lipschitz constant of the Fréchet derivative of the intensity operator I_D and A_2 the upper frame bound, then if $R > A_2 L \sqrt{J_\alpha(\mathbf{a}))}$, the former fixed point iteration is a contraction and the inner sequence of iterates associated to the fixed point iteration converges. Given the current iterate $\mathbf{c}_k$, the next estimate of the wavelet coefficient is obtained iteratively with $\mathbf{c}_{k,l} = \Psi_{\alpha,R}(\mathbf{c}_{k,l-1}, \mathbf{c}_k)$. The fixed point iterations are stopped for the index l such that the difference between two iterates is below the error bound τ_2:

$$\|\mathbf{c}_{k,l} - \mathbf{c}_{k,l-1}\|_{l_2} < \tau_2 \tag{8.19}$$

and then $\mathbf{c}_{k+1} = \mathbf{c}_{k,l}$. Similarly, the outer iterations are stopped when:

$$\|\mathbf{c}_{k+1} - \mathbf{c}_k\|_{l_2} < \tau_1. \tag{8.20}$$

In the proposed iterative scheme, the starting point $\mathbf{c}_0$ is obtained with the wavelet coefficient of various linear methods (Chapter 3) and an optimal R is chosen by trial-and-error. A large value of R is first chosen to ensure the convergence of the fixed point iteration. Then, the convergence speed of the method is increased by reducing R with a dichotomy strategy. The proposed iterative scheme is summarized as in the Algorithm 1.

Algorithm 1 RTS iterative algorithm

Require: For given noise level δ, a starting point $\mathbf{c}_0$ is picked
Require: Two tolerances τ_1 and τ_2 are picked.
Require: An admissible C is chosen.
$\mathbf{c}^*_\alpha = \text{Iteration}(I_D, I_\delta, C, \alpha, \tau_1, \tau_2)$
$k = 0$
$I(\mathbf{a}) = I_D(\mathbf{a}) - I_\delta(\mathbf{a})$
$I(\mathbf{a}) = I(\mathbf{a})/C$
while $\|\mathbf{c}_{k+1} - \mathbf{c}_k\|_{l_2} \geq \tau_1$ **do**
  $l = 0$
  $\mathbf{c}_{k,0} = \mathbf{c}_k$
  while $\|\mathbf{c}_{k,l} - \mathbf{c}_{k,l+1}\|_{l_2} \geq \tau_2$ **do**
    $l = l + 1$
    $\mathbf{c}_{k,l} = \Psi_{\alpha,C}(\mathbf{c}_{k,l-1}, \mathbf{c}_k)$
  end while
  $\mathbf{c}_{k+1} = \mathbf{c}_{k,l}$
  $k = k + 1$
end while
$[\mathbf{c}^*_\alpha] = [\mathbf{c}_k]$

8.3.3 Initialization and Stopping Rules

We have tested the proposed algorithms for different starting points obtained with various linear methods and for different noise levels. The 3D Shepp-Logan phantom described in Section 6.3.2 for a single distance $D = 0.035$ m has been used in our comparison. In order to refine the linear phase maps the NL (nonlinear algorithm), the WNL (wavelet nonlinear algorithm) and the RTS (Ramlau and Teschke Scheme) algorithms were then applied. These algorithms use a single phase contrast image obtained at distance $D = 35$ cm. The convergence speed of the nonlinear algorithms is influenced by the regularization parameters. In all the studied methods, the regularization parameters are chosen carefully.

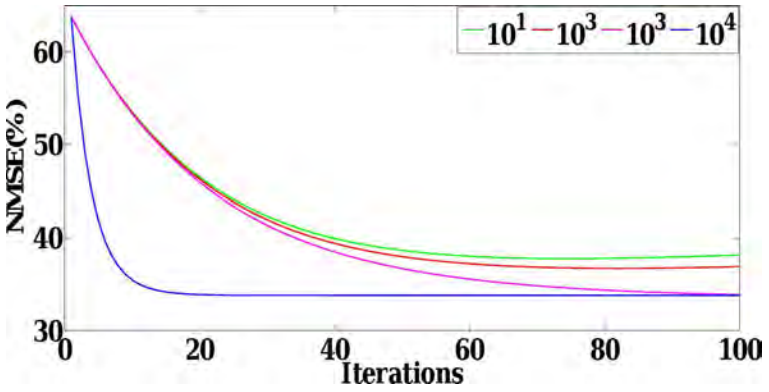

Figure 8.9: Evolution of the NMSE[%] as a function of iterations for different values of the regularization parameters R used in RTS algorithm.

Large and small values of the parameters leading to poor reconstruction results are first

chosen. The optimal values of the parameters are then gradually refined by trial-and-error with a decreasing interval. For WNL, the two regularization parameters α and ζ are set to $1.5 * 10^{-4}$. For the RTS algorithm, the value of R has been chosen to 10^4. As displayed in Figure 8.9, this value ensures the best convergence properties of the algorithm. In our tests, τ_1 (Eq. 8.20) and τ_2 (Eq. 8.19) are fixed to 10^{-6} and 10^{-15} respectively. In the WNL algorithm, the iterations are stopped the conditions from Eq. 8.12 (with ω set at 0.001 by trial-and-error) are fulfilled. The stagnation of the WNL algorithm was avoided by switching between the two methods presented in section 8.2.1 and 8.1.1 when the following condition is fulfilled:

$$\|\varphi_k - \varphi_{k-1}\|_{L_2(\Omega)} \leq \omega \|\varphi_k\|_{L_2(\Omega)}. \tag{8.21}$$

8.3.4 Wavelet implementation, error measurements

In this section, we have used the orthonormal Daubechies wavelet *db*4 (Matlab implementation). For the nonlinear proposed method WNL, only 100 low resolution wavelet coefficients have been used (the red square in Figure 8.10(b)). The convex part of the functional to be minimized is differentiable with a gradient of Lipschitz constant $\|\mathcal{W}\mathcal{O}\mathcal{W}^*\|^2$. Following [Chaari *et al.* (2009)], given an initial wavelet vector $\mathbf{x}_0$ and $\mathcal{C} = \mathcal{W}\mathcal{O}\mathcal{W}^*$, we construct a sequence $(\mathbf{x}_n)$ such that $\mathbf{x}_n = \mathcal{C}^*\mathcal{C}\mathbf{x}_{n-1}$. After convergence, $\lim_{n\to\infty} \frac{\|\mathbf{x}_n\|}{\|\mathbf{x}_{n-1}\|} = \|\mathcal{W}\mathcal{O}\mathcal{W}^*\|^2$. Since the ideal phase is available, quantitative measurements of the errors are made using normalized mean square error (NMSE) (Eq. 6.10).

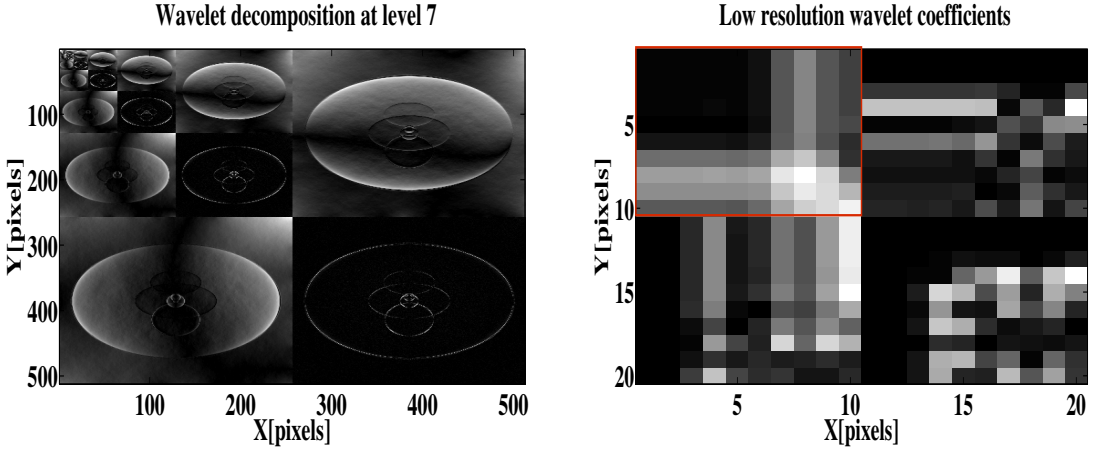

(a) (b)

Figure 8.10: (a) Wavelet decomposition of the phase map and (b) low approximation wavelet coefficients used in WNL.

8.3.5 Results and discussions

In this work, we have made an extensive comparison of the nonlinear algorithms: NL, WNL and RTS for various initialization phase maps obtained with the linear methods at different noise levels. The simulations have been performed on a computer Dell with a 1.73 GHz Intel Core(TM) i7CPU and 8Gbytes random access memory. The algorithms have been implemented Matlab (R2010b) running under Windows 7. A complete optimization step in the case of the RTS algorithm is composed by 5 inner iterations and 11 outer iterations. These iteration numbers are controlled by τ_1 and τ_2. At the end of these 55 iterations a single NMSE value is obtained. This process will be repeated 100 times and thus 5500 iterations needed for convergence and retrieval of the final phase map. The reconstruction total time for RTS is 5205 seconds and for WNL 1025 seconds.

Table 8.2: NMSE(%) for different algorithms and noise levels. The error bar is estimated to 0.5%

PPSNR[dB]	Initialization [NMSE]		NL [NMSE]	WNL [NMSE]	RTS [NMSE]
without noise	TIE	25.5%	9.6%	**8.9**%	18.5%
	CTF	42.5%	24.6%	**6.5**%	35.6%
	Mixed	26.8%	11.4%	**7.5**%	20%
48dB	TIE	35.5%	18.6%	**11.1**%	27.7%
	CTF	33.7%	11.8%	**8.9**%	26.5%
	Mixed	26%	13.7%	**8.7**%	20.6%
24dB	TIE	262.1%	207.4%	98%	**91.1**%
	CTF	56.5%	26.8%	**14**%	40.6%
	Mixed	63.8%	41.9%	**12.1**%	33.3%
12dB	TIE	791.6%	791.6%	**81.7**%	99.6%
	CTF	123.4%	101.4%	**36.4**%	51.9%
	Mixed	57.3%	57.3%	**28.5**%	42.6%

To summarize all the results, the Normalized Mean Square Errors (NMSE Eq. 6.10) for the all the approaches used in this work are presented in Table 8.2. The error bar for the NMSE can be estimated to 0.5% for variations of the regularization parameters of 10% around their optimal values. The WNL algorithm increases drastically the accuracy of the phase retrieval for a single intensity image compared with the linear methods [Zabler *et al.* (2005), Paganin (2006), Guigay *et al.* (2007)]. Our results show that, in most cases, despite the fact that the two former methods include sparsity constraints, the WNL method gives better numerical results that the RTS approach. In very few simulations, the final reconstruction errors are similar.

To illustrate this result, the evolution of the NMSE obtained at convergence as a function of the initial PPSNR[dB] is displayed in Figure 8.11 for the various cases investigated. In Figure 8.11(a), it can be observed that the mixed approach yields more accurate reconstructions for higher noise levels compared with the CTF and TIE approaches. In

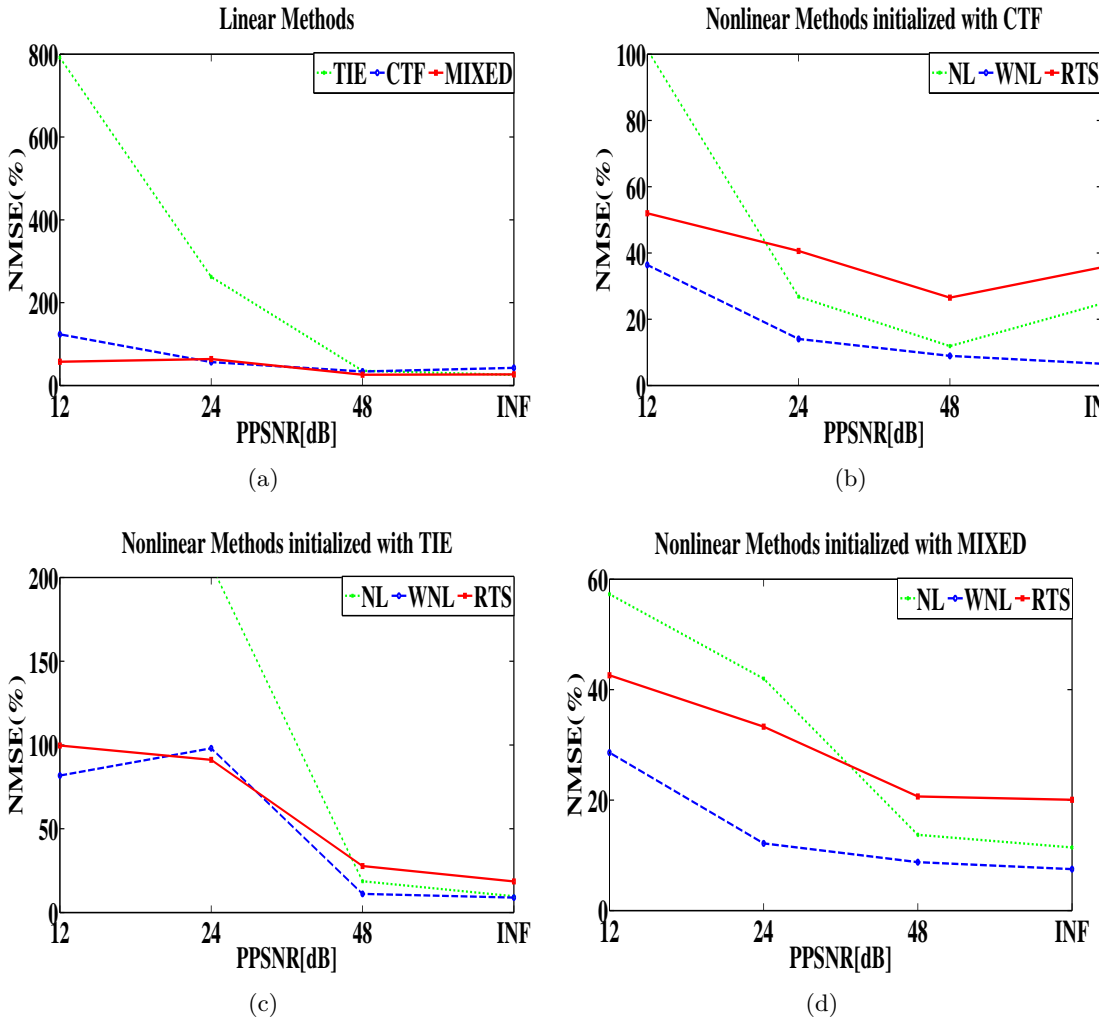

Figure 8.11: Evolution of the NMSE as a function of the PPSNR for: (a) linear algorithms and nonlinear (NL, WNL and RTS) algorithms initialized with (b) CTF, (c) TIE and (d) mixed solutions.

Figure 8.11(b), the three nonlinear solutions have been obtained with the CTF initialization, in Figure 8.11(c) with the TIE initialization and in Figure 8.11(d) with the mixed initialization respectively. The lower errors are always obtained with the WNL scheme.

An example of evolution of the NMSE as a function of the number of iterations is displayed in Figure 8.12, for the WNL method and the RTS method initialized with the solution obtained with the linear CTF algorithm, without noise. The successive errors decreases associated with the two steps of the WNL scheme are clearly visible. A progressive refinement of the solution is obtained. The final NMSE is lower for the WNL algorithm.

A comparison of the diagonal profiles of the ideal phase to be retrieved, of the initialization phase and of the retrieved nonlinear solutions is displayed in Figure 8.14(a), 8.14(b), 8.14(c) and 8.14(d) for different initializations and various initial noise levels. The WNL approach yields the most accurate phase map with the better edge reconstruction,

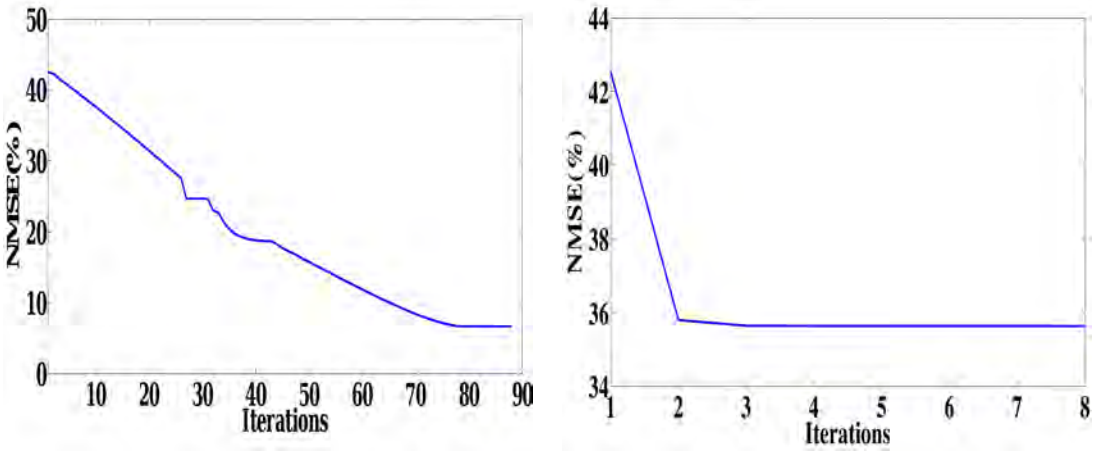

(a) (b)

Figure 8.12: Normalized mean square error for the phase versus iteration number for (a)WNL and (b) RTS approach initialized with CTF solution without noise.

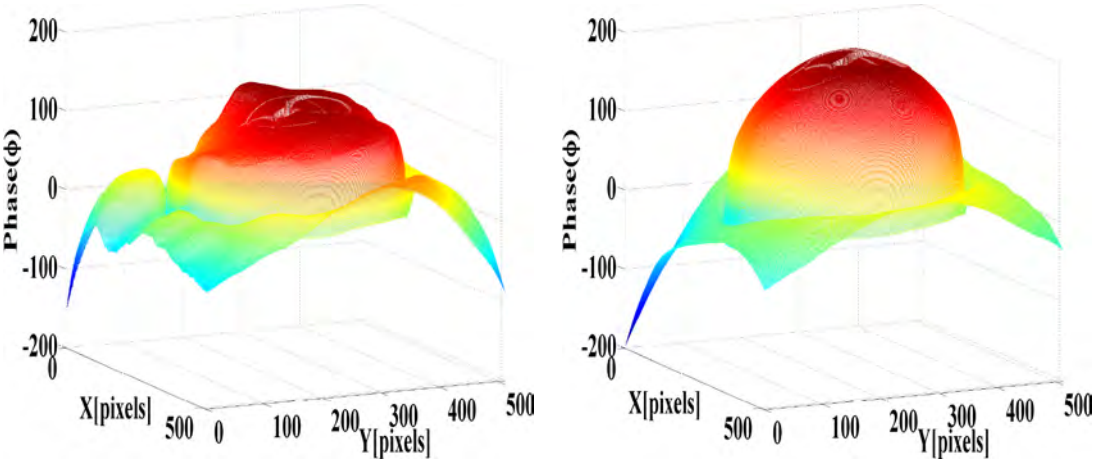

(a) (b)

Figure 8.13: Error maps retrieved with (a) WNL and (b) RTS initialized with the CTF solution with PPSNR=12dB (Figure 8.15(b)).

but this method remains sensitive to noise.

The phase retrieval error maps obtained with the nonlinear algorithms initialized with the CTF solution for noisy data (PPSNR=12dB) are displayed for WNL in Figure 8.13(a) and in Figure 8.13(b) for the RTS approach. The reconstructed WNL phase maps seem less sensitive to noise that the ones recovered with the RTS approach, but remain underestimated.

The phase maps obtained for this case are displayed in Figure 8.15(c) for the WNL method and in Figure 8.15(d) for the RTS approach. The original phase map to be retrieved is displayed in Figure 8.15(a) together with the linear solution yielded by CTF (PPSNR=12dB) in Figure 8.15(b), used as initialization for these simulations. To con-

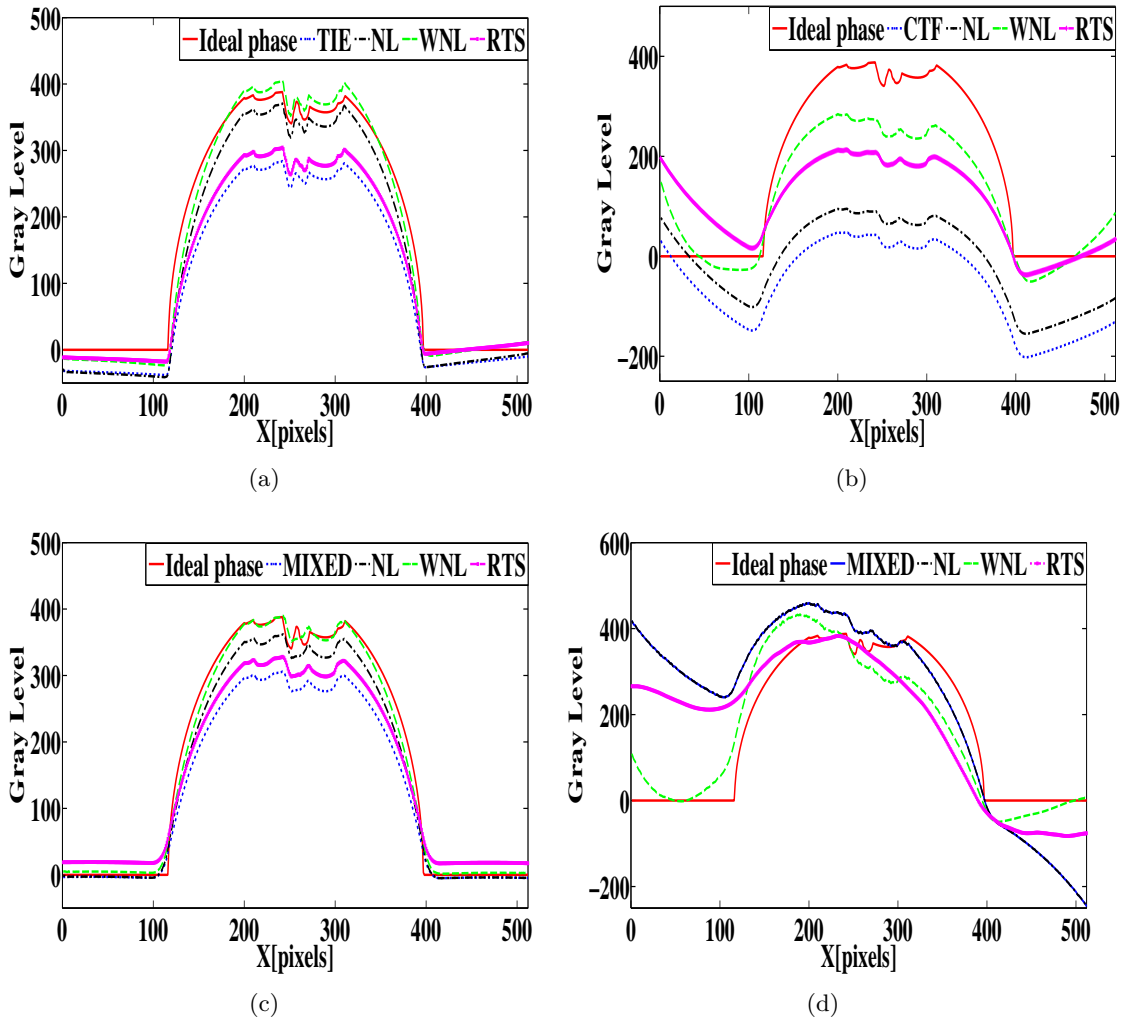

Figure 8.14: Diagonal profiles for the Shepp-Logan phantom obtained with the nonlinear methods for different initializations: (a) TIE (PPSNR=48dB), (b) CTF (PPSNR=12dB), (c) mixed (PPSNR=48dB) and (d) mixed (PPSNR=12dB).

clude, the best numerical results are obtained with the WNL approach. This fact may be related to the two-step strategy of this approach where the high and low frequency ranges are optimized separately.

8.3.6 Conclusions

The aim of the proposed simulations in this section was to evaluate quantitatively several linear and nonlinear approaches based on Tikhonov or sparse regularizations for in-line phase retrieval using only one contrast-image. The comparison was performed using a numerical phantom, without and with white Gaussian noise. The phase maps retrieved with the nonlinear and linear algorithms were compared in terms of NMSE measurements. The main regularity assumptions for the convergence of the algorithms have been demonstrated for the forward Fresnel intensity operator. In order to seek for

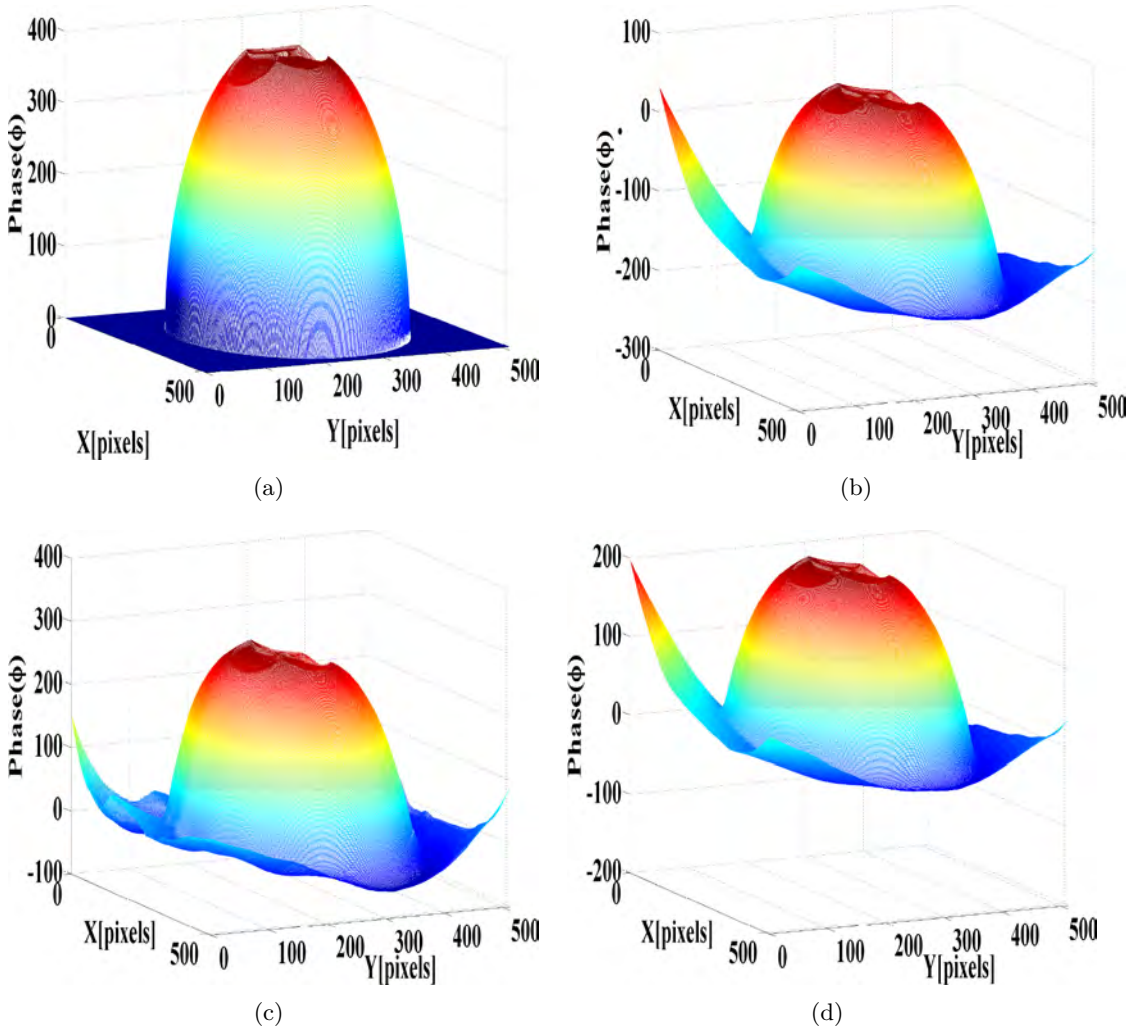

Figure 8.15: (a) True phase to be recovered, (b) phase map obtained for PPSNR=12dB with CTF method and corresponding phase maps obtained using (b) as starting point with (c) WNL and (d) RTS methods.

an efficient and robust phase retrieval approach with a single diffraction pattern, this paper demonstrates the potential of the Wavelet Nonlinear method (WNL). This algorithm alternates a nonlinear treatment of the phase retrieval problem based on the Fréchet derivative of the intensity and a Landweber type scheme, and an iterative solution of the linear problem in wavelets coordinates with a l_1 norm regularization. Our results indicate that the WNL approach performs better and is more robust to noise that the Ramlau and Teschke scheme (RTS), one which is a general method for nonlinear problems with a sparsity regularization. Significant improvements over the linear methods for the reconstructed phase maps have been obtained using the proposed algorithm.

IV Nonlinear phase retrieval for microtomography

Résumé général

Dans cette partie du manuscrit, nous étudions la résolution du problème d'estimation de phase par une méthode non linéaire dans le cadre de la tomographie de phase en ligne. La première section de cette partie est consacrée à une brève présentation du principe de la tomographie et de la méthode de reconstruction tomographique conventionnelle par rétroprojection filtrée (FBP) (Section 9.1.2).

Dans la section 9.1.4, nous avons décrit le principe de la tomographie de phase par propagation qui consiste à faire plusieurs scans de l'objet enregistrés pour différentes distances D échantillon-détecteur (Section 2.3.4). Lorsque on applique directement la méthode FBP à ces images, on obtient sous certaines conditions, un effet de rehaussement de contraste sur l'image d'atténuation. Toutefois, pour réellement obtenir une image 3D de la partie réelle de l'indice de réfraction, il est nécessaire d'appliquer une étape d'estimation de la phase avant la reconstruction FBP.

Un tel système d'acquisition a été développé à l'Installation Européenne de Rayonnement Synchrotron (ESRF) sur la ligne ID19, située à 145m de la source et délivrant des faisceaux de rayons X à la fois cohérents et parallèles. À l'ESRF, le logiciel standard utilisé pour la reconstruction tomographique à partir des projections ou des sinogrammes est *PyHST*, où l'acronyme " HST" signifie " tomographie à haute vitesse". Ce programme est basé sur l'approche de rétroprojection filtrée et est implémenté en Python. Toutes les informations concernant PyHST peuvent être trouvées ici `http://www.esrf.eu/computing/scientific/HST/HST_REF/hst.html`. Les reconstructions tomographiques obtenues dans ce manuscrit ont été réalisées avec PyHST.

Le traitement mis en oeuvre pour reconstruire une image en tomographie de phase comporte donc deux étapes:

1. pour chaque angle de projection θ, une méthode d'estimation de phase est appliquée aux radiographies acquises aux différentes distances. En utilisant soit, un des algorithmes linéaires (Chapitre 3) soit une approche non linéaire ayant comme initialisation une solution linéaire, on obtient alors une carte de phase.

2. l'algorithme par rétroprojection filtrée (FBP), disponible à l'ESRF (PyHst) (Section 9.1.2), est alors appliqué à l'ensemble des cartes de phase φ_θ construites à la première étape. On obtient ainsi la reconstruction tomographique 3D de l'indice de réfraction δ_r.

La plupart des algorithmes linéaires utilisés pour la première étape de la tomographie de phase nécessitent la connaissance de l'absorption. Les projections 2D du coefficient d'atténuation $\mu(x, y, z)$ (Eq. 2.6) correspondent aux données acquises à la distance échantillon-détecteur $D = 0$m. Plus de détails sur le coefficient d'atténuation ont été présentés dans la section 2.2.2.

L'algorithme non linéaire proposé pour l'estimation de phase est une approche itérative qui implique des temps de calcul importants. La dimension typique d'une radiographie 2D de contraste de phase est 2048×2048 pixels. Par exemple, si 2000 angles de projection sont utilisés pour quatre distances de propagation, le nombre total de projections utilisées pour obtenir une image tomographique 3D est donc de 8000 (typiquement plus de 64Gb de données). En prenant en compte que l'algorithme proposé utilise normalement un minimum de 5 itérations pour chaque ensemble de radiographies 2D, les temps de calculs peuvent être rédhibitoires. Une attention particulière a donc été accordée à l'implémentation de la méthode pour réduire les temps de calculs. La solution retenue a été d'utiliser la parallélisation compte tenu que les calculs d'estimation de phase correspondants à chaque angle sont indépendants. La méthode a été implémentée en Octave et parallélisée en utilisant le système OAR à l'ESRF (`http://oar.imag.fr/sources/2.4/Docs/documentation/OAR-DOCUMENTATION-USER`).

Dans la section 9.2 la méthodologie pour appliquer l'algorithme non linéaire, basée sur la méthode de Landweber et l'expression analytique de la dérivée de Fréchet et de son adjoint (Section 5.2.3), à la reconstruction tomographique est détaillée. L'approche non linéaire (NL) minimise la fonctionnelle de régularisation (Eq. 9.18) pour chaque angle θ. La méthode de Landweber classique est modifiée avec un pas variable $\tau_{\theta,k}$ choisi en utilisant une stratégie de dichotomie.

Dans un premier temps, l'algorithme de reconstruction de phase a été testé sur un fantôme 3D Shepp-Logan, avec et sans bruit. Il a été appliqué à partir de trois distances et couplé à la reconstruction par FBP afin de pouvoir évaluer les erreurs de reconstruction directement sur l'indice 3D de réfraction. L'analyse quantitative a été réalisée en termes de NMSE. Les approches d'estimation de phase comparées sont l'algorithme linéaire mixte et la méthode non linéaire itérative basée sur la dérivée de Fréchet. La méthode non linéaire donne les plus faibles écarts à la théorie sur l'indice 3D de réfraction.

Dans la section 9.3, le même algorithme a été appliqué à des données expérimentales acquises à l'ESRF, pour différentes initialisations mixtes. Le dispositif expérimental utilisé est équivalent à celui décrit dans la section 2.3.4. Ces acquisitions ont eu lieu sur la ligne ID19 de l'ESRF. Les intensités de diffraction de Fresnel pour 1500 angles de projection ont été enregistrées à l'aide d'une caméra CCD FRELON avec 2048×2048 pixels pour l'énergie de 22.5keV à quatre distances $D = [2, 10, 20, 45]mm$. Le champ de vue de l'image est de 1.4 mm pour une taille de pixel de 0.68 μm. Le fantôme imagé est un objet composé de fils de divers matériaux de différents diamètres: 125 μm Aluminium (Al), 200 μm polyéthylène téréphtalate ($PETE$), 20μm d'alumine (Al_2O_3) et 28μm polypropylène (PP). L'algorithme mixte de récupération de phase a été appliqué sans aucun a priori sur la phase [Guigay *et al.* (2007)] (initialisation (A)) et avec un a priori $\delta_r/\beta = 367$ correspondant à l'aluminium (initialisation (B)) [Langer *et al.* (2010)]

Nous avons appliqué la même méthode d'évaluation que précédemment. Les résultats

montrent que l'erreur globale sur les indices de réfraction 3D des différents matériaux est plus faible avec la méthode non linéaire qu'avec l'approche mixte sans [Guigay *et al.* (2007)] ou avec a priori [Langer *et al.* (2010)].

Chapter 9

In-line phase tomography using nonlinear phase retrieval

Contents

In this part of the manuscript we study the resolution of the phase tomography problem where phase retrieval with an iterative nonlinear method is coupled to tomographic reconstruction. The first section of this part is devoted to a brief presentation of the

principles of tomography and of the filtered back projection. In Section 9.2 the methodology of the nonlinear algorithm, based on the Fréchet derivative and its adjoint, adapted for tomographic reconstruction is shown. This phase retrieval algorithm is tested for a 3D Shepp-Logan phantom in the presence of noise. In Section 9.3 the same algorithm is applied to experimental data acquired at ESRF, for different mixed initializations.

9.1 Principles of tomography

The principle of tomographic imaging relies on two steps: data acquisition and image reconstruction. Historically, medical tomography has its origins in the work presented by Godfrey Newbold Hounsfield in 1973, when radiographic projections for various multiple angles were recorded by rotating the object of interest over 360°. A main contribution to the mathematical basis of the tomographic reconstruction was made by Allan McLeod Cormack in 1963. Hounsfield and McLeod Cormack received the Nobel Prize in 1979 for this discovery.

The development of computed tomography made it possible to visualize internal structures of an object non-destructively. In the literature the terms such as computed tomography, computerized tomography, computed axial tomography, computer assisted tomography or simply tomography nowadays are employed to specify the method. The main idea is to acquire projections of an object, which correspond to different angles. The X-ray angular radiographs recorded during the rotation of the sample can be regarded as 2D projections of the object. Starting from these 2D angular projections a three-dimensional (3D) distribution of the investigated object is obtained using a suitable reconstruction algorithm. The foundations of the reconstruction algorithm is the mathematical approach attributed to Johann Radon in 1917. The principles of tomography has been described in detail in books like [Kak and Slaney (1989), Hsieh (2003)].

Let us consider a function $f(x, z)$ for a parallel X-ray beam. The coordinate system is fixed with respect to the sample and will be denoted with (x, z), and the coordinate system (x', z') is fixed with respect to the source and detector (Figure 9.1). The 3D reconstruction of the investigated object will be denoted with $f(x, y, z)$, where y is the rotation axis. A projection can be seen as a rotation of the coordinate system (x', z') with an angle θ where the rotation of the (x', z') coordinate system is :

$$\begin{bmatrix} x' \\ z' \end{bmatrix} = \begin{bmatrix} \cos\theta & \sin\theta \\ -\sin\theta & \cos\theta \end{bmatrix} \begin{bmatrix} x \\ z \end{bmatrix} = \begin{bmatrix} x\cos\theta + z\sin\theta \\ -x\sin\theta + z\cos\theta \end{bmatrix}. \tag{9.1}$$

The equation of the straight line for a fixed angle θ and position along x' defines the parallel projection as [Peyrin and Engelke (2012)]:

$$P_\theta(x') = \int_D \mu(x'\cos\theta - z'\sin\theta, x'\sin\theta + z'\cos\theta)dz' \tag{9.2}$$

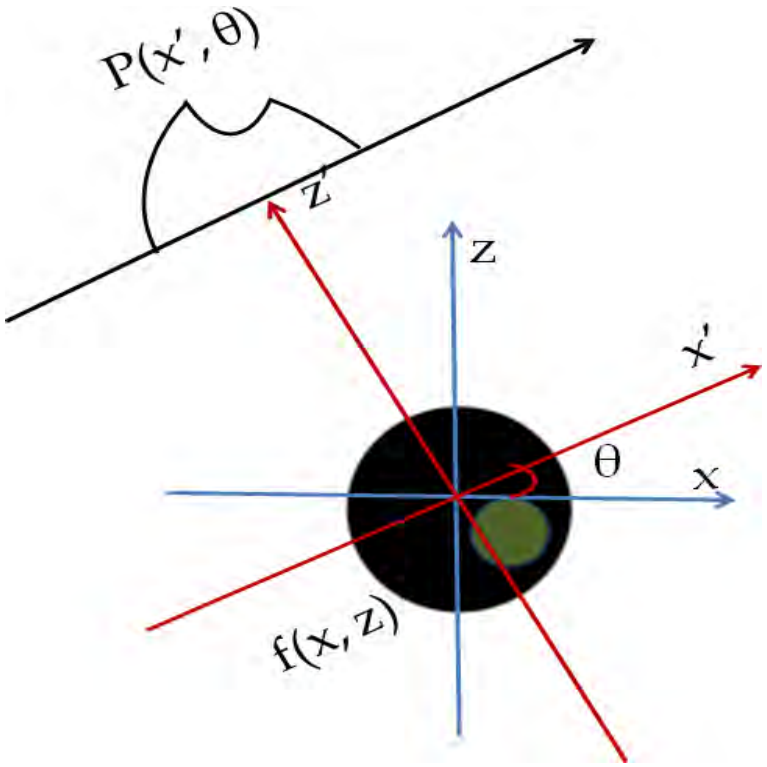

Figure 9.1: System geometry for a parallel projection. The object is composed by two different materials and is defined on the support represented in black. The coordinate system used in tomography (x, z) and it is fixed with respect to the sample. The image plane coordinate system (x', z') is fixed with respect to the source and detector and is rotated around the object with $\theta°$.

where D is the X-ray beam path and μ is the linear attenuation coefficient expressed as [Peyrin and Engelke (2012)]:

$$\ln\left(\frac{I_0}{I}\right) = \int_D \mu(x, z)dz'. \tag{9.3}$$

I_0 denotes the incident intensity and I the transmitted intensity. If θ vary between 0 and π the corresponding set of projections constitutes the Radon transform (Figure 9.2).

9.1.1 The Fourier slice theorem

The Fourier slice theorem or projection-slice theorem is the basis for the Fourier-based inversion techniques. In Figure 9.3 the principle of the Fourier slice theorem is represented. From a mathematical point of view, this principle can be formulated thanks to the two-dimensional (2D) Fourier transform. The Fourier transform of the investigated object $f(x, z)$ is given by:

$$F(u, v) = \int_{-\infty}^{\infty}\int_{-\infty}^{\infty} f(x, z)\exp[-i2\pi(ux + vz)]dxdz. \tag{9.4}$$

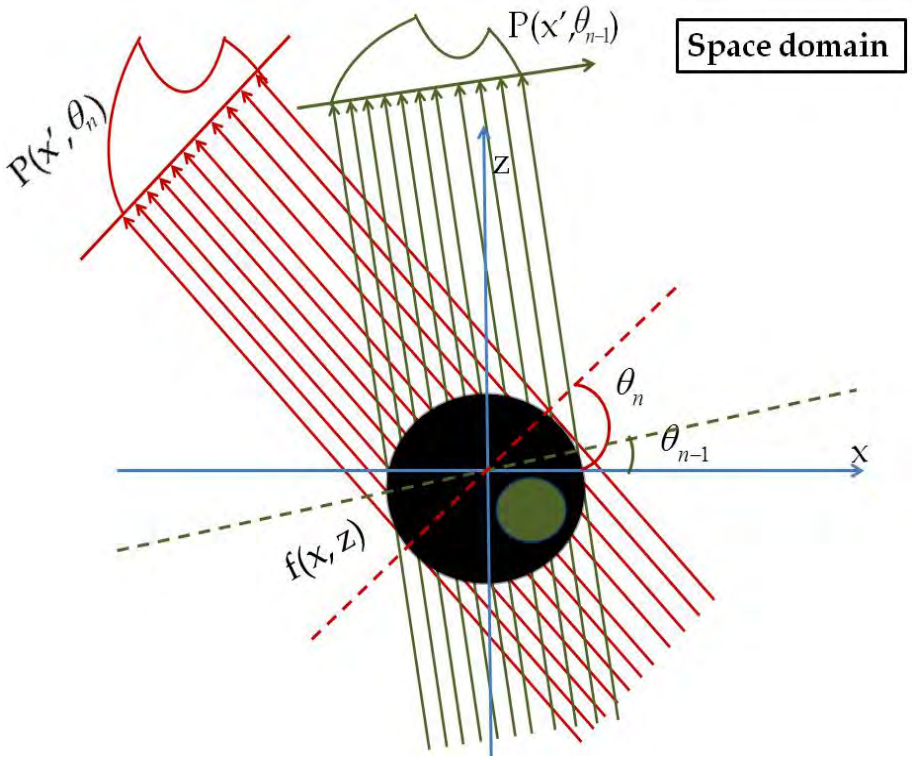

Figure 9.2: The principle for parallel projection tomography. The set of $P(x', \theta_n)$ constitutes the *Radon transform* of the function $f(x, z)$ and are also known as *sinograms*.

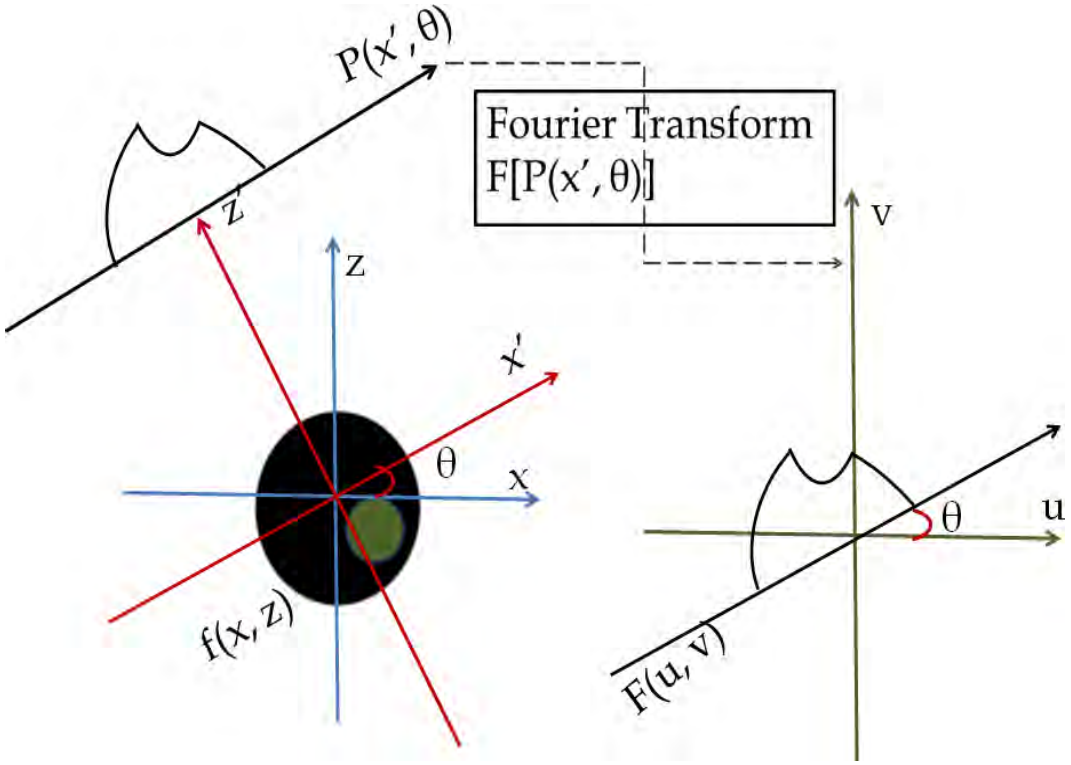

Figure 9.3: Fourier slice theorem illustration.

The Fourier transform of a projection for an angle θ is then:

$$F\{P_\theta\}(\mathbf{f}) = \tilde{P}_\theta(\mathbf{f}) = \int_{-\infty}^{\infty} P_\theta(x)\exp(-i2\pi\mathbf{f}x)dx. \tag{9.5}$$

Let us consider the simplest case where the frequency variable v is set to zero, hence the above equation yields:

$$F(u,0) = \int_{-\infty}^{\infty}\Big[\underbrace{\int_{-\infty}^{\infty} f(x,z)dz}\Big]\exp(-i2\pi ux)dx. \tag{9.6}$$

The first term of the previous equation is known as *parallel projection* at an angle θ along lines of constant x, which is denoted with $P_{\theta=0}(x)$ and has the following form:

$$P_{\theta=0}(x) = \int_{-\infty}^{\infty} f(x,z)dz. \tag{9.7}$$

The relationship between the projection and the 2D transform of the object function is given by substituting Eq. 9.7 in Eq. 9.6:

$$F(u,0) = F\{P_{\theta=0}\}(u) = \int_{-\infty}^{\infty} P_{\theta=0}(x)\exp(-i2\pi ux)dx. \tag{9.8}$$

Generally speaking, the Fourier transform $\tilde{P}_\theta(\mathbf{f})$ of the projection $P_\theta(x)$ is equal to the values along a line through the origin of the 2D Fourier transform of the object perpendicular to the projection direction. This is the **Fourier slice theorem** [Kak and Slaney (1989)]. In other words, the projection-slice theorem at a spatial frequency of $u = \mathbf{f}\cos$ and $v = \mathbf{f}\sin$ can be express as:

$$F\{P_\theta\}(\mathbf{f}) = \tilde{P}_\theta(\mathbf{f}) = \tilde{f}(u,v) = \tilde{f}(\mathbf{f}\cos\theta, \mathbf{f}\sin\theta). \tag{9.9}$$

9.1.2 The Filtered Back-Projection (FBP) algorithm

The Fourier reconstruction step involves the recovery of $f(x,z)$ starting from $\tilde{f}(u,v)$. By computing all the projections and the corresponding Fourier transforms for all angles $\theta(\theta_1,\theta_2.....\theta_n)$, the value of $\tilde{f}(u,v)$ can be determined on radials lines [Kak and Slaney (1989)]. If an infinite number of projections can be taken all the points in the frequency domain will be known, then the object function can be recovered directly through the inverse Fourier transform in polar coordinates $(\mathbf{f},\theta)$:

$$f(x,z) = \int_0^{\pi}\left[\int_{-\infty}^{\infty}\tilde{P}_\theta(\mathbf{f})\,|\mathbf{f}|\exp[i2\pi\mathbf{f}(x\cos\theta + z\sin\theta)]d\mathbf{f}\right]d\theta. \tag{9.10}$$

The changes of the variables from rectangular coordinates into polar coordinates are done with a Jacobian. By multiplying the Fourier transform of the projection with the frequency response of the filter given by $|\mathbf{f}|$ the high frequencies are increased [Kak and Slaney (1989)].

Eq. 9.10 gives the algorithm known in literature as the *filtered back projection* (FBP). We can reconstructed a single slice $f(x,z)$ using the above equation in an another form:

$$f(x,z) = \frac{1}{2}\int_0^{\pi} \Omega_\theta(x\cos\theta + z\sin\theta)d\theta \tag{9.11}$$

with

$$\Omega_\theta(x') = (P_\theta * h)(x') \tag{9.12}$$

where $*$ is the convolution operator and h is the reconstruction filter. The back-projection step is given by the Eq. 9.11 of the "filtered projection" $\Omega_\theta(x')$ (Eq. 9.12). The Fourier transform of the reconstruction filter has to fulfill the following condition:

$$F_1 h(A) = |A| \qquad \text{for} \qquad A \in [-a,a] \tag{9.13}$$

where $[-a,a]$ is the bandwidth interval of the projection and F_1 is the 1D Fourier transform operator. The final reconstructed image represent the sum of the back-projections of all the filtered projections for all the projection angles.

FBP gained its reputation over the years because the reconstruction time is significantly decreased compared with others methods. For this reason and for its simplicity FBP is the most used method in clinical scanners.

9.1.3 3D parallel beam FBP at ESRF

The tomography principles outlined above can be applied straightforward if a parallel X-ray beam is available. Since the ESRF (ID19) system is placed at a distance of 145m from the X-ray source, we can consider that the X-ray beam geometry is parallel.

In this thesis a parallel X-ray beam geometry set-up with a 2D detector is used as illustrated in Figure 9.4. In this case, the transition from 2D to 3D is trivial, since the X-ray beam path is straight through the object and perpendicular to the 2D detector. 2D individual reconstructions or 2D slices are given by each row of the detector and a final 3D stack is created using FBP.

At the European Synchrotron Radiation Facilities (ESRF) the standard program used for tomographic reconstruction from projection data or sinograms is *PyHST*, where the acronym "HST" means "High Speed Tomography". This program is based on the filtered back projection approach and is implemented in Python. All the information concerning PyHST can be found here `http://www.esrf.eu/computing/scientific/HST/HST_REF/hst.html`. The tomographic reconstructions performed in this manuscript are obtained with PyHST.

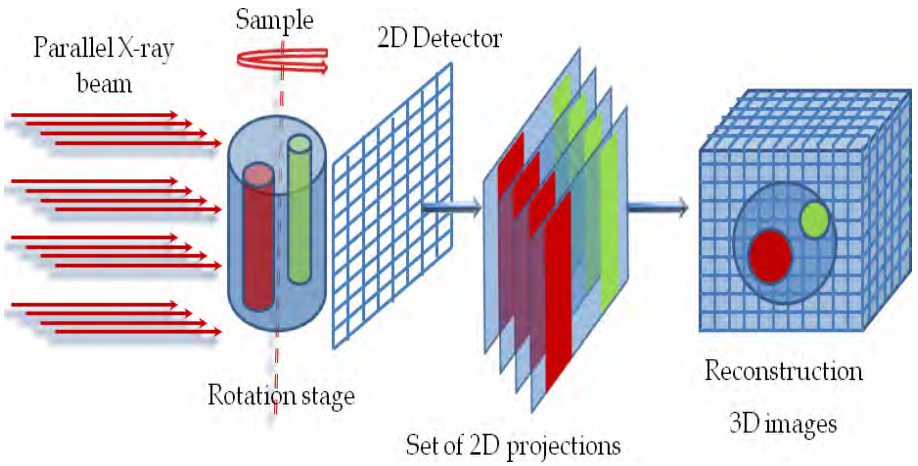

Figure 9.4: Principels of tomographic reconstruction with a parallel geometry X-ray beam.

9.1.4 Phase contrast tomography

In this section, we define the *phase contrast tomographic* reconstruction when the 2D phase contrast projections are used to generate a 3D tomographic reconstruction. These 2D phase contrast projections are acquired using the propagation based technique (Section 2.3.4).

The projection assumes flat illumination and is defined as the logarithm of the intensity measurement $I_D(\mathbf{x})$ (Eq. 3.12):

$$-\ln[I_D(\mathbf{x})] = \frac{4\pi}{\lambda}\int_{-\infty}^{\infty}\beta(x,y,z)dz - D\Big(\frac{\partial^2}{\partial x^2}+\frac{\partial^2}{\partial y^2}\Big)\int_{-\infty}^{\infty}\delta_r(x,y,z)dz. \tag{9.14}$$

The absorption and the phase shift induced by the object can be considered as projections of the absorption index (Eq. 2.24) and of the refraction index decrement (Eq. 2.25) respectively. This equation is only valid for weak absorption. The final tomographic reconstruction image is performed taking into the account these two terms using the filtered back projection method (Section 9.1.2), which is a linear operation. The 3D distribution is given by:

$$f(x,y,z) = \mu(x,y,z) + D\Big(\frac{\partial^2}{\partial x^2}+\frac{\partial^2}{\partial y^2}+\frac{\partial^2}{\partial z^2}\Big)\delta_r(x,y,z). \tag{9.15}$$

The first term is the attenuation coefficient $\mu(x,y,z)$ (Eq. 2.6) and is obtained from the absorption data acquired at sample-to-detector distance $D = 0$ m. More details about the attenuation coefficient have been presented in Section 2.2.2. The contribution of the second term is significant if there are strong variations in the refractive index decrement, such as boundaries between different phases, regime known as "edge enhancement" [Cloetens (1999)].

9.1.5 Phase tomography

As we have seen throughout this thesis, starting from a set of 2D phase contrast images it is possible to retrieve the phase of the X-ray beam. If a phase retrieval algorithm (Chapter 3) is applied over this set of 2D phase contrast projections the phase retrieval step is then performed and a phase map is obtained for each angle θ. By coupling the phase retrieval step and the tomographic reconstruction a 3D image is obtained. This two step process is called *phase tomography* and is illustrated in Figure 9.5

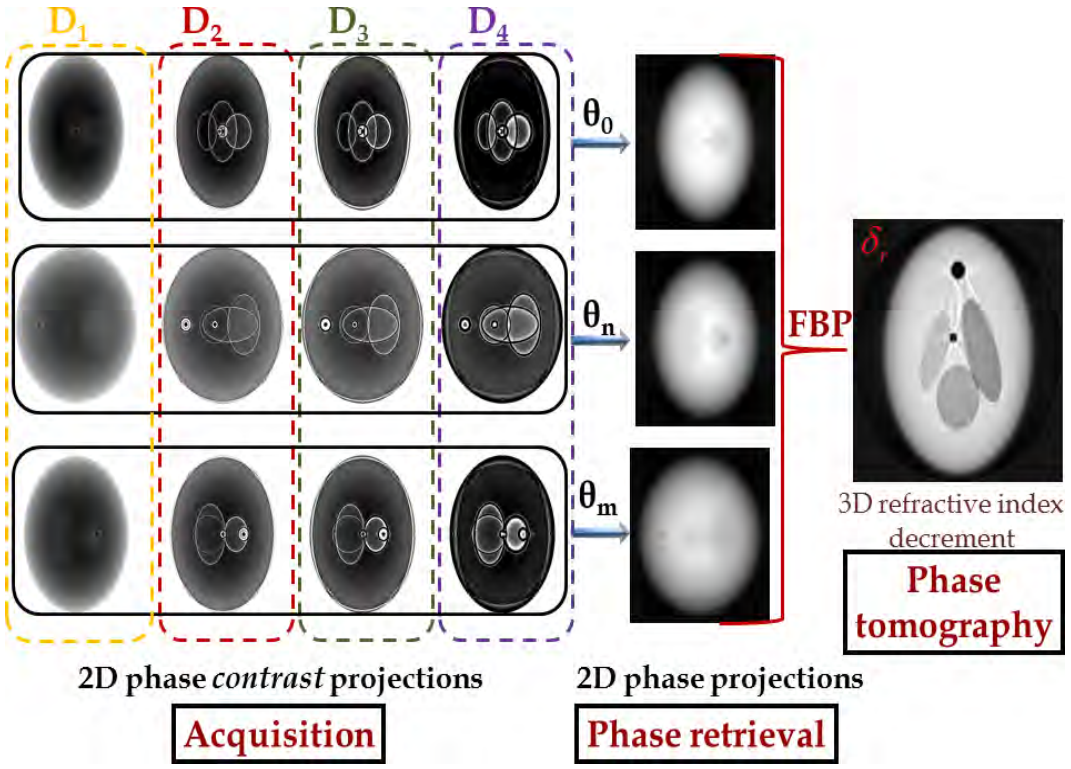

Figure 9.5: Principles of phase tomography. For each sample-to-detector distance (D_1 (blue dashed line), D_2 (red dashed line), D_3 (green dashed line) and D_4 (purple dashed line)) 2D phase contrast images are acquired. For each projection distance, the sample is rotated over minimum 180° and different 2D projection angles are considered (three angles are displayed θ_0=0°, θ_n= 15° and θ_m= 150°). For each angle θ, the phase map is retrieved using the 4 phase contrast images. Starting from these phase maps, the FBP is applied and the 3D refractive index decrement reconstruction is obtained.

9.2 Phase microtomography on simulated data

In this section we have applied the iterative nonlinear algorithm to phase tomography on simulated objects composed by soft and hard materials. The phase retrieval algorithm, based on the Landweber method with an analytic calculation of the Fréchet derivative adjoint (see Section 5.2.3), uses three phase contrast images. A quantitative analysis is performed for simulated and experimental data using the nonlinear method and the linear

mixed algorithm.

As detailed in Chapter 3, the most common algorithms for the phase retrieval problem for short propagation distances rely on the linearization of the Fresnel diffraction relationship valid under restrictive assumptions. In this section, we first summarize this new nonlinear scheme, and then details the results obtained for a tomographic reconstruction on simulated and experimental data.

The interaction of X-rays with matter can be described by the transmittance function $\mathcal{T}_\theta$ at each projection angle θ:

$$\mathcal{T}_\theta(\mathcal{X}) = \exp[-B_\theta(\mathcal{X}) + i\varphi_\theta(\mathcal{X})] = a_\theta(\mathcal{X}) \exp[i\varphi_\theta(\mathcal{X})], \tag{9.16}$$

where $a_\theta(\mathcal{X})$ is the amplitude modulation and $\varphi_\theta(\mathcal{X})$ is the phase shift induced by the object for the projection angle θ. The intensity distribution $\mathcal{I}_{D,\theta}(\mathcal{X})$ at the angle θ is calculated by the following expression:

$$I_{D,\theta}(\mathcal{X}) = |\mathcal{T}_\theta(\mathcal{X}) * \mathcal{P}_D(\mathcal{X})|^2, \tag{9.17}$$

where $*$ denotes the 2D convolution of the transmittance function $\mathcal{T}_\theta$ with the corresponding Fresnel propagator at distance D (Eq. 3.6).

In phase tomography the data sets run into thousands by thousands of pixels and thousands of projection angles. For this reason the phase retrieval approaches are based on the linearization of the Eq. 9.17 valid under the assumption that the absorption is slowly varying. The convolution from Eq. 9.17 yields the direct problem, which can be written in terms of Fourier transform (Section 3.2.6).

9.2.1 Methodology

The results of this section have been published in the following article:
V. Davidoiu, B. Sixou, M. Langer, and F. Peyrin,
"In-line phase tomography using nonlinear phase retrieval" Annals of the University of Bucharest (Mathematical Series), vol. 4 (LXII), pp. 115–122, 2013.

The purpose of this section is to extend the nonlinear algorithm based on Fréchet derivative without projection operators, presented in Section 6.3, from the radiographic case to the tomographic case.

The tomographic process consists of two steps:

1. for each projection angle θ the nonlinear approach is applied. The phase map is retrieved using as stating point the linear solution given by the mixed algorithm. The

three propagation distances are taken into account randomly during the nonlinear algorithm.

2. the filtered back projection algorithm (FBP), implemented at ESRF (PyHst) (Section 9.1.2), is applied from the whole set of phase maps φ_θ, yielding the 3D tomographic reconstruction of the refractive index decrement δ_r.

For each projection angle θ, the aim of the nonlinear approach (NL) is to minimize the regularization functional:

$$J_\alpha(\varphi_\theta) = \frac{1}{2}\|\mathcal{I}_{D,\theta}(\varphi_\theta) - \mathcal{I}^\delta_{D,\theta}\|^2_{L_2(\Omega)} + \frac{\alpha}{2}\|\varphi_\theta\|^2_{L_2(\Omega)}, \tag{9.18}$$

where $\mathcal{I}^\delta_{D,\theta}$ is the noisy intensity for the noise level δ at distance D for the projection angle θ. The minimizer of the regularization functional is calculated iteratively with a Landweber type scheme:

$$\varphi_{\theta,k+1} = \varphi_{\theta,k} - \tau_{\theta,k}\{\mathcal{I}'_{D,\theta}(\varphi_{\theta,k})^*[\mathcal{I}_{D,\theta}(\varphi_{\theta,k}) - \mathcal{I}^\delta_{D,\theta}] + \alpha\varphi_{\theta,k}\}. \tag{9.19}$$

The iterative formula is based on the explicit calculation of the Fréchet derivative of the intensity $\mathcal{I}'_{D,\theta}(\varphi_{\theta,k})$, and of its adjoint $\mathcal{I}'_{D,\theta}(\varphi_{\theta,k})^*$ (Section 5.2.2). The classical Landweber method is modified with a variable step $\tau_{\theta,k}$ chosen using a dichotomy strategy.

9.2.2 Implementation at ESRF

The nonlinear phase retrieval proposed algorithm is an iterative approach which involves important computational time. The dimension of a 2D phase contrast projection is 2048×2048 pixels. Four propagation distances are used (including the absorption) and at each of these distances 1500 phase contrast angle projections are acquired. The total number of projection used to obtain a 3D tomographic reconstruction is 6000. Taking into account that the proposed algorithm use normally minimum 5 iterations/(set phase projections) and the large volume of data a special attention was devoted to computing efficiency. The proposed method was implemented in Octave. The phase reconstructions were performed using the OAR (batch scheduler) system at the ESRF (`http://oar.imag.fr/sources/2.4/Docs/documentation/OAR-DOCUMENTATION-USER`).

9.2.3 Simulations on a Shepp-Logan phantom

The imaging system was simulated in a deterministic fashion using theoretical values of the refractive index decrement for different materials in the different regions of the Shepp-Logan phantom as in Section 6.3.2. The 3D Shepp-Logan is a classical phantom in tomography and consists of a series of ellipsoids on which the projections are based. Two phantoms were defined, one for the absorption coefficients and one for the refractive index decrement displayed in Figure 9.6. For each of the three propagation distances

(a) (b)

Figure 9.6: Central slice of the 3D Shepp-Logan phantom used in the simulations. (a) Absorption index β ($D = 0$ m) and (b) refractive index decrement δ_r.

($D = [0.035, 0.072, 0.222]$ m) 1200 angular views were used, sampled on a 2048×2048 grid and down-sampled to 512×512 pixels. The reconstructed tomographic central slices for each distance are displayed in Figure 9.7. These reconstructions are also known as phase contrast tomographic central slices and were obtained using as input in FBP the 2D phase contrast projections (see the *Acquisition* step in Figure 9.5). These central slices are obtained if the phase retrieval step is not performed. The 3D phase tomographic central slices reconstructed after retrieving the phase for each 2D phase contrast projection set are displayed in Figure 9.8 and Figure 9.9. Simulations were performed with an additive Gaussian noise with zero mean (PPSNR=12 dB) and without noise. The refractive index decrement reconstructions $\delta_r(\mathbf{x})$ can be compared directly with the theoretical refractive index decrement $\delta_r^*(\mathbf{x})$ to be recovered using the NMSE (normalized mean square error):

$$\text{NMSE} = 100 \times \left(\frac{\sum |\delta_r(\mathbf{x}) - \delta_r^*(\mathbf{x})|^2}{\sum |\delta_r(\mathbf{x})|^2} \right)^{1/2}. \tag{9.20}$$

9.2.4 Results and discussions

Figure 9.8 and Figure 9.9 show the reconstructed tomographic central slices of the refractive index decrement theoretical phantom using all the distances in the phase retrieval process. For noiseless data, Figure 9.8(a) and Figure 9.8(b) displays the reconstructed central slice of the refractive index decrement using the mixed algorithm and the nonlinear method respectively. For noisy simulated data (PPSNR=12 dB) the central slice of the 3D phantom obtained with the linear method is shown in Figure 9.9(a) and the one with the proposed algorithm in Figure 9.9(b).

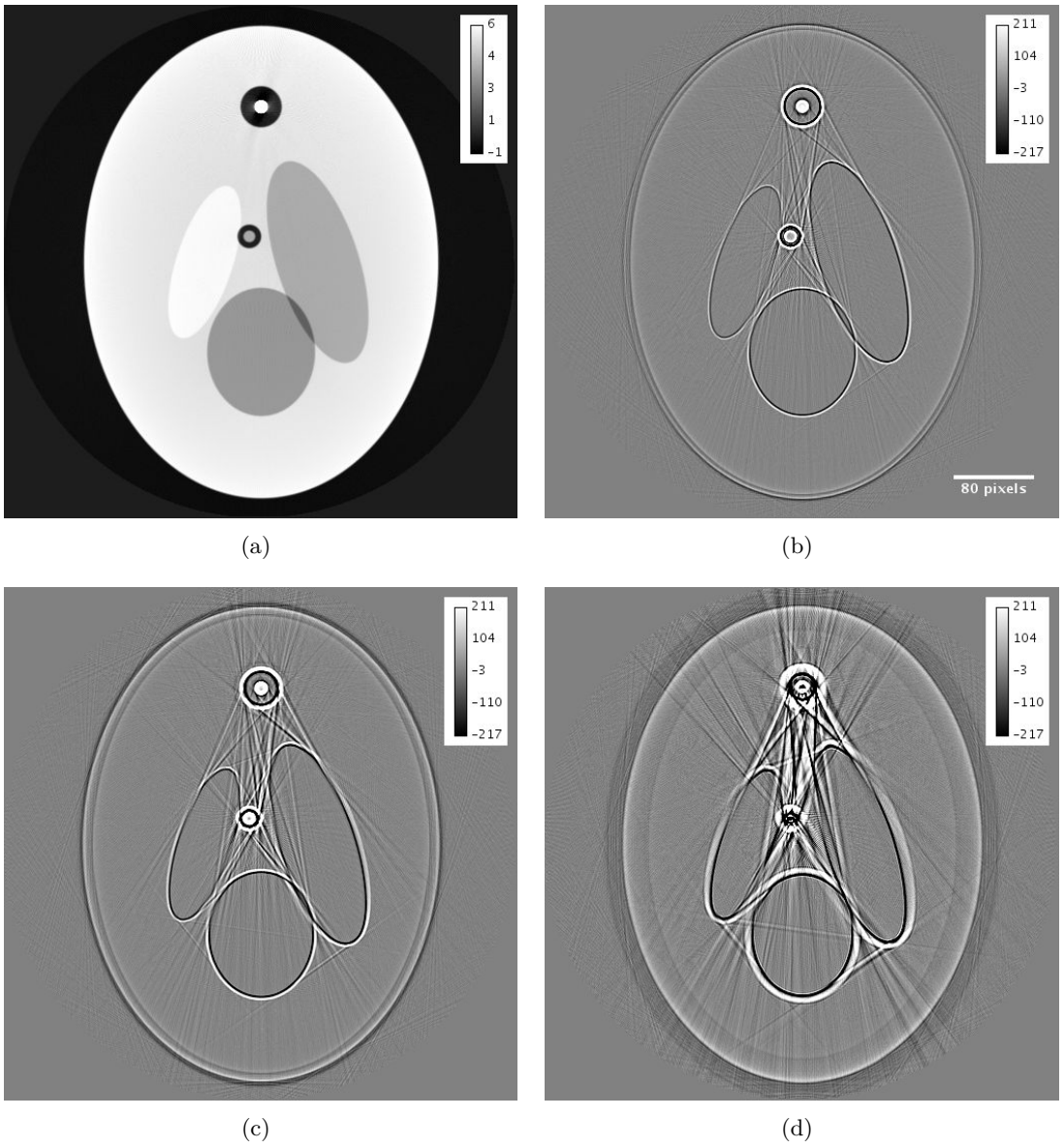

Figure 9.7: Phase contrast tomographic central slices of the reconstructed refractive index decrement using noiseless data for the Fresnel diffraction pattern at propagation distances (a) $D = 0$ m (absorption), (b) $D = 0.035$ m, (c) $D = 0.042$ m and (d) $D = 0.222$ m.

Table 9.1: The NMSE(%) values for the central slice of the reconstructed refractive index decrement.

PPSNR[dB]	Mixed [NMSE(%)]	Nonlinear [NMSE(%)]
Without noise	30.04%	**22.4**%
12 dB	38.1%	**27.1**%

The NMSE for the two compared phase retrieval methods is presented in Table 9.1, which demonstrates that the proposed nonlinear algorithm gives better results that the linear mixed algorithm. The global improvement of the proposed method compared with

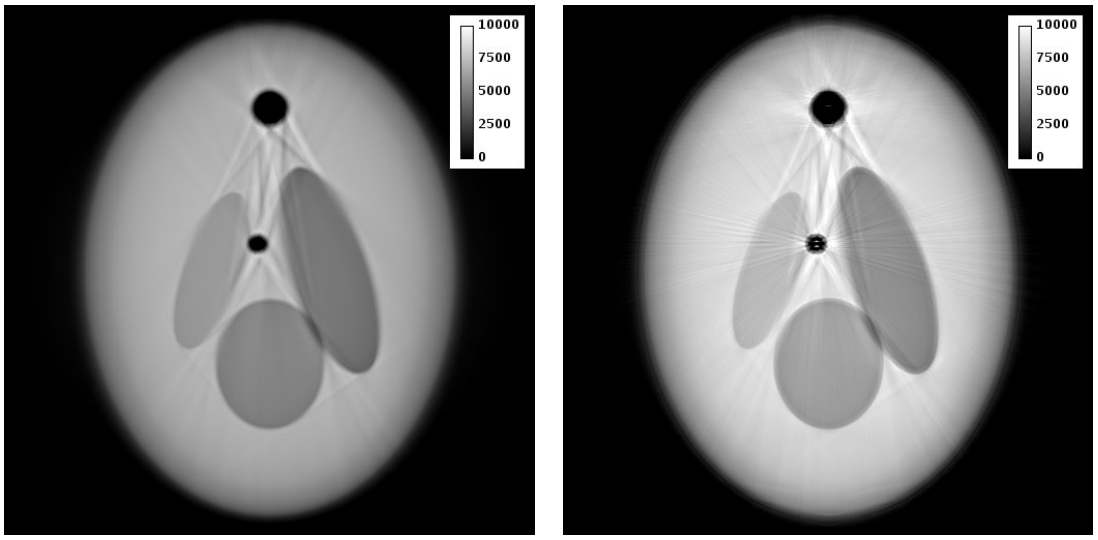

(a) (b)

Figure 9.8: Central slice of the reconstructed refractive index decrement for the simulated data without noise obtained with (a) the mixed algorithm and (b) the nonlinear method.

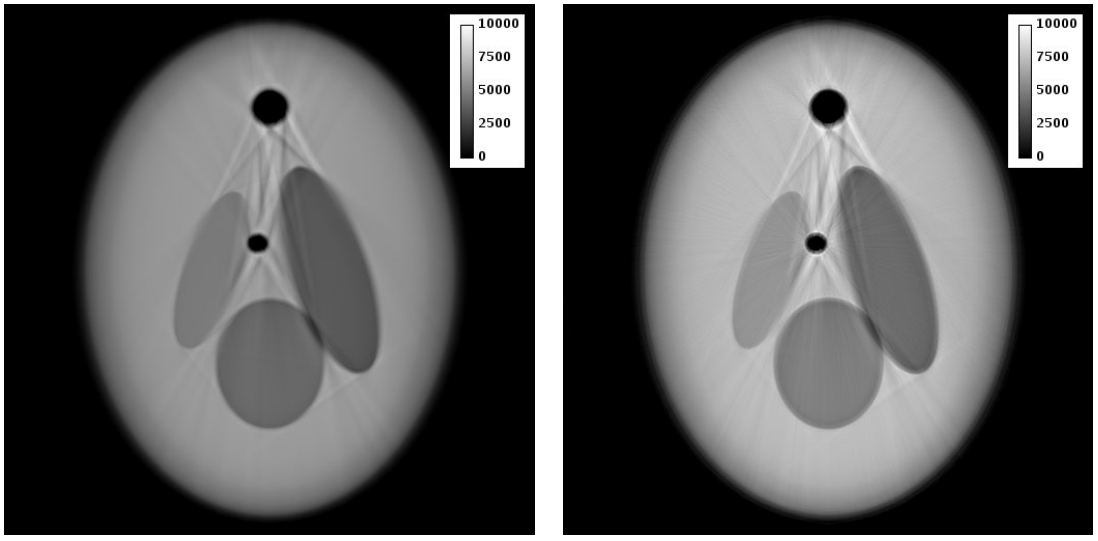

(a) (b)

Figure 9.9: Central slice of the reconstructed refractive index decrement for the simulated data with PPSNR=12 dB with (c) the mixed algorithm and (d) the nonlinear method.

the linear approach, is 25.43% for the noise-free data and 28.87% for a PPSNR of 12 dB respectively.

Figure 9.10(a) displays a comparison of the diagonal profiles obtained without noise for the central slice of the ideal refractive index decrement to be retrieved, and of the refractive index decrement maps obtained with the mixed or with the nonlinear methods. The same profiles are displayed for a PPSNR=12 dB in Figure 9.10(b). In these reconstructions is obvious that the phase algorithms are influenced by noise which show typical artifacts

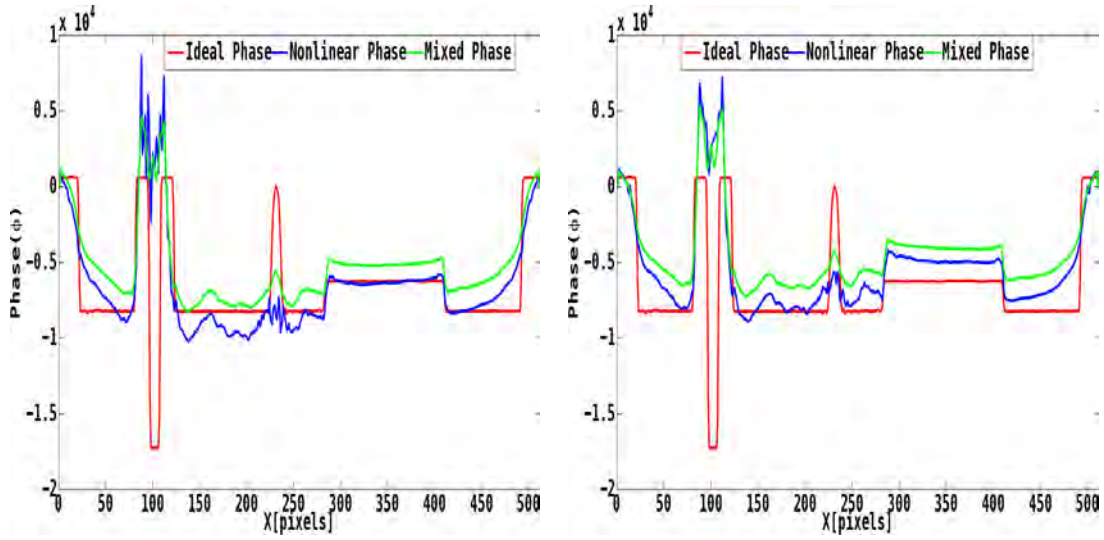

Figure 9.10: Diagonal profiles for the central slice of the reconstructed refractive index decrement for the Shepp-Logan phantom obtained with the nonlinear method for mixed initialization: (a) without noise and (b) with PPSNR=12dB.

at low-frequency. The nonlinear approach yields the most accurate phase map, but rest sensitive to noise.

9.2.5 Conclusions

The reconstruction quality for two phase retrieval methods in in-line phase tomography has been quantitatively evaluated. The phase retrieval algorithms were coupled to tomographic reconstruction scheme to compare the refractive index reconstruction errors. The first approach is the linear mixed algorithm and the second one is an iterative method based on the Fréchet derivative of the intensity. The reconstructions were compared using a simulated phantom, with and without noise, in terms of NMSE. The nonlinear method gives the best refractive index decrement reconstructions.

9.3 Phase microtomography on experimental data

9.3.1 Data acquisition

The experimental setup used is equivalent to the one for the standard propagation based technique described in [Langer *et al.* (2010)], at the beam line ID19 at the European Synchrotron Radiation Facility (ESRF). The Fresnel diffraction intensity patterns for 1500 projection angles were recorded using a FRELON CCD camera with 2048×2048 pixels for the energy 22.5keV at four short distances $D = [2; 10; 20; 45]$mm. The field of view was 1.4mm for the given pixel size 0.68μm. The multi-material object used is composed of

125μm Aluminum (Al), 200μm Polyethylene Terephthalate ($PETE$) monofilaments and 20μm of Alumina (Al_2O_3) wires. Phase retrieval with the mixed approach was applied without any prior on δ_r/β [Guigay *et al.* (2007)] (initialization (A)) and with $\delta_r/\beta = 367$ [Langer *et al.* (2010)] corresponding to aluminium (initialization (B)).

The reconstructed projections for the angle of view $\theta = 120°$ retrieved with the mixed algorithms in these two cases are displayed in Figure 9.11(a) and in Figure 9.11(b), respectively. The nonlinear phase map obtained for the initialization map given in Figure 9.11(a) is shown in Figure 9.11(c). Figure 9.11(d) displays the phase retrieved with NL with the starting point given by the linear solution displayed in Figure 9.11(b). Starting from these images the FBP is applied and the 3D refractive index decrement δ_r is reconstructed.

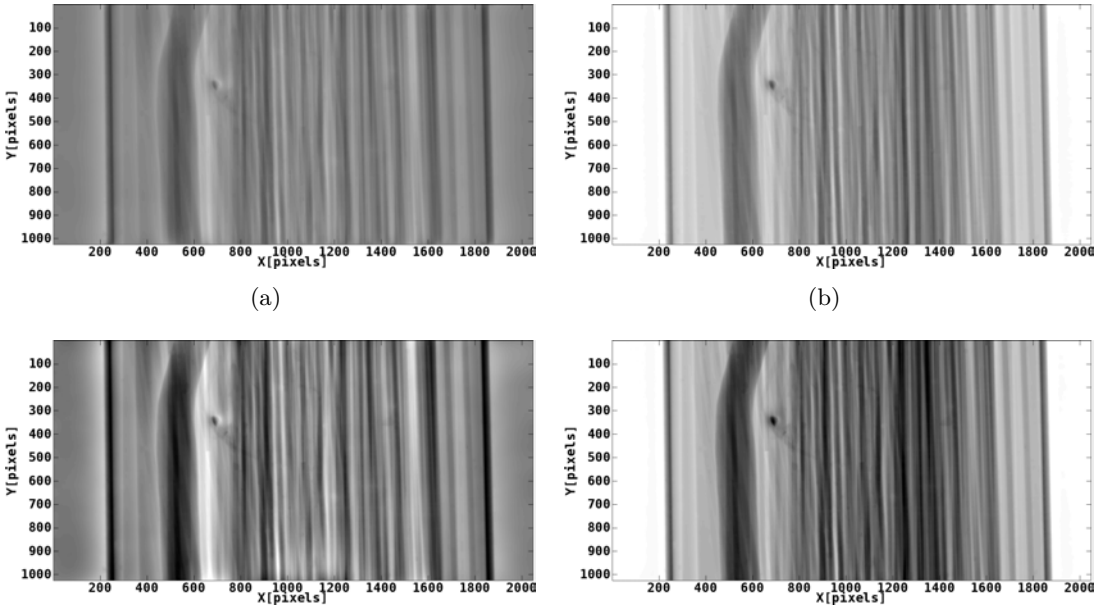

Figure 9.11: Projection images corresponding to the angle of view 120° obtained after the phase retrieval step with the mixed algorithm (a) without a priori information [Guigay *et al.* (2007)] and (b) with $\delta_r/\beta = 367$ (Al) [Langer *et al.* (2010)]. The projections obtained using NL initialized with these mixed solutions are displayed in (c) and (d) respectively. Gray-scale windows in (a), (c) is $[-30\ 30]$ and in (b), (d)

The tomographic central slices of the refractive index decrement, in the case of the mixed algorithm with a standard Tikhonov regularization without any a priori knowledge on the ratio δ_r/β, is displayed in Figure 9.12(a). The corresponding central slice obtained with the nonlinear approach initialized with this linear phase solution is shown in Figure 9.12(c). In order to have a quantitative estimate of the reconstruction errors, the theoretical values for $2\pi\delta_r/\beta$ and the values estimated with the linear algorithm or with the nonlinear approach are summarized in Table 9.2. The tomographic central slice obtained with the mixed approach is displayed in Figure 9.12(a), the corresponding reconstruction using this linear initialization is shown in Figure 9.12(c). In this case the reconstructed

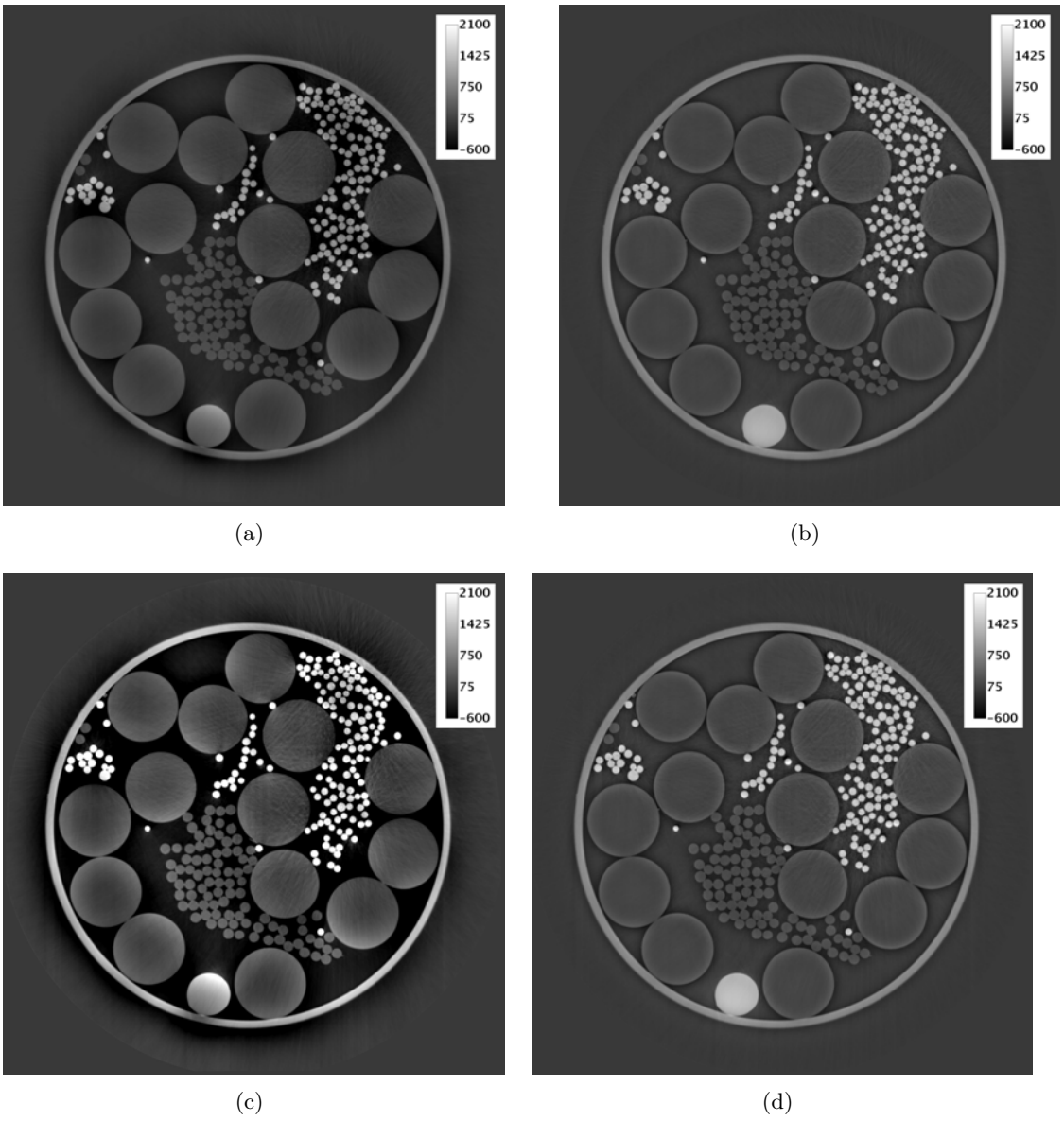

Figure 9.12: Tomographic central slice reconstructed with the mixed algorithm (a) without a priori information [Guigay *et al.* (2007)] and (b) with a priori information $\delta_r/\beta = 367$ (corresponding to aluminum) [Langer *et al.* (2010)]. Corresponding central slice obtained with the nonlinear algorithm initialized with the linear solution (c) without a priori (initialization displayed in (a)) and (d) with a priori information $\delta_r/\beta = 367$ (initialization displayed in (b)).

refractive index decrement obtained with NL algorithm is better estimated in all the components of the sample (Table 9.2). In Table 9.3 the relative standard deviations (RSD[%]) and the normalized errors (NE[%]) for the four component materials have been measured for all reconstructions approaches. The RSD and the NE values were measured using:

$$\mathrm{RSD} = 100 \times \frac{\mathrm{SD}}{\left(\frac{2\pi\delta_r}{\lambda}\right)_{\mathrm{measured}}} \tag{9.21}$$

and

$$\mathrm{NE} = 100 \times \frac{(\frac{2\pi\delta_r}{\lambda})_{\text{theoretical}} - (\frac{2\pi\delta_r}{\lambda})_{\text{measured}}}{(\frac{2\pi\delta_r}{\lambda})_{\text{theoretical}}}, \tag{9.22}$$

where SD represent the standard deviation, $(\frac{2\pi\delta_r}{\lambda})_{\text{theoretical}}$ the theoretical value to be obtained and $(\frac{2\pi\delta_r}{\lambda})_{\text{measured}}$ the measurements (given in Table 9.2). The theoretical values $(\frac{2\pi\delta_r}{\lambda})_{\text{theoretical}}$ were obtained using the tabulated values in the XOP software [Sanchez del Rio and Dejus (2004)]. The standard deviation SD was measured using *ImageJ* and is defined as:

$$\sigma = \sqrt{\frac{1}{N}\sum_{i=1}^{N}(x_i - \mu)^2} \tag{9.23}$$

where

$$\mu = \frac{1}{N}\sum_{i=1}^{N} x_i. \tag{9.24}$$

and each value $x_1, x_2, x_3, ..., x_N$ has the same probability.

Table 9.2: Theoretical and measured values with different algorithms

	Al	Al_2O_3	PETE	PP
$\left(\frac{\delta_r}{\lambda}\right)_{\text{theoretical}}$	367	570	2203	2930
$\left(\frac{2\pi\delta_r}{\lambda}\right)_{\text{theoretical}}$	1220	1793	701.7	408.5
$\left(\frac{2\pi\delta_r}{\lambda}\right)_{\text{measured}}$ ± SD with (A) mixed, no prior	553.43±221.92	934.92±199.45	101.11±74.99	154.61±65.58
$\left(\frac{2\pi\delta_r}{\lambda}\right)_{\text{measured}}$ ± SD with NL, initialization (A)	1184.77±470.37	2000.23±431.02	219.28±158.92	333.72±139
$\left(\frac{2\pi\delta_r}{\lambda}\right)_{\text{measured}}$ ± SD with (B) mixed $\frac{\delta_r}{\lambda}$=367	1204.22±61.10	1313±116.33	149.79±56.78	190.79±45.75
$\left(\frac{2\pi\delta_r}{\lambda}\right)_{\text{measured}}$ ± SD with NL, initialization (B)	1351.2 ±69.66	1473.99±131.84	169.83± 63.18	215.81±50.85

Table 9.3: Values for relative standard deviation (RSD) and normalized error (NE) obtained with different algorithms

	Al		Al_2O_3		PETE		PP		**TOTAL**	
	%NE	%RSD	%NE	%RSD	%NE	%RSD	%NE	%RSD	%NE	%RSD
(A) mixed, no prior	-54.63	40.1	-47.85	21.33	-85.59	74.16	-62.14	42.41	62.55	44.5
NL, initialization (A)	-2.88	39.7	11.55	21.54	-68.74	72.47	-18.30	41.65	25.36	43.8
(B) mixed $\frac{\delta_r}{\lambda}$=367	-1.29	5.07	-26.75	8.85	-78.65	37.90	-53.29	23.97	39.99	18.95
NL, initialization (B)	10.75	5.15	-17.79	8.94	-75.79	37.2	-47.17	23.56	37.87	18.7

The proposed approach reduces the global error in the reconstructed materials compared to the two linear initialization solutions. For most materials, the lowest error values are obtained by the nonlinear algorithm. Moreover, the total values of the normalized errors (Table 9.3) have been improved by the nonlinear algorithm. Nevertheless, most materials are underestimated (minus sign of NE in Table 9.3) which can also be related to imperfection of the detector not taken into account in this study.

If the a priori ratio is not included in the initialization algorithm the proposed approach reduces the total NE% by 6%. In the case, where the exact value of the a priori ratio is not known, which is the case for biomedical samples, this result shows that the nonlinear

algorithm is an interesting extension of the mixed approach. If the a priori information corresponding to *Al* is introduced in the phase shift, the mixed algorithm [Langer *et al.* (2010)] yields the central slice displayed in Figure 9.12(b). Comparing this reconstruction (Figure 9.12(b)) with that one where the a priori was not introduced (Figure 9.12(a)) in the mixed method, it can be observed that low-frequency noise artifacts are alleviated. Yet, the nonlinear solution retrieved using as starting point the linear solution with $\delta_r/\beta = 367$ provides more accurate reconstructions (Figure 9.12(d)). In this case the NE[%] value corresponding to Al is overestimated with the proposed nonlinear method, but the NE[%] for Al_2O_3 is reduced with 33.5% (Table 9.3).

The error maps between the compared methods are shown in Figure 9.13 to further illustrate the interest of the nonlinear method, initialized with the mixed algorithm with an a priori value of δ_r/β.

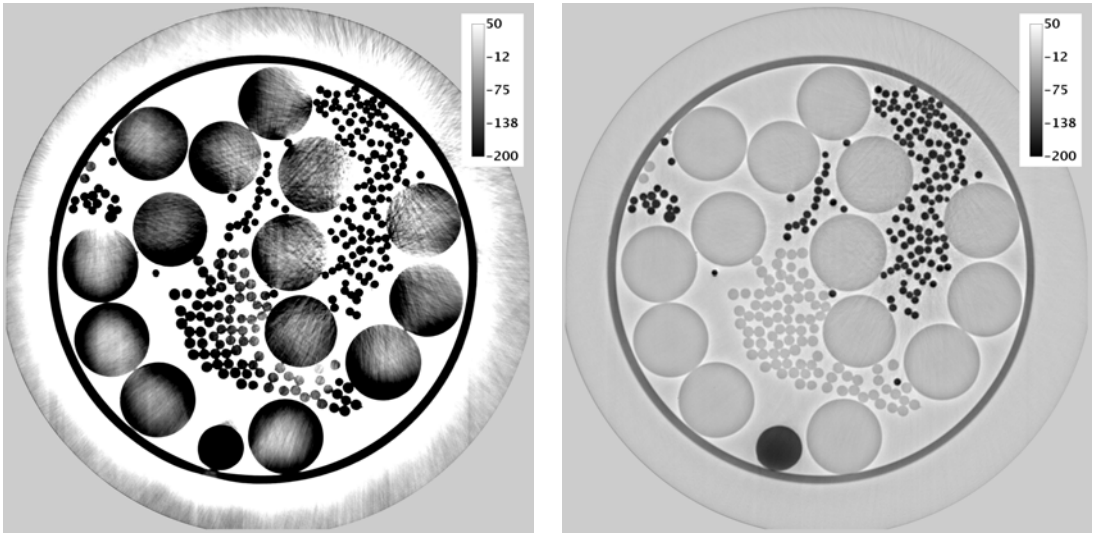

(a) (b)

Figure 9.13: Error map of the tomographic central slice obtained (a) between the mixed solution without a priori [Figure 9.12(a)] and the corresponding nonlinear tomographic map [Figure 9.12(c)] and (b) between the mixed map including the a priori ratio of $\delta_r/\beta = 367$ [Figure 9.12(b)] and the nonlinear reconstruction obtained using this initialization [Figure 9.12(d)] .

9.3.2 Conclusions

We have proposed a nonlinear phase retrieval method for phase tomography in Fresnel space. The method has been evaluated quantitatively from experimental data acquired at three different propagation distances on a synchrotron X-ray micro-CT setup. The proposed method decreases globally the reconstruction errors compared to the mixed algorithm applied with various priors [Guigay *et al.* (2007), Langer *et al.* (2010)]. Then, the results suggest that the refractive index decrement for a non homogeneous object can

be retrieved more exactly if the nonlinearity of the phase problem is taken into account. Though the linear solution is necessary for the initialization of the algorithm.

Conclusions et perspectives

La mise au point des synchrotrons de troisième génération a ouvert la possibilité de développer de nouvelles techniques d'imagerie par rayons X basées sur l'imagerie de contraste de phase. Le couplage de ces techniques avec la micro-tomographie par rayons X (μCT) améliore la sensibilité de plusieurs ordres de grandeur. La relation entre le décalage de phase induit par un échantillon et l'intensité enregistrée à une distance échantillon-détecteur donnée repose sur la théorie de la diffraction de Fresnel. L'information de phase à partir d'un champ d'onde diffracté n'est pas explicitement enregistrée dans l'intensité mesurée et doit être extraite à partir des diagrammes de diffraction de Fresnel. Ce processus est connu sous le nom d'estimation de phase et il peut être couplé également à la tomographie.

Dans la littérature, plusieurs méthodes d'estimation de phase ont été proposées. Ces approches reposent sur la linéarisation de la relation phase-intensité et sont valables sous certaines hypothèses restrictives, entraînant ainsi quelques approximations du problème direct de la formation de l'image de contraste de phase (Chapitre 3). Les méthodes linéaires les plus courantes sont: l'équation de transport de l'intensité (TIE) (Section 3.2.1), la fonction de transfert de contraste (CTF) (Section 3.2.5), ou l'approche mixte (Section 3.2.6). Malgré certaines limitations, en raison de la linéarisation du problème direct, ces méthodes ont trouvé de nombreuses applications dans la pratique.

Ces approches linéaires peuvent être affinées par d'autres méthodes qui tiennent compte de la non linéarité du problème de phase. Toutefois, les effets de la non linéarité n'ont pas été beaucoup étudiés dans la littérature, jusqu'à récemment, lorsque de nouvelles approches non linéaires ont été proposés pour le cas radiographique [Moosmann *et al.* (2010), Moosmann *et al.* (2011)] et le cas tomographique [Hofmann *et al.* (2011), Langer *et al.* (2012)b, Moosmann *et al.* (2013)].

L'objectif principal de ce travail était de proposer et d'évaluer de nouveaux algorithmes, en tenant compte de la non linéarité du problème direct. Nos travaux se sont basés sur la dérivée de Fréchet de la relation entre la phase et l'intensité à des distances différentes de propagation. L'objectif était de développer un nouveau modèle mathématique utilisant comme initialisation les solutions de phase linéaire afin d'améliorer la résolution et réduire le bruit à basse fréquence. Plusieurs types de régularisation ont été étudiés.

Nous avons proposé plusieurs schémas itératifs pour résoudre le problème de l'estimation de phase non linéaire. Toutes ces approches utilisent un type d'itération Landweber pour minimiser la fonctionnelle de régularisation et la dérivée de Fréchet de l'opérateur intensité. Afin de surmonter des difficultés de temps de calcul et une trop grande exigence de taille mémoire pour les calculs avec des différences finies, la dérivée de Fréchet et son adjoint ont été calculées de manière analytique (Section 5.2). En nous basant sur des données simulées, nous avons comparé dans la 5.2.4, la convergence de plusieurs algorithmes

basés sur le gradient calculé avec différence finie ou sur l'expression analytique du gradient. Dans ce cas, le problème inverse est régularisé avec la norme L_2 du gradient de la phase. Les meilleurs résultats ont été obtenus en utilisant l'expression analytique du gradient, lorsque les distances sont prises en compte de façon cyclique. Cette méthode a été affinée en utilisant des opérateurs de projection sur des ensembles convexes ou non convexes comme dans les algorithmes proposés par Fienup (Section 6).

Dans la section 6.3, l'algorithme non linéaire a été testé sur un fantôme plus complexe. Le terme de régularisation avec le carré du gradient de la phase (Chapitre 5) est remplacé par le terme de régularisation de Tikhonov classique avec la norme L_2 de la phase. Ce type de régularisation utilisant aussi les opérateurs de projections a été évalué sur le fantôme Shepp-Logan pour trois initialisation par les solution linéaires: TIE, CTF et l'approche mixte. Trois distances de propagation ont été utilisées d'une manière aléatoire. La qualité de la reconstruction pour la projection du fantôme 3D Shepp-Logan a été évaluée quantitativement pour des phases variables présentant des variations fortes ou faibles. L'évaluation de la méthode a été réalisée en utilisant des données simulées, avec et sans bruit. Les cartes de phase récupérées avec les algorithmes non linéaires et linéaires ont été comparées en termes d'erreur quadratique moyenne normalisée. Pour la phase fortement variable et des données bruitées la méthode non linéaire surpasse les méthodes linéaires.

Afin d'améliorer la reconstruction de basse fréquence de la phase, une régularisation parcimonieuse a été proposée dans la section 8.1. Tout d'abord, une solution itérative du problème linéaire en coordonnées ondelettes est obtenue en utilisant la norme de régularisation l_1. Cette approche a été évaluée pour des données bruitées, en utilisant une seule distance de propagation. Ensuite, la méthode d'estimation de phase non linéaire avec la dérivée de Fréchet de l'intensité et des opérateurs de projection (Partie II) a été combinée avec l'algorithme de seuillage de type Landweber en coordonnées ondelettes (Section 8.1). La méthode combinée (WNL) donne de meilleurs résultats que les méthodes linéaires, l'approche non linéaire sans projections et sans le traitement en coordonnées ondelettes (Section 8.2).

Une comparaison entre l'algorithme WNL et une méthode itérative de type point fixe basée sur une fonction de substitution utilisée pour minimiser la fonctionnelle de régularisation, appelé ici RTS (Ramlau et Teschke Schéma) a été effectuée dans la section 8.3.2. Le but de cette comparaison était d'évaluer quantitativement plusieurs approches linéaires et non linéaires basées sur Tikhonov ou des régularisations de type parcimonieux pour l'estimation de phase en ligne en utilisant une seule image de contraste de phase. Nos résultats indiquent que l'approche WNL est meilleure et plus robuste au bruit que le Ramlau et Teschke Schéma (RTS), qui est une méthode générale pour des problèmes non linéaires avec une régularisation parcimonieuse.

Dans la dernière partie de ce manuscrit, les reconstructions tomographiques pour des

données simulées et expérimentales ont été effectuées en utilisant le schéma itératif non linéaire proposé pour le cas radiographique dans la section 6.3 avec et sans bruit. Avec l'algorithme itératif non linéaire, les erreurs de reconstruction tomographique de la coupe centrale finale sont diminuées.

Les perspectives concernant ce travail sont les suivantes. Un aspect important est le choix automatique du paramètre de régularisation. Il est bien connu que le paramètre de régularisation joue un rôle crucial dans la convergence des méthodes itératives, par conséquent, il doit être choisi avec soin. Dans toutes les études de ce travail, les valeurs petites et grandes des paramètres conduisant à de mauvais résultats de la reconstruction sont d'abord choisies. Ensuite, la valeur optimale du paramètre de régularisation est progressivement affinée par essais, avec un intervalle décroissant. Plusieurs systèmes ont été étudiés récemment pour le choix du paramètre de régularisation pour les problèmes non linéaires, fondés sur des approches de type bayesienne. Il pourrait être intéressant de tester ces méthodes sur des données simulées ou réelles. Lors de la reconstruction tomographique, la valeur du paramètre de régularisation a été fixée. Elle est identique pour toutes les projections. Il est possible qu'en faisant varier ce paramètre de régularisation en fonction de l'angle de projection, une reconstruction plus précise sera atteinte.

Des améliorations significatives par rapport aux méthodes linéaires pour les reconstructions de phase dans le cas radiographique pour les données simulées ont été obtenues. Nous pouvons observer que ces améliorations, en termes d'erreur quadratique moyenne normalisée, sont réduites lorsque la reconstruction tomographique est effectuée. Une perspective importante pour ce travail est la mise en oeuvre de notre algorithme WNL pour le cas tomographique avec des applications à l'imagerie d'échantillons biomédicaux à l'ESRF. Il sera aussi possible de développer d'autres algorithmes qui incluent l'a priori que le rapport phase/absorption (δ_r/β) est constant par morceaux dans le cas radiographique ou le cas tomographique. Enfin, une perspective intéressante est l'étude de la reconstruction conjointe de la phase et de l'absorption qui soulève un problème encore plus mal posé mais qui aurait une implication pratique importante.

Chapter 10

Conclusions and perspectives

The availability of third-generation synchrotrons has opened the possibility to develop new X-ray imaging techniques based on phase contrast imaging. Coupling these techniques with X-ray microtomography (μCT) the sensitivity is improved by several orders of magnitude. The relationship between the phase shift induced by a sample and the intensity recorded at a sample-to-detector distance D relies on Fresnel diffraction theory. The phase information from a diffracted wave field is not explicitly recorded in the measured intensity and must be extracted from the Fresnel diffraction patterns. This process is known as phase retrieval and it may be coupled also to tomography.

In the literature, various phase retrieval methods have been proposed. These approaches rely on the linearization of the relation phase-intensity and are valid under some restrictive assumptions, thus involving some approximations of the direct problem of phase contrast image formation (Chapter 3). The most common linear methods are: Transport Intensity Equation (TIE) (Section 3.2.1), the Contrast Transfer Function (CTF) (Section 3.2.5), or mixed approach (Section 3.2.6). Despite some limitations, due to the linearization of the direct problem, these methods have found various applications in practice.

These linear approaches can be refined by other methods which take into account the nonlinearity of the phase problem. However, the effects of the nonlinearity have not been much investigated in the literature until recently, when new nonlinear schemes have been proposed for the radiographic case [Moosmann *et al.* (2010), Moosmann *et al.* (2011)] and the tomographic case [Hofmann *et al.* (2011), Langer *et al.* (2012)b, Moosmann *et al.* (2013)].

The main purpose of this work was to propose and evaluate new algorithms, taking

into account the nonlinearity of the direct problem. These methods are based on the Fréchet derivative of the phase-intensity relationship at different propagation distances. The objective was to develop a new mathematical model using as input the linear phase solutions in order to improve the resolution and decrease low frequency noise. Several types of regularization have been investigated.

For simulated data, we have proposed several iterative schemes to solve the nonlinear phase retrieval problem. All these approaches use a Landweber type algorithm to minimize the regularization functional and are based on the Fréchet derivative of the intensity operator. In order to overcome the long computation time and large memory requirement of calculations with finite differences, the Fréchet derivative and its adjoint were calculated in an analytical way (Section 5.2). We have compared in Section 5.2.4, the convergence rates for several algorithms based on the finite differences gradient or on the analytic expression of the gradient. In the later case, the inverse ill-posed problem is regularized with the smoothing L_2 norm of the phase gradient. The best results have been obtained using the analytic expression of the gradient, when the distances are taken into account in a cyclical way. This method has been refined by using projection method on convex or non-convex sets as in the Fienup algorithms (Section 6).

In Section 6.3, the nonlinear algorithm is has been tested on a more realistic phantom. The regularization term with the square of the gradient phase term (Chapter 5) was replaced by the classical Tikhonov regularization term with the L_2 norm of the phase. This type of regularization using Fienup like projections operators has been evaluated on the 3D Shepp-Logan phantom for three linear starting points chosen as the solutions provided by the linear methods, TIE, CTF and mixed approach. Three propagation distances were used in a random way. The reconstruction quality for a projection of a 3D Shepp-Logan phantom has been quantitatively evaluated for strongly and weakly varying phases. The evaluation of the method was performed using simulated data, both with and without noise. The phase maps retrieved with the nonlinear and linear algorithms were compared in terms of NMSE (normalized mean square error). For the strongly varying phase and the noisy data the nonlinear method outperforms the linear methods.

In order to improve the low frequency reconstruction of the phase, a sparse regularization has been proposed in Section 8.1. An iterative solution of the linear problem in orthogonal wavelets coordinates is obtained using the l_1 norm regularization. This approach has been evaluated for noisy data, using a single propagation distance. Moreover, the nonlinear phase retrieval method with the Fréchet derivative of the intensity and projection operators (Part II) was combined with the iterative thresholded Landweber algorithm in wavelet coordinates (Section 8.1). The combined method (WNL) outperforms the linear methods, the nonlinear one without projections and without the wavelet treatment (Section 8.2).

A comparison between the WNL and a fixed point iterative method based on a surro-

gate functional used to minimize the regularization functional, called here RTS (Ramlau and Teschke Scheme) has been performed in Section 8.3.2. The aim of this comparison was to evaluate quantitatively several linear and nonlinear approaches based on Tikhonov or sparse regularizations for in-line phase retrieval using only one contrast-image. Our results indicate that the WNL approach performs better and is more robust to noise that the Ramlau and Teschke Scheme (RTS), which is a general method for nonlinear problems with a sparsity regularization.

In the last part of this manuscript, the tomographic reconstruction for simulated and experimental data has been performed using the nonlinear iterative scheme proposed for the radiographic case in Section 6.3 with and without additional noise. The results show that the global reconstruction error in the tomographic phase image is decreased with the nonlinear iterative algorithm.

There are several perspectives to this work. An important one is the automatic choice of the regularization parameter. It is well known that the regularization parameter plays a crucial role in the convergence of the iterative methods, therefore it has to be chosen carefully. In all the studies of this work, large and small values of the parameters leading to poor reconstruction results are first chosen. Then, the optimal value of the regularization parameter is gradually refined by trial-and-error with a decreasing interval. Several schemes have been investigated recently for the choice of the regularization parameter for nonlinear problems, based on a bayesian approach. It could be interesting to test these methods on simulated or real data. During the tomographic reconstruction, the value of the regularization parameter was fixed and had the same value for all the projections. Maybe, by choosing a specific value of the regularization parameter for set of intensity measurements for each projection angle θ and by varying this initial value during the iterations as a function of noise a more accurate reconstruction will be achieved.

Another important perspective of this work is also the implementation of our WNL algorithm for the tomographic case.

Significant improvements over the linear methods for the reconstructed phase maps in the radiographic case for simulated data have been obtained. We can observe that these improvements, in terms of normalized mean square error (NMSE), are reduced when the tomographic reconstruction is performed. By introducing priors like TV-norm in the object domain, which are not appropriate to apply in the projection domain, we could try to improve the tomographic reconstruction.

This work demonstrating the potential of nonlinear refinements in phase retrieval schemes open many perspectives and should be further evaluated in various applications in biomedical imaging at ESRF.

List of publications

Peer-reviewed Journal Articles

- V. Davidoiu, B. Sixou, M. Langer, and F. Peyrin, **"Non-linear iterative phase retrieval based on Frechet derivative", OSA, Optics Express**, vol. 19, No. 23, pp. 22809-22819, 2011.
  - Selected by the Editors, Andrew Dunn and Anthony Durkin, for publication in **Virtual Journal for Biomedical Optics (VJBO)**, vol. 7(1), pp. 22809, 2012.
- V. Davidoiu, B. Sixou, M. Langer, and F. Peyrin, **"Nonlinear phase retrieval and projection operator combined with iterative wavelet thresholding", IEEE Signal Processing Letters (SPL)**, vol. 19, No. 9, pp. 579 - 582 ,2012.
- B. Sixou, V. Davidoiu, M. Langer, and F. Peyrin, **"Absorption and phase retrieval in phase contrast imaging with nonlinear Tikhonov regularization and joint sparsity constraint regularization", Inverse Problem and Imaging (IPI)**, vol. 7, No. 1, pp. 13, 2013.
- V. Davidoiu, B. Sixou, M. Langer, and F. Peyrin, **"In-line phase tomography using nonlinear phase retrieval", Annals of the University of Bucharest (Mathematical Series)**, vol. 4(LXII), pp. 115–122, 2013.
- V. Davidoiu, B. Sixou, M. Langer, and F. Peyrin, **"Nonlinear approaches for the single-distance phase retrieval problem involving regularizations with sparsity constraints", OSA, Applied Optics**, vol. 52, No. 17, pp. 3977 - 3986, 2013.
- V. Davidoiu, B. Sixou, M. Langer, and F. Peyrin, **"Nonlinear phase tomography using Fréchet derivative", OSA, Optics Letters**, submitted, July 2013.
- B. Sixou, V. Davidoiu, M. Langer, and F. Peyrin, **"Simultaneous reconstruction of absorption and phase from a single-distance Fresnel diffraction pattern", IEEE Signal Processing Letters (SPL)**, submitted, April 2013.

Conference Proceedings

- B. Sixou, V. Davidoiu, M. Langer, and F. Peyrin, **"Non-linear phase retrieval from Fresnel diffraction patterns using the Frechet derivative", IEEE International Symposium on Biomedical Imaging - ISBI2011**, Chicago, USA, pp. 1370-1373, 2011.

- V. Davidoiu B. Sixou, M. Langer, and F. Peyrin, **"Restitution de phase par seuillage itératif en ondelettes", GRETSI2011**, Bordeaux, 2011.

- V. Davidoiu, B. Sixou, M. Langer, and F. Peyrin, **"Non-linear iterative phase retrieval based on Frechet derivative and projection operators", IEEE International Symposium on Biomedical Imaging - ISBI2012**, Barcelona, Spain, pp. 106-109, 2012.

- V. Davidoiu, B. Sixou, M. Langer, and F. Peyrin, **"Non-linear phase retrieval combined with iterative thresholding in wavelet coordinates", 20th European Signal Processing Conference - EUSIPCO2012**, Bucharest, Romania, pp. 884-888, 2012.

- V. Davidoiu, B. Sixou, M. Langer, et F. Peyrin,**"Reconstruction non linéaire de la phase avec operateurs de projection combinée avec un seuillage itératif en ondelettes", XIeme CFR de Mathématiques Appliquées**, Romania, Bucarest, pp. 70-71, 2012.

- B. Sixou, V. Davidoiu, M. Langer, and F. Peyrin, **"Absorption and phase retrieval in phase contrast imaging with non linear Tikhonov regularization", New Computational Methods for Inverse Problems - NCMIP2012**, Paris, France, 2012.

- V. Davidoiu, B. Sixou, M. Langer, et F. Peyrin, **"Reconstruction non linéaire itératif des images de phase en rayons X", Imagerie du vivant**, France, Lyon, 2012.

- V. Davidoiu, B. Sixou, M. Langer, et F. Peyrin, **"Nonlinear phase retrieval in hard X-rays projections", International Workshop DROITE**, Lyon, France, 2012.

- B. Sixou, V. Davidoiu, M. Langer, and F. Peyrin, **"Level-set regularization for nonlinear absorption and phase retrieval and in X-rays phase contrast tomography, IEEE International Symposium on Biomedical Imaging - ISBI2013**, San Francisco, USA, 2013.

Bibliography

[Alifanov *et al.* (1995)] Alifanov, O. M., Artyukhin, E. A., and Rumyantsev, S. V. (1995). *Extreme methods for solving ill-posed problems with applications to inverse heat transfer problems.* Begell House Inc., New York, USA.

[Allen and Oxley (2001)] Allen, L. J. and Oxley, M. P. (2001). Phase retrieval from series of images obtained by defocus variation. *Opt. Comm.*, 199:65–75.

[Als-Nielsen and McMorrow (2010)] Als-Nielsen, J. and McMorrow, D. (2010). *Elements of modern X-ray physics.* John Wiley & Sons Inc., England.

[Bakushinsky (1992)] Bakushinsky, A. B. (1992). The problem of the convergence of the iteratively regularized Gauss-Newton method. *Comput. Math. Math. Phys.*, 32:1353–1359.

[Bakushinsky and Smirnova (2005)] Bakushinsky, A. B. and Smirnova, A. (2005). On application of generalized discrepancy principle to iterative methods for nonlinear ill-posed problems. *Numer. Funct. Anal. Optm.*, 26:5–48.

[Barty *et al.* (1998)] Barty, A., Nugent, K. A., Paganin, D., and Roberts, A. (1998). Quantitative optical phase microscopy. *Opt. Lett.*, 23:817–819.

[Baruchel *et al.* (2000)] Baruchel, J., Buffière, J., Maire, E., Merle, P., and Peix, G. (2000). *X-Ray tomography in material science.* Hermes Science Publication, Paris, France.

[Baruchel *et al.* (2006)] Baruchel, J., Buffière, J., Cloetens, P., Di Michiel, M., Ferrie, E., Ludwig, W., Maireb, E. and Salvo, L. (2006). Advances in synchrotron radiation microtomography. *Scripta Mater.*, 55:41–46.

[Bauschke *et al.* (2002)] Bauschke, H. H., Combettes, P. L., and Luke, D. R. (2002). Phase retrieval, error reduction algorithm, and Fienup variants: a view from convex optimization. *J. Opt. Soc. Am. A*, 19:1334–1345.

[Bayat *et al.* (2005)] Bayat, S., Apostol, L., Boller, E., Brochard, T., and Peyrin, F. (2005). In vivo imaging of bone micro-architecture in mice of with 3D synchrotron radiation micro-tomography. *Nucl. Instrum. Methods Phys. Res.*, A548:247–252.

[Bech (2009)] Bech, M. (2009). *X-ray imaging with a grating interferometer.* PhD thesis, University of Copenhagen.

[Beck and Teboulle (2009)] Beck, A. and Teboulle, M. (2009). A fast iterative shrinkage-thresholding algorithm for linear inverse problems. *SIAM J. Imaging Sci.*, 2:183–202.

[Becker and Bonse (1974)] Becker, B. P. and Bonse, U. (1974). The skew-symmetric two-crystal X-ray interferometer. *J. Appl. Cryst.*, 7:593–598.

[Beleggia *et al.* (2004)] Beleggia, M., Schofield, M. A., Volkov, V. V., and Zhu, Y. (2004). On the transport of intensity technique for phase retrieval. *Ultramicroscopy*, 102:37–49.

[Beltran *et al.* (2010)] Beltran, M. A., Paganin, D. M., Uesugi, K., and Kitchen, M. J. (2010). 2D and 3D X-ray phase retrieval of multi-material objects using a single defocus distance. *Opt. Express*, 18:6423–6436.

[Bilderback *et al.* (2005)] Bilderback, D., Elleaume, P., and Weckert, E. (2005). Review of third and next generation synchrotron light sources. *J. Phys. B: At. Mol. Opt. Phys.*, 38:S773–S797.

[Björck (1996)] Björck, A. (1996). *Numerical methods for least squares problems*. SIAM, Philadelphia, USA.

[Boettinger and Kuriyama (1979)] Boettinger, W. and Kuriyama, H. B. M. (1979). X-ray magnifier. *Rev. Sci. Instrum.*, 50:26–30.

[Bonse (1999)] Bonse, U. (1999). *Developments in X-ray tomography II*. SPIE (3772), Bellingham, WA, USA.

[Bonse and Hart (1965)] Bonse, U. and Hart, M. (1965). An X-ray interferometer. *Appl. Phys. Lett.*, 6:155–156.

[Born and Wolf (1997)] Born, M. and Wolf, E. (1997). *Principles of optics*. Cambridge University Press, United Kingdom.

[Bravin (2003)] Bravin, A. (2003). Exploiting the X-ray refraction contrast with an analyser: the state of the art. *J. Phys. D. Appl. Phys.*, 36:24–29.

[Bravin *et al.* (2007)] Bravin, A., Keyriläinen, J., and Fernandez, M. (2007). High-resolution CT by diffraction-enhanced X-ray imaging: mapping of breast tissue samples and comparison with their histopathology. *Phys. Med. Biol.*, 52:2197–2211.

[Bronnikov (2002)] Bronnikov, A. V. (2002). Theory of quantitative phase-contrast computed tomography. *J. Opt. Soc. Am. A*, 19:472–480.

[Burvall *et al.* (2011)] Burvall, A., Lundström, U., Takman, P. A. C., Larsson, D. H., and Hertz, H. M. (2011). Phase retrieval in X-ray phase-contrast imaging suitable for tomography. *Opt. Express*, 19:10359–10376.

[Cancedda *et al.* (2007)] Cancedda, R., Cedola, A., Giuliani, A., Komlev, V., Lagomarsino, S., Mastrogiacomo, M., Peyrin, F., and Rustichelli, F. (2007). Bulk and interface investigations of scaffolds and tissue-engineered bones by X-ray microtomography and X-ray microdiffraction. *Biomaterial*, 28:2505–2524.

[Candes *et al.* (2006)] Candes, E. J., Romberg, J., and Tao, T. (2006). Robust uncertainty principles: exact signal reconstruction from highly incomplete frequency information. *IEEE Trans. Inf. Theory*, 52:489–509.

[Candes *et al.* (2011)] Candes, E. J. ., Eldar, Y. C., Strohmer, T., and Voroninski, V. (2011). Phase retrieval via matrix completion. Technical report, http://arxiv.org/abs/1109.0573

[Candes and Li (2012)] Candes, E. J. and Li, X. (2012). Solving quadratic equations via PhaseLift when there are about as many equations as unknowns. Technical report, http://arxiv.org/abs/1208.6247.

[Castelli *et al.* (2011)] Castelli, E., Tonutti, M., Arfelli, F., Longo, R., Rigon, E. Q. L., Sanabor, D., Zanconati, F., Dreossi, D., Abrami, A., Quai, E., Bregant, P., Casarin, K., Chenda, V., Menk, R., Rokvic, T., Vascotto, A., Tromba, G., and Cova, M. (2011). Mammography with synchrotron radiation: first clinical experience with phase-detection technique. *Radiology.*, 259:684–694.

[Cecilia *et al.* (2011)] Cecilia, A., Rack, A., Douissard, P. -A., Martin, T., dos Santos Rolo, T., Vagovic, P., Hamanna, E., van de Kamp, T., Riedel, A., Fiederle, M., and Baumbach, T. (2011). LPE grown LSO:Tb scintillator films for high-resolution X-ray imaging applications at synchrotron light sources. *Nucl. Instrum. Methods Phys. Res. A*, 648:S321–S323.

[Chaari *et al.* (2009)] Chaari, L., Pustelnik, N., Chaux, C., and Pesquet, J. (2009). Solving inverse problems with overcomplete transforms and convex optimization techniques. *SPIE San Diego, Californie, USA*.

[Chapman *et al.* (1997)] Chapman, D., Thomlinson, W., Johnston, R. E., Washburn, D., Pisano, E., Gmur, N., Zhong, Z., Menk, R., Arfelli, F., and Sayers, D. (1997). Diffraction enhanced X-ray imaging. *Phys. Med. Biol.*, 42:2015–2025.

[Chappard *et al.* (2006)] Chappard, C., Basillais, A., Benhamou, L., Bonassie, A., Brunet-Imbault, B., Bonnet, N., and Peyrin, F. (2006). Comparison of synchrotron radiation and conventional X-ray microcomputed tomography for assessing trabecular bone microachitecture of human femoral heads. *Med. Phys.*, 33:3568–3577.

[Chaux *et al.* (2007)] Chaux, C., Combettes, P., Pesquet, J., and Wajs, V. (2007). A variationnal formulation for frame-based inverse problems. *Inverse Probl.*, 23:1495–1518.

[Clarke (2004)] Clarke, J. A. (2004). *The science and technology of undulators and wigglers*. Oxford University Press, USA.

[Cloetens *et al.* (1996)] Cloetens, P., Barrett, R., Baruchel, J., Guigay, J. P., and Schlenker, M. (1996). Phase objects in synchrotron radiation hard X-ray imaging. *J. Phys. D*, 29:133–146.

[Cloetens *et al.* (1997)a] Cloetens, P., Guigay, J. P., Martino, C. D., Baruchel, J., and Schlenker, M. (1997a). Fractional Talbot imaging of phase gratings with hard x rays. *Opt. Lett.*, 22:1059–1061.

[Cloetens *et al.* (1997)b] Cloetens, P., Pateyron-Salomé, M., Buffiere, J. Y., Peix, G., Baruchel, J., Peyrin, F., and Schlenker, M. (1997b). Observation of microstructure and damage in materials by phase sensitive radiography and tomography. *J. Appl. Phys.*, 81:5878–5886.

[Cloetens *et al.* (1999)] Cloetens, P., Ludwig, W., Baruchel, J., Guigay, J.-P., Pernot-Rejmànkovà, P., Salomé-Pateyron, M., Schlenker, M., Buffiere, J.-Y., Maire, E., and Peix, G. (1999). Hard X-ray phase imaging using simple propagation of a coherent synchrotron radiation beam. *J. Phys. D: Appl. Phys.*, 32:A145–A151.

[Cloetens (1999)] Cloetens, P. (1999). *Contribution to phase contrast imaging, reconstruction and tomography with hard synchrotron radiation.* PhD thesis, Vrije Universiteit Brussel, Belgium.

[Cloetens *et al.* (2002)] Cloetens, P., Ludwig, W., Boller, E., Helfen, L., Salvo, L., Mache, R., and Schlenker, M. (2002). Quantitative phase contrast tomography using coherent synchrotron radiation. *Proc. SPIE*, 4503:82–91.

[Cloetens *et al.* (2006)] Cloetens, P., Mache, R., Schlenker, M., and Lerbs-Mache, S. (2006). Quantitative phase tomography of Arabidopsis seeds reveals intercellular void network. *Proc. Nat. Acad. Sci.*, 103:14626–14630.

[Combettes and Wajs (2005)] Combettes, P. and Wajs, V. (2005). Signal recovery by proximal forward-backward splitting. *Multiscale Model. Simul.*, 4:1168–1200.

[Daubechies (1992)] Daubechies, I. (1992). *Ten lectures on wavelets.* SIAM, Philadelphia, PA, USA.

[Daubechies *et al.* (2004)] Daubechies, I., Defrise, M., and Mol, C. D. (2004). An iterative thresholding algorithm for linear inverse problems with a sparsity constraint. *Communi. Pure Appl. Math.*, 57:1413–1457.

[Daubechies *et al.* (2008)] Daubechies, I., Fornasier, M., and Loris, I. (2008). Accelerated projected gradient method for linear inverse problems with sparsity constraints. *J. Fourier Anal. Appl.*, 14:764–792.

[David *et al.* (2002)] David, C., Nohammer, B., Solak, H. H., and Ziegler, E. (2002). Differential X-ray phase contrast imaging using a shearing interferometer. *Appl. Phys. Lett.*, 81:3287–3289.

[Davis *et al.* (1995)] Davis, T., Gao, D., Gureyev, T., Stevenson, A., and Wilkins, S. (1995). Phase-contrast imaging of weakly absorbing materials using hard X-rays. *Nature*, 373:595–598.

[Davis and Wong (1996)] Davis, G. and Wong, S. (1996). X-ray microtomography of bones and teeth. *Physiol. Meas.*, 17:121–146.

[Dicken (1999)] Dicken, V. (1999). A new approach towards simultaneous activity and attenuation reconstruction in emission tomography. *Inverse Probl.*, 15:931–960.

[Diemoz *et al.* (2011)] Diemoz, P., Coan, P., Zanette, I., Bravin, A., Lang, S., Glaser, C., and Weitkamp, T. (2011). A simplified approach for computed tomography with an X-ray grating interferometer. *Opt. Express*, 19:1691–1698.

[Dilmanian *et al.* (2000)] Dilmanian, F. A., Zhong, Z., Ren, B., Wu, X. Y., Chapman, L. D., Orion, I., and Thomlinson, W. C. (2000). Computed tomography of X-ray index of refraction using the diffraction enhanced imaging method. *Phys. Med. Biol.*, 45:933–946.

[Donath *et al.* (2010)] Donath, T., Pfeiffer, F., Bunk, O., Grünzweig, C., Hempel, E., Popescu, S., Vock, P., and David, C. (2010). Toward clinical X-ray phase-contrast CT: Demonstration of enhanced soft-tissue contrast in human specimen. *Invest. Radiol.*, 45:445–452.

[Donoho (2006)] Donoho, D. (2006). Compressed sensing. *IEEE Trans. Inf. Theory*, 52:1289–1306.

[Douissard *et al.* (2010)] Douissard, P.-A., Cecilia, A., Martin, T., Chevalier, V., Couchaud, M., Baumbach, T., Dupre, K., Kuehbacher, M., and Rack, A. (2010). A novel epitaxially grown LSO-based thin-film scintillator for micro-imaging using hard synchrotron radiation. *J. Synchrotron Radiat.*, 17:571–583.

[Dupe *et al.* (2009)] Dupe, F., Fadili, J., and Starck, J. (2009). A proximal iteration for deconvolving Poisson noisy images using sparse representations. *IEEE Trans. Image Process.*, 18:310–321.

[Dyer (2001)] Dyer, S. A. (2001). *Survey of instrumentation and measurement*. New York: John Wiley, USA.

[Engelhardt *et al.* (2007)] Engelhardt, M., Baumann, J., Schuster, M., Kottler, C., Pfeiffer, F., Bunk, O., and David, C. (2007). High-resolution differential phase contrast

imaging using a magnifying projection geometry with a microfocus X-ray source. *Appl. Phys. Lett.*, 90:224101–224103.

[Engl *et al.* (1989)] Engl, H., Kunish, K., and Neubauer, A. (1989). Convergence rates for Tikhonov regularization of non-linear ill posed problems. *Inverse Probl.*, 5:523–540.

[Esser (2009)] Esser, E. (2009). Applications of Lagrangian-based alternating direction methods and connections to split Bregman. Technical report, ftp://ftp.math.ucla.edu/pub/camreport/cam09-31.pdf.

[Facchinei and Pang (2003)] Facchinei, F. and Pang, J. S. (2003). *Finite-dimensional variational inequalities and complementarity problems*. Springer Ser. Oper. Res., Springer-Verlag, New York, USA.

[Fiedler *et al.* (2004)] Fiedler, S., Bravin, A., and Keyriläinen, J. (2004). Imaging lobular breast carcinoma: comparison of synchrotron radiation DEI-CT technique with clinical CT, mammography and histology. *Phys. Med. Biol.*, 49:175–188.

[Fienup (1982)] Fienup, J. (1982). Phase retrieval algorithms: a comparison. *Appl. Opt.*, 21:2758–2769.

[Figueiredo and Nowak (2003)] Figueiredo, M. A. T. and Nowak, R. D. (2003). An EM algorithm for wavelet-based image restoration. *IEEE Trans. Image Process.*, 12:906–916.

[Gaass *et al.* (2012)] Gaass, T., Potdevin, G., Nol, P., Tapfer, A., Willner, M., Herzen, J., and Haase, A. (2012). Compressed sensing for phase contrast CT. *AIP Conference Proceedings*, 1466:150–153.

[Gilmore and Kelley (1985)] Gilmore, P. and Kelley, C. (1985). An implicit filtering algorithm for optimization of functions with many local minima. *SIAM J.Optm.*, 5:269–285.

[Desbat and Girard (1995)] Desbat, L. and Girard, D. (1995). The "minimum reconstruction-error" choice of regularization parameters: some more efficient methods and their application to deconvolution problems. *SIAM J. Scientific and Statistical Computing*, 16:1387–1403.

[Groso *et al.* (2006)] Groso, A., Stampanoni, M., Abela, R., Schneider, P., Linga, S., and Muller, R. (2006). Phase contrast tomography: an alternative approach. *Appl. Phys. Lett.*, 88:214104.

[Grubel *et al.* (2007)] Grubel, G., Stephenson, G., Gutt, C., Sinn, H., and Tschentscher, T. (2007). XPCS at the European X-ray free electron laser facility. *Nucl. Instrum. Methods Phys. Res.*, B262:357–367.

[Guigay (1977)] Guigay, J. (1977). Fourier transform analyis of Fresnel diffraction patterns in in-line holograms. *Optik*, 46:12–125.

[Guigay *et al.* (2007)] Guigay, J. P., Langer, M., Boistel, R., and Cloetens, P. (2007). A mixed contrast transfer and transport of intensity approach for phase retrieval in the Fresnel region. *Opt. Lett.*, 32:1617–1619.

[Gureyev (2003)] Gureyev, T. (2003). Composite techniques for phase retrieval in the Fresnel region. *Opt. Commun.*, 220:49–58.

[Gureyev *et al.* (1995)] Gureyev, T. E., Roberts, A., and Nugent, K. A. (1995). Partially coherent fields, the transport-of-intensity equation, and phase uniqueness. *J. Opt. Soc. Am. A*, 12:1942–1946.

[Gureyev *et al.* (1999)] Gureyev, T. E., Raven, C., Snigirev, A., Snigireva, I., and Wilkins, S. W. (1999). Hard X-ray quantitative non-interferometric phase-contrast microscopy. *J. Phys. D.:Appl. Phys.*, 32:563–567.

[Gureyev and Nugent (1996)] Gureyev, T. and Nugent, K. (1996). Phase retrieval with the transport of intensity equation. II. orthogonal series solution for non uniform illumination. *J. Opt. Soc. Am. A*, A13:1670–1682.

[Hale *et al.* (2007)] Hale, E., Yin, W., and Zhang, Y. (2007). A fixed-point continuation method for l1-regularized minimization with applications to compressed sensing. Technical report, Rice University, Houston,TX, http://www.caam.rice.edu/~zhang/reports/tr0707.pdf.

[Hanke (1991)] Hanke, M. (1991). Accelerated Landweber iterations for the solution of ill-posed equations. *Numer. Math.*, 60:341–373.

[Hanke *et al.* (1995)] Hanke, M., Neubauer, A., and Scherzer, O. (1995). A convergence analysis of the Landweber iteration for nonlinear ill-posed problems. *Numer. Math.*, 72:21–37.

[Hansen (1987)] Hansen, P. C. (1987). *Rank-deficient and discrete ill-posed Problems: Numerical aspects of linear inversion.* SIAM, Philadelphia, USA.

[Hofmann (2004)] Hofmann, A. (2004). *The physics of synchrotron radiation.* Cambridge University Press.

[Hofmann *et al.* (2011)] Hofmann, R., Moosmann, J., and Baumbach, T. (2011). Criticality in single-distance phase retrieval. *Opt. Express*, 19:25881–25890.

[Hsieh (2003)] Hsieh, J. (2003). *Computed tomography: principles, design, artifacts, and recent advances.* SPIE Press, Bellingham, WA, USA.

[Ingal and Beliaevskaya (1995)] Ingal, V. N. and Beliaevskaya, E. A. (1995). X-ray plane-wave topography observation of the phase contrast from a non-crystalline object. *J. of Physics D*, 28:2314–2317.

[Ito *et al.* (2006)] Ito, M., Ejiri, S., Jinnai, H., Kono, J., Ikeda, S., Nishida, A., Uesugi, K., Yagi, N., Tanaka, M., and Hayashi, K. (2006). Bone structure and mineralization demonstrated using synchrotron radiation computed tomography (SR-CT) in animal models: preliminary findings. *J. Bone Miner. Metab.*, 21:3568–3577.

[Kak and Slaney (1989)] Kak, A. C. and Slaney, M. (1989). *Principles of computerized tomographic imaging*. IEEE Press, New York, USA.

[Kazakia *et al.* (2008)] Kazakia, G. J., Burghardt, A. J., Cheung, S., and Majumdar, S. (2008). Assessment of bone tissue mineralization by conventional X-ray microcomputed tomography. *Med. Phys.*, 33:3170–3179.

[Kelley (1999)] Kelley, C. (1999). *Iterative methods for optimization*. SIAM, Philadelphia, USA.

[Kostenko *et al.* (2013)] Kostenko, A., Batenburg, K. J., King, A., Offerman, S. E., and van Vlie, L. J. (2013). Total variation minimization approach in in-line X-ray phase-contrast tomography. *Opt. Express*, 21:12185–12196.

[Koyama *et al.* (2003)] Koyama, I., Yoshikawa, H., and Momose, A. (2003). Phase-contrast X-ray imaging with a triple-Bragg-case interferometer. *Jpn. J. Appl. Phys.*, 42:80–82.

[Krol (2011)] Krol, A. (2011). *Holography, research and technologies: Chapter 21: "In-line hard X-ray holography for biomedical imaging"*, INTECH, http://www.intechopen.com/books/holography-research-and-technologies/in-line-hard-X-ray-holography-for-biomedical-imaging.

[Labiche *et al.* (2007)] Labiche, J. C., Mathon, O., Pascarelli, S., Newton, M. A., Ferre, G. G., Curfs, C., Vaughan, G., Homs, A., and Carreiras, D. F. (2007). The fast readout low noise camera as a versatile X-ray detector for time resolved dispersive extended X-ray absorption fine structure and diffraction studies of dynamic problems in materials science, chemistry, and catalysis. *Rev. Sci. Instrum.*, 78:091301.

[Langer *et al.* (2008)] Langer, M., Cloetens, P., Guigay, J., and Peyrin, F. (2008). Quantitative comparison of direct phase retrieval algorithms in in-line phase tomography. *Med. Phys.*, 35:4556–4565.

[Langer *et al.* (2009)] Langer, M., Cloetens, P., and Peyrin, F. (2009). Fourier-wavelet regularization of phase retrieval in X-ray in line phase tomography. *J. Opt. Soc. Am. A*, 28:1877–1882.

[Langer *et al.* (2010)] Langer, M., Cloetens, P., and Peyrin, F. (2010). Regularization of phase retrieval with phase attenuation duality prior for 3D holotomography. *IEEE Trans. Image Process.*, 19:2425–2436.

[Langer *et al.* (2012)a] Langer, M., Cloetens, P., Pacureanu, A., and Peyrin, F. (2012a). X-ray in-line phase tomography of multimaterial objects. *Opt. Lett.*, 37:2151–2153.

[Langer *et al.* (2012)b] Langer, M., Pacureanu, A., Suhonen, H., Grimal, Q., Cloetens, P., and Peyrin, F. (2012b). X-ray phase nanotomography resolves the 3D human bone ultrastructure. *PLoS ONE*, 7:e35691.

[Langer *et al.* (2013)] Langer, M., Cloetens, P., Hesse, B., Suhonen, H., Pacureanu, A., Raum, K., and Peyrin, F. (2013). Priors for X-ray in-line phase tomography of heterogeneous objects. *Phil. Trans. A.*, In press.

[Lewis (2004)] Lewis, R. (2004). Medical phase contrast X-ray imaging: current status and future prospects. *Phys. Med. Biol.*, 49:3573–3583.

[Mallat (1999)] Mallat, S. (1999). *A Wavelet tour of signal processing.* Academic Press.

[Margaritondo *et al.* (2003)] Margaritondo, G., Hwu, Y., and Tromba, G. (2003). Synchrotron light: From basics to coherence and coherence-related applications. *Synchrotron radiation: fundamantals, methodologies and application (SIF Bologna)*, 25–53.

[Marinescu *et al.* (2013)] Marinescu, M., Langer, M., Durand, A., Olivier, C., Chabrol, A., Rositi, H., Chauveau, F., Cho, T. H., Nighoghossian, N., Berthezène, Y., Peyrin, F., and Wiart, M. (2013). Synchrotron radiation micro-computed tomography as a new method to detect iron oxide nanoparticles in the brain. *Mol. Imaging Biol.*, Epub ahead of print.

[Martin and Koch (2006)] Martin, T. and Koch, A. (2006). Recent developments in X-ray imaging with micrometer spatial resolution. *J. Synchrotron Radiat.*, 13:180–194.

[Mayo *et al.* (2003)] Mayo, S. C., Davis, T., Gureyev, T., Miller, P., Paganin, D., Pogany, A., Stevenson, A., and Wilkins, S. W. (2003). X-ray phase-contrast microscopy and microtomography. *Opt. Express*, 11:2289–2302.

[Mayo *et al.* (2012)] Mayo, S. C., Stevenson, A. W., and Wilkins, S. W. (2012). In-line phase-contrast X-ray imaging and tomography for materials science. *Materials*, 5:937–965.

[Millson (2002)] Millson, D. M. (2002). *Third-generation hard X-ray synchrotron radiation sources: source properties, optics, and experimental techniques.* John Wiley, INC.

[Modregger *et al.* (2007)] Modregger, P., Lübbert, D., Schäfer, P., and Köhler, R. (2007). Two dimensional diffraction enhanced imaging algorithm. *Appl. Phys. Lett.*, 90:193501–193503.

[Mollenhauer *et al.* (2002)] Mollenhauer, J., Aurich, M., and Zhong, Z. (2002). Diffraction-enhanced X-ray imaging of articular cartilage. *Osteoarthr. Cartilage*, 10:163–171.

[Momose (1995)] Momose, A. (1995). Demonstration of phase-contrast X-ray computed tomography using X-ray interferometer. *Nucl. Inst. and Meth. in Phys. Research A*, 352:622–628.

[Momose and Fukuda (1995)a] Momose, A. and Fukuda, J. (1995). Phase-contrast radiographs of nonstained rat cerebellar specimen. *Med. Phys.*, 22:375–380.

[Momose *et al.* (1995)b] Momose, A., Takeda, T., and Itai, Y. (1995). Phase-contrast X-ray computed tomography for observing biological specimens and organic materials. *Rev. Sci. Instrum.*, 66:1434–1436.

[Momose *et al.* (1996)] Momose, A., Takeda, T., Itai, Y., and Hirano, K. (1996). Phase-contrast X-ray computed tomography for observing biological tissues. *Nat. Med.*, 2:473–475.

[Momose *et al.* (1998)] Momose, A., Takeda, T., Itai, Y., Yoneyama, A., and Hirano, K. (1998). Phase-contrast tomographic imaging using an X-ray interferometer. *J. Synchrotron Radiat.*, 5:309–314.

[Momose *et al.* (2003)] Momose, A., Kawamoto, S., Koyama, I., Hamaishi, Y., Takai, K., and Suzuki, Y. (2003). Demonstration of X-ray Talbot interferometry. *Jpn. J. Appl. Phys*, 42:L866–L868.

[Momose *et al.* (2009)a] Momose, A., Yashiro, W., Maikusa, H., and Takeda, Y. (2009a). High-speed X-ray phase imaging and X-ray phase tomography with Talbot interferometer and white synchrotron radiation. *Opt. Express*, 17:12540–12545 (2009).

[Momose *et al.* (2009)b] Momose, A., Yashiro, W., and Takeda, Y. (2009b). *X-ray phase imaging with Talbot interferometry, biomedical mathematics: promising directions in imaging, therapy planning, and inverse problems*, 281–320, Medical Physics Pub Corp.

[Moosmann *et al.* (2010)] Moosmann, J., Hofmann, R., Bronnikov, A., and Baumbach, T. (2010). Nonlinear phase retrieval from single-distance radiograph. *Opt. Express*, 18:25771–25785.

[Moosmann *et al.* (2011)] Moosmann, J., Hofmann, R., and Baumbach, T. (2011). Single-distance phase retrieval at large phase shifts. *Opt. Express*, 19:12066–12073.

[Moosmann *et al.* (2013)] Moosmann, J., Ershov, A., Altapova, V., Baumbach, T., Prasad, M. S., LaBonne, C., Xiao, X., Kashef, J., and Hofmann, R. (2013). X-ray phase-contrast in vivo microtomography probes new aspects of Xenopus gastrulation. *Nature* , 497:374–378.

[Morozov (1984)] Morozov, V. A. (1984). *Methods for solving incorrectly posed problems.* New York: Springer, USA.

[Mukherjee and Seelamantula (2012)] Mukherjee, S. and Seelamantula, C. S. (2012). An iterative algorithm for phase retrieval with sparsity constraints: application to frequency domain optical coherence tomography. *Proc. IEEE Int. Conf. Acoust. Speech and Sig. Proc., Kyoto, Japan*, 553–556.

[Namkung (2010)] Namkung, W. (2010). Review of the third generation light sources. *Int. Particle Accelerator Conf., Kyoto, Japan*.

[Nesterov (2005)] Nesterov, Y. (2005). Smooth minimization of non-smooth functions. *Math. Program.*, 103:127–152.

[Neubauer (1989)] Neubauer, A. (1989). Tikhonov regularisation for non-linear ill-posed problems: optimal convergence rates and finite-dimensional approximation. *Inverse Probl.*, 5:541–557.

[Newton (2012)] Newton, M. C. (2012). Compressed sensing for phase retrieval. *Phys. Rev. E*, 85:056706.

[Nugent *et al.* (1996)] Nugent, K. A., Gureyev, T., Cookson, D., Paganin, D., and Barnea, Z. (1996). Quantitative phase imaging using hard X-rays. *Phys. Rev. Lett.*, 77:2961–2964.

[Nugent (2010)] Nugent, K. A. (2010). Coherent methods in the X-ray sciences. *Adv. Phys.*, 59:1–99.

[Nuzzo *et al.* (2002)] Nuzzo, S., Peyrin, F., Cloetens, P., Baruchel, J., and Boivin, G. (2002). Quantification of the degree of mineralization of bone in three dimensions using synchrotron radiation microtomograph. *Med. Phys.*, 29:2672–2681.

[Ohlsson *et al.* (2012)] Ohlsson, H., Yang, A., Dong, R., and Sastry, S. (2012). CPRL - an extension of compressive sensing to the phase retrieval problem. *Neural Information Processing Systems (NIPS), Nevada, USA*.

[Onuki and Elleaume (2002)] Onuki, H. and Elleaume, P. (2002). *Undulators, wigglers and their applications.* CRC Press.

[Paganin (2006)] Paganin, D. (2006). *Coherent X-ray optics.* Oxford University Press, New York, USA.

[Paganin *et al.* (2002)] Paganin, D., Mayo, S. C., Gureyev, T., Miller, P. R., and Wilkins, S. W. (2002). Simultaneous phase and amplitude extraction from a single defocused image of a homogeneous object. *J. Microsc.*, 206:33–40.

[Paganin and Nugent (1998)] Paganin, D. and Nugent, K. A. (1998). Noninterferrometric phase imaging with partially coherent light. *Phys. Rev. Lett.*, 80:2586–2589.

[Pagot *et al.* (2003)] Pagot, E., Cloetens, P., Fiedler, S., Bravin, A., Coan, P., Baruchel, J., Härtwig, J., and Thomlinson, W. (2003). A method to extract quantitative information in analyzer-based X-ray phase contrast imaging. *Appl. Phys. Lett.*, 82:3421–3423.

[Passty (1979)] Passty, G. B. (1979). Ergodic convergence to a zero of the sum of monotone operators in Hilbert space. *J.Math. Anal. Appl.*, 72:383–390.

[Pavlov *et al.* (2004)] Pavlov, K. M., Gureyev, T. E., Paganin, D., Nesterets, Y. I., Morgan, M. J., and Lewis, R. A. (2004). Linear systems with slowly varying transfer functions and their application to X-ray phase-contrast imaging. *J. Phys. D Appl. Phys.*, 37:2746–2750.

[Peyrin and Engelke (2012)] Peyrin, F. and Engelke, K. (2012). *Handbook of Particle Detection and Imaging: CT Imaging: Basics and New Trends*, 883–915, S. Verlag.

[Pfeiffer *et al.* (2006)] Pfeiffer, F., Weitkamp, T., Bunk, O., and David, C. (2006). Phase retrieval and differential phase-contrast imaging with low-brilliance X-ray sources. *Nature Phys.*, 2:258–261.

[Phillips *et al.* (2002)] Phillips, W., Stewart, A., Naday, M. S. I., and Ingersoll, C. (2002). High-sensitivity CCD-based X-ray detector. *J. Synchrotron Radiat.*, 9:36–43.

[Ramlau (2002)] Ramlau, R. (2002). A steepest descent algorithm for the global minimization of the Tikhonov functional. *Inverse Probl.*, 18:381–405.

[Ramlau and Teschke (2006)] Ramlau, R. and Teschke, G. (2006). A Tikhonov-based projection iteration for nonlinear ill-posed problems with sparsity constraints. *Numer. Math.*, 104:177–203.

[Raoux (1993)] Raoux, D. (1993). *Introduction to synchrotron radiation and to the physics of storage rings.* Neutron and synchrotron radiation for condensed matter studies, Volume I: Theory, instruments and methods (1993), 37–78.

[Rose (1946)] Rose, A. (1946). A unified approach to the performance of photographic film, television pickup tubes, and the human eye. *J. Smpe.*, 47:273–294.

[Salomé *et al.* (1999)] Salomé, M., Peyrin, F., Cloetens, P., Odet, C., Laval-Jeantet, A., Baruchel, J., and Spanne, P. (1999). A synchrotron radiation microtomography system for the analysis of trabecular bone samples. *Med. Phys.*, 26:2194–2204.

[Sanchez del Rio and Dejus (2004)] Sanchez del Rio, M. and Dejus, R. (2004). Status of XOP: an X-ray optics software toolkit. *Proc. SPIE*, 5536: 171–174.

[Scherzer *et al.* (1993)] Scherzer, O., Engl, H., and Kunisch, K. (1993). Optimal a posteriori parameter choice for Tikhonov regularization for solving nonlinear ill-posed problems. *SIAM J. Numer. Anal.*, 30:1796–1838.

[Scherzer *et al.* (2008)] Scherzer, O., Grasmair, M., Grossauer, H., Haltmeier, M., and Lenzen, F. (2008). *Variationnal methods in imaging.* Springer Verlag, New York, USA.

[Shannon and Weaver (1964)] Shannon, C. and Weaver, W. (1964). *The matehematical theory of communication.* The University of Illiniois Press: Urbana.

[Snigireva *et al.* (1995)] Snigireva, A., Kohn, I., Kuznetsov, V., and Schelokov, I. (1995). On the possibilities of X-ray phase contrast microimaging by coherent high-energy synchroton radiation. *Rev. Sci. Instrum.*, 66:5486–5492.

[Spanne *et al.* (1999)] Spanne, P., Raven, C., Snigireva, I., and Snigirev, A. (1999). In-line holography and phase-contrast microtomography with high energy X-rays. *Phys. Med. Biol.*, 44:741–749.

[Stampanoni *et al.* (2006)] Stampanoni, M., Borchert, G., and Abela, R. (2006). Progress in microtomography with the Bragg magnifier at SLS. *Rad. Phys. and Chem.*, 75:1956–1961.

[Stoneking *et al.* (1992)] Stoneking, D., Bilbro, G., Trew, R., Gilmore, P., and Kelley, C. (1992). Yield optimization using a GaAs process simulator coupled to a physical device model. *IEEE T. Microw. Theory*, 1353–1363.

[Strang and Nguyen (1996)] Strang, G. and Nguyen, T. (1996). *Wavelets and filter banks.* Wellesley College; 2nd edition.

[Suleski (1997)] Suleski, T. J. (1997). Generation of Lohmann images from binary-phase Talbot array illuminators. *Appl. Opt.*, 36:4686–4691.

[Tafforeau *et al.* (2006)] Tafforeau, P., Boistel, R., Boller, E., Bravin, A., Brunet, M., Chaimanee, Y., Cloetens, P., Feist, M., Hoszowska, J., Jaeger, J., Kay, R., Lazzari, V., Marivaux, L., Nel, A., Nemoz, C., Thibault, X., Vignaud, P., and Zabler, S. (2006). Applications of X-ray synchrotron microtomography for non-destructive 3D studies of paleontological specimens. *Appl. Phys. A*, 83:195–202.

[Takeda *et al.* (1995)] Takeda, T., Momose, A., Itai, Y., Wu, J., and Hirano, K. (1995). Phase-contrast imaging with synchrotron X-rays for detecting cancer lesions. *Acad. Radiol.*, 2:799–803.

[Talbot (1836)] Talbot, H. F. (1836). Facts related to optical science. *Phil. Mag.*, 9:401–407.

[Teague (1982)] Teague, M. R. (1982). Irradiance moments: their propagation and use for unique retrieval of phase. *J. Opt. Soc. Am. A*, 72:1199–1209.

[Teague (1983)] Teague, M. R. (1983). Deterministic phase retrieval: a Green's function solution. *J. Opt. Soc. Am. A*, 73:1434–1441.

[Teschke and Ramlau (2007)] Teschke, G. and Ramlau, R. (2007). An iterative algorithm for nonlinear inverse problems with joint sparsity constraints in vector valued regimes and an application to color image inpainting. *Inverse Probl.*, 23:1851–1870.

[Tikhonov and Arsenin (1977)] Tikhonov, A. and Arsenin, V. (1977). *Solutions of ill-posed problems*. VH Winston and Sons, Washington, DC, USA.

[Turner *et al.* (2004)] Turner, L., Dhal, B., Hayes, J., Mancuso, A., Nugent, K., Paterson, D., Scholten, R., Tran, C., and Peele, A. (2004). X-ray phase imaging: demonstration of extended conditions for homogeneous objects. *Opt. Express*, 12:2960–2965.

[Vetterli and Kovacevic (1995)] Vetterli, M. and Kovacevic, J. (1995). *Wavelets and subband coding*. Prentice Hall PTR, Englewood Cliffs, New Jersey, USA.

[Vogel (2002)] Vogel, C. R. (2002). *Computational methods for inverse problems*. SIAM.

[Waldspurger *et al.* (2012)] Waldspurger, I., D'Aspremont, A., and Mallat, S. (2012). Phase recovery, MaxCut and complex semidefinite programming. Technical report http://arxiv.org/abs/1206.0102.

[Wang (2007)] Wang, Y. (2007). Intuitive dimensional analyses of the energy and atomic number dependences of the cross sections for radiation interaction with matter. *J. X-Ray Sci. Technol.*, 15:169—175.

[Weitkamp *et al.* (2005)] Weitkamp, T., Diaz, A., David, C., Pfeiffer, F., Stampanoni, M., Cloetens, P., and Ziegler, E. (2005). X-ray phase imaging with a grating interferometer. *Opt. Express*, 13:6296–6304.

[Weitkamp *et al.* (2008)] Weitkamp, T., David, C., Bunk, O., Bruder, J., Cloetens, P., and Pfeiffer, F. (2008). X-ray phase radiography and tomography of soft tissue using grating interferometry. *Eur. J. Radiol.*, 68:13–17.

[Weitkamp *et al.* (2010)] Weitkamp, T., Tafforeau, P., Boller, E., Cloetens, P., Valade, J. P., Bernard, P., Peyrin, F., Ludwig, W., Helfen, L., and Baruchel, J. (2010). Status and evolution of the ESRF beamline ID19. *AIP Conference Proceedings*, 1221.

[Weitkamp *et al.* (2011)] Weitkamp, T., Haas, D., Wegrzynek, D., and Rack, A. (2011). AnkaPhase: software for single-distance phase retrieval from inline X-ray phase-contrast radiographs. *J. Synchrotron Radiat.*, 18:617–629.

[Wilkins *et al.* (1996)] Wilkins, S. W., Gureyev, T., Gao, D., Pogany, A., and Stevenson, A. W. (1996). Phase contrast imaging using polychromatic hard x-rays. *Nature*, 384:335–337.

[Wright *et al.* (2009)] Wright, S., Nowak, R., and Figueiredo, M. (2009). Sparse reconstruction by separable approximation. *IEEE Trans. Signal. Process.*, 57:2479–2493.

[Wu *et al.* (2005)] Wu, X., Liu, H., and Yan, A. (2005). X-ray phase-attenuation duality and phase retrieval. *Opt. Letters*, 30:379–381.

[Zabler *et al.* (2005)] Zabler, S., Cloetens, P., Guigay, J.-P., Baruchel, J., and Schlenker, M. (2005). Optimization of phase contrast imaging using hard X-rays. *Rev. Sci. Instrum.*, 76:1–7.

[Zanette (2011)] Zanette, I. (2011). *Interférométrie X à réseaux pour l'imagerie et l'analyse de front d'ondes au synchrotron.* PhD thesis, École Doctorale de Physique, Grenoble, France.

[Zhou and Brahme (2008)] Zhou, S. and Brahme, A. (2008). Development of phase-contrast X-ray imaging techniques and potential medical applications. *Physica Medica.*, 24:129–148.

FOLIO ADMINISTRATIF

THESE SOUTENUE DEVANT L'INSTITUT NATIONAL DES SCIENCES APPLIQUEES DE LYON

NOM : **DAVIDOIU** DATE de SOUTENANCE : 26 Septembre 2013
Prénoms : Valentina-Geta

TITRE : Approches non linéaire en imagerie de phase par rayons X dans le domaine de Fresnel

NATURE : Doctorat **Numéro d'ordre** : 2013-ISAL-0089

Ecole doctorale : Electronique, Electrotechnique, Automatique

Spécialité : Images et Systèmes

RESUME :

Le développement de sources cohérentes de rayons X offre de nouvelles possibilités pour visualiser les structures biologiques à différentes échelles en exploitant la réfraction des rayons X. La cohérence des sources synchrotron de troisième génération permettent des implémentations efficaces des techniques de contraste de phase. Une des premières mesures des variations d'intensité dues au contraste de phase a été réalisée en 1995 à l'Installation Européenne de Rayonnement Synchrotron (ESRF). L'imagerie de phase couplée à l'acquisition tomographique permet une imagerie tridimensionnelle avec une sensibilité accrue par rapport à la tomographie standard basée sur absorption. Cette technique est particulièrement adaptée pour les échantillons faiblement absorbante ou bien présentent des faibles différences d'absorption. Le contraste de phase a ainsi une large gamme d'applications, allant de la science des matériaux, à la paléontologie, en passant par la médecine et par la biologie. Plusieurs techniques de contraste de phase aux rayons X ont été proposées au cours des dernières années. Dans la méthode de contraste de phase basée sur le phénomène de propagation l'intensité est mesurée pour différentes distances de propagation obtenues en déplaçant le détecteur.

Bien que l'intensité diffractée puisse être acquise et enregistrée, les informations de phase du signal doivent être "récupérées" à partir seulement du module des données mesurées. L'estimation de la phase est donc un problème inverse non linéaire mal posé et une connaissance a priori est nécessaire pour obtenir des solutions stables. Si la plupart de méthodes d'estimation de phase reposent sur une linéarisation du problème inverse, les traitements non linéaires ont été eux très peu étudiés. Le but de ce travail était de proposer et d'évaluer des nouveaux algorithmes, prenant en particulier en compte la non linéarité du problème direct.

Dans la première partie de ce travail, nous présentons un schéma de type Landweber non linéaire itératif pour résoudre le problème de la récupération de phase. Cette approche utilise l'expression analytique de la dérivée de Fréchet de la relation phase-intensité et de son adjoint. Nous étudions aussi l'effet des opérateurs de projection sur les propriétés de convergence de la méthode. Dans la deuxième partie de cette thèse, nous étudions la résolution du problème inverse linéaire avec un algorithme en coordonnées ondelettes basé sur un seuillage itératif. Par la suite, les deux algorithmes sont combinés et comparés avec une autre approche non linéaire basée sur une régularisation parcimonieuse et un algorithme de point fixe. Les performances des algorithmes sont évaluées sur des données simulées pour différents niveaux de bruit. Enfin, les algorithmes ont été adaptés pour traiter des données réelles acquises en tomographie de phase à l'ESRF à Grenoble.

MOTS-CLES : Contraste de phase, récupération de la phase du rayon X, diffraction de Fresnel, l'imagerie cohérente, problème inverse, problème non linéaire, dérivée de Fréchet, imagerie par rayons X, microscopie à rayons X, tomographie de phase en ligne, optimisation non linéaire.

Laboratoire (s) de recherche :

CREATIS (CNRS UMR 5520, INSERM U630)

Directeur de thèse:
Dr. Bruno SIXOU Maître de Conférence INSA

co-Directeur de thèse:
Dr. Françoise PEYRIN Directeur de recherche INSERM

Président de jury :

Composition du jury : Prof. Laurent DESBAT Rapporteur
Prof. Tilo BAUMBACH Rapporteur
Prof. Ali Mohammad DJAFARI Examinateur
Dr. Peter CLOETENS Examinateur
Dr. Max LANGER Invité